Optimisation de la mesure de champ de déformation à haute température et caractérisation thermomécanique de matériaux réfractaires d'alumine spinelle

Robert Piotr Kaczmarek

Ph.D. Thesis

University of Limoges

Doctoral School n°609: Materials Science and Engineering, Applied Mechanics and Energetics (SIMME)

Institute of Research for Ceramics (IRCER)

Thesis submitted for the degree of

Doctor of Philosophy of the University of Limoges

Specialization: Ceramic Materials and Surface Treatments

Presented by

Robert Piotr KACZMAREK

on 22nd December 2021

Improvement of strain field monitoring at high temperature and thermomechanical characterization of alumina spinel refractory materials

Supervised by Mr. Marc HUGER, Mr. Ion-Octavian POP and Mr. Jean-Christophe DUPRE

JURY:

President of the Jury

Mr. Nicolas Schmitt, Professor, LMT, Paris-Saclay University

Reviewers

Mr. Dietmar Gruber, Associate Professor, Chair of Ceramics, Montanuniversität Leoben (Austria)

Mr. Giovanni Bruno, Professor, BAM Berlin, Potsdam University (Germany)

Examiners

Mr. Marc Huger, Professor, IRCER, University of Limoges

Mr. Jean-Christophe Dupré, CNRS Researcher, Pprime Institute, University of Poitiers

Mr. Ion-Octavian Pop, Associate Professor, GC2D, University of Limoges

Invited

Mr. Eric Blond, Professor, LaMé, University of Orléans

Mr. Christoph Wöhrmeyer, Science & Technology Director, Imerys (Germany)

Mr. Sido Sinnema, Knowledge Group Leader, Tata Steel Europe (Netherlands)

Rights

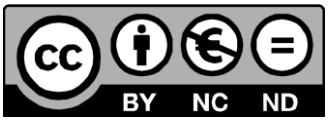

Acknowledgements

This PhD study is a part of ITN-ETN (Innovative European Training Network) ATHOR project (standing for “Advanced Thermomechanical multiscale modelling of Refractory linings”). This research project was supported by the European Commission through the funding scheme of Horizon 2020 Marie Skłodowska-Curie Actions (grant No. 764987). First and foremost, I would like to express my utmost gratitude to everyone involved in preparation and execution of the successful ATHOR proposal. This funding, being so far very exceptional in the field of refractory materials, opened a whole range of opportunities both for involved institutional members and for early stage researchers (including myself). For many of us, participation in this project was a life-changing experience and we are proud of conquering challenges as an ATHOR team working together with the key academic and industrial partners from refractory fields.

I would like to begin more personal acknowledgements by sincere thanking Marc Huger - coordinator of ATHOR and my main supervisor from the University of Limoges. His almost unlimited availability in scientific discussions and insightful criticism allowed me to successfully complete all topics assigned to my position. Moreover, his great passion for refractory materials inspired me to continue my career in this field (what is in line with educational objectives of ATHOR project and FIRE network).

My sincere thanks also go to Jean-Christophe Dupre and Pascal Doumalin, my supervisors from the University of Poitiers, for providing precious scientific advices during the whole period of my PhD studies and for sharing hands-on expertise related to usage of their own Digital Image Correlation (DIC) softwares. Great thanks also go to Octavian Pop, my supervisor from the University of Limoges (located in Egleton), for his strong support in scientific discussions.

Beside my supervisors, I would like to express utmost gratitude to the jury members, including Nicolas Schmitt, Dietmar Gruber, Giovanni Bruno, as well as Eric Blond, Christoph Wöhrmeyer and Sido Sinnema. It was a great honour to receive insightful feedbacks on my work from such experienced researchers and to see how many of you decided to attend my PhD defence in person in Limoges despite Covid’19 pandemic.

Special thanks go to Cyrille Deteuf and Christoph Wöhrmeyer, my industrial mentors from Imerys, for fruitful discussions, openness and strong support. My sincere thanks also go to the whole Tata Steel CRC team, especially to Sido Sinnema, Pieter Put, Bruno Luchini, Kirill Andreev, Stefan Melzer and Enno Zinngrebe for making a very supportive and pleasant working environment during my secondment at their laboratory. It was great to learn from you and to experience how researchers in industrial environment can enjoy

their work. I would also like to thank the team of Eric Blond from the University of Orleans, in particular Lucas Teixeira, Toum Cam and Jean Gillibert for sharing their hands-on experience with high temperature mechanical tests and for common discussions on progress of my study.

I am also very grateful to all my friends and colleagues from Poland (in particular from Pila and Wroclaw), France (especially from Limoges) and other places for many great moments during this challenging time. I am especially happy that I could work at IRCER Axe 4 with many great young scientists such as Diana, Aliz, Karolina, Siham, Andrzej, Farid, Imad, Thi, Raphael and Guy. ATHOR PhD students created even more international network and we had together many unforgettable experiences in different places of the glob, including in France, Italy, Belgium Austria, Germany, the Netherlands, Japan, China, and in the USA. We worked together, we faced similar challenges and we had a lot of fun.

Last but not least, I would like to thank my family, in particular my father Leszek, and my girlfriend Klaudia for continuous support, being proud of my achievements on the educational path and for daily dose of happiness.

Contribution of all of you made this challenging journey very pleasant and successful. Once again, many thanks to each and every inveacholved person from the bottom of my heart!

Table of contents

Introduction

Refractories are ceramic materials designed to operate in harsh conditions, including high temperatures, severe thermal shocks, corrosive environments and thermomechanical loadings. They are indispensable i.a. in cost-effective production of many popular materials, including metals, glasses and cements. It implies that each user of daily life products, being made of these materials, also indirectly consumes some refractories. Over the years, their design developed significantly, leading to improved safety, lower environmental impact, prolonged service life, higher quality of final products (fewer defects, stricter tolerances) and optimized production costs.

The present study was performed with a rather wide scope thanks to friendly cooperation between European partners working on improvement of refractories. This crucial cooperation originates from FIRE network (abbreviation of “Federation for International Refractory Research and Education”) that promotes education of young researchers within a network consisting of academic and industrial partners. Relationships developed in framework of FIRE became a cornerstone for foundation of a European ITN-ETN ATHOR project (standing for ”Advanced THermomechanical multiscale mOdelling of Refractory linings”). This project gave unique chances to 15 PhD students to develop their skills in a network consisting of 7 academic and 8 industrial partners. Such partnership was helpful in this particular study to access different research centres, including IRCER laboratory (University of Limoges in France), LaMé laboratory (Polytech Orléans in France) and Ceramics Research Centre (Tata Steel Europe in the Netherlands).

ATHOR project was dedicated to iron & steel industry which correspond to the highest share of refractories consumption among all industries. More specifically, the core of this project was exclusively focussed on steel ladle, a vessel accounting for the highest consumption of refractories in the whole steelmaking process. The fifteen involved PhD students cooperated to **improve prediction of the lining’s performance by numerical modelling** (using finite element and discrete element methods). In this general context, the present PhD work aimed to provide accurate material parameters (as input parameters), as well as innovative characterization methods with target application in validation of numerical approaches. Despite this strong focus of the project on modelling, the present PhD thesis is mainly

focused on experimental results with two general objectives, which are briefly described in two following paragraphs.

The first is to **better understand in-use behaviour of alumina spinel refractories** to enable future product improvements. In particular, the focus is on thermomechanical behaviour in relation to microstructural changes. Investigated alumina spinel materials have been selected for this study thanks to outstanding performance, high popularity and not well-known thermomechanical behaviour (in particular concerning alumina spinel bricks). They are often selected in steelmaking thanks to their carbon-free composition (no carbon pickup by steel) and low wear rate in several zones of steel ladle (possible increase of ladle capacity by reduction of lining thickness).

The second general objective of this study concerns **improvements of innovative devices**, mainly related to accurate strain field monitoring at high temperature. In this context, investigations involving two different experimental setups have been performed. The first one, being dedicated to high-temperature mechanical tests, has been **improved to monitor kinematic fields at higher temperature** (than before) **and with increased precision**. With this aim, a particular investigation has been carried out to optimize speckle pattern preparation and numerical pre-treatments of recorded images. The second considered experimental setup is an advanced thermal shock bench (ATHORNA, standing for “Advanced measurement for in-situ thermo-mechanical monitoring of large sample under thermal gradient”). On one hand, it was used to attempt **validation of numerical model** and, on the other hand, to verify potential application in comparison of materials resistance to thermal shocks (performed on magnesia-based materials exhibiting significant differences in fracture behaviour). Considering the above-mentioned points, the structure of this PhD manuscript is organized as follows.

The first chapter introduces the key aspects about steelmaking, application vessel (with key wearing mechanisms), materials design and exemplary behaviours. This chapter summarizes the current state-of-the-art being relevant for understanding different fields discussed in this PhD thesis.

The second chapter firstly introduces ATHOR with contribution of the present study to this project. Then, the main microstructural characterization methods and rather conventional thermo-physical techniques are briefly presented.

The third chapter is focused on strain field and crack monitoring at high temperature. Its first half introduces particular experimental methods related to strain field measurements. Then, the second half presents the study on improvement of experimental setup for high-temperature mechanical tests coupled with optical measurements. A special attention has been paid to investigation of different speckle patterns and related numerical treatments aiming to optimize displacement and strain fields measurements at high temperature.

The fourth chapter deals with investigations performed on alumina spinel refractories. The first section focuses on an industrial alumina spinel brick, in particular, on evolution of its microstructure with related thermomechanical properties. The second section is dedicated to model alumina spinel castables with a special focus on impact of different components (aggregates, reactive aluminas and cements) on evolution of castable microstructure and thermomechanical properties.

The fifth chapter is devoted to improvement of the novel thermal shock monitoring device (ATHORNA) and is divided in two parts. The first section introduces recently developed capabilities of the device related to experimental measurements of displacement, strain, temperature and acoustic activity. The second part is dedicated to comparison of selected experimental results with numerical FEM calculations. Such approach allows to better understand temperature and strain fields during thermal shock tests. Additionally to this fifth chapter, other very interesting results, provided in Annex A, present a study aiming to verify potential application of ATHORNA device in comparing materials resistance to thermal shocks.

Chapter 1

Chapter 1. State of art concerning thermomechanical properties of refractories

Many everyday products are made of steel, cement, glass, aluminium, copper or plastic, all of which require refractories to be produced. This often-overlooked group of materials is commonly used to line vessels operating at high temperatures. It is interesting to notice that the major part of refractories produced worldwide is directed to the iron and steel industry, at which the main consumption is attributed to steel ladle. Refractories applied to this vessel vary between zones as they are subjected to different wearing mechanisms.

This chapter aims to **introduce general knowledge about steelmaking, application vessel** (with key wearing mechanisms) and **alumina spinel materials investigated in other chapters**. The first section presents an overview of steel production, as well as steel ladle lining and wearing mechanisms for different zones of ladle lining. The second one is mainly dedicated to alumina spinel refractories with an explanation of microstructural aspects related to these materials. The subsequent part concerns thermomechanical behaviour of refractories, being related to several wearing mechanisms, and helps to understand relevance of selected testing methods.

1-1. Refractory materials in steel industry

1.1.1. Refractory materials consumption in the EU

In order to well understand the context of this PhD study, it is essential to shed some light on a few global market features. Currently, the European Union is the second-largest producer of refractory materials with a global production share accounting for 13 %.[1] This group of materials is used by five major industries but only one of them, the iron and steel industry, is responsible for the consumption of as much as 60 % of the global production of refractories.[2] The European Union, is the second-largest steel producer,[3] directly employing more than 360 000 people and producing 178 million tons per year (corresponding to ~11 % of the global production).[4] From the consumption side it is interesting to notice, that annually each European citizen consumes on average 332 kg (in 2018) of steel in finished products.[5] That's because steel is a versatile material present in many application areas, including construction, automotive & transport, energy, packaging and appliances.

As mentioned above, the European Union is a global vice-leader in production of refractories and steel, which are very closely related. In the last decades, the drive

for better steel quality led to fostered development of refractories. For instance, 30 years ago, the refractory consumption in steelmaking was about 30 kg per ton of steel, while currently, it is only 10 kg.[6] Despite this unusual improvement, there are still areas to ameliorate. As already mentioned, this study focuses on steel ladle, accounting for the highest refractory consumption in steelmaking (~25 %).[7]

1.1.2. How is steel produced what is the role of steel ladle?

As presented in Figure 1-1, there are two most popular primary steelmaking processes, one of them involves Blast Furnace (BF) and the other one Electric Arc Furnace (EAF). In 2016, in 28 European Union's countries, the BF route accounted for 60.2 %, while the EAF route accounted for 39.2 %.[8] In recent years, share of the latter one had an upward trend, as the EAF process leads to lower CO_2 emissions.[9]

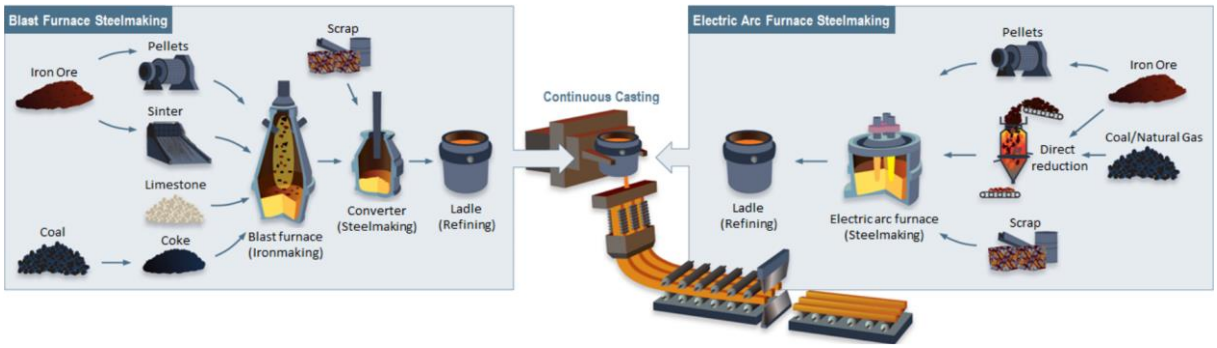

Figure 1-1. Overview of steelmaking processes.[10]

1.1.2.1 *Blast furnace steelmaking*

Iron ore (in form of pellets or sinters), coke and limestone are supplied to blast furnace, where iron ore transforms to molten iron by reaction with carbon monoxide. Calcium oxide, originating from limestone, reacts with acidic impurities (mainly silica), forming slag. In the next step, pig iron is transported from blast furnace to converter and during this process, lime is added to reduce sulphur content. In converter, steel is produced out of carbon-rich molten pig iron and scrap. At this stage, oxygen is blown through molten metal and ignites dissolved carbon, thereby reducing carbon content and generating heat. At this point, steel reaches ~1700 °C allowing removal of unwanted elements. Additionally, fluxes, such as burnt lime or dolomite are added to absorb impurities. Then, primarily refined steel is tapped to steel ladle, where the secondary refining process takes place.

1.1.2.2 *Electric arc furnace steelmaking*

In electric arc furnace steelmaking, scrap and directly reduced iron (some iron ore can be added) are melted, using heat generated by high power electric arcs. Heat is also generated by extensive exothermic oxidation reactions, thanks to oxygen blowing. Application of slag formers (mainly burnt lime and dolomite) and oxygen blowing, purify the melt from impurities (such as silicon, sulphur, aluminium, phosphorus, manganese and calcium). Addition of coke aims to reduce iron oxide (directly added as iron ore or originating from oxygen blowing) and to form foaming slag, by CO bubbling (improving arc's stability and decreasing thermal losses). Content of impurities, having lower affinity to oxygen than iron, can only be controlled by careful selection of input raw materials. After processing in EAF, steel is further refined in a steel ladle.

1.1.2.3 *From secondary refining to solidified steel*

Steel ladles have two major roles. Firstly, they are used to transfer liquid steel from converter (in blast furnace steelmaking) or electric arc furnace (in electric arc furnace steelmaking) to casting system. Secondly, liquid steel is being refined, through removal of unwanted phases or elements (oxides, lead, zinc, tin, sulphur etc.), reduction of carbon content, decrease of dissolved gases and alloying of steel.[11] Additionally, argon or nitrogen bubbles pass through liquid steel, allowing floatation of impurities, improving interactions between melt and slag, as well as equalizing temperature and composition within the ladle.

How does a typical steel ladle process flow look like? Figure 1-2 presents an exemplary schema of the steel ladle process flow. In general, this process can be divided into seven stages. The first two of them take place, when the ladle is introduced to the production cycle either for the first time (just built), after wear of refractory lining or after a long downtime. The next five of them (operations three to seven) represent a typical operation cycle when the ladle does not need general maintenance nor preheating. An exemplary duration for the sequence, comprising the steps from three to seven, can be about three hours.[12]

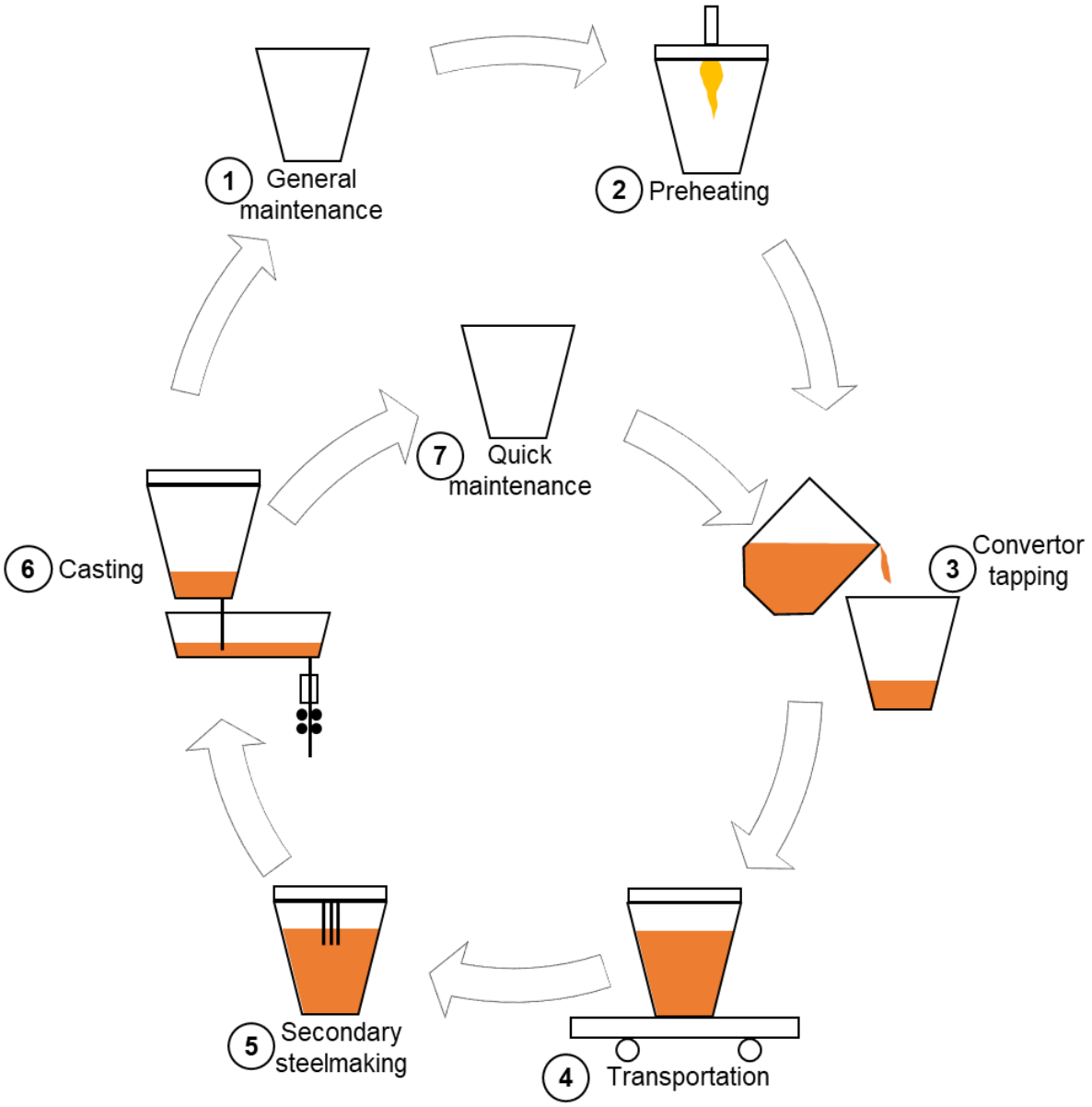

Figure 1-2. Schema of steel ladle process flow (inspired by the publication of P. Samuelsson and B. Sohlberg[13]).

The first stage involves construction of the ladle or replacement of worn lining areas with new refractories. In the second one, the ladle is preheated with a burner (e.g. up to ~1040 °C[12] or ~1350 °C[14]). This operation is crucial, as it decreases temperature difference, between refractory lining and liquid steel (~1600-1700 °C), resulting in lower stresses generated within refractory lining during tapping (hot thermal shock). The third step (in blast furnace steelmaking) consists in tapping liquid steel from a converter to the ladle from a significant height (up to ~10 meters). In order to reduce excessive wear of refractories, ladle design includes a so-called impact pad, being an area with high erosion resistance, which is targeted during tapping. At the fourth stage, the ladle is transported to stage number five where secondary

steelmaking takes place. This stage requires more explanation, as it often consists of several operations.

Secondary steelmaking has several objectives, such as homogenization (of bath's temperature and chemical composition), removal of gases (oxygen, nitrogen, hydrogen) and non-metallic elements, adjustment in chemistry of liquid steel (e.g. by decarbonisation and additions of ferroalloys) and potential re-heating of steel's temperature before casting.[15] Homogenization is achieved by so-called rinsing, which stands for bath agitation by argon injection, occurring usually through a purging plug, located at the ladle's bottom. Moreover, rinsing improves interactions between metal and slag, allows floatation of non-metallic inclusions and improves degassing of lower parts of steel bath. Removal of nitrogen and hydrogen can be performed by degassing in non-recirculating systems, such as VAD (vacuum arc degassing) or VOD (vacuum oxygen decarburization) or in recirculating systems, including RH (Ruhrstahl Heraeus), RH-OB (Ruhrstahl Heraeus - Oxygen Blowing) or RH-KTB (Ruhrstahl Heraeus-Kawasaki top blowing). Degassing in vacuum, also decreases the amount of carbon and oxygen dissolved in steel. A further decrease in carbon content can be supported by processes involving oxygen blowing. A further reduction in oxygen content is mainly achieved by addition of deoxidizing materials. Desulphurization and dephosphorization are performed by adjusting slag's composition. Calcium can be added at high depth for inclusion morphology modification, in order to transform solid Al_2O_3 and SiO_2 inclusions into liquid Ca-aluminate and Ca-silicate phases. Before casting, steel must have temperature required by casting process. Therefore, it may sometimes require re-heating by means of electric power or exothermic reactions (oxidation of Al, Si, C).

After secondary steelmaking, steel is poured into a tundish and then flows into casting system. Hot ladle's lining, during/after casting, undergoes cold thermal shock. Depending on required mechanical properties and dimensional tolerances, steel can be cold- or hot-rolled. At the seventh stage, the ladle is cleaned, sanded, inspected (e.g. using laser scanners) and teeming nozzles are exchanged. After that, it is ready for another production cycle. It is worth to notice that ladles are often covered at different stages to decrease heat losses.

1.1.3. Design of steel ladles

1.1.3.1 *Lining zones of steel ladles*

The drawing of a typical steel ladle with specified zones is presented in Figure 1-3. Usually, ladle lining is composed of four layers:

- Working lining - in direct contact with liquid steel or slag. Therefore, it is subjected to severe wear and requires regular replacements (typically every 15-250 heats[16]). Wearing mechanisms differ significantly between areas of the ladle lining. It is thus usually divided into four zones: slagline, barrel, bottom and impact pad.
- Safety lining - located behind working lining to protect against breakouts, in case of failure of working lining. This safety lining does not need to be changed regularly. In agreement with local working lining, this safety lining is usually divided into three zones: slagline, barrel and bottom.
- Insulation - placed between safety lining and steel shell. Its key role is to decrease thermal losses and thus save energy.
- Steel shell - outer layer, casing for refractory linings that provides rigidity of a steel ladle during crane manipulation.

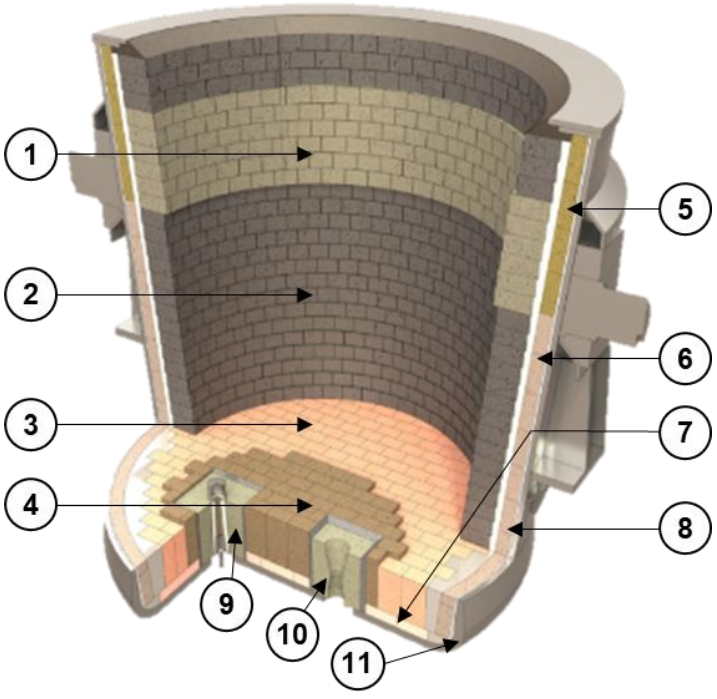

No.	Lining layer/zone	
1	Working Lining	Slagline
2		Barrel
3		Bottom
4		Impact pad
5	Safety Lining	Slagline
6		Barrel
7		Bottom
8	Insulation	
9	Stirring system	
10	Casting system	
11	Steel Shell	

Figure 1-3. A drawing presenting typical steel ladle lining zones.[10]

Ladles are also equipped with refractory systems for stirring (purging plug) and casting (well block). They could also be equipped with a cover to reduce heat losses.

1.1.3.2 *Wearing of working lining*

Selection of refractory materials for different sections of working lining is based on many criteria, including resistance to predominant wearing mechanisms (including corrosion, erosion, thermal shock), inertness to steel, ability to conserve heat, potential harmful health effects, environmental impact and cost per ton of steel.[12,17,18] Table 1-1 presents requirements for each zone of a typical steel ladle lining and exemplary materials. These requirements comprise five aspects: thermal stability (stable chemistry and dimensions vs. temperature), thermo-mechanical stability (stable mechanical properties vs. temperature), erosion and corrosion resistances, as well as potential for stress relaxation (ability to reduce stress, which can arise from thermal gradient).[18] The first two are related to ability to withstand thermal loads (e.g. tapping temperature, exothermic reactions or electric arc heating) and thermo-mechanical loads (e.g. ladle transport and tilting, long steel residence). The next two of them describe resistance to erosion (e.g. during stirring or tapping, crack infiltration by metal) and corrosion (e.g. by aggressive slag). The last one is related to potential for relaxation of stresses (arising due to e.g. hot thermal shock during tapping or cold thermal shock during/after casting).

Depending on a given zone of working lining, refractories are exposed to different wearing factors and therefore, required material properties are not the same. As already mentioned in the previous section, steel ladle undergoes hot thermal shock during tapping and cold thermal shock during/after casting. The negative effect of thermal shocks can be reduced by preheating a cold ladle, covering it between heats and assuring efficient usage of hot ladles (to reduce idle times).[12] All zones of working lining are exposed to above-mentioned thermal shocks. Additionally, the purging plug also undergoes cold thermal shock when cold gas passes through it. In Table 1-1 resistance to thermal shocks is represented by “Potential for stress relaxation” and maximal importance is indicated for all zones/elements, being in contact with liquid steel.

Slagline, being in direct and long contact with slag, is exposed to severe corrosion. This corrosion can be reduced by applying slag attack-resistant refractories

(such as magnesia-carbon), adding magnesia to slag (increasing magnesia saturation within slag), avoiding slag overheating (higher temperature involves higher corrosion kinetics), as well as controlling alumina content and slag basicity (both influencing slag viscosity).[12] To minimize corrosion, refractory material in this area should also exhibit high thermal stability (stable chemistry vs. temperature).

Barrel zone requires high potential for stress relaxation, not only due to thermal shocks, but also due to possible deformation of steel shell (during loading or manipulation), which could lead to high level of stresses within refractory lining. Corrosion resistance is also important, especially at the barrel's lower part, due to contact with residual slag during (or after) casting until slag dumping.[12] Additionally, in some cases, specific tapping practises or intense stirring may lead to high erosion. Therefore, it could be necessary to use more erosion-resistant materials.[18] Due to lower wear rate in this barrel zone, in comparison to other working lining zones, this area may be thinned to increase steel ladle capacity.[12]

Ladle's bottom is mainly subjected to erosion due to stirring and deskulling (during quick maintenance), as well as to corrosion due to presence of residual slag (remaining since the end of casting until slag dumping).[12] Impact pad is a part of ladle bottom, being targeted during tapping. Due to intense erosion by strikes of high-momentum steel stream, material applied in this area requires high erosion resistance (high hot strength).[12] In general, for ladle bottom, volumetric stability under high temperature and pressure is also highly required to avoid cracking and thus excessive wear.[18] Impact pad can be thicker (to compensate higher wear) and/or can be made of higher quality refractories (to reduce wear).

Having in mind, that the author's principal objective, is to improve understanding of refractories' behaviour with the highest wear, the main focus of this chapter is on working lining. The last column of Table 1-1, shows that majority of working lining zones can be made of alumina-based spinel-containing (Al_2O_3 + $MgAl_2O_4$) or spinel-forming (Al_2O_3 + MgO) materials. This is related to numerous advantages of these materials, which are introduced in the next sub-chapter.

Table 1-1. Refractory requirements for selected steel ladle regions.

Lining zone (exemplary maximal temperature during operation)			Main purpose	Thermal stability	Thermo--mechanical stability	Erosion resistance	Corrosion resistance	Potential for stress relaxation	Exemplary refractories
1	**Working Lining** (1680 °C [14])	**Slagline**	Resistance to slag attack	+++*	+*	+*	+++*	+++*	MgO-C bricks[10,19]
2		**Barrel**	Avoid carbon contamination	++ [18]	+ [18]	+ [18]	++ [18]	+++ [18]	Al_2O_3-$MgAl_2O_4$ bricks,[20] Al_2O_3-MgO-$MgAl_2O_4$ or Al_2O_3-MgO castables[18]
3		**Bottom**	Resist against thermal shock	++ [18]	+++ [18]	++ [18]	++ [18]	+++ [18]	Al_2O_3-$MgAl_2O_4$ bricks[20], Al_2O_3-$MgAl_2O_4$ castables[18]
4		**Impact pad**	Resist against impact	++ [18]	+++ [18]	+++ [18]	+++ [18]	+++ [18]	Al_2O_3-$MgAl_2O_4$ and Al_2O_3-MgO castables[18]
5	**Safety Lining** (1100-1250 °C [14])	**Slagline**	Prevent steel/slag penetration	+*	+*	+*	+*	++*	Bauxite or andalusite bricks[10]
6		**Barrel**		+*	+*	+*	+*	++*	
7		**Bottom**		+*	+*	+*	+*	++*	
8	**Insulation** (<800 °C)[14]		Reduce heat losses	+++*	+*	+*	+*	+*	Vermiculite brick[10]
10	**Stirring system (purging plug)**		Allow efficient steel treatment	+++ [18]	+++ [18]	+++ [18]	++ [18]	+++ [18]	Al_2O_3-$MgAl_2O_4$ or Al_2O_3-Cr_2O_3 castables[18,21]
9	**Casting system (well block)**		Flow control during continuous casting	+++ [18]	+++ [18]	+++ [18]	++ [18]	+++ [18]	Al_2O_3-$MgAl_2O_4$ or Al_2O_3-C castables[10,18]
11	**Steel Shell** (260-290 °C,[22] 330-390 °C [14])		Determines vessel's shape, assembly rigidity for manipulation	-	-	-	-	-	-

*required level estimated by the author

1-2. Alumina-based refractories with in-situ or preformed spinel

The first part of this section introduces historic development of refractories dedicated to steel ladle. Then, the following ones present the key points related to design of alumina spinel materials, being of interest in this PhD study.

1.2.1. Evolution of refractories applied in steel ladle's lining since the 1950s

At the beginning, let's consider the evolution of refractories dedicated to steel ladle since the mid of XXth century. In the 1950s and the 1960s, dense siliceous fireclay was typically used in steel ladle lining.[23] In the 1960s, secondary refining and continuous casting became increasingly popular and, as a consequence, refractories were exposed to more severe conditions which led to transition from high-silicate bricks to zircon bricks.[24,25] Wider application of castables around 1970 (aiming to extend lining life by castable reparations and to reduce refractory work) led to usage of zircon-based castables.[23,24]

In the late 1970s, alumina castables (based on tabular alumina and corundum) were also commonly used in several steelmaking applications, including ladle lining. However, their low resistance to penetration by slag, containing FeO, MnO or CaO, induced structural spalling of refractory linings and led to relatively high wear. Several additions were then tested, in order to improve the slag penetration resistance and spinel was one of them. In the late 1980s, alumina-based spinel-containing castables (called briefly alumina spinel castables) were successfully developed, leading to a significant decrease in slag penetration depth.[24,26,27] Since then, they became increasingly popular in working linings of steel ladles (below slag line) and as pre-cast shapes (impact pads, purging plugs, well-blocks).[18] In the following years, alumina-based spinel-forming castables (called briefly alumina magnesia castables) were developed, as a group of materials, being cheaper (less expensive raw materials), as well as more resistant to corrosion and thermal shocks (in comparison to alumina-based spinel-containing castables).[18,24,28]

Nevertheless, castable lining requires significant initial investments (in mixers, mould and pumping system), as well as special drying and preheating procedure (to prevent steam spalling).[29] Moreover, each change of lining geometry requires changing the mould. For these reasons, some plants still prefer to use refractory bricks,

e.g. alumina-based materials with spinel or magnesia additions. Thanks to excellent performance of these materials, they are widely used until now.

The evolution of refractories cannot be complete without mentioning basic materials that were applied in ladles since the early 1960s. The first applied were pitch and tar bonded doloma, magnesia-doloma and magnesia bricks. Then, since the 1980s, resin bonded and MgO-graphite became increasingly popular. Their application resulted in an increased lifetime of refractory lining thanks to low wettability (improved corrosion resistance), high thermal conductivity (improved thermal shock resistance) and protective effect of in-situ reactions between MgO and C (formation of dense protective magnesia layer). Currently, MgO-C bricks are the most widely used type of materials in the steel industry and are even now almost always applied in slag lines of steel ladles (even if the other zones are based on alumina spinel refractories).[30]

1.2.2. Spinel – structural considerations

From the crystallographic point of view, the general formula of spinel is AB_2O_4, where A stands for divalent (e.g. Mg, Mn, Fe, Ni, Zn) and B for trivalent (e.g. Al, Mn, Fe, Cr) metal ions.[31] Spinel structure is built by a cubic dense packing of oxygen anions with half of the octahedral sites, being occupied by trivalent cations, and only every eight tetrahedral site, being occupied by divalent cations.[32] Two types of spinel, $MgAl_2O_4$ and $MgCr_2O_4$ are well-known for their interesting combination of physical and chemical properties, including resistance to chemical attack and high refractoriness.[33] $MgCr_2O_4$ is progressively eliminated due to possible formation of carcinogenic hexavalent chromium Cr^{6+} in the form of CrO_3.[34,35] Formation of the toxic compound was observed in chromite-containing refractories when exposed to high temperature, high pressure and chemical contact with alkali or alkaline-earth oxides.[35] For example, such toxic compound has been found in chrome-bearing materials, being in contact with calcium aluminates. Long exposure to Cr^{6+} leads to harmful health effects, such as lungs cancer, as well as damage to nose, throat, eyes, skin, etc.[35] For these reasons, magnesium-aluminate spinel, having similar set of properties and lower health risks, is usually preferred and is of interest in this study.

Magnesium-aluminate spinel ($MgAl_2O_4$), abbreviated as spinel, has a high melting point of 2135°C (higher than alumina), low density and low thermal conductivity (lower than the reactants).[36] Wagner's mechanism describes solid-state spinel formation from alumina and magnesia reactants, occurring by counter-diffusion of Al^{3+}

and Mg^{2+} cations (see Figure 1-4).[37] Diffusion of these ions occurs in opposite directions while maintaining electroneutrality (3 Mg^{2+} and 2 Al^{3+} ions). Due to density differences between reactants (Al_2O_3 - 3.97 g/cm^3, MgO - 3.60 g/cm^3) and product ($MgAl_2O_4$ - 3.55 g/cm^3), spinel formation leads to a volumetric expansion of 8.67 % (theoretical value based on calculations of density differences).[38] Even if spinel is usually described as $MgAl_2O_4$, corresponding to stoichiometric spinel, it is in fact a solid solution, with a composition that can vary with temperature, as can be observed in Figure 1-5. The stoichiometric spinel has a MgO/Al_2O_3 molar ratio of 1 and consists of 28.33 wt. % of MgO and 71.67 wt. % of Al_2O_3. Above 1000°C, the spinel is represented by an enlarging phase region, containing alumina- and magnesia-rich regions. High-temperature stability of non-stoichiometric phases allows producing (by rapid cooling) commercially available magnesia-rich (MR66 - with 66 wt. % of alumina) or alumina-rich spinels (AR78 and AR90 with 78 or 90 wt. % of alumina, respectively). The magnesia-rich MR66 is mainly used in spinel-containing bricks, while the alumina-rich spinels, AR78 and AR90, are usually used in castables.[34]

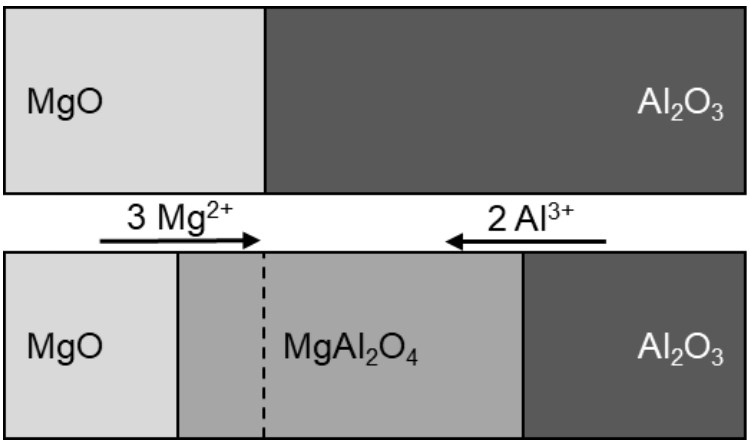

Figure 1-4. Wagner's mechanism for spinel formation (inspired by M.A.L. Braulio et al.[36]).

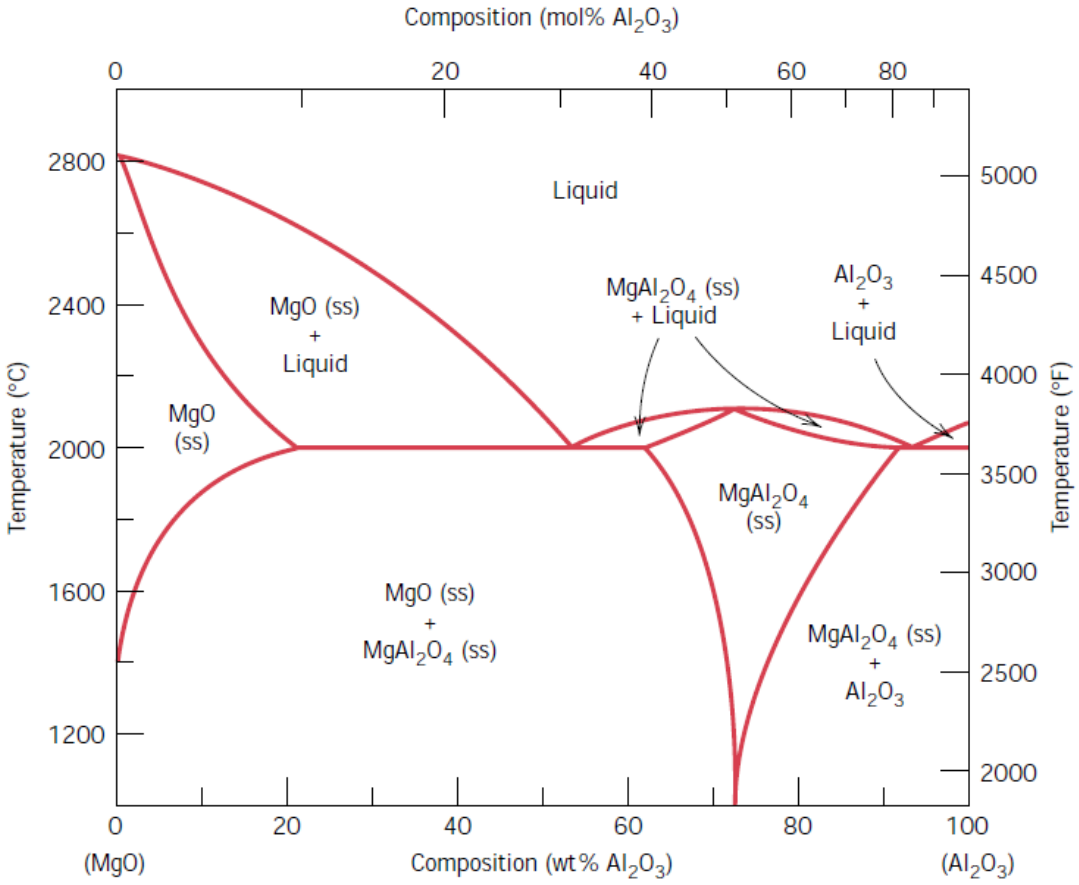

Figure 1-5. Phase equilibria diagram for MgO-Al_2O_3 system.[39]

Based on the structure of stoichiometric spinel, explained before, non-stoichiometric spinels imply some modifications within the crystal structure. On one hand, in alumina-rich spinels, some tetrahedral sites are occupied by Al^{3+}, which replaced Mg^{2+} ions and charge is compensated by cation vacancies on the octahedral sites.[34] Due to lower ionic radius of Al^{3+} (0.050 nm), than Mg^{2+} (0.065 nm), unit cell volume decreases with increasing alumina content. On the other hand, in magnesia-rich spinel, excessive MgO leads to a structure with a deficit of oxygen anions.[34] The increase of MgO content induces a slight increase of the lattice constant. Therefore, determination of the unit cell parameter allows analysing the degree of non-stoichiometry of investigated spinel structure. Figure 1-6 presents the evolution of lattice constant vs. alumina content.[39-41] A discrepancy between values reported by different authors can be observed. Despite this discrepancy, the authors agree, that increase in alumina content leads to a decrease of lattice constant.

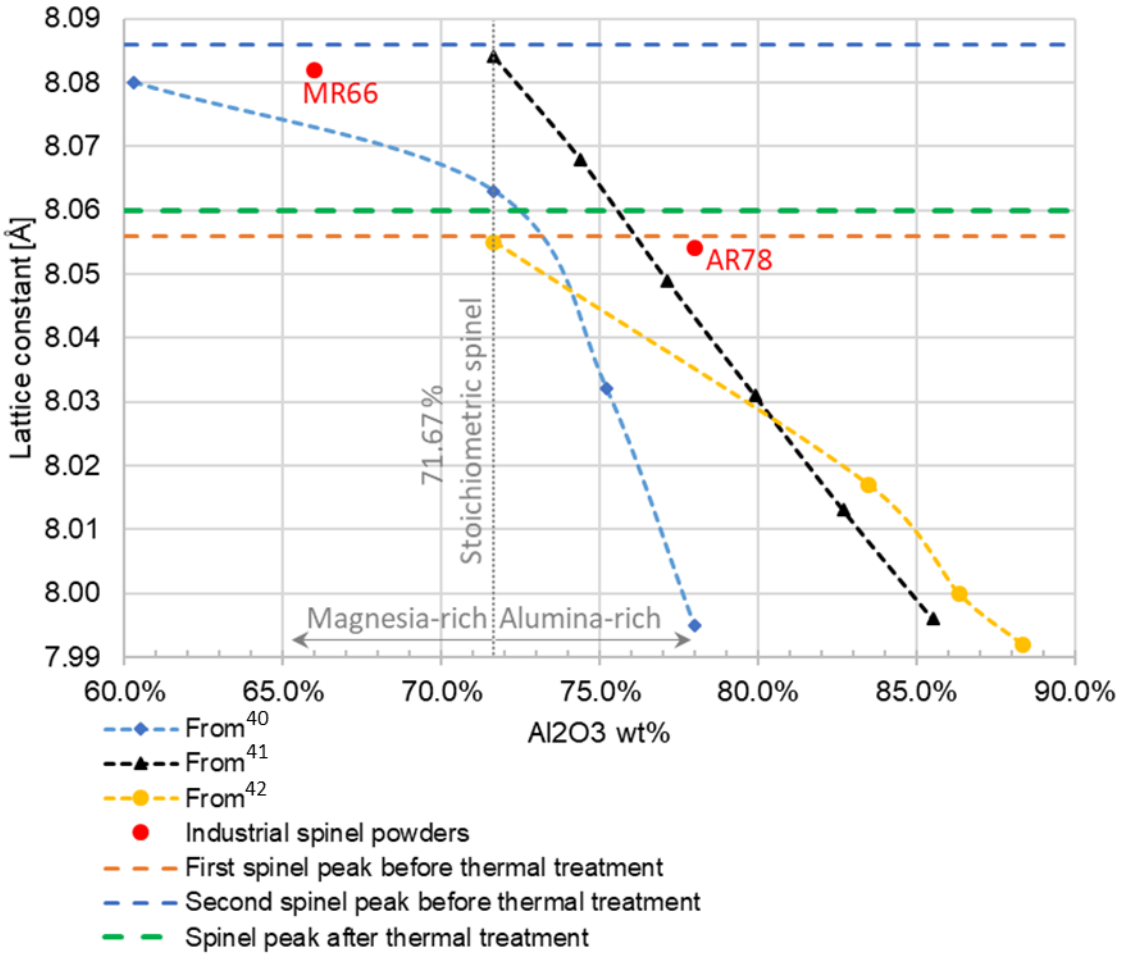

Figure 1-6. Lattice constant vs. alumina content in spinel based on results from different articles[40–42]. This figure contains also experimental results which will be introduced in section 4.2.

1.2.3. Alumina-based spinel-containing and spinel-forming refractories

Alumina-based spinel-containing and spinel-forming refractories have several advantages when applied to steel ladle lining. To begin with, these groups of refractories allow producing steel with low carbon content, as they do not contribute to carbon pickup[43] from the lining, in contrast to carbon-containing refractories. In addition, lack of carbon content and low intrinsic thermal conductivities of constituents result in a relatively low thermal conductivity of alumina-based spinel-containing and spinel-forming refractories. This factor is essential in reduction of heat losses and leads to increased energy savings. Furthermore, their exploitation does not cause harmful health effects, as they do not contain well-known carcinogenic products (e.g. containing Cr^{6+}). In fact, this refractory family offers several advantageous technical features that lead to an outstanding performance of refractory lining.

A key technical feature of alumina-based spinel-containing and spinel-forming refractories is the high adaptability of their composition, based on different raw materials that allow achieving diverse sets of properties. On one hand, it is possible to design a refractory (spinel-forming) with good corrosion and penetration resistance, which is compromised by lower thermal shock resistance, and lower mechanical properties (at high temperature), such as low erosion resistance or low hot strength.[18] On the other hand, it is also possible to design a material (spinel-containing) with high thermal shock resistance, high mechanical properties (erosion resistance and hot strength), and slightly lower (but still significant) corrosion resistance. Moreover, thermal expansion can also be adjusted (to some extent). As already mentioned, there are several modifiable material parameters and few possibilities are discussed in the coming paragraphs.

1.2.3.1 *Typical composition*

Alumina-based spinel-forming or spinel-containing refractories can be prepared as unshaped castables or shaped bricks (burnt or unburnt). The typical composition includes alumina, high alumina cement (in case of castables), as well as preformed spinel or magnesia (for in-situ spinel formation). The content of alumina should be high enough to achieve good erosion and slag penetration resistance and the optimal amount is estimated between 60-80 wt. %.[26] The amount of high alumina cement in castables is usually a few weight percent (for example 2.5-5[18] or 6 wt. %),[44,45] but it may be even up to 25 wt. %. The higher the level of cement is, the more it can react with spinel, producing a significant amount of products melting at around 1350 °C, which lower erosion resistance.[26] Amount[26,46] and size[26,47] of spinel, present in alumina-based refractories, play a key role mainly in slag corrosion and penetration resistance. The best corrosion and penetration results are achieved when the total amount of spinel is about 20 wt. % and when the maximum particle size of spinel is lower than 0.5 mm.[26,46] Fine-grained spinel is more uniformly distributed in the material, thus it better fills gaps in the matrix by turning FeO and MnO into solid solution.[26] When the spinel content is too low, both resistances to corrosion and penetration decrease, but when it is too high, penetration increases significantly.[46] In spinel-forming refractories, the amount of magnesia should be between 0.5-4 wt. %, as higher content may lead to too high volume expansion, resulting in material damage by metal penetration and spalling. The magnesia particles should not exceed 3 mm,

nor be lower than 0.1 mm (especially in castables, as small particles are more prone to hydration).[26]

1.2.3.2 *The key role of spinel in resistance to corrosion and penetration*

High resistance to slag's corrosion and penetration of alumina-based spinel-containing or spinel-forming refractories is one of the main reasons why these materials are usually selected for steel ladle lining. Spinel plays a key role here. Its structure enables substitutional solid-solutioning, meaning that ions can be exchanged or incorporated into the spinel structure. This feature is advantageous for corrosion and penetration resistance of alumina-rich spinels against slag. The mechanism is believed to dissolve spinel in slag and then incorporate slag ions, such as Fe^{2+} and Mn^{2+} into the spinel structure. This is supposed to result in an increase in slag viscosity and thus decrease slag penetration.[18,34]

Alumina-based spinel-forming refractories have better corrosion and penetration resistance than alumina-based spinel-containing materials.[48] This can be explained by the presence of finer, in-situ formed spinel,[49] as well as by densification of microstructure, due to expansive spinel formation under restraint (denser structure decreases slag penetration).[24,29]

Stoichiometry of preformed spinel (in alumina-based spinel-containing refractories) also influences corrosion. It has been found, that AR90 has better slag penetration resistance, than AR78.[50,51] It can be explained by reaction between AR90 and CaO (from CMAS slag), resulting in CA_6 production, which results in a local increase of viscosity (due to relatively higher SiO_2 content in slag).[50] Another reason is linked with crystal structure of AR90, which has more cation vacancies and thus, can incorporate more Fe^{2+} and Mn^{2+} (from a slag), forming a layer of complex spinel (that suppress penetration).[51] Studies performed on castables with different types of preformed spinels indicate also that addition of MgO-rich spinel leads to better corrosion resistance in comparison with alumina-rich spinels.[52] The improved corrosion resistance of castable with MgO-rich spinel is also probably linked with higher magnesia content, which has lower solubility in silica slag, than alumina.[53]

1.2.3.3 *Impact of composition on physical and mechanical properties*

Another important parameter after corrosion is the Permanent Linear Change (PLC). It highly depends, whether a refractory type is spinel-forming

or spinel-containing. In spinel-forming refractories, thermal expansion is higher, than in the spinel-containing ones, due to in-situ spinel formation, which was reported to occur at temperatures above ~1200 °C (while rapid expansion occurs above ~1400 °C).[24,54–56] Spinel generated at 1400 °C is nearly stoichiometric, but at higher temperatures it progressively becomes alumina-richer.[56] The expansion can be adjusted to the required level by adjusting magnesia content.[26] This expansion contributes to a positive PLC, which in unburned alumina-based spinel-forming refractories is limited to a given thickness (by temperature) from the hot face.[24] It means, that the expansion can occur locally and progressively. Moderate positive expansion can be advantageous for refractory linings made of bricks, as it contributes to joints closure, preventing steel and slag penetration. However, if the thermal expansion (linked with spinel formation) is too large, it can lead to a concentration of mechanical stresses and thermal spalling. Therefore, 0.5-1 wt. % of fumed silica is usually added to spinel-forming refractories, in order to counterbalance the thermal expansion by formation of a liquid phase. The addition of silica also improves workability of the castables during processing.[18]

Although the silica addition could have a positive impact to limit expansion, the presence of liquid phase also has a great impact on mechanical properties: decrease of Refractoriness Under Load (RUL), a decrease of Hot Modulus of Rupture (HMOR). Spinel-containing castables without silica addition do not soften until 1650 °C (measurement limit) and exhibit high HMOR at 1500 °C (23 MPa).[18] Whereas, spinel-forming castables with 0.5 wt. % of silica begin to soften already at ~1200 °C and exhibit low HMOR at 1500 °C (lower than 3 MPa).[18] It has also been found, that the addition of fumed silica to a matrix of calcium aluminate leads to growth of pore size at temperatures higher than 1000 °C[57] and formation of small CA_6 crystals embedded in a glassy phase.[58] The softening caused by formation of a liquid phase, allows to release thermal stresses and can thus be very advantageous when applied e.g. to the barrel part of steel ladle lining. That's because this area is exposed i.a. to quite high deformation (during manipulation by crane), which could lead to stress concentration. Therefore, potential to stress relaxation and expansion associated with closure of joints can be advantageous. However, lower erosion resistance and decreased hot strength, being the effects of silica addition, may not be key factors, if the process does not require high local mechanical properties due to tapping or stirring practices.

Spinel-containing castables have better thermal shock resistance, in comparison to spinel-forming castables (compared both with and without microsilica addition). The advantage of spinel-containing castables is linked with thermal expansion mismatch between alumina and spinel, which leads to microcracks formation, acting as crack arresters.[18] Magnesia, present in spinel-forming castables, has a high coefficient of thermal expansion, which leads to a decrease of thermal shock resistance.[18] Another explanation indicates that superior thermal shock resistance of spinel-containing castables can be linked with a lower amount of glassy phase (leading to smaller pores, which are more densely distributed and act as crack arresters) than in spinel-forming castables (both with or without silica addition).[59] The addition of 0.75 wt. % of silica to spinel-forming castables decreased the thermal shock resistance even more.

Refractories with preformed spinel are preferred, if high erosion resistance, high hot strength and/or high volumetric stability are required at high temperature. Therefore, they are often applied at the bottom of steel ladle working lining, for the impact pad and for the purging plug.[18] In comparison to alumina castables (without spinel nor magnesia), the addition of preformed spinel has a significant influence on mechanical properties. It leads to higher mechanical strength, in comparison to alumina castables without spinel,[60–62] which can be related to bond linkage between CA_6, alumina-rich spinel and alumina.[60,62] Moreover, the addition of magnesia-rich spinel leads to a slightly higher modulus of rupture, in comparison to alumina-rich spinels.[52]

From the mechanical point of view, a better understanding of potential plastic behaviour at high temperatures is also very important. In this context, it has been found, that at high temperature (~1200°C), alumina-rich spinel exhibits plastic behaviour.[63] It has been explained by enhanced mass transport, caused by increased concentration of cation vacancies.[64] Enrichment of stoichiometric spinel in alumina (explained as “dissolution” of alumina grains in stoichiometric spinel) has also been described as potential driving force of structure loosening in alumina-based spinel-forming castables above 1400°C, where stoichiometric spinel is out of equilibrium.[56]

1.2.4. Microstructure design and evolution during heat treatment

1.2.4.1 *Particle size distribution*

Particle Size Distribution (PSD) is an important design step with the main goal of achieving maximum packing density. This packing results in minimized void space and thus increases refractory properties, such as density, strength, resistance to corrosion or abrasion.[65] Two concepts of PSD exist: discrete or continuous.

The first of them is the discrete particle size distribution, where all particles are added in several fractions (usually two or three fractions with narrow size ranges) with relatively high ratio between mean diameters of the subsequent fractions (e.g. 100). These fractions do not overlap, do not represent all particle sizes of a material's PSD range. This discrete packing is often used to design refractory bricks.

The second concept is the continuous particle size distribution, where particles are also added in fractions, but in this case all subsequent fractions overlap and thus represent all particle sizes of a material's PSD range. This packing is often applied to castables in order to ensure good flowability, thanks to the separation of aggregates by the matrix (arbitrarily defined for grains lower than 45 µm),[66] which helps to reduce friction between coarse particles.[65]

There are three well-known packing models: the Furnas,[67,68] the Andreasen,[69,70] as well as the Dinger-Funk models.[69,71,72] The last one is the most realistic and therefore is commonly used. In fact, the Dinger-Funk model is an improved version of the Andreasen model, which is dedicated to a continuous particle size distribution and was initially based on an empirical formulation. The Andreasen model is based on similarity condition, meaning that at any magnification, the variation of particle size and packing arrangements are similar. A. H. M. Andreasen developed a linear Equation 1-1, relating the Cumulative Percent Finer Than (CPFT) with the particle diameter D, the largest particle diameter D_L and a distribution coefficient q. In fact, this first approach is not complete, as it does not take into account effects of lack of small particles (e.g. smaller than 1 nm). It allows to calculate the CPFT value, even if very fine particles are not present in reality.[69,70] The Dinger-Funk PSD equation (see Equation 1-2), developed later, is also called the modified Andreasen equation, where the smallest particle diameter D_S is introduced.

$$\frac{CPFT}{100} = \left(\frac{D}{D_L}\right)^q$$ Equation 1-1

$$\frac{CPFT}{100} = \frac{D^q - {D_S}^q}{{D_L}^q - {D_S}^q}$$ Equation 1-2

Initially, Andreasen found that the distribution coefficient q is crucial in order to obtain optimal packing density and proposed values between 0.33 and 0.5. Later, according to Dinger and Funk, the optimum value of the q parameter has been determined as 0.37 thanks to their computational model. Figure 1-7 illustrates the difference between the two approaches when the same distribution coefficient of q=0.37 is used in the Andreasen and Dinger-Funk models. The Andreasen equation leads to higher content of fines, than the Dinger-Funk PSD equation. The difference is related to the smallest particle diameter D_S.

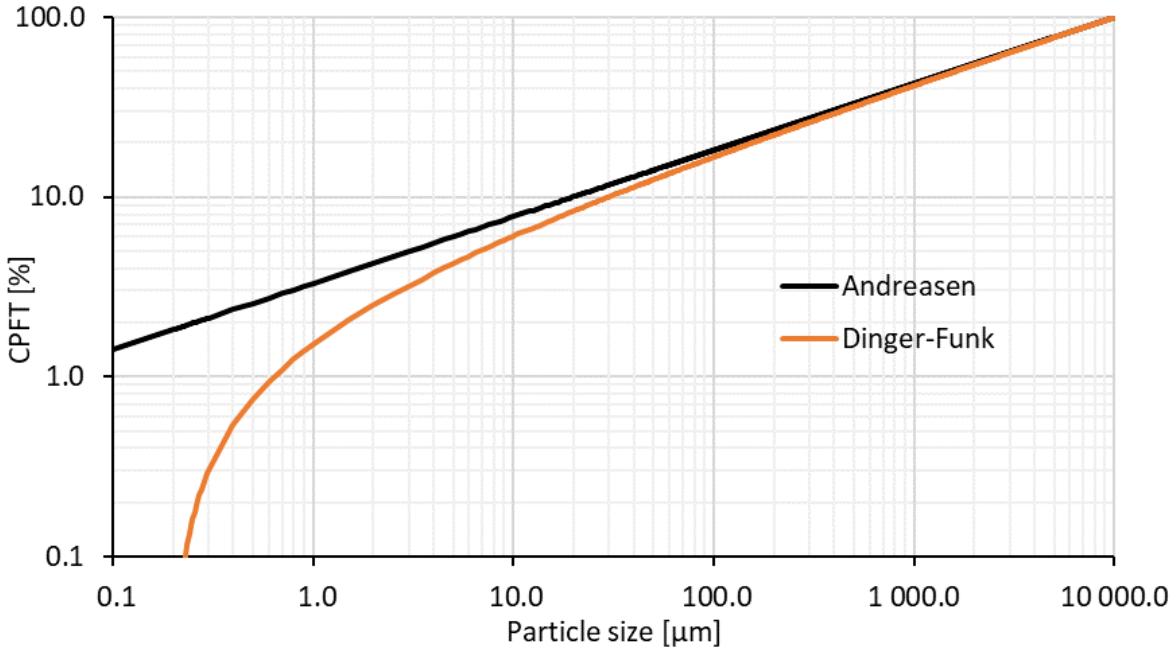

Figure 1-7. Comparison of particle size distributions obtained by Andreasen and Dinger-Funk models, with q=0.37, D_L=10000 um and D_S=0.2 um.

One should take into account, that these models operate on ideally spherical particles (not the real ones) and consider a perfectly fluid grain assembly (no friction between particles). As a consequence, in reality, achieving the densest packing is limited by the shape or surface roughness of particles, and by the actual rheology of the grain assembly. More recent works demonstrate that a good flowability can be achieved for systems with a slightly larger amount of fine particles, corresponding to q values between 0.2 and 0.3.[73] As a consequence, castables with

higher q values (close to 0.3 for better packing) have a higher proportion of coarser particles, but in order to flow they need external energy (vibrating castables). Castables with lower q values (lower compactness) have a higher content of fines and are characterized by better flowability (q values lower than 0.25 indicate self-flowing behaviour - no need for external energy).[70,74–76]

1.2.4.2 *Cement chemist notation*

Long chemical formulas are often simplified, based on cement chemist notation. The main oxides, being of interest in this work are represented by the following symbols: C - CaO; A - Al_2O_3; M - MgO and S - SiO_2.

The most commonly used compounds are the following:

- CA - $CaO \cdot Al_2O_3$ (calcium monoaluminate)
- CA_2 - $CaO \cdot 2\ Al_2O_3$ (calcium dialuminate)
- CA_6 - $CaO \cdot 6\ Al_2O_3$ (calcium hexaluminate)
- MA - $MgO \cdot Al_2O_3$ (spinel)
- CAS_2 - $CaO \cdot Al_2O_3 \cdot 2\ SiO_2$ (anorthite)
- C_2AS - $2\ CaO \cdot Al_2O_3 \cdot SiO_2$ (gehlenite)

1.2.4.3 *Introduction of two refractory cement types*

In the context of this study, two types of binders are worth to be considered: a standard Calcium Aluminate Cement (usually abbreviated as CAC) and a novel Calcium Magnesium Aluminate cement (usually abbreviated as CMA). The schematic representation of particles, as well as chemical and mineralogical compositions, are presented in Figure 1-8 and Table 1-2, respectively. Both types of cement contain about 70 wt.% of Al_2O_3 and traces of SiO_2 (in form of gehlenite), but different contents of CaO and MgO. The CAC contains about 30 wt.% of CaO and traces of MgO, while the CMA contains about 10 wt. % of CaO and about 20 wt. % of MgO. Significant differences are observed on the microstructural level. The microstructure of the CAC is mainly built of CA and CA_2 phases (with low amount of $C_{12}A_7$ and Aα)[77] and the microstructure of the CMA cement mainly consists of MA matrix with inclusions of CA and CA_2. The introduction of stoichiometric spinel into cement is beneficial from the corrosion point of view, as the areas usually occupied only by CA_x phases, contain spinel, which can improve local corrosion and penetration resistance (influence of fine and well-dispersed spinel particles is described in one of the previous sub-chapters).

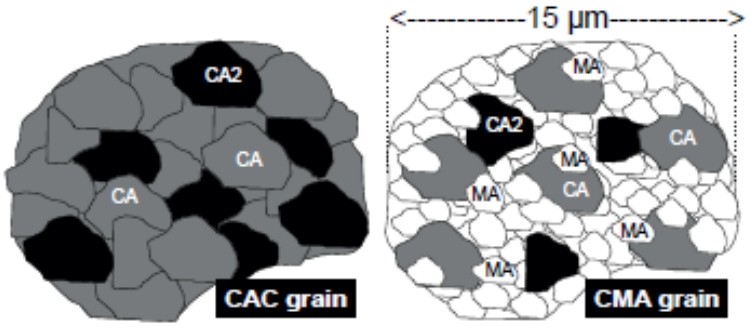

Figure 1-8. Schematic representation of CAC and CMA grains (medium grain diameter of 15 µm).[78]

Table 1-2. CAC and CMA cements - chemical and mineralogical compositions.[78]

Cement type	Chemistry				Mineralogy			
	Al_2O_3	CaO	MgO	SiO_2	CA	CA_2	MA	C_2AS
CAC	68.7-70.5	28.5-30.5	<0.5	0.2-0.6	56-61	39-44	0	<1
CMA	69-71	8-11	16-22	<1.0	18-22	8-12	68-72	<1

1.2.4.4 *Hydration, dehydration and firing of the typical calcium aluminate cement*

The particles of calcium aluminate cement (CAC) are mainly built of CA and CA_2 phases. Hydration rates depend upon the C/A ratio and temperature. Relative hydration rates of $C_{12}A_7$, CA and CA_2 are fast, moderate and slow, respectively. CA is the major phase in this cement and it develops the highest strength (from considered phases) in a short time dedicated to hydration of refractory castables, therefore it is the only phase, being considered here. When cement and water are mixed, the hydraulic minerals dissolve, forming a saturated solution of Ca^{2+} and $Al(OH)^{4-}$ ions.[66] Then hydration products nucleate and crystal growth creates an interlocking network, leading to setting and increase of strength.[79] In more detail, the CA phase hydrates by dissolution and nucleation (from that solution) of metastable hexagonal hydrates CAH_{10} (detected after 6-24 hours) and C_2AH_8 (detected after 24h). If the temperature rises above 21°C, the metastable hexagonal hydrates start to convert into stable and denser C_3AH_6 and AH_3 compounds.[80,81] Usually during experimental investigations, castables are dried at 110°C, in order to ensure complete conversion to C_3AH_6 and AH_3 products.[82]

All hydrated compounds of the CAC dehydrate up to ~550°C.[81] The CAH_{10} dehydrates through C_2AH_8 phase into stable cubic C_3AH_6, what leads to an increase of porosity and decrease of mechanical strength.[73,81,83,84] The C_3AH_6 dehydrates in two steps: at ~300°C and ~500°C, losing at each step 4.5 and 1.5 molecules of water,

respectively.[85] Gibbsite or AH_3 gel dehydrate between 210°C and 300°C or convert to boehmite (AH), which dehydrates at 530-550°C.[66]

During firing, all the hydrates decompose to CA_x phases ($C_{12}A_7$, CA, CA_2, CA_6). Starting from 400 °C, $C_{12}A_7$ forms (from the dehydrated phases). At 900 °C, $C_{12}A_7$ reacts with alumina, forming elongated CA, which then at 1000-1200 °C reacts with alumina to form coarse, globular CA_2. Hexagonal platelets of CA_6 phase are formed above 1300 °C from the reaction between CA_2 and alumina.[66]

1.2.4.5 *Additional complexity during microstructural evolution of the CMA cement (in comparison to CAC)*

Hydration mechanism of the CMA cement follows the same mechanism, as the CAC: at the beginning, the process is dominated by nucleation and crystal growth and then diffusion becomes the dominant process.[86] However, the process is not exactly the same, as particles of the CMA cement are built of MA and CAx phases. There are not many publications on this topic yet, but it has already been stated, that distribution of MA phases among reactive phases is important, as MA can hinder contact between reactive phases and water, thus increasing setting time. When MA and CA phases are distributed crossly the contact between water and CA phase is the highest, among tested distributions of the CMA cements, and leads to the shortest setting.[87]

The MA phases have a significant impact on microstructural evolution during firing. In order to well understand the current state-of-the-art on the firing of the CMA cement, one needs to introduce the CMA phases from the alumina-rich part of the CaO-Al_2O_3-MgO system. The first study on these phases was published in 1995.[88,89] The key new phases in the part of the CaO-Al_2O_3-MgO ternary diagram (see Figure 1-9) are denoted as CMA-I (CM_2A_8 - $CaMg_2Al_{16}O_{27}$) and CMA-II (CMA_7 - $Ca_2Mg_2Al_{28}O_{46}$) and their compositions lie on the line connecting hibonite (CA_6 - $CaAl_{12}O_{19}$) and spinel (MA - $MgAl_2O_4$). According to this study, the formation route for CMA-I and CMA-II phases could consist in the incorporation of MgO into CA_6 structure (being formed prior to formation of these CMA phases). Another study on related topic was published in 2000, where solid-state compatibilities and melting of the high-alumina region of the CaO-Al_2O_3-MgO system was investigated.[90] According to the publication, the CMA-I and CMA-II phases melt incongruently at ~1820 °C and ~1830 °C, respectively (see Equation 1-3 and Equation 1-4) and

formation of CA_6 is preceded by decomposition of the CMA phases. The latter statement contrasts with the initial hypothesis (from 1995), as CA_6 is not assumed here to be formed prior to formation of the CMA phases, but the CMA phases form firstly and then decompose i.a. to CA_6. It should be noticed, that these two studies were conducted on powder mixtures, specifically designed to study the phase equilibria diagram.

In 2012, an interesting investigation was published about the in-depth microstructural evolution of cement-bonded spinel refractory castables.[91] The authors concluded that the reactions involving CMA phases take place in three steps. At first, above 1200 °C, CMA-I phase precipitates out of C_2AS-like liquid (which contains Mg^{2+} ions from previously dissolved MA crystals). Then, between 1300 °C and 1500 °C, CMA-I decomposes in two steps (similar to Equation 1-3 and Equation 1-4), forming MA, CMA-II, CA_6 and liquid(s). They also stated, that CMA-II is a transient phase and that location of the CA_6 crystals is associated with the presence of MgO sources (from MA). Above-mentioned publications contributed to a better understanding of microstructure evolution in alumina spinel refractory castables, as the formation of CA_6 phase was (or sometimes still is) solely associated with the reaction between CA_2 and A.

From the crystallographic point of view, there are similarities between the structures of CA_6 and the CMA phases. All of them have anisotropic structures: CA_6 has the magnetoplumbite structure, while CMA phases are built of stacked layers of magnetoplumbite and spinel. The difference between CMA-I and CMA-II is related to a different number of magnetoplumbite and spinel layers within their structures. CMA-I, having higher MgO content, has a higher number of spinel layers.

$$CMA - I \rightarrow MA + CMA - II + liquid \qquad \text{Equation 1-3}$$

$$CMA - II \rightarrow MA + CA6 + liquid \qquad \text{Equation 1-4}$$

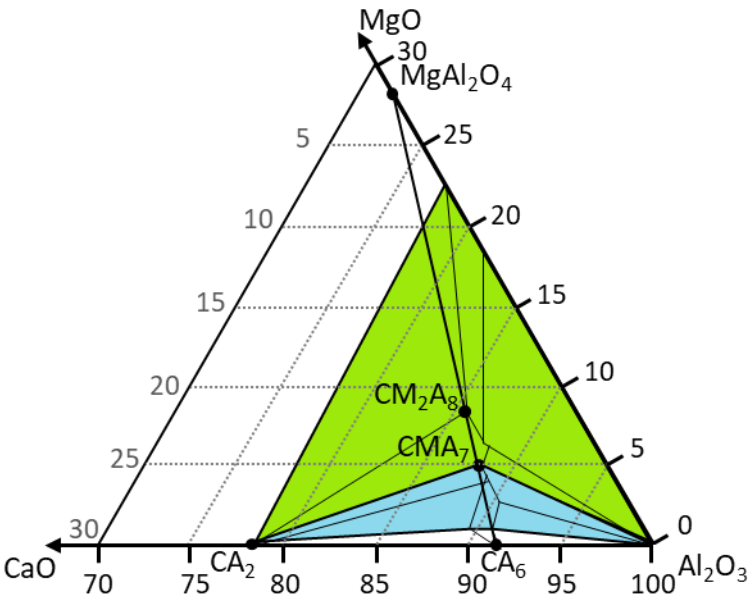

Figure 1-9. Part of the ternary diagram Al_2O_3-MgO-CaO, presenting isothermal section at 1650°C. Blue and green colours represent areas, where CMA I (CM_2A_8) and CMA II (CMA_7) are stable. This diagram has been redrawn from the publication written by Sako et al.[91]

1.2.4.6 *Comparison of two alumina aggregates: WFA & TA*

High alumina aggregates (Al_2O_3 > 99 %) are one of the main components of alumina spinel castables dedicated to steel ladle. Two aggregate types are the most popular: Tabular Alumina (TA) and White Fused Alumina (WFA). TA is produced by sintering of calcined alumina agglomerates where grain coarsening is promoted with a rather high-temperature process (typically 1700-1750 °C). This processing route for which a high speed of grain coarsening is targeted allows quite homogenous chemistry but leads to entrapment of porosity during sintering. WFA is produced by melting of calcined alumina above at a very high temperature (above 2072 °C). This processing route for which all components are firstly melted and then solidified with different cooling rates (depending on the position within fused blocks) allows production of more dense grains but leads to some inhomogeneity in chemistry. In fact, due to the difference in cooling rates between the inner and the outer part of the alumina block, different properties could be observed and segregation of β-alumina (NA_{11}) could occur in the upper central part of the block.[92] After cooling, high-quality parts of fused blocks could be selected to separate parts where impurities could accumulate. In the end, both TA and WFA products are crushed and screened to obtain the aggregates in the targeted size range.

Due to the intrinsic differences between production processes, TA aggregates are more homogenous than WFA ones both regarding the distribution of impurities, crystal size, as well as size and repartition of pores. Moreover, WFA aggregates exhibit higher density (ρ=3.66 g/cm3) and larger crystal size, than TA ones (ρ=3.60 g/cm3), which could potentially lead to better corrosion resistance of WFA.[92] Additionally, shapes of those aggregates also differ, as a result of different fracture behaviour during crushing.[92] WFA aggregates exhibit more angular shapes than TA (which are more round). The rounder shape of TA aggregates can thus lead to higher flowability, compared to WFA ones.[92] Furthermore, some differences in the amount and distribution of pores can also be observed. TA has a significant amount of small, mostly closed pores (< 10 µm), while pores in WFA (if present, as porosity varies) are relatively large (e.g. 30-50 µm).[92,93]

Considering TA and WFA aggregates in refractory applications, X. Liu et al.[94] found, that corundum bricks based on TA aggregates have much higher density, higher strength and lower apparent porosity, compared to bricks based on WFA. S. Möhmel et al.[95] also observed, that TA-based alumina castables have higher strength, but contrary to the above-quoted article, the TA-based castables led to lower bulk density (than the ones based on WFA). This paper also demonstrates, that castables based on TA aggregates lead to a higher Creep in Compression (CiC) rate at 1600°C and lower Refractoriness under Load (RuL) with softening beginning at temperature ~100 °C lower than for WFA. The lower performance of TA-based castables during RuL and CiC tests has been linked to higher availability of sodium originating from TA aggregates. Both WFA and TA contain sodium impurities, but sodium present in TA seems to be “not so much incorporated in the structure” and due to more porous TA structure and more homogenous sodium distribution, it could release sodium much easier at lower temperatures (compared to WFA). This sodium can react with other impurities forming a liquid phase which negatively impact castable performance during RuL and CiC tests.

1.2.4.7 *Comparison of two very fine castable components: Fumed silica vs. reactive alumina*

Reactive alumina or silica fume are very fine particles (typically ranging between 0.3-6 µm), which is an important constituent of castable matrix together with other fines. Matrix has a significant impact on numerous castable properties, including

flowability, density, porosity, strength or corrosion resistance. There are two major differences between silica and alumina fines. First of all, industrial silica fume, due to the production process (condensation and solidification of SiO vapour during the production of e.g. silicon) has a spherical shape, which has a positive impact on castable rheology, while reactive alumina has an angular shape (as a result of grinding of larger particles), what leads (potentially) to lower flowability of products containing reactive alumina. Secondly, the presence of even a low quantity of silica fume (e.g. 0.5 wt. %) decreases hot mechanical properties and thus is often avoided in some applications (as mentioned in 1.2.3.3 in the case of alumina-based spinel-forming castables). In those cases, reactive alumina is preferred.

Considering the context of the current study where alumina castables with preformed spinel are investigated, reactive alumina is of main interest, as it does not decrease mechanical properties at high temperature (as silica does) and usually, for materials containing preformed spinel, material softening (which could compensate high expansion) is not required. Regarding Particle Size Distribution (PSD), fine alumina can be added as monomodal or multimodal. Desired particle packing is usually achieved by combining several modes of PSD.[96] Level of impurities, such as soda or silica, are of great importance as they can also impact e.g. hot mechanical properties. For this reason, these impurities are strictly controlled and their content is decreased, if necessary. For instance, soda content in alumina can be reduced by modifying hydrate precipitation condition or by using a soda removal process.[97]

1-3. Thermomechanical behaviour

This section introduces the current state of the art about investigation of refractories thermomechanical behaviour. In fact, a good understanding of materials behaviour in use at high temperature requires diverse sophisticated mechanical characterizations and deep analysis in order to transpose results of these laboratory tests to real behaviour of materials in their applications. Usually, material performance is evaluated by investigation of several temperature-dependent behaviours, including: thermal behaviour (coefficient of thermal expansion - α, thermal conductivity - λ), elastic behaviour (static/dynamic Young's modulus - E), damage (tensile/compressive/flexural strength - σ, stress-strain law, fracture energy - G_f), as well as plastic behaviour (creep parameters and/or refractoriness under load).

1.3.1. Origin of thermal stresses

In general, thermal stresses originate when thermally-induced material expansion/shrinkage is restricted. Origin of thermal stresses is usually considered on two levels: on microstructural and on brick/lining levels.

On microstructural level, different mechanisms can be active. Usually, microstructures of refractories are complex, as they include several different phases, with different grain sizes and temperature-dependent properties, as well as a significant amount of porosity. On this level, thermal stresses can originate from restriction of thermal expansion/shrinkage between different constituents. These stresses are related to different (temperature-dependent) Coefficients of Thermal Expansions (so-called CTE mismatch). This feature is very important in a designing step, due to its impact on fracture behaviour, and thus it will be more detailed in the next section.

On lining/brick level, two types of restriction are considered: a self-restriction (type A), being related with high-temperature gradients within the refractory, or a mechanical restriction (type B), linked with an external mechanical constraint, limiting expansion/shrinkage of the refractory.[98] The following paragraphs detail more these two types of restriction.

In the type A restriction (self-restriction),[98] there is no external constraint. During a hot thermal shock, caused by a one face heating (so-called hot face) of an isothermal brick, a temperature gradient is induced, leading to an expansion and causing stress gradient within the brick. In this case, compressive stresses would develop close to the hot face (the expansion is restricted by the cooler part of the material) and tensile stresses would develop at a given distance from the hot face. The heat flow over time, leads to movement of the transition zone, located where compressive and tensile stresses alternate, towards the cold face. A failure mode of this one-side heated, self-restricted brick consists in formation of an internal crack, having perpendicular orientation to the hot face (see Figure 1-10a). In case if heating would occur from two neighbouring sides (corner), the typical failure occurs at 45° (perpendicular to the highest principal stress direction) to both faces, leading to spalling of the edge (see Figure 1-10b). During a cold thermal shock, the opposite stress state occurs (tensile stresses are developed at the external face and compressive stresses inside the brick).

a) 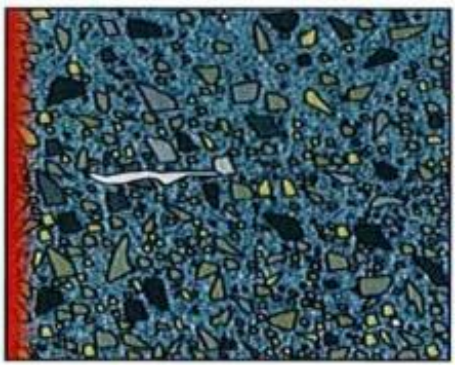 b) 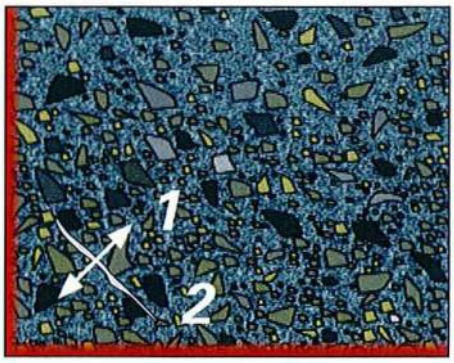

Figure 1-10. Typical failures occurring in a self-restricted isothermal brick: a) heated from one side; b) heated from two neighbouring sides (where 1 - maximal principal stress; 2 - crack formation).[98]

In the type B restriction[98], a material cannot expand, due to the presence of an external constraint. During hot thermal shock, the isothermal brick is under compressive loads, which lead to irreversible compressive strains, possibly inducing creep or failure. A typical failure for this restriction type is thus compressive or shear failure. During cold thermal shock of a lining, the joints between bricks may open. Globally, this origin of thermal stresses has been explained very shortly here. More information on thermal stresses in refractory linings could be found in the cited publications.[98–100]

In an industrial vessel, such as steel ladle, preheating is very important, as it closes joints between bricks, as well as it increases temperature of the lining and of the steel shell (allows lining to expand), leading to a reduction of temperature gradient during tapping (and thus decreases tensile stresses generated due to hot thermal shock).[98] Shape of the bricks and appropriate preheating procedure are especially important in the type A restriction (joints closure). According to Brochen et al.[101], hot thermal shocks, due to their sudden character are more severe, than cold shocks and thus lead to higher damage for most refractory linings.

1.3.2. Microstructure design related to mechanical behaviour

Refractories should be able to deform, under thermomechanical loadings, without significant loss of strength. Two types of mechanical behaviour can help to fulfil this criterion.[102]

Objective of the first one is to maximize strain required for crack initiation (σ_t/E). Once the strain is higher than the critical one, a failure process begins. Material behaviour can be described as brittle, with a crack propagating right after being formed, what could lead to a critical failure. Therefore, this type of behaviour is only useful

in applications where material deformations are lower than the critical strain value (in order to avoid crack initiation). In such case of brittle material, considering a typical microstructure based on matrix and aggregates, the matrix should be strong and thus crack propagates through aggregates.

The aim of the second type of mechanical behaviour is to maintain a high residual strength after cracking (cracks are allowed to initiate during service, but their propagation should be very low). It can be achieved by designing a material (having non-linear behaviour) with reduced material strength, but exhibiting a high level of fracture energy. In this case of material with reduced brittleness, considering a typical microstructure based on matrix and aggregates, the matrix should promote the occurrence of microcracks, especially along aggregates boundaries. This type of behaviour is applied when cracking cannot be avoided (e.g. in a steel ladle) and it is considered as safer, than the first type, because it prevents sudden failure thanks to a significantly reduced brittleness. Stress-strain behaviour of different types of refractory materials are presented in Figure 1-11.

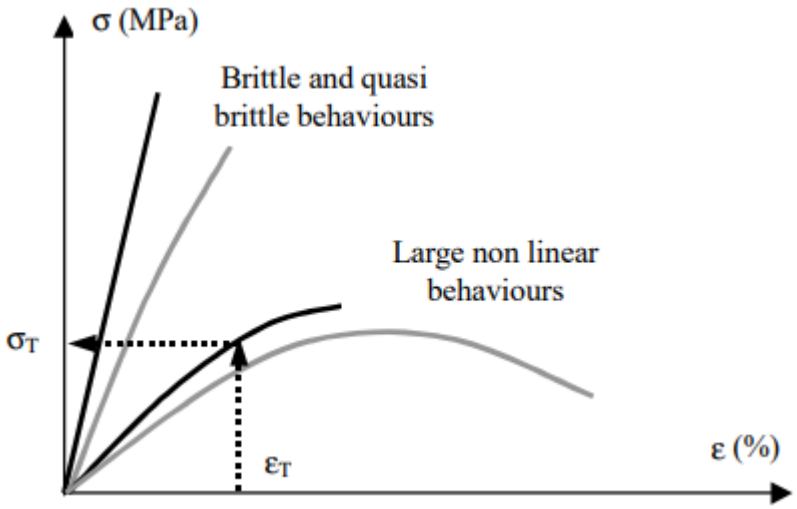

Figure 1-11. Different types of refractory materials, regarding their stress-strain behaviour.[103]

In order to better understand microstructure design that could promote microcracks within the matrix, let us consider a two-phase material with determined CTE values for matrix (α_m) and inclusions (α_i). An important parameter, is the CTE mismatch ($\Delta\alpha=\alpha_m-\alpha_i$), being a simple difference between the CTE values of the two phases.[103] The CTE mismatch influences stress state, which could emerge the matrix/inclusion interface during cooling, what may lead to e.g. debonding

at the interface (if Δα<0) or formation of radial microcracks (if Δα>0). Figure 1-12 shows the influence of the CTE mismatch on state of interfacial stresses emerged during cooling and resulting microstructure.

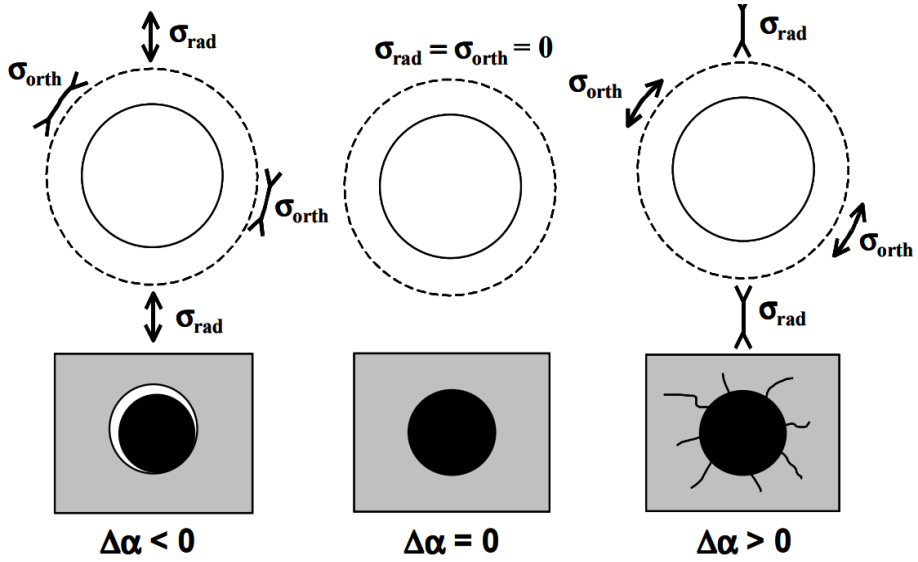

Figure 1-12. Influence of thermal expansion mismatch of a spherical inclusion within an infinite isotropic matrix on internal stresses induced during cooling and effect on microstructure.[103]

1.3.3. Elastic behaviour - exemplary results

Elastic behaviour of refractories is usually investigated by measuring Young's modulus E. This parameter is very often used for non-destructive quality control of refractories and it is a key parameter required to evaluate the stress state within a refractory lining (by FEM), induced by a thermal cycle. Additionally, measuring the evolution of Young's modulus versus temperature could also be very valuable to understand microstructural evolution during thermal treatment (mimicking life cycle of materials). This elastic property can be determined using two types of measurements: a quasistatic one (often referred to as static), derived from the slope of a stress-strain curve during a mechanical test, or a dynamic one, based on a measurement of resonant-frequency or of the speed of ultrasonic waves.[104,105] Those two different approaches could sometimes lead to discrepancies between experimental results, most probably when measurements are not very accurately performed. In fact, some authors could have measure dynamic Young's modulus E_{dyn} even 4-8 times higher than the static one E_{st},[106–110] since the behaviour of investigated materials was probably not purely elastic. This difference is more pronounced at high temperatures, as static measurements could significantly underestimate E_{st} values due to creep. That is why H. Harmuth and R.C. Bradt suggest using only E_{dyn}

at high temperatures, as according to them only the dynamic parameter represent meaningful values.[102] The discrepancy between the two approaches can be reduced by targeting to measure static Young's modulus (slope of stress-strain curve) at the very beginning of tensile or compression tests. Taking into account that the present PhD study is more focused on microstructural investigations, the following paragraph will introduce some exemplary results where Young's modulus was used to investigate material evolution versus temperature.

It is useful starting with the very typical influence of temperature on E_{dyn}, for a material with a stable microstructure. The microstructure of dense alumina, tested in Figure 1-13a, is stable until 1400 °C. This can be observed on the $E_{dyn}=f(T)$ curve through a reversible linear dependence. A subsequent significant decrease of E_{dyn}, observed above 1400 °C, could usually be attributed to viscous phenomena at grain boundaries, related to segregation of impurities or sintering additives.

Figure 1-13b shows Young's modulus evolution curves during the first heating cycle of two alumina-based castables. The first one is named castable C12.5 and has 12.5 wt. % of cement, while the second one, being named as castable C12.5S1, is very similar to the first one, with the 1 wt. % addition of silica fume. During the first heating of the C12.5 castable, one can distinguish three major trends. Below 400 °C, one observes a decrease of E_{dyn}, due to conversion of CAH_{10} (to C_3AH_6 and AH_3) and subsequent dehydration of C_3AH_6 and AH_3. Then, until sintering and phase changes (until 900 °C), the E_{dyn} stays at relatively low and stable values. During sintering and phase changes ($C_{12}A_7 \rightarrow CA \rightarrow CA_2 \rightarrow CA_6$), Young's modulus increases significantly. Formation of CA, CA_2 and CA_6 phases occur from 900 °C, 1100 °C and 1450 °C, respectively (but different temperatures, also lower ones, can also be found in the literature).[84,111,112] During cooling, in the case of C12.5, Young's modulus increases with a constant rate, indicating a stable microstructure. By comparing the E_{dyn} evolution of the two castables (with and without silica addition), one can observe a significant influence of silica fume on microstructure evolution at temperatures higher than 900 °C. The addition of silica leads to three major differences. Firstly, it leads to viscous sintering, which increases E_{dyn} at lower temperatures during heating (starting from 950 °C). Secondly, at temperatures higher than 1350-1400 °C, a non-equilibrium liquid could develop, causing a significant decrease in E_{dyn}. Lastly, a progressive solidification of the glassy phase is the probable cause of the steep increase of E_{dyn} during cooling between 1200 °C and 1000 °C.

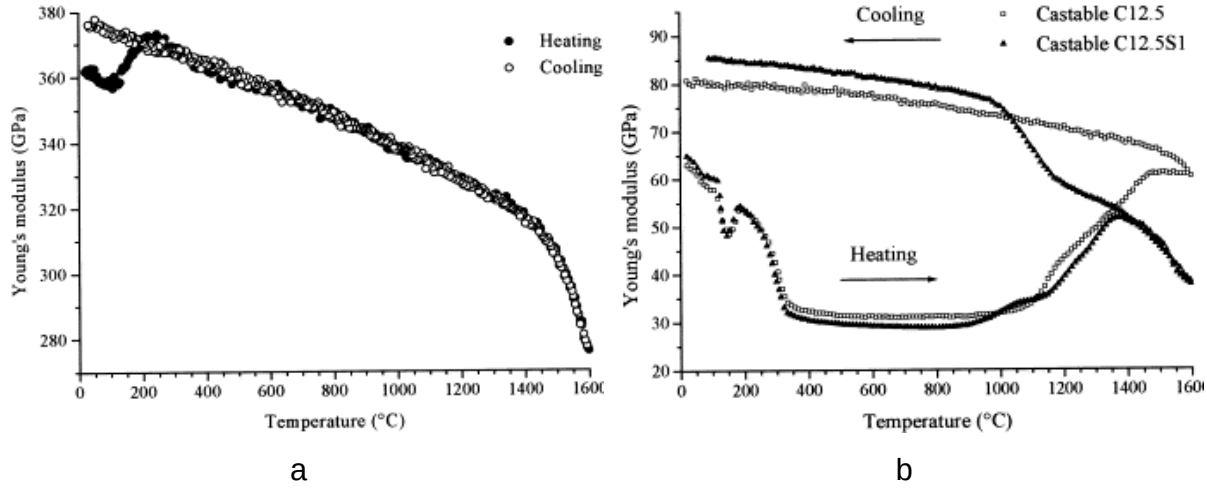

a b

Figure 1-13. Young's modulus evolution during thermal treatment (obtained by ultrasonic technique) for: a) a dense polycrystalline alumina sample, b) alumina-based castables C12.5 (12.5 wt. % of cement) and S12.5S1 (12.5 wt. % of cement and 1 wt. % of silica fume).[84]

1.3.4. (Pseudo-)Plastic behaviour - exemplary results

In the past, the notion of plasticity was not often considered in literature in the context of refractories. It was probably due to the fact that ceramic materials are known to exhibit rather brittle behaviour in a large temperature range. However, refractories behaviour in some specific conditions can actually be plastic or resemble it. Those specific types of non-linear behaviour are addressed in this section with an illustration of some exemplary results.

At low temperatures and for very low strain levels, the mechanical behaviour of refractories could generally be considered as linear elastic. However, as strain increases, refractories can exhibit non-linear stress-strain behaviour in tension (or compression), which could resemble a "plastic" behaviour. An example of such behaviour is presented in Figure 1-16a. Alumina refractory castable, tested at ambient temperature (but pre-treated at different temperatures), deforms non-linearly and Young's modulus (measured at the beginning of unloading for each cycle) gradually decreases with each subsequent cycle (see Figure 1-16b). This reduction of Young's modulus after each cycle, being related to the specific heterogeneous microstructure of refractories, can be explained by an extension of the microcracks network (diffused damage) during loading.[113,114] Even if this decrease of stiffness is due to damage progression, this type of behaviour is sometimes qualified as pseudo-plastic, due to its resemblance to plasticity.

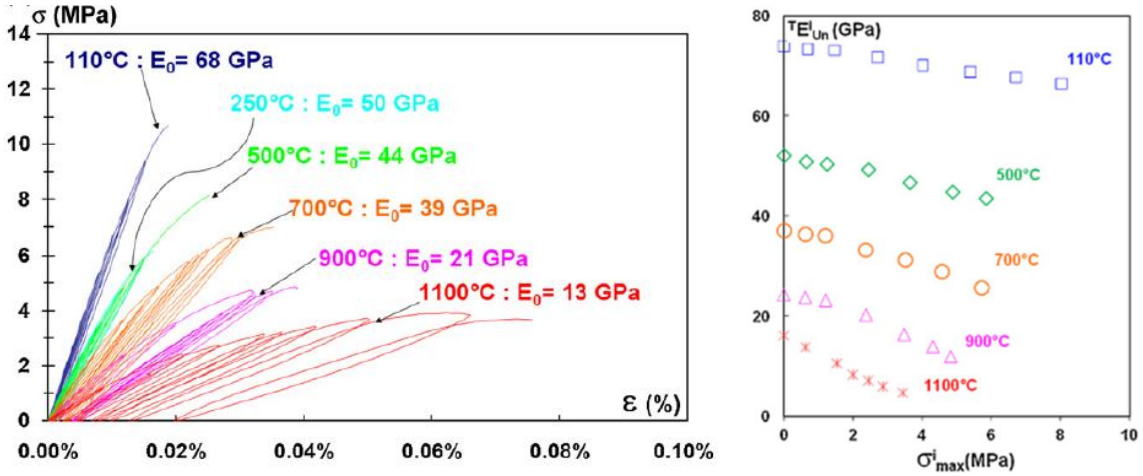

a b

Figure 1-14. Results of tensile-cyclic tests (limited to positive strains) performed at ambient temperature on a low cement andalusite castable (pre-treated at different temperatures): a) stress-strain curves in tension, b) Young's modulus measured at the beginning of each unloading cycle vs. maximum applied stress.[114]

At high temperatures and for rather low strain levels, materials could behave viscoelastically or viscoplastically. These types of behaviour can be determined with the help of symmetric alternate loading tests (tension and compression). Exemplary results of such tests performed on zirconia-based refractories are presented in Figure 1-15. The three different types of material behaviour can be observed depending on temperature: linear-elastic (below 900 °C), viscoelastic (950 °C, 1100 °C) and viscoplastic (1300 °C). Viscoelastic behaviour is detected by the presence of a hysteresis loop and viscoplastic one by a significant level of permanent deformation, which, in this case, leads to failure.

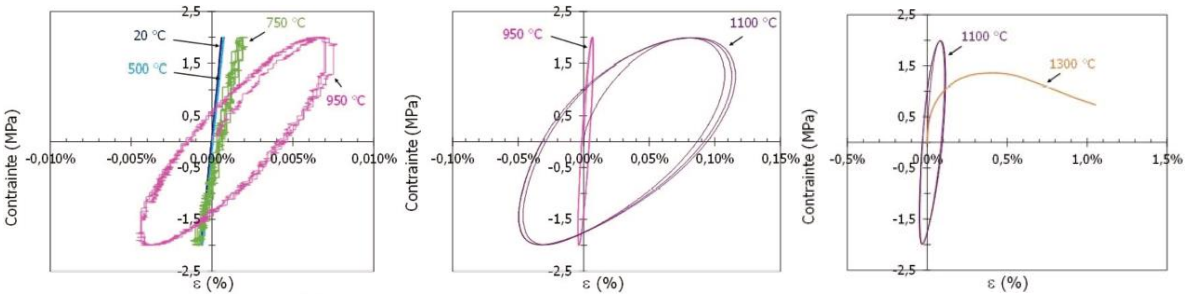

Figure 1-15. Stress-strain curves from symmetric alternate loading tests performed at different temperatures on zirconia-based material.[110]

Performance of alternate loading tests on refractory materials require following time-consuming procedure for sample preparation and testing samples at different temperatures, as well as quite complex experimental setup, mainly due to the need

for very accurate and stable extensometers dedicated to high-temperature tests (up to 1500 °C). Therefore, plastic behaviour is much more often investigated by performing Refractoriness Under Load (RUL) or Creep In Compression (CIC) tests, which are easier to perform and allow to obtain information in a short time. The main information, which could be obtained by these methods include temperature at which material starts to deform significantly (for example $T_{0.5}$ value for RUL) and secondary creep rates ($\dot{\varepsilon}$) for given temperatures and pressures (for CIC).

Exemplary RUL and CIC results, obtained on high-purity alumina refractories with WFA or TA aggregates, are presented in Figure 1-16. WFA-based refractory exhibits higher RUL (see Figure 1-16a) and lower creep rate (see Figure 1-16b). The higher load applied during shaping by uniaxial pressing of materials increases the RUL of both refractories and improves the creep resistance of TA-based refractory.

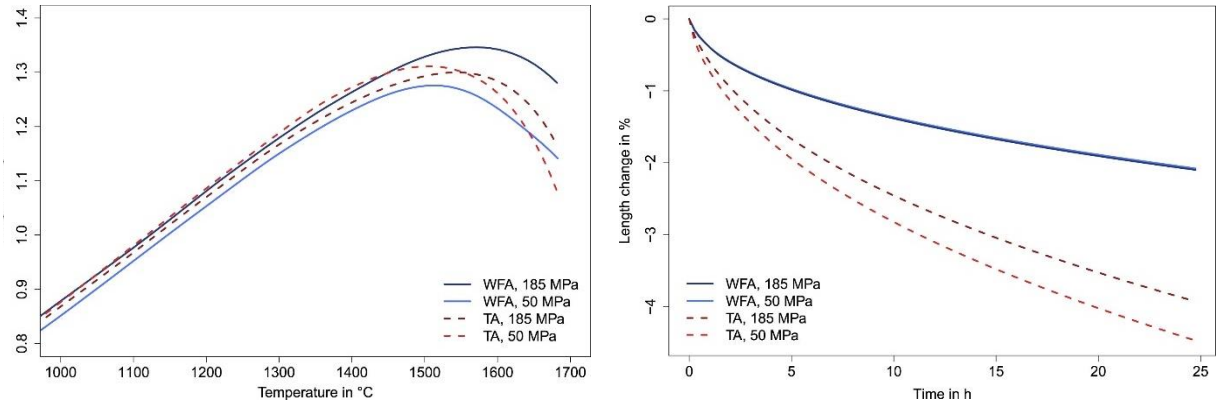

a b

Figure 1-16. Effects of load applied during shaping by uniaxial pressing on refractories with WFA or TA aggregates: a) Refractoriness Under Load; b) Creep In Compression.[115]

1.3.5. Fracture behaviour

As already mentioned (in section 1.3.4), at low temperature and for significant strain levels, refractories could exhibit pseudo-plastic behaviour, which is linked to an extension of microcracks network. Resistance to damage is usually investigated by studying fracture behaviour. Currently, one of the most adequate techniques used for investigation of fracture behaviour is Wedge Splitting Test (WST), which specifically targets a stable crack propagation in mode I (opening). Even if more details about this experimental technique will be given in section 3.1.1, an exemplary result of WST is presented here in Figure 1-17. Pure magnesia refractory exhibits a small post-peak

behaviour, in comparison to other materials, which contain inclusions of hercynite. With such specific inclusions, a very large post-peak behaviour could be observed. This very important difference in fracture behaviour is related to CTE mismatch (explained in section 1.3.2), between magnesia matrix and hercynite inclusions, which promotes the formation of a microcracks network during material processing (cooling after sintering). The pre-existence of such small microcracks is extremely useful during loading, as it promotes diffused damage, allowing the material to withstand relatively high strain while maintaining a significant strength (characteristic for materials with large non-linear behaviour). Pure magnesia refractory does not contain such feature and therefore exhibits a rather brittle behaviour.

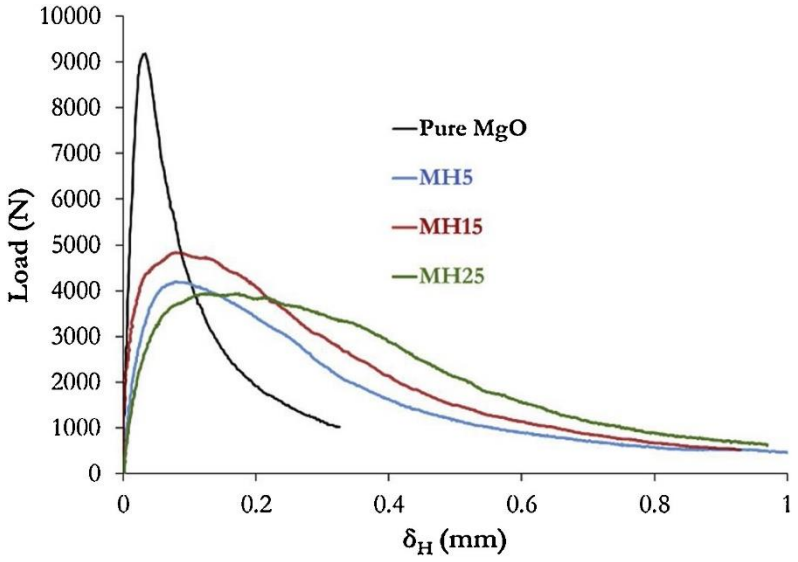

Figure 1-17. Horizontal load-displacement curves obtained by WST for pure magnesia refractory and magnesia hercynite composites: MH5, MH15, MH25 with 5, 15 and 25 wt. % of hercynite inclusions, respectively.[116]

As a first attempt to compare materials, one can determine the area below the curve, which mainly corresponds to the energy consumed to break the sample. When this total fracture energy is divided by the projected area of fracture, it becomes the specific fracture energy G_f. Coming back, to the materials from Figure 1-17, one can compare their specific fracture energies. The specific fracture energy is inversely proportional to brittleness (which will be introduced later) and higher value usually indicates better fracture resistance. The G_f' (in this case only measured until load drops to 15 % of maximal load) is about 130 J/m^2 for pure magnesia refractory, and about 213, 266 and 281 J/m^2 for magnesia hercynite materials: MH5, MH15 and MH25, respectively.[116] For comparison, it is worth mentioning that the surface

energy of pure magnesia, which is equal to 1.2 J/m^2,[117] is in fact two orders of magnitude lower than the fracture energies of these investigated refractory materials. This huge difference is simply due to strong additional energy dissipation phenomena, promoted by the specific microstructure of refractories. Figure 1-18 illustrates such phenomena (tortuous crack propagation and potential crack branching), which can be quite different between a pure magnesia refractory and magnesia hercynite composite. Such crack deflection and crack branching can be easily observed, especially for MH15 in Figure 1-18b, and leads to much higher fracture energy.

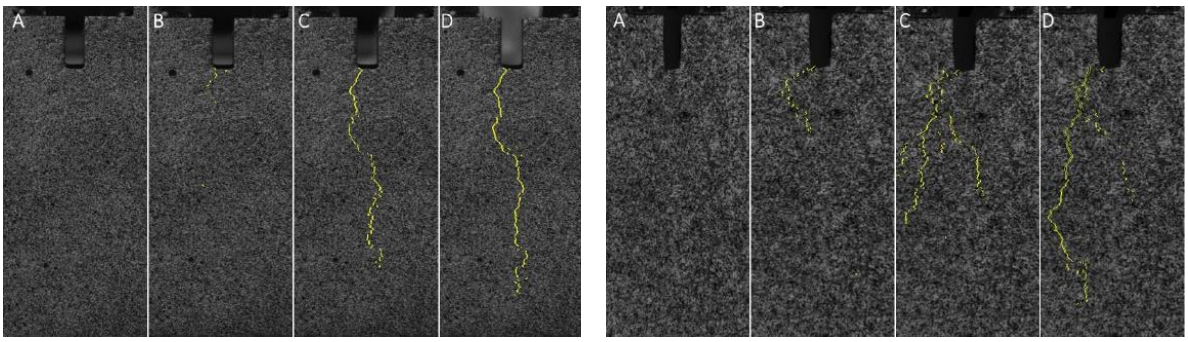

a b

Figure 1-18. Images of instantaneous crack propagation during wedge splitting test revealed by 2P-DIC for: a) a pure magnesia refractory, b) a magnesia hercynite composite with 15 wt. % of hercynite (MH15).[116]

1-4. Conclusion

Reading this introductory chapter, one understands that studies on refractory materials are complex due to several reasons. First of all, they are **very heterogeneous** and should be **designed in relation to predominant wearing factors** in each application. Secondly, in the case of investigated alumina spinel materials, their microstructure can be **designed in different ways** allowing to obtain a set of properties adapted to target application. Thirdly, **thermomechanical properties** are **closely related to microstructure** which can **evolve during thermal treatment**. Therefore, studying in-use microstructural evolution is crucial in understanding material behaviour what facilitates further improvements. Finally, a need to better understand materials behaviour in more realistic conditions promotes development of advanced testing approaches that integrate recent improvements in technology. Studies in the field of refractories require knowledge of different experimental methods which will be more detailed in the following chapters.

Chapter 2

Chapter 2. ATHOR project, investigated materials and characterization methods

This chapter aims to **introduce ATHOR project and rather classical experimental techniques** (used in investigations presented in Chapter 4).

2-1. ATHOR project

2.1.1. International context

FIRE (Federation for International Refractory Research and Education) is a worldwide network coupling the world's leading academic institutions, as well as the key industrial partners (including raw minerals suppliers, materials producers and end-users) from the field of refractories. Network developed within this non-profit organization became a cornerstone for founding international and ambitious European project named ATHOR (Advanced THermomechanical multiscale mOdelling of Refractory linings). This project allows 15 PhD students to develop their skills within the network of 7 academic and 8 industrial partners from the refractory sector (see Figure 2-1). This cooperation is carried out in framework of prestigious Marie Skłodowska-Curie Actions (Grant H2020-MSCA-ITN-2017-764987), which supports innovative training of young researchers in both academic and industrial fields.

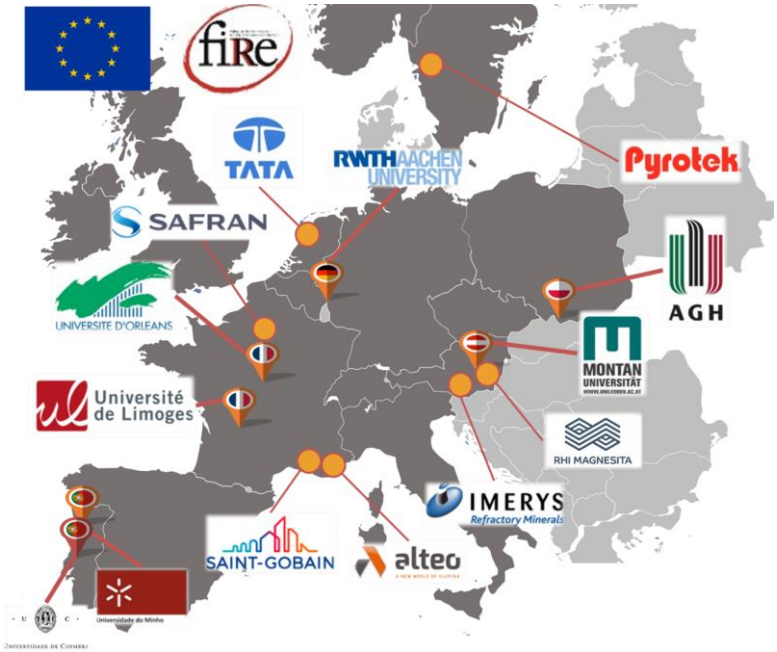

Figure 2-1. ATHOR consortium including 7 academic and 8 industrial partners (updated map originating from the project proposal).[10]

2.1.2. Scientific approach

The scientific core of ATHOR project (presented in Figure 2-2), can be divided into four parts (referred to as Work Packages, abbreviated as WP). They cover improvement of measurement tools (WP1), characterization of refractories (WP2), multi-level modelling (WP3) and validation of numerical models (WP4). Each WP contains specified tasks, which are assigned to 15 early stage researchers involved in this project.

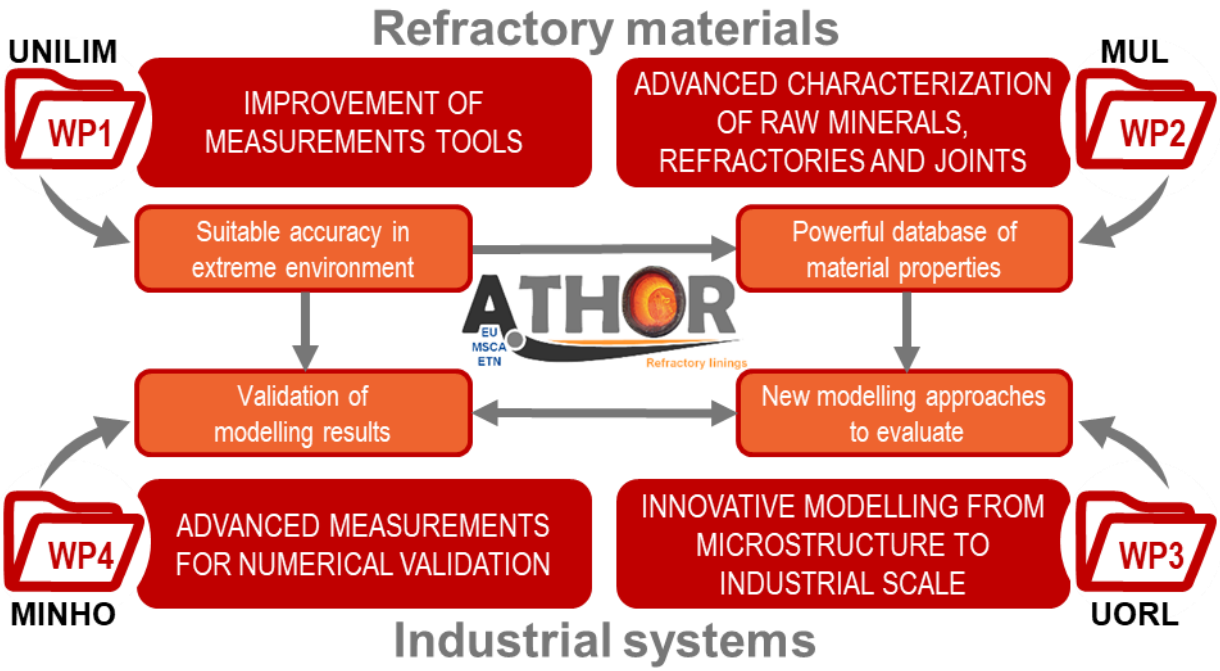

Figure 2-2. Diagram presenting the scientific structure of ATHOR.

2.1.3. Contribution of the present thesis

Scientific scope of this PhD study, presented in Figure 2-3, covers several tasks from three work packages (WP1, WP2 and WP4). They are related to improvement of two novel experimental methods and to thermomechanical characterization of several alumina spinel refractories.

High-temperature Brazilian test and a special thermal shock bench are the two devices that had to be improved. Optical chain of the first experimental method has been adapted to high temperature conditions and precision of optical measurements has been increased (by optimizing a number of parameters). The second device, named ATHORNA (referring both to the association of “ATHOR” and “New Aquitaine”, as well as to “Advanced measurement for in-situ THermo-mechanical mOnitoRing of large sample uNder thermal grAdient”), was mainly developed with objective to

validate numerical FEM approaches dedicated to thermal shocks. For that purpose, key outputs from DIC strain fields were investigated in order to compare experimental results (from ATHORNA device) with numerical ones (from FEM). Additionally, a deep comparative study of thermal shock resistance was carried out on model magnesia-spinel materials (see Annex A).

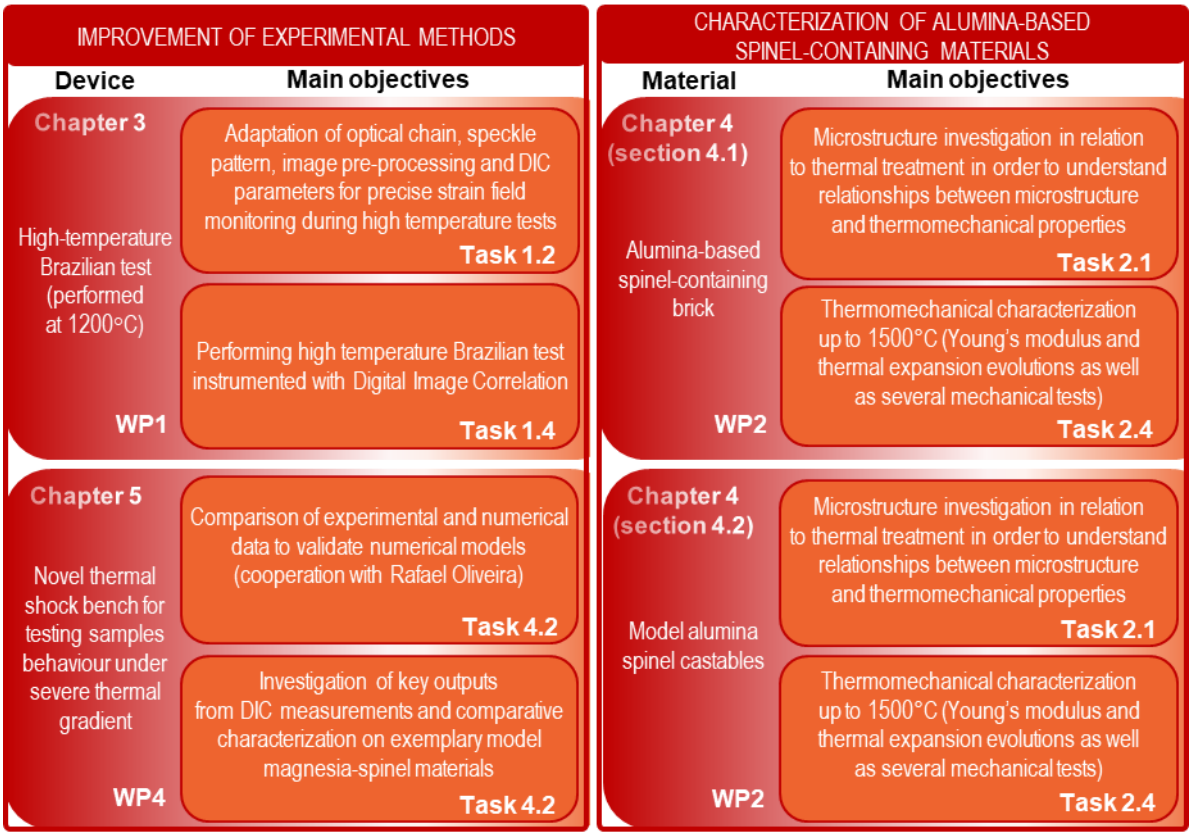

Figure 2-3. Key items considered within the present PhD with corresponding chapters.

The work dedicated to characterization of materials is divided in two parts. The first one concerns industrial fired alumina spinel bricks currently used in steel ladles, while the second one concerns model alumina spinel castables. The general objectives of both parts are to characterize in-use behaviour of materials microstructure and thermomechanical properties, as well as to understand relationships between microstructural phenomena and thermomechanical properties. It should be noted that the industrial brick has a fixed composition and well-defined processing route, thus only characterization related to in-use behaviour (*a posteriori* thermal treatment) could be performed. The approach is different in case of model castables, which were initially designed to compare influence of compounds (cements, aggregates, reactive alumina) on high-temperature thermomechanical behaviour. The

studies concerning industrial alumina spinel bricks and model alumina spinel castables are presented in sections 4-1 and 4-2, respectively.

2-2. Microstructural characterization methods

2.2.1. XRD with Rietveld refinement

X-Ray Diffraction (XRD) technique provides access to both qualitative and quantitative information about the crystalline phases of materials. For this purpose, powder was obtained by dry grinding in a planetary ball mill rotating with a speed of 250 rpm for 20 minutes, which allowed to reduce its size, typically to about 8 µm. The grinding tools are made of tungsten carbide, thus traces of WC can sometimes be detected. Qualitative analysis was performed with the DIFFRAC.EVA software (from Bruker), using the database of the International Centre for Diffraction Data (ICDD - a previous abbreviation of the preceding organization name was JCPDS).

In order to improve quantitative analysis, with measurement uncertainty below 1%, experimental procedure has been managed to reach a high number of counts (about 100.000 for the highest peak). Quantitative analysis was carried out with TOPAS software (from Bruker), using Rietveld refinement method.[118] This method employs least-squares fitting of the experimental curves from the standard patterns of each compounds, identified during qualitative analysis. This fitting consists on modification of different parameters related to each compound and its proportion (as well as some parameters of the experimental setup) in order to adjust positions, shapes and intensities of analysed peaks. The order of the refining parameters is as follows: first the parameters related to peaks positions, then peak shape-related parameters and, at the end, peak intensity-related parameters.[119]

Two types of XRD tests were performed using different setups (see Table 2-1). The ambient temperature and high-temperature tests were performed using D8 ADVANCE (at IRCER, Limoges) and X'Pert³ MRD (at Tata Steel CRC, Ijmuiden) systems, respectively. Both diffractometers use Bragg-Brentano geometry, as well as an anti-scatter knife edge and a narrow divergence slit.

Table 2-1. Types of XRD equipment used for ambient and high-temperature measurements.

	XRD system	Target material	Sample holder material	2Θ range [°]	Step [°]	Time per step [s]	Total acquisition time [h]
Ambient temp. test	D8 ADVANCE (IRCER)	Copper	Acrylic glass (PMMA)	5-75	0.01	0.48	~1.0
High-temp. test	X'Pert³ MRD (Tata Steel)	Cobalt*	Platinum strip	5-75	0.01	0.25	~0.5

*Cobalt target installed due to frequent testing of iron-containing samples

High temperature XRD tests were performed in air using a platinum strip-heater type chamber (HTK 2000N). Such setup requires calibration, performed before each measurements, which takes into account the potential vertical shift of a sample. This calibration was performed based on the position of the most intense alumina peak. High-temperature XRD experiments were performed with a heating/cooling rate of 5 °C/min and with multiple 1h dwells, executed every 100 °C from 900 to 1500 °C (7 dwells). At each dwell, XRD program (with total acquisition time of ~30 min.) was automatically launched after 30 minutes of temperature stabilization. Due to the better precision of ambient temperature experimental setup, all materials tested at high temperature were also tested at ambient temperature before and after thermal treatments.

2.2.2. Microstructure observations (SEM & EDS)

Microstructural observations were performed using several Scanning Electron Microscopes (SEM) with Energy-Dispersive X-ray Spectroscopy (EDS) detector. Signal from BackScattered Electrons (BSE) detector, depending on atomic number Z, was used when chemical contrast between different phases was targeted. In some cases, when chemical contrast was not required, Secondary Electrons (SE) detector was also used.

Samples were impregnated under vacuum with epoxy IP-type resin (from Presi). After 30 minutes of impregnation, sample was put aside for 24 hours in order to complete polymerization of the resin. The next step consisted on manual surface preparation (grinding and polishing) using the following discs: MD-Piano 120, MD-Piano 220, MD-Piano 500, MD-Piano 1200, MD-Piano 2000 and MD-Piano 4000. Right before observations under SEM, polished surface was covered with a thin

conductive Au/Pt or C layer and then connected to the metallic sample, using paths made of silver paste.

2-3. Thermo-physical characterization techniques

2.3.1. Thermal expansion measurement (dilatometry)

Dilatometric measurements were performed on the horizontal dilatometer NETZSCH DIL 402C. The cuboidal-shaped samples were tested in air atmosphere, using the experimental conditions presented in Table 2-2. The applied heat treatment consisted of three steps: constant heating until 1500 °C, a dwell at the maximal temperature and constant cooling. Each test was preceded by an accurate measurement of the system dilatation itself thanks to a well-known alumina standard. This system dilatation was later subtracted from the raw experimental results to calculate only thermal expansion of the sample.

Table 2-2. Experimental conditions for dilatometry measurement.

Sample dimensions [mm^3]	Atmosphere	Heating/cooling rate [°C/min]	Dwell temp. [°C]	Dwell duration [min]
5x5x25	Air	3 or 5	1500	60

2.3.2. Refractoriness under load and creep in compression

Refractoriness Under Load (RUL) allows determining deformation behaviour of refractories under constant load and increasing temperature (detailed in ISO 1893:2007). Creep In Compression (CIC) is typically performed after RUL, maintaining the maximal temperature (detailed in ISO 3187:1989). In this study, each tested specimen was firstly tested on RUL (constant load of 0.2 MPa, heating rate of 5 °C/min, max. temperature 1600 °C) and then on CIC (constant load of 0.2 MP, temperature of 1600 °C, duration of about 5 hours). The specimen is a cylinder with dimensions of Ø50x50 mm^3 and co-axial bore of Ø12.5x50 mm^3.

2.3.3. Dynamic Young's modulus measurement by ultrasounds

Ultrasonic devices can be used to investigate elastic properties of refractory materials. In this study, a long bar configuration of the ultrasonic device, being suitable for high-temperature measurements, has been selected to investigate temperature-dependent evolution of Young's modulus. This method, which has been

specifically developed in Limoges since many years (1970's), is not as classical as standard characterisation methods and thus it is briefly described here.

The experimental setup, used in this study, is presented in Figure 2-4. The method consists of generation of longitudinal ultrasonic waves by a transducer (composed of a magnetostrictive rod surrounded by a copper coil), which then propagates through an alumina waveguide (glued to the magnetostrictive rod) and the cuboidal sample (glued to alumina waveguide using a high-temperature resistant ceramic binder). Some ultrasonic waves are reflected at the interface between the waveguide and the sample and the other ones, are reflected from the end of the sample (multi-reflections are possible). The transducer is also used to detect reflected ultrasonic waves which are then presented on an ultrasonic echogram. The key variable, being measured from the echogram, is the time of flight of ultrasonic wave within the sample τ. This variable together with sample density ρ and sample length L allow to determine Young's modulus E_{US}, according to Equation 2-1. Measurement of Young's modulus evolution during thermal treatment is possible thanks to the coupling between the ultrasonic device and the furnace, operating up to 1750 °C.

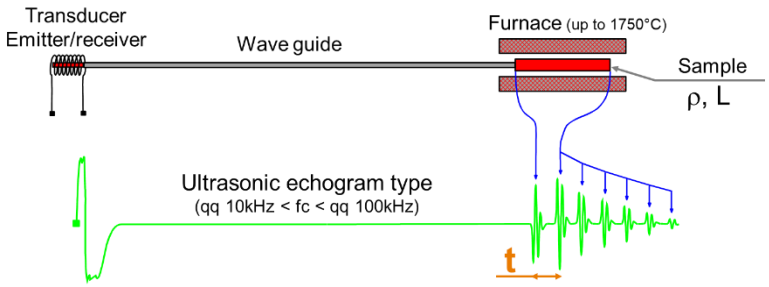

Figure 2-4. Schema of the ultrasonic device used for measurement of elastic properties at high temperature.[100]

$$E_{US} = \rho . \left(\frac{2L}{\tau}\right)^2 \qquad \text{Equation 2-1}$$

The typical experimental conditions, similar to the ones used for this study, are presented in Table 2-3.

Table 2-3. Typical experimental conditions used for measurement of Young's modulus evolution with temperature, using the ultrasonic device.

Typical sample dimensions [mm^3]	Waveguide diameter [mm]	Transducer frequency [kHz]	Atmosphere	Heating/cooling rate [°C/min]	Dwell temp. [°C]	Dwell duration [min]
12x12x120	10	30 or 90	Air	3 or 5	1500	60

2.3.4. Dynamic Young's modulus measurement by resonance

Resonant Frequency and Damping Analysis (RFDA) is a non-destructive method often used to investigate elastic properties of refractories, which has been commercialized since the 2000s. This method is based on the Impulse Excitation Technique (IET) which involves excitation of the sample to induce resonant vibrations. These vibrations are then recorded by a microphone to determine both resonant frequencies and their damping values. The sample is excited by a light impact (e.g. using a small hammer) near an anti-node of vibration. Depending on the impact area, the position of supports and the sample shape, different vibration modes can be excited (flexural, torsional, longitudinal).

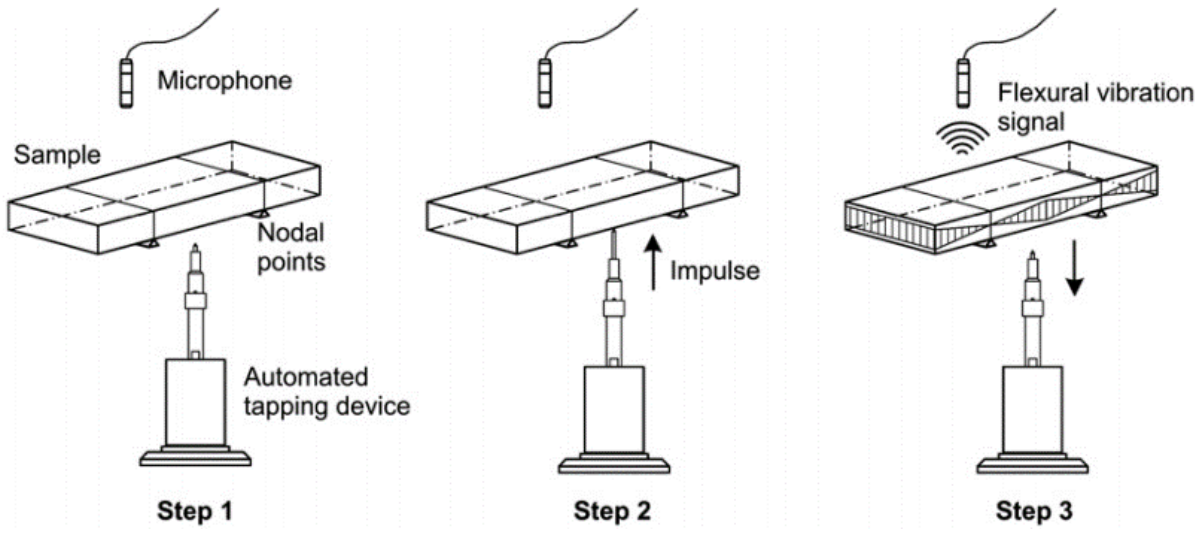

Figure 2-5. Schematic representation of the IET principle.[120]

Measurements during this study were performed at Tata Steel CRC in IJmuiden on the RFDA HTVP1600 device (from IMCE) with induction of flexural vibrations in tested samples (see Figure 2-5). The cuboidal sample is positioned on two parallel supports and struck from the bottom, generating flexural vibrations which are then recorded by a microphone from the top-side of a tested specimen. Young's modulus E_{RFDA} is determined using Equation 2-2,[104] where variables represent sample

properties, such as mass *m*, length *L*, width *b*, thickness *t*, as well as correction parameter *A* (being a function of *L*, *t* and ν, where ν is Poisson's ratio) and flexural frequency f_f.

$$E_{RFDA} = 0.94565 \left(\frac{m f_f^2}{b}\right)\left(\frac{L^3}{t^3}\right) A \qquad \text{Equation 2-2}$$

Experimental results of Young's modulus evolution with temperature, obtained by RFDA, are very similar to the ones obtained by the ultrasonic device and has already been presented in the previous section. Typical experimental conditions used during this study are presented in Table 2-4.

Table 2-4. Typical experimental conditions used for measurement of Young's modulus evolution with temperature by RFDA.

Typical sample dimensions [mm³]	Atmosphere	Heating/cooling rate [°C/min]	Dwell temp. [°C]	Dwell duration [min]
20x25x120	Air	5	1500	300

2.3.5. Uniaxial tensile test

A uniaxial tensile or compression device, equipped with highly precise extensometers, is used in this study to investigate the stress-strain behaviour of alumina spinel bricks up to 1200 °C. Tensile testing of refractories requires following a strict sample preparation protocol, ensuring precise alignment of the sample with the loading axis. Additionally, since strain to rupture of refractories is very low (typically lower than 0.15%), highly precise extensometers are strongly required. All these challenges have been addressed in the PhD thesis of M. Kakroudi and resulted in establishment of a successful experimental procedure.[121] This device and experimental procedure are briefly described here.

Figure 2-6 shows a schematic representation of the device. It is based on an INSTRON 8862 testing machine with a rigid frame (100 kN), well-aligned hydraulic grips and a load cell (capacity of 5 kN). Tests at high temperature are possible thanks to the combination of the testing machine and an induction furnace (with a molybdenum bi-silicide susceptor, T_{max} = 1600 °C). Precise strain measurements at high temperature are managed by two capacitive extensometers with SiC rods, being located on the opposite sample sides. Both the furnace and the extensometers are covered by sealed water-cooled casing, which improves

the precision of strain measurements and enables testing under a controlled atmosphere (air, argon).

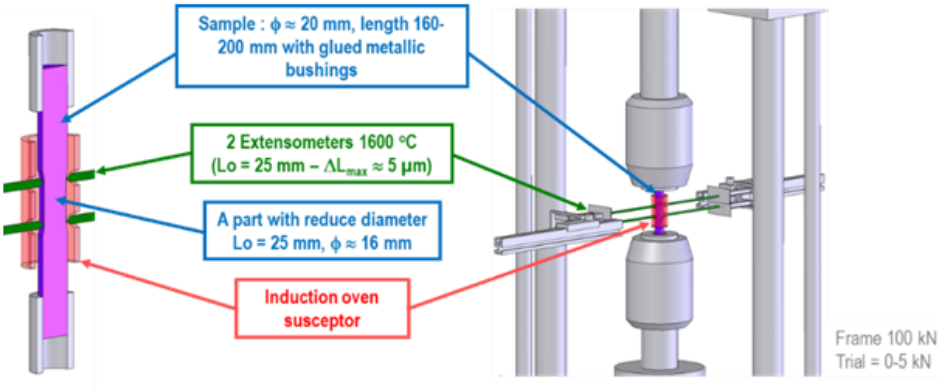

Figure 2-6. Schema of uniaxial tensile/compression test.[100]

Sample preparation consists in machining (sawing and core drilling) of a refractory rod (Ø20x170 mm^3), gluing it (with MgO-based ceramic adhesive) on both sides to metallic bushings (used for clamping) and precise cylindrical grinding of the two metallic bushings, as well as the central part of the sample. The central sample part is machined to the dimensions Ø16x35 mm^2 in order to concentrate stresses in the area where extensometers (with a gauge length of 25 mm) are positioned.

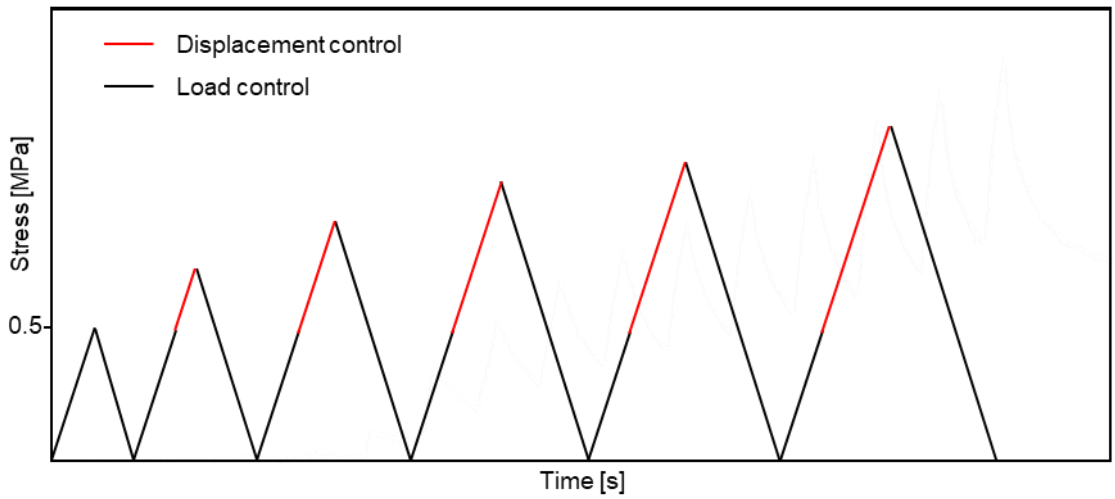

Figure 2-7. Schema of the control during the incremental tensile test (schema inspired by the PhD thesis of Fanny Gouraud).[110]

Presented testing machine was used to perform incremental cyclic tensile test and symmetrical alternating tensile-compression test. The first type of test consists in cyclic tensile sample loading (loading rate of 0.01 kN/s) up to approx. 100 N (corresponding to 0.5 MPa), with load control before switching to displacement control (displacement rate of 0.001 mm/s) until reaching the displacement of 0.002 mm + (n-1)

* 0.001 mm, where n corresponds to cycle number. The subsequent unloading is also load-controlled at each cycle. This type of loading allows observing potential non-linear behaviour, which would be difficult to observe while using only load control. A schema of this loading procedure is presented in Figure 2-8. Exemplary results of incremental tensile tests have already been presented in section 1.3.4.

Additionally, tests of symmetrical alternated tensile-compression loading (see Figure 2-8) were applied at different temperatures: 20, 800, 900, 1000, 1100 and 1200 °C. At each temperature, a dwell of 45 minutes (for stabilization of thermal conditions) preceded loading applied in three sinusoidal cycles with a frequency of 0.00625 Hz and an amplitude of 30 N (corresponding to 0.15 MPa). Exemplary results of tensile-compression tests have already been presented in section 1.3.4.

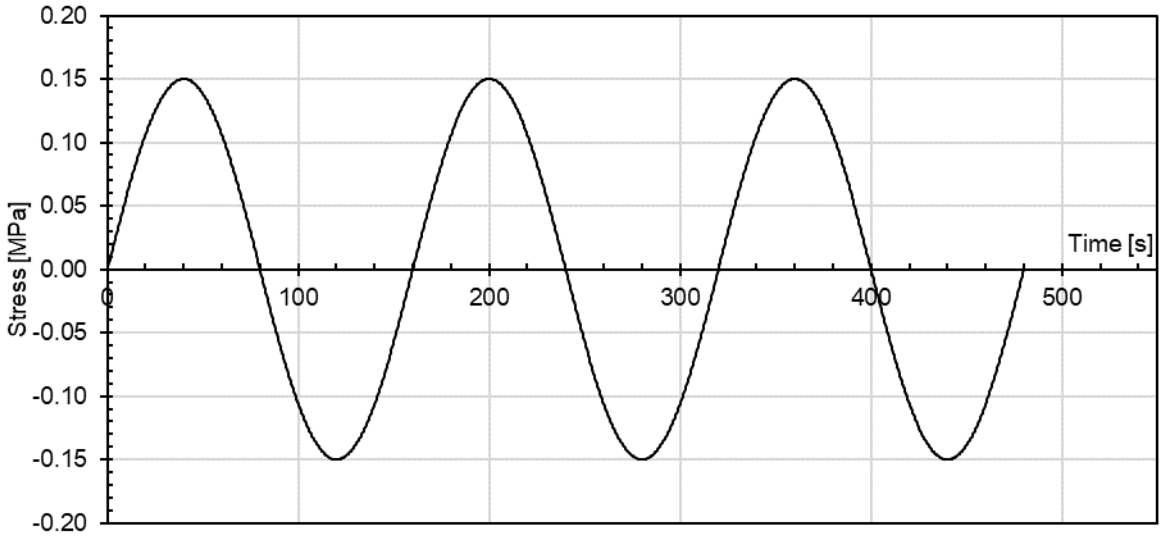

Figure 2-8. Applied loading cycle for symmetrical alternating tensile-compression loading test.

2-4. Conclusion

This chapter provided **description of rather classical characterization techniques** which were used in this study. Taking advantage of recent developments in more advanced measurement tools (in particular strain field at high temperature), other less classical experimental techniques, which were not only used but also improved in frames of this study, are presented later. A particular attention has been paid to adapt digital image correlation method to high temperature environment (Chapter 3) and to improve the thermal shock bench, named ATHORNA (Chapter 5).

Chapter 3

Chapter 3. Strain field and crack monitoring at high temperature

This chapter is focused on selected loading devices (see section 3-1) and optical methods for strain field monitoring (see section 3-2), as well as on the **development of an experimental protocol for precise high-temperature DIC measurement** (see sections 3-3 and 3-4). The main focus of this chapter is on the latter point which is related to an **investigation of different high-temperature resistant speckle patterns** and **image pre-treatments** to find the **optimized experimental procedure** for high-temperature strain field monitoring. This problem was investigated due to the persistent need for highly precise strain measurements required in characterization refractory materials, which originates from their low strain to crack initiation and to final rupture.

It is worth to mention that some experiences regarding crack monitoring with DIC methods have already been acquired at the IRCER laboratory (located in Limoges, France) during the PhD studies of Younes Belrhiti and Imad Khlifi.[99,122] However, until the beginning of this present work, these measurements were performed in IRCER lab only at ambient temperature and therefore, one of the goals for this PhD study was to perform mechanical tests with strain field monitoring by optical methods at high-temperature. This part of the work has been performed using the Brazilian test but the developed methodology and suggested improvements are useful also in other high-temperature tests coupled with the DIC method.

3-1. Considered loading devices

3.1.1. Wedge splitting test

Wedge Splitting Test (WST) has already been briefly introduced in the part dedicated to fracture behaviour (section 1.3.5). The main objective of the present section is to describe the experimental setups that have been used and to introduce fracture-related parameters. As already mentioned, wedge splitting test is currently one of the most interesting techniques for an investigation of fracture behaviour in mode I (opening). This test aims to target a stable crack propagation enabling comparison of pre-peak and post-peak behaviour and determination of several fracture-related parameters, such as nominal notch tensile strength, specific fracture energy or brittleness number.

Figure 3-1 presents a simplified schema of the experimental setup which consists of a specially machined sample (often a cube with a groove and a notch - see Figure 3-2), loading parts (wedge, rolls, transmission pieces, linear support), and image acquisition setup (camera with dedicated lighting). The testing machine applies a vertical load through the wedge, rolls and the load transmission pieces to the sample (which is loaded horizontally, in mode I - opening). During the test, the camera acquires images of the front sample surface, which are then analysed using digital image correlation techniques.[122]

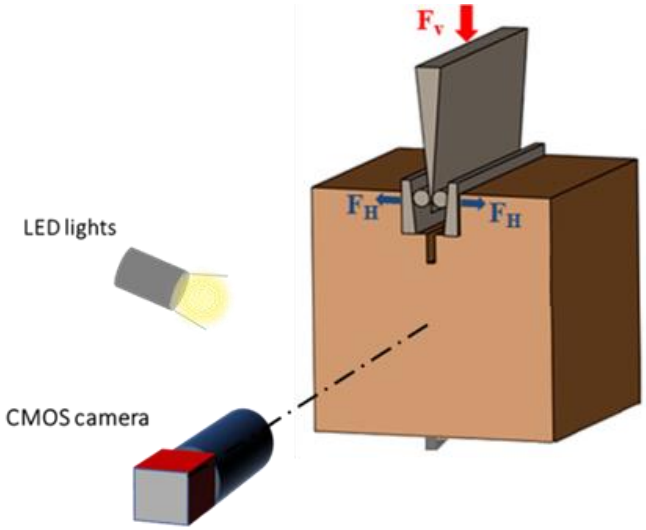

Figure 3-1. Schema of the experimental setup used for wedge splitting test with image acquisition.[122]

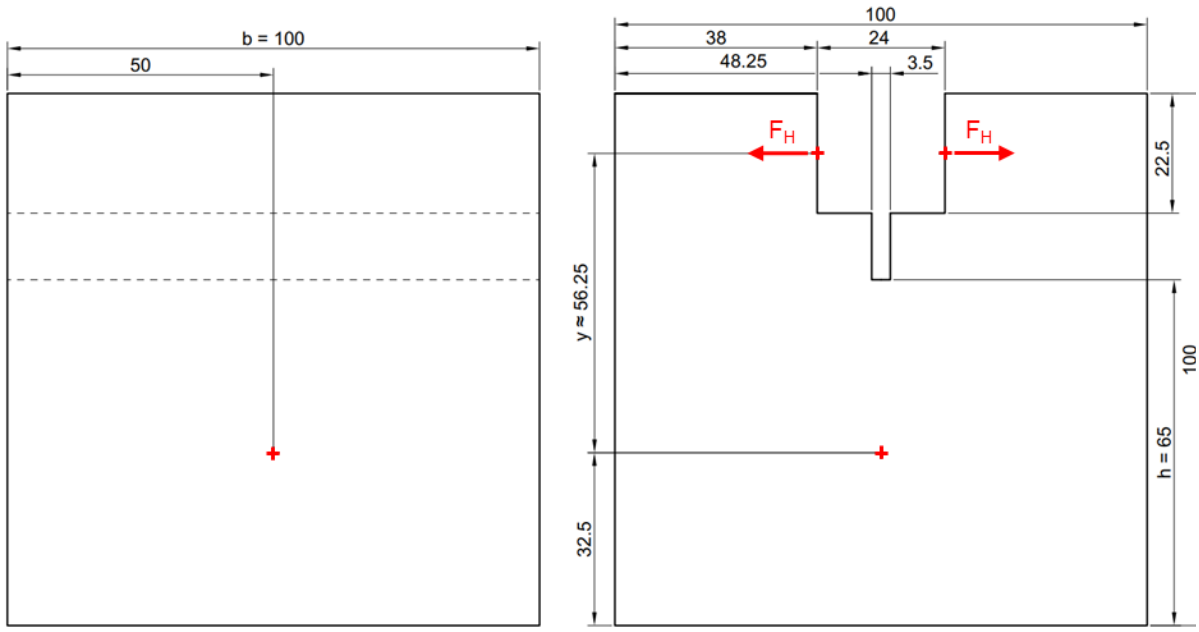

Figure 3-2. Typical sample dimensions for wedge splitting test.

Many experimental parameters are related to the load-displacement curve. This curve is plotted using the horizontal load applied to the specimen (recalculated from vertical load applied by the machine) and the horizontal displacement δ_H between right and left parts of the sample (determined by DIC). Among several parameters, which can be determined from WST, the most important ones in the context of this study, are nominal notch tensile strength σ_{NT}, specific fracture energy G_f' and brittleness number B. The first one characterizes material strength and is determined using Equation 3-1, where b and h are specimen dimensions (b - thickness, h - distance between starter notch and the bottom of the sample), $F_{H\,max}$ is the maximal horizontal load and y is the vertical distance between the point of application of horizontal force and the middle of h (h is the distance between the starter notch and the bottom of the specimen). The second parameter corresponds to the mean work per unit of projected fracture area required for crack propagation. Specific fracture energy is calculated from Equation 3-2, where A is fracture surface, F_H is horizontal load, and $\delta_{15\%\,F_{H\,max}}$ is horizontal displacement corresponding to drop of F_H until 15% of $F_{H\,max}$. The third one is a ratio of elastically stored strain energy at crack initiation to the fracture surface energy necessary for total failure.[102] Brittleness number can be calculated from Equation 3-3, where E is Young's modulus.

$$\sigma_{NT} = \frac{F_{H\,max}}{b.h} + \frac{6F_{H\,max}.y}{b.h^2} \qquad \text{Equation 3-1}$$

$$G_f{}' = \frac{1}{A}\int_0^{\delta_{15\%\,F_{H\,max}}} F_H\,.\,d\delta \qquad \text{Equation 3-2}$$

$$B = \frac{{\sigma_{NT}}^2 \cdot h}{G_f{}' \cdot E} \qquad \text{Equation 3-3}$$

Brittleness number is especially interesting to characterize the resistance of materials to thermal shocks. Materials that exhibit a low value of brittleness number (less brittle) are much more adapted to thermal shocks (higher value of R'''' parameter defined by Hasselman).[123]

3.1.2. Brazilian test at high temperature

Brazilian fracture test (or indirect tensile test) is usually used to determine the tensile strength of rocks. Nevertheless, it has been shown over the years that this technique can also be useful in the determination of other material parameters, such as Poisson's ratio or Young's modulus.[124] Despite its numerous advantages (easy

to machine sample shape, simple loading setup, access to tensile material behaviour), this technique is not very common on refractories. Thus, most of the literature on this topic concerns other materials. The principle of testing consists in compressive loading of a cylindrical sample from two opposite sides until failure (see Figure 3-3). This type of loading induces a biaxial stress state within the sample, including quite uniform horizontal tensile stresses along the vertical diameter and compressive stresses reaching the highest values close to the contact zones. This setup aims to promote fracture in tension in the central sample part. However, depending on selected loading jaws (especially on the internal diameter), the compressive stresses close to the loading zones can sometimes lead to failure. Therefore, in order to reduce these contact stresses, many configurations of experimental setup have been proposed in literature.

Taking into account the recommendations from literature,[125,126] and considering heterogenous microstructures of refractory materials (with a typical grain size of a few mm), sample dimensions were selected as Ø50x12.5 mm^3 and Ø50x25 mm^3. Even if at IRCER-Limoges some expertise on Brazilian test at room temperature were acquired, a secondment of 3 months at LaMé-Orleans has been useful to adapt the Brazilian test to high-temperature conditions. The experimental setup, used during this study, is located at the LaMé laboratory in Orleans. It consists of an INSTRON 4507 testing machine (with a 5 kN load cell), temperature-resistant loading jaws, a dedicated furnace and an image acquisition setup that can be used to monitor strain field by DIC. The loading tools (see Figure 3-3) consist of two alumina jaws, with an internal diameter of 65 mm (to reduce the concentration of compressive stresses in contact zones and assure correct stress distribution within the disk's centre) and an alumina rod (transferring load from the upper grip to the upper jaw). A furnace allows mechanical testing up to 1250 °C and acquisition of images through a build-in window. The image acquisition setup (described in section 3.3.3) is used to acquire images during high-temperature tests in order to analyse displacement and strain fields by the means of DIC. In order to allow direct measurements, the sample surface has to be covered with a special speckle pattern. The main objective of the several tests performed in Orleans (during 3-months of secondment) was to develop a reliable high-temperature speckle pattern which will be explained in section 3.3.1.

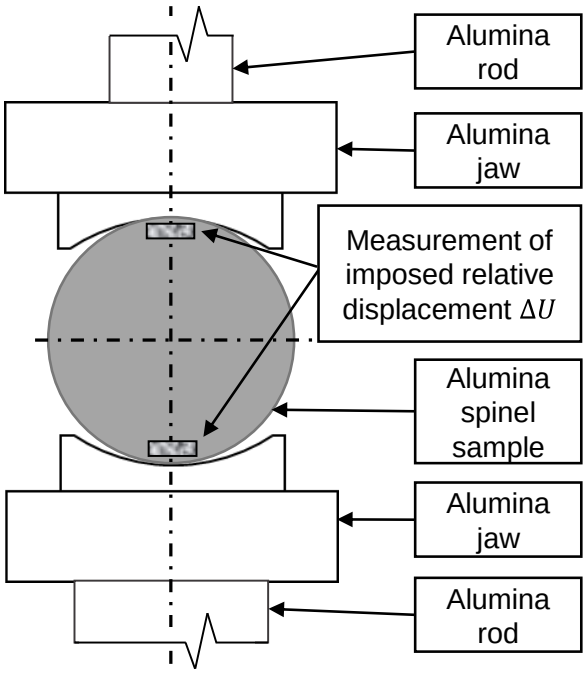

Figure 3-3. Schema of the high-temperature Brazilian test setup.

Most of parameters determined from Brazilian test are related to the stress-strain curve reflecting tensile behaviour. For this curve, tensile stress is calculated from Equation 3-4 (P, t_h and D are applied load, sample thickness and sample diameter, respectively) and strain can be measured as horizontal deformation near central point of the sample.[124,127]

$$\sigma_t = \frac{2 \cdot P}{\pi \cdot t_h \cdot D} \qquad \text{Equation 3-4}$$

3.1.3. A brief introduction to a novel thermal shock bench (ATHORNA device)

ATHORNA device (referring both to the association of “ATHOR” and “New Aquitaine”, as well as to “Advanced measurement for in-situ THermo-mechanical mOnitoRing of large sample uNder thermal grAdient”) is a novel thermal shock bench which was developed to obtain pertinent experimental measurements that can be used to validate numerical FEM approaches dedicated to thermal shocks. For detailed description of this device see Chapter 5.

This device allows to heat a disk-shaped refractory sample (typical dimensions of Ø100x10 mm^3) from the upper face using CO_2 laser pulses. During the test, the heating source was even able to melt magnesia-based refractory material at the impact area (above 2850 °C), but the bottom surface, which is monitored using an infrared camera, is usually much colder (during the tests performed until now), typically reaching temperatures up to ~600 °C. The bottom surface, being monitored

by stereovision system (for determination of displacement and strain fields using DIC method), requires special surface preparation with temperature-resistant speckle pattern. There are commercial black and white paints which can be used to elaborate speckle patterns resistant to 600 or 700 °C. However, future improvement of this device may require resistance of speckle pattern to higher temperatures for which any commercial solutions are not available. Therefore, the development of high-temperature resistant speckle patterns (described in section 3-3 and 3-4) is also useful in the context of ATHORNA device.

3-2. Optical methods

High-temperature measurements of 2D or 3D kinematic fields are relatively new in the field of refractory materials and have been under dynamic development for about a decade. This type of measurement operates on a higher number of measurement points, allowing better understanding of material behaviour in comparison to classical techniques (e.g. extensometers). Moreover, high-temperature tests seem to be more relevant than ambient temperature ones for predicting materials performance in applications (which for refractories usually exceed 1000 °C). High-temperature measurements of kinematic fields are naturally more complex, as some additional aspects need to be considered. However, the current state-of-the-art allows to overcome these challenges. Section 3.2.1 contains a brief overview of different optical measurement methods, while sections 3.2.2-3.2.5 introduce general principles of the used methods.

Note: In all applied digital optical methods, one assumes that captured grey levels follow strain of tested samples.

3.2.1. Full-field measurement methods with a focus on DIC

High-temperature mechanical tests can be combined with several strain measurement methods, which can be divided into the ones requiring contact (classical strain gauges, extensometers) or the contactless ones (interferometric methods, marker tracking or digital image correlation). All contact-requiring methods are limited to some predefined measuring points that do not allow full-field measurements. Therefore, investigation of strain fields is performed by contactless methods, such as moiré interferometry, speckle interferometry, marker tracking or digital image correlation (DIC). These full-field measurement methods are shortly presented here.

Interferometric methods have the same principle - they are based on the superimposition of two laser beams coming from the same laser but having different optical paths. Delay between these laser beams is linked to the assessed kinematic values. A combination of two laser beams forms the interference fringes which are then analysed to measure kinematic values. In the case of in-plane measurement, using Moiré interferometry, a deformable grating is prepared (before testing) on a flat sample surface. Then, the reference grating is formed by superimposition of two coherent beams, being oriented under α angle to the camera axis and located on the opposite sides of the camera.[128]

In the case of in-plane measurement, using Electronic Speckle Pattern Interferometry (ESPI), the two coherent beams (coming from the same laser beam, having the same incident angle with the camera axis and opposite locations in regard to the axis) interact with natural roughness of sample surface. At the beginning of the test a reference image is acquired. Once the sample is deformed, another image is acquired which is then subtracted from the reference one, generating a fringe pattern. Interferometric methods are very accurate (resolution in some cases can reach even tenths of a nanometre),[129] what could be interesting regarding low strain level in case of refractories. However, they are very sensitive to changes in test environment (such as vibration, acoustic noise, air turbulence, humidity and temperature) and thus require stable experimental conditions, as well as complex and well-positioned optical system (composed of camera, laser, mirrors and beam splitter). This complexity limits application of these methods mainly to laboratory environment.[130] The mark tracking[131,132] and the DIC[133,134] methods are diametrically different than the interferometric ones.

The main advantage of mark tracking and DIC over interferometric methods is simplicity of experimental setups. Optical chains are, in these methods, usually composed of only one or two cameras (depending on type of measurement: 2D or 3D). Therefore, no laser, mirrors nor beam splitters are needed. In some cases, additional lighting may be required, but even then, there is no strict requirement concerning position nor orientation of the lighting sources.

Mark tracking method requires deposition of markers on a sample surface. Their size and coordinates are determined at the beginning of calculations, based on a reference image. In the next step, a dedicated algorithm searches the same markers in deformed images and identifies their new positions within a zone of interest.[131] When

large deformations are detected, the research zone is automatically shifted by the displacement from the previous step. In the case of DIC methods, preparation of a typical sample surface is slightly different, as it requires random speckle pattern (natural sample contrast or specific coating; with speckles adapted to pixel size of acquired images). A virtual grid of subsets (being groups of adjacent pixels) is defined at the first image and then positions are calculated for each analysed step. The algorithm consists in comparing two digital images, which represent a reference and a deformed state of a sample. Both techniques assume that strains measured on the sample surface follow strains of a tested material.[133,134] Both mark tracking and DIC exhibit similar precision,[131–134] which is often sufficient for many applications, even though it is significantly lower than interferometric techniques.[135]

Comparing mark tracking with DIC, one can notice that the first method is not as flexible in post-treatment as the second one. It is due to the fact that once the markers are deposited on a sample surface, they cannot be modified after the test. However, the markers are less sensitive to illumination variations.[131,132] In contrary to the mark tracking, the random speckle pattern in the case of the DIC method allows significant flexibility of post-treatment analysis, mainly concerning a convenient selection of interesting areas on the investigated surface. The DIC method, due to its ease of use and flexibility, is of interest in this study.

Many types of DIC method have been developed over the past decades, some of which will be briefly described here. In general, DIC methods could cover both local and global approaches. In the local ones, position of each subset is calculated independently of other subsets, while in the case of the global approaches, continuous displacements are determined by connecting all the measuring points with a mesh and by calculating displacements for all nodes at the same time (compatibility with FEM).[136] There are also other variations of DIC, such as Integrated-DIC (I-DIC).[137]

The main objective of I-DIC is to inversely identify material parameters (instead of determining displacement or strain field as in the classical DIC method). It consists in the comparison of two types of images: theoretically deformed ones (real reference image in initial state with an imposed strain field corresponding to FEM simulated deformation) with experimental images in deformed state (see Figure 3-4). Using an updating numerical technique, this approach allows thus to find the best material parameters in FEM modelling that perfectly fit the experimental strain field.

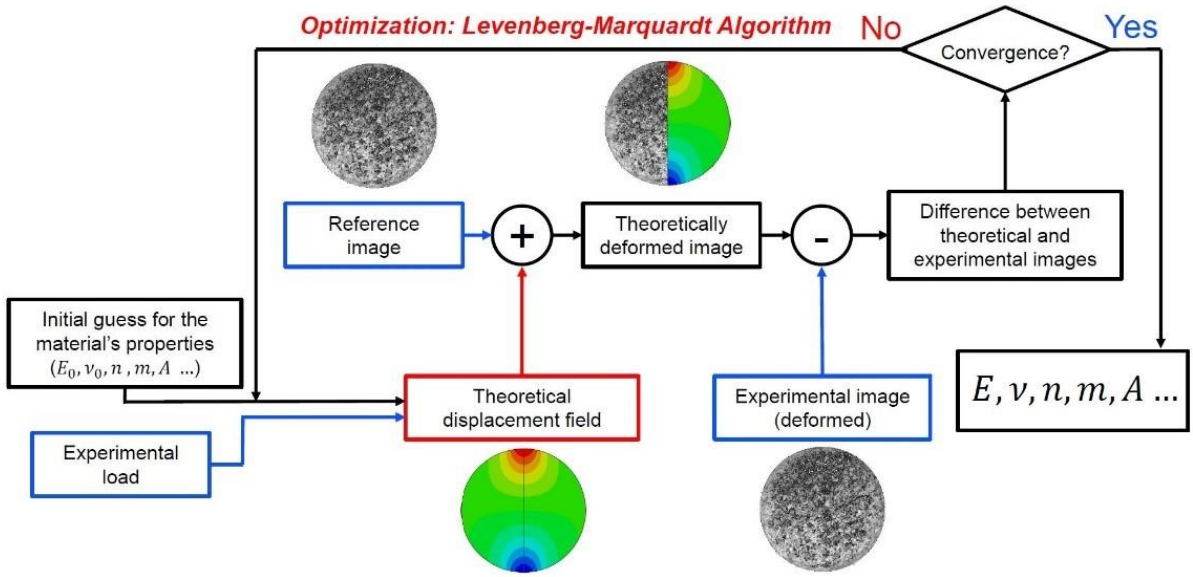

Figure 3-4. Schema of I-DIC algorithm.[137]

When local discontinuities should be taken into account, other variations of DIC could be of interest, such as Two-Parts DIC (2P-DIC).[138] This technique has been developed to improve crack resolution and to precisely monitor crack features during fracture tests. 2P-DIC operates on many subsets (such as local DIC techniques), which have a specific feature, enabling subset to split in two parts (see Figure 3-5a) if a local discontinuity (e.g. crack) occurs. Contrary to classical DIC, this approach does not assume material continuity within each subset, in order to account for the occurrence of a potential local crack. Such specific approach results in an improved precision for the localisation of these displacement discontinuities (see Figure 3-5b, c).

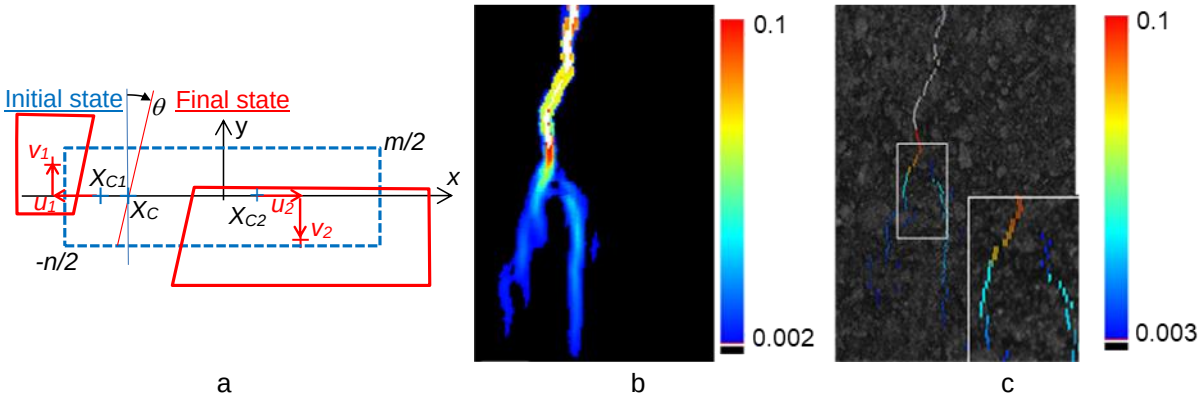

Figure 3-5. a) Schema demonstrating the ability of 2P-DIC subset to split in two parts, b) Exemplary strain field calculated by classical DIC, c) Exemplary crack opening calculated by 2P-DIC.[138]

3.2.2. Mark tracking for displacement and strain field monitoring

Mark tracking method is used in this study to investigate stability of the thermal shock bench (applied in Chapter 5) and, if necessary, it can also be used

as a reference (boundary conditions) in order to correct a global displacement of the sample on a given considered mechanical device. This method has already been briefly introduced in section 3.2.1. An exemplary surface preparation for this technique is presented on a ring from Figure 3-6 (dedicated to ATHORNA). It is usually made of black and white paints using potentially a stencil in order to obtain a regular distribution of markers. The basic principles of the method and its sensitivity to experimental parameters are presented in more details in the article of Bretagne et al.[131]

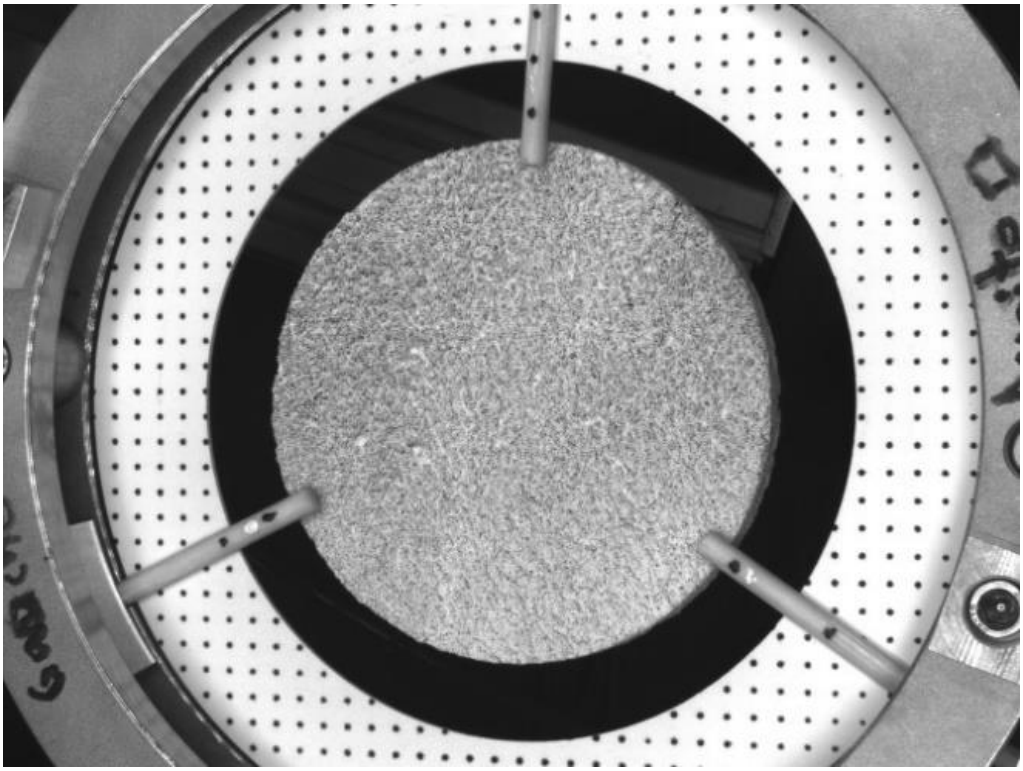

Figure 3-6. Exemplary picture from ATHORNA device using a silica ring with markers (for mark tracking) and a disk-shaped sample with speckle pattern (for DIC).

At the beginning of analysis, each marker used for investigation should be surrounded by a subset of pixels, thus determining an initial area taken into account during calculations (see Figure 3-7a). In order to determine which pixels belong to the marker in a given subset, there is a need to set a value of the intensity level I_s, as presented in Figure 3-7b. In the following step, the coordinates of all investigated markers $\vec{C}$ are calculated for each state (each image), according to Equation 3-5 (where I_i - intensity of the i-indexed pixel which has x_i, y_i coordinates). Then, during calculations, this intensity threshold is automatically adjusted, following changes of the mean subset intensity, and each subset is displaced, taking into account the previous steps.

$$\vec{C} = \begin{pmatrix} Cx \\ Cy \end{pmatrix} = \begin{pmatrix} \frac{\sum_i x_i(I_i - I_s)}{\sum_i (I_i - I_s)} \\ \frac{\sum_i y_i(I_i - I_s)}{\sum_i (I_i - I_s)} \end{pmatrix}$$ Equation 3-5

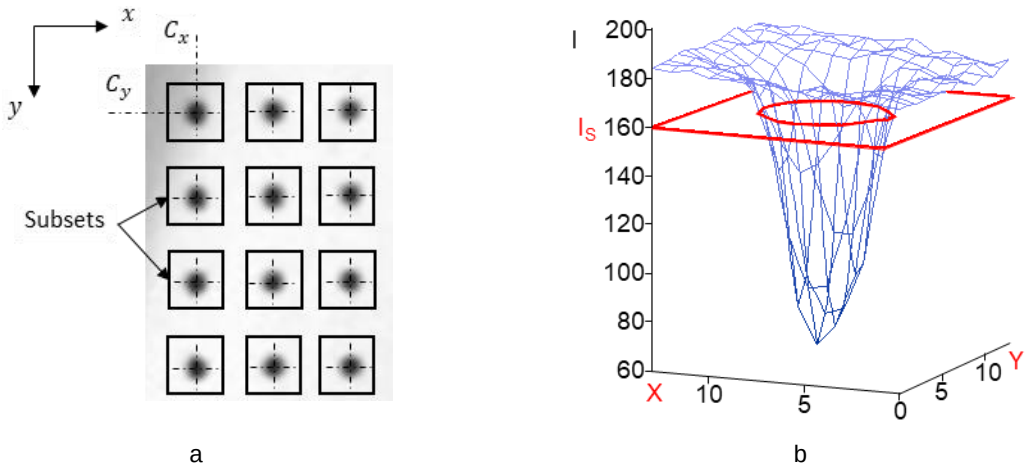

a b

Figure 3-7. Principle of mark tracking method: a) Exemplary subsets and associated coordinates (C_x, C_y) for each subset, b) 3D representation of greyscale intensity levels throughout a subset, I_S representing the threshold which separates the marker (lower grey levels) from the bright background (higher grey levels).

3.2.3. Classical DIC for displacement and strain field monitoring

Classical digital image correlation method[133,134,139] has been used in this study for two purposes: to monitor strain fields (applied in this chapter and in Chapter 5) and to measure (in some cases) a local relative displacements between a set of predefined subsets (applied in this chapter as well as in Chapter 4 and Chapter 5). This method has already been briefly introduced in section 3.2.1. An exemplary surface preparation with speckle pattern is presented on the disk-shaped sample from Figure 3-6. The uncertainty of the method depends on speckle pattern properties, such as speckle size, speckle edge sharpness and contrast.[139–142]

At the beginning of analysis, a zone of interest has to be defined together with dimensions of subsets (typically squared: *m*×*m* pix.^{2}) and spacing between their centres. Based on these parameters, a regular grid of subsets is generated and is later used during calculations. Then, analysis is performed by comparison of pairs of digital images (one in a reference state and one in a deformed state) in order to locally match subsets from the reference image to the deformed one.

A local transformation of material between two images can be described by at least two rigid displacement parameters (u,v), but depending on the studied

problem, four local gradients $\left(\frac{\partial u}{\partial x},\frac{\partial u}{\partial y},\frac{\partial v}{\partial x},\frac{\partial v}{\partial y}\right)$ can also be added. Therefore, for each subset D, the unknown set of parameters can be represented by a vector $\vec{q}=\left(u,v,\frac{\partial u}{\partial x},\frac{\partial u}{\partial y},\frac{\partial v}{\partial x},\frac{\partial v}{\partial y}\right)$, which is determined by minimization of correlation coefficient C, according to Equation 3-6. In this equation, f and g represent the grey levels of pixels in the reference and in the deformed state, while $\overline{f}_D$ and $\overline{g}_D$ are their averages on the subset *D* and on its transformation ∅(*D*).

$$C=1-\frac{\sum_{X\in D}(f(\vec{X})-\overline{f_D})\cdot(g(\emptyset(\vec{x}))-\overline{g_D})}{\sqrt{\sum_{X\in D}(f(\vec{X})-\overline{f_D})^2}\cdot\sqrt{\sum_{X\in D}(g(\emptyset(\vec{x})-\overline{g_D})^2}} \qquad \text{Equation 3-6}$$

The solution for $\vec{q}$ is searched by first gradient minimization thanks to an iterative Newton scheme. Measurement of displacement in subpixel scale is obtained by a bilinear subpixel interpolation of grey levels of the deformed image. Associated with this interpolation, it should be noted here that an improvement of the accuracy can be achieved by application of a spatial smoothing, using e.g. averaging filter. Searching for a very high level of accuracy in the case of ceramics materials it is also possible to apply a temporal smoothing.

The displacement field is then used to calculate strain field by finite differences scheme: ε_{XX}, ε_{YY}, ε_{XY} (local strains) from displacements of the centres of the four neighbouring subsets.[134] Gauge length L_0 is thus equal to the distance between two of them. This approach is more detailed in case of 3D measurement (see section 3.2.5).

3.2.4. 2P-DIC for crack monitoring

The 2P-DIC method has been used in this study to monitor crack with a high resolution, to measure local crack opening (applied in Chapter 5) and to calculate a total instantaneous crack length (applied in the present chapter and in Chapter 5). This method has already been briefly introduced at the end of section 3.2.1, but much more technical aspects will be detailed in this section.

2P-DIC is based on the classical DIC process. In the same way, at the beginning of analysis, a zone of interest has to be defined together with dimensions of subsets and spacing between their centres. In the case of 2P-DIC, subsets are voluntarily chosen with a rectangular shape (height m being smaller than width n) and are

regularly-displaced with steps of p_x and p_y (where p_x=n/2 and p_y=m/2). Its main feature consists in allowing the subset *D* to split in two parts, as presented in Figure 3-8.

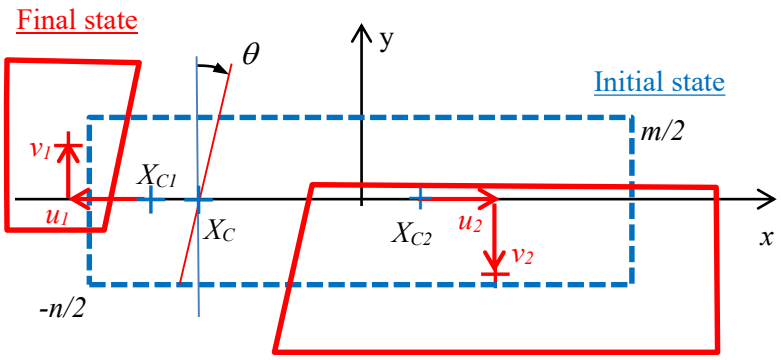

Figure 3-8. Principle of the 2P-DIC, decomposition of a subset, considering a crack occurring at a given position X_C and a given orientation θ.

Splitting can occur within the initial subset D at a given position X_C with a given orientation θ and thus, two parts can be formed D_1 ($x < X_C$) and D_2 ($x > X_C$).[116,138] In such case, the correlation coefficient is divided in two components, as presented in Equation 3-7. In this equation $\overrightarrow{q_i} = \left(u_i, v_i, \frac{\partial u_i}{\partial x}, \frac{\partial u_i}{\partial y}, \frac{\partial v_i}{\partial x}, \frac{\partial v_i}{\partial y}\right)$ is the vector of material transformation parameters in a given part D_i (i=1,2). The vector $\vec{Q}$ represents the two vectors $\overrightarrow{q_1}$ and $\overrightarrow{q_2}$ combined.

$$C_{XC}(\vec{Q}) = \sum_{D_1} c^2(\overrightarrow{q_1}) + \sum_{D_2} c^2(\overrightarrow{q_2}) \qquad \text{Equation 3-7}$$

The best set of X_C, θ, and $\vec{Q}$ parameters is searched by matching with a use of a dedicated minimization algorithm,[116,138] rather similar to classical DIC. The correlation coefficient C_{XC} (X_C, θ, and $\vec{Q}$) is minimized by classically varying $\vec{Q}$ as well as by varying X_C (with a step of one pixel from -n/4 to n/4) and θ (with a step of 5° from -60° to 60°). In order to represent the quasi-brittle behaviour of a studied material, only four components of rigid-body displacements are calculated in $\vec{Q}$ (the parameters of local gradients are neglected). In the case of Wedge Splitting and Brazilian tests, the rectangular shape of subset was chosen to achieve a relatively high vertical spatial definition of crack path for cracks occurring close to vertical direction. The above steps are performed for all the subsets defined on the analysed image.

Crack detection is possible thanks to calculation of a pseudo strain within each subset, as presented in Equation 3-8. Once the pseudo strains are calculated, a strain threshold $\boldsymbol{\varepsilon}_{Thres}$ has to be set in order to separate pertinent values (strain values higher than strain threshold value) from noise. This strain threshold should normally be set to the value of the strain corresponding to crack initiation. Due to the fact that the strain measurement uncertainty by 2P-DIC is usually higher than the strain at crack initiation, the value of $\boldsymbol{\varepsilon}_{Thres}$ is often related to strain measurement uncertainty.

$$\varepsilon = \frac{\sqrt{(X_{C2} - X_{C1} + u_1 - u_2)^2 + (v_2 - v_1)^2}}{|X_{C2} - X_{C1}|} - 1 \qquad \text{Equation 3-8}$$

In accordance with Figure 3-8 and 2P-DIC parameters, the total instantaneous crack length can be measured as the sum of all relevant lengths of each segment (local pseudo strain above $\boldsymbol{\varepsilon}_{Thres}$, considering the local angle of the crack path as well as half-length of segment because of the step p_y=m/2).

3.2.5. Stereovision for 3D displacement and strain field monitoring

Stereovision combined with mark tracking or DIC methods has been used in this study to calculate both in-plane and out-of-plane displacements of a sample surface (applied in Chapter 5). The two cameras are positioned on either sides of the surface normal to the specimen surface and they are synchronized to record pairs of images at the same moments.

Prior to each measurement, there is a need for calibration of the experimental setup by combining stereovision and mark tracking method. Equation 3-9 presents a set of equations allowing to pass from 2D to 3D coordinates (by triangulation), where $\bar{\bar{G}}_1$, $\bar{\bar{G}}_2$ are the transformation matrices (comprising magnifications and positions of two cameras), $\bar{\bar{R}}_1$, $\bar{\bar{R}}_2$ are the angular positions and $\overrightarrow{C_{C1}}$, $\overrightarrow{C_{C2}}$ are the coordination vectors.[143–145] The components of transformation and rotation matrices are identified during the calibration process, involving two cameras and a reference object. Pictures of a sample, having a grid of marks with known positions $\vec{X}$, are acquired from both cameras and then used in the calibration process.

$$\begin{cases} \bar{\bar{R}}_1 \vec{X} = \bar{\bar{G}}_1 \overrightarrow{C_{C1}} \\ \bar{\bar{R}}_2 \vec{X} = \bar{\bar{G}}_2 \overrightarrow{C_{C2}} \end{cases} \qquad \text{Equation 3-9}$$

Once the calibration is performed (positions and orientations of both cameras are defined), the triangulation process is applied to obtain the 3D coordinates of analysed markers or subsets $\vec{X} = (X, Y, Z)$ in the 3D coordinate system. Then, relative displacement is calculated for each measurement point $\vec{U}(U_x(X,Y,Z), U_y(X,Y,Z), U_z(X,Y,Z))$ from differences in their positions between two mechanical states (reference and deformed). It is important to notice that the Z component is determined only on a sample surface (i.e. Z(X,Y)).

Then, the deformations of the sample surface can be calculated by finite differences based on displacements of four neighbouring markers. In this aim, the vectors in an initial state $d\overrightarrow{X_1}$, $d\overrightarrow{X_2}$ and in a deformed one (see Figure 3-9) $d\overrightarrow{x_1}$, $d\overrightarrow{x_2}$ are calculated. These vectors are used just after to determine a local gradient tensor $\bar{\bar{F}}$ (see Equation 3-10) by finite differences scheme, solving the system $d\overrightarrow{x_i} = \bar{\bar{F}} d\overrightarrow{X_i}$ with i=1,2.[131,146] In fact, since the measurements are only performed on the sample surface, no data can be obtained about the gradient tensor $\bar{\bar{F}}$ in direction Z (F_{XZ}, F_{YZ}, F_{ZZ}). Thus, only the other components are determined:

$$\bar{\bar{F}} = \begin{bmatrix} F_{XX} & F_{XY} & * \\ F_{YX} & F_{YY} & * \\ F_{ZX} & F_{ZY} & * \end{bmatrix}$$

Equation 3-10

*undetermined

In any case, the known components of $\bar{\bar{F}}$ are sufficient to deduce the XY plane components of the Green-Lagrange tensor ε_{XX}, ε_{YY}, ε_{XY} through Equation 3-11. It is worth to notice that the gauge length (L_0) is determined as the distance between two neighbouring subsets.

$$\bar{\bar{\varepsilon}} = \frac{1}{2}(\bar{\bar{F}}^T \bar{\bar{F}} - \bar{\bar{I}})$$

Equation 3-11

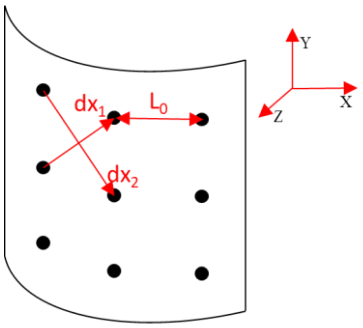

Figure 3-9. Principle of strain calculation in deformed state with dots representing the centres of the subsets and the pair of vectors $d\overrightarrow{x_1}$, $d\overrightarrow{x_2}$ used for calculation of the local gradient tensor.

3-3. Adaptation of the protocol for high-temperature DIC measurements

This section is an introductory part of more detailed study presented in section 3-4. It is known that high-temperature optical measurements are more complex than ambient-temperature ones, as one has to cope with three additional challenges: high-temperature resistance of speckle pattern, heat haze and black body radiation (see section 3.3.1). Section 3.3.2 introduces high-temperature resistant speckle patterns that have been selected for investigation in frames of this work, while section 3.3.3 introduces used experimental setup. This device is coupled with optical acquisition system that required several improvements in order to minimize image distortion caused by heat haze and black body radiation at high temperatures.

3.3.1. Adaptation of optical methods to high-temperature measurements

Application of the optical measurements at high temperatures (typically in a range of 1000-1500 °C) pose three additional challenges when compared to ambient temperature measurements. These challenges are heat haze (variation of refraction index between camera and sample due to hot air), black body radiation (thermally-induced sample radiation) and chemical stability (no reaction with sample, no change in colour and shape) of speckle pattern at high temperatures. This section summarizes the latest research, where these topics have been successfully addressed.

Heat haze varies refraction index of the air between camera and sample (due to irregular flow of hot air) and is an origin of an artefact leading to loss of accuracy. Effect of this distortion can be reduced by:

- Stabilizing air refraction index close to the sample, through a suitable furnace design with an internal air deflector, which assures constant air flow in front of the hot sample;
- Stabilizing air refraction index close to the window by a local cooling of this window;
- Stabilizing air refraction index between the window and the camera by using an external fan to blow out hot air;[147]
- Application of a long picture integration time (averaging noise) with neutral density filter (uniformly reducing the brightness, in fact, increased by longer integration time).[148]

The effects of the black body radiation (thermally-induced radiation) from the sample can be reduced by:

- Applying a light filter, which cuts as much as possible these thermally-induced radiation (close to infrared - higher than 700 nm). That means, using a bandpass filter, being transparent to the lowest possible wavelengths which in the visible spectrum correspond to blue light (e.g. blue bandpass filter - transparent in the range of 440-460 nm);
- Being as much as possible independent from internal illumination coming from the furnace itself. Thus, an additional illumination with wavelengths corresponding to the ones transmitted by bandpass filter could be very useful.

High-temperature resistance of speckle pattern (speckle stability) is also very important, especially for mechanical tests with a long duration, such as creep tests:

- Usage of natural contrast of investigated sample could obviously be the most valuable speckle pattern (when possible). Nevertheless, this natural distribution of contrast is, in most cases, not well-adapted to the targeted spatial resolution;[149]
- When natural contrast cannot be used, different solutions can be applied. An artificial speckle pattern can be obtained by deposition of high-temperature resistant material (see Table 3-1).[150]

Table 3-1. Summary of a bibliographical review about experimental conditions (light filtering, high-temperature resistant speckle pattern) specifically developed for high-temperature DIC experiments.

Specimen	Testing temperature	Reduction of black body radiation	High temperature resistant speckle pattern	Year [Ref]
Stainless steel	1200°C	Blue bandpass filter	Black cobalt oxide blended with commercial high-temperature inorganic adhesive	2010 [151]
Carbon fibre	2600°C	Blue bandpass filter	Plasma sprayed tungsten coating	2014 [150]
Zirconium silicate	1350°C	Blue bandpass filter	Silicon carbide powder	2015 [148]
Stainless steel	1150°C	Blue bandpass filter	White yttria–based and black silica-based ceramic paints	2016 [152]
Stainless steel	900°C	Blue bandpass filter	White yttria–based and black silica-based ceramic paints	2017 [153]

The information coming from the state-of-the-art will be considered later in this PhD study to select the best possible option for thermomechanical characterization of refractory materials, using DIC at high temperature.

3.3.2. Speckle patterns preparation for high-temperature measurements

All selected types of speckle patterns, used for comparative purposes, are based on fired alumina-based spinel-containing refractory. It is assumed that this material is relatively stable at 1200 °C (temperature applied in this study) regarding its typical firing temperature of about 1680 °C.[160] Taking into account the literature review presented in section 3.3.1, several types of speckle patterns have been defined and prepared according to the block diagram presented in Figure 3-10.

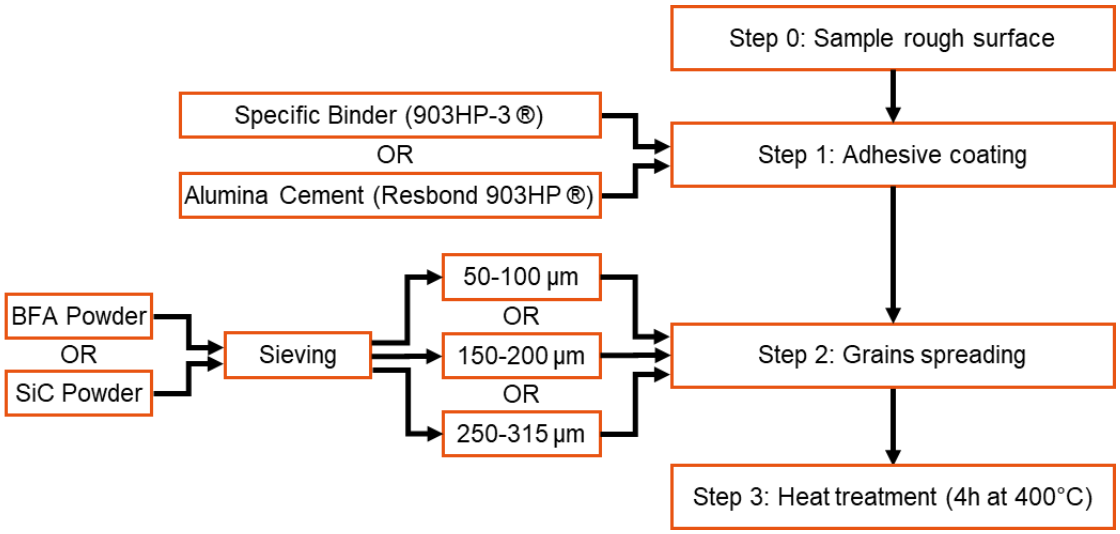

Figure 3-10. Speckle pattern preparation procedure in a form of block diagram.[154]

In the following sections, each speckle pattern is later identified by a reference, as presented in Table 3-2. Each reference comprises three information, concerning types of used adhesive and powder, as well as a grain size range of a powder (separated by sieving). Two types of adhesives (providing adhesion for ceramic particles) were used: the commercial Resbond 903HP white alumina cement (symbol: C), having a maximal application temperature of 1790 °C and a specific binder (symbol: B), being the transparent liquid component of this cement. Two types of ceramic powder have been selected: Silicon Carbide (symbol: SiC) and Brown Fused Alumina (symbol: BFA). The selection of powder was mainly related to a good contrast with rather white sample or white adhesive, as well as their thermodynamic stability under testing conditions. The grain sizes were separated by sieving and their size was adjusted to be of about 3 pixels (regarded as the smallest recommended pixel size) and higher (to study an influence of speckle size).

Table 3-2. References of samples with their characteristics.[154]

Reference	Adhesive coating	Powder type	Grain diameter [µm]

B_SiC_50-100	Specific binder	SiC	50-100
C_SiC_50-100	Alumina cement	SiC	50-100
C_SiC_150-200	Alumina cement	SiC	150-200
C_SiC_250-315	Alumina cement	SiC	250-315
C_BFA_250-315	Alumina cement	BFA	250-315

3.3.3. High-temperature optical acquisition and loading setups

The high-temperature Brazilian test setup (see Figure 3-11a), located at the LaMé laboratory in Orleans, has been used to characterize different speckle patterns at high temperature. Before this study, the Brazilian testing device was already equipped with a high-resolution image acquisition setup but back then the tests were limited to lower temperatures (below 900 °C).[137] That was mainly due to intense black body radiation, which at high temperatures (and with the previously applied protocol) significantly reduced the contrast of speckle pattern hindering DIC analysis. Therefore, the initial objective of the present study was to improve the optical acquisition system, allowing more precise image acquisition at higher temperatures. The following two paragraphs introduce the high-temperature mechanical testing device and the image acquisition setup adapted to high temperatures.

The high-temperature mechanical testing setup consists of the INSTRON 4507 testing machine, a load cell (with a capacity of 5 kN), loading parts (alumina rods and jaws) and a dedicated furnace with a window (max. temp. of 1250 °C). Figure 3-11b presents the Brazilian test setup (already introduced in section 3.1.2) with a cylindrical sample located between two alumina jaws. Two types of mechanical tests were performed: the so-called stability test and the well-known Brazilian test. In the case of the first one, a sample was tested at a given temperature under a low constant load of 50 N (just to keep the different parts of the setup together), while in the case of the Brazilian test, a sample undergone a compressive displacement with a constant rate of 0.05 mm/min. The relative vertical displacement ΔU was measured on a sample surface (to avoid contact effects) and was based on a displacement of two zones (128x32 pixels), which were located close to the jaws (see Figure 3-11b). This displacement is used to plot the load-displacement curve presented in section 3-4.

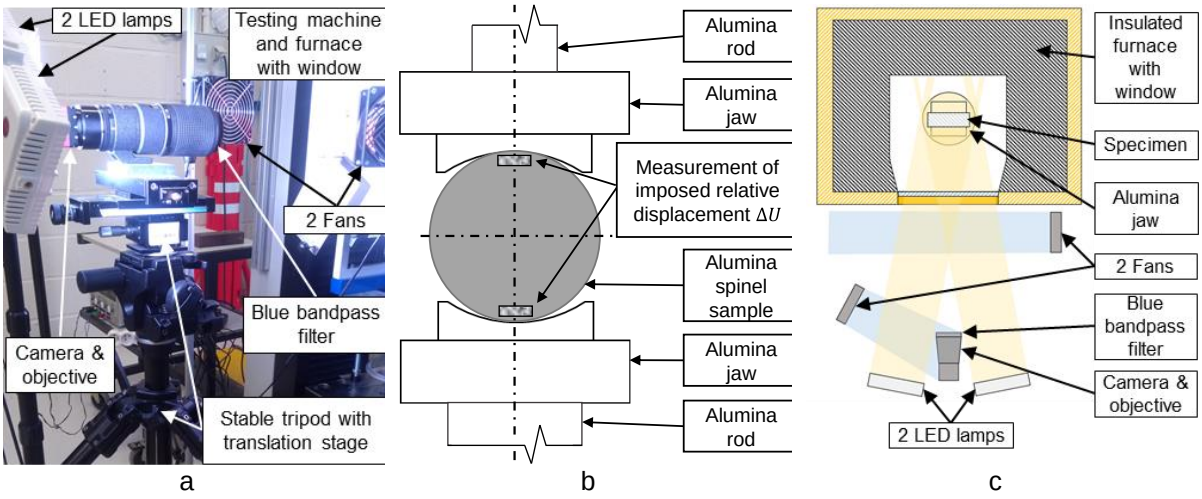

Figure 3-11. High-temperature Brazilian test: a) a picture of the experimental setup, b) a schema of the experimental setup for image acquisition, c) a schema of Brazilian test setup.[154]

The image acquisition setup, has been significantly improved during this study (in cooperation with Lucas Breder-Teixeira - another ESR from ATHOR project) and can be observed in Figure 3-11a and Figure 3-11c. It consists of a high-resolution camera (PROSILICA GX 6600 - 6576x4384 pixels), an optical lens (AF Micro-Nikkor 200 mm f/4D IF-ED), a blue bandpass filter (MIDOPT BP470), which reduces black body radiation thanks to transparency in a blue light wavelength range of 425-495 nm, and a furnace with built-in glass ceramic window. Additionally, two LED lamps (LINKSTAR LED VD-416D-K2 with light temperature of 5500 K) provide a powerful external light (and thus ameliorate contrast) and two fans are also used: one for cooling the camera and one for blowing out the hot air in proximity to the furnace window (reduction of heat haze). The resolution of acquired images is approximately 0.014 mm/pix and stability at given temperatures are investigated in the next section.

3-4. Analysis and optimization of the adapted protocol

3.4.1. Comparison of basic speckle pattern features

The basic speckle pattern features which are discussed in this section are grey level histogram, grey level gradient (related to contrast) and speckle size. Figure 3-12 presents pictures of investigated speckle patterns acquired at 1200 °C. For all samples, magnified images are presented in the upper-right corners and greyscale histograms in the bottom right corners. According to these images and histograms, one can observe that all speckle patterns exhibit significant contrasts between the backgrounds and the speckles. It is worth to notice that experimental conditions

have been adjusted to acquire bright, but not saturated, images (targeted greyscale below 255). Nevertheless, some pixels are saturated due to the intense light reflections from SiC and BFA ceramic particles.

As introduced in section 3.3.1, there are differences in types and sizes of ceramic particles used for preparation of speckle patterns. Particles with a given size range were firstly separated by sieving, and then the average size has been estimated by measuring the Full Width at Half Maximum (FWHM) of autocorrelation curve. Autocorrelation curves for all speckle patterns are presented in Figure 3-13.

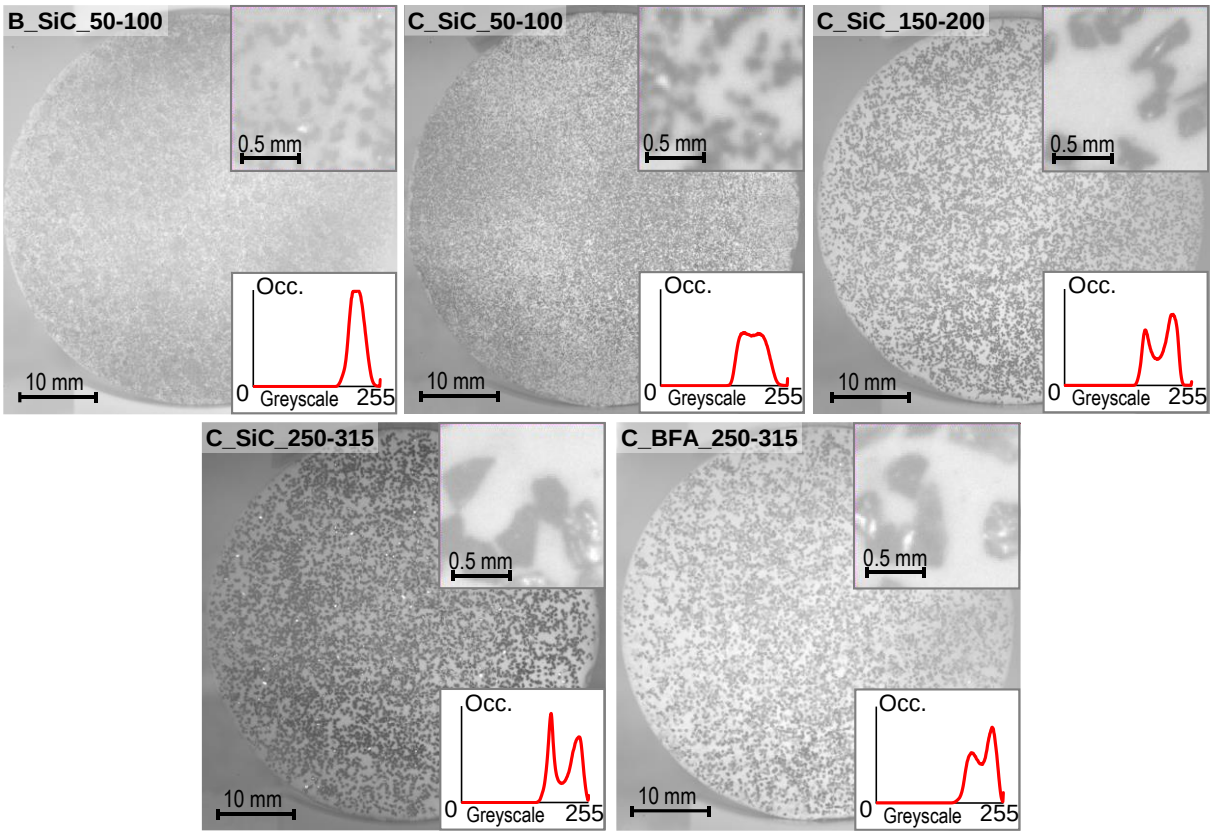

Figure 3-12. Pictures of the entire samples (resolution of 0.014 mm/pixel) and selected areas with 15x magnification (upper right) as well as greyscale histograms (bottom right).[154]

Table 3-3 presents summarized results, comprising standard deviations of grey level histograms σ_{GL}, square root of the average of squared grey level gradients $\sqrt{\overline{\nabla g^2}}$ (related to contrast) and speckle sizes (both determined by sieving and by autocorrelation).

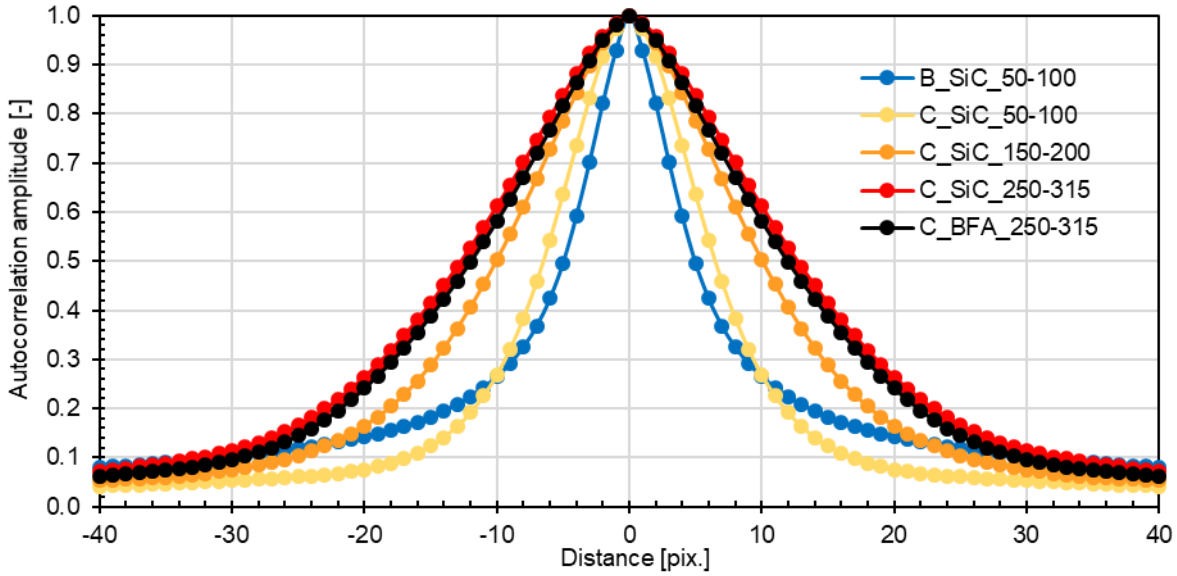

Figure 3-13. Normalized autocorrelation curves for different speckle patterns measured at 1200°C.[154]

Table 3-3. Selected speckle pattern features at 1200°C determined on entire images (full resolution, without numerical filters).[154]

	Std. dev. of grey levels σ_{GL}	**Average grey level gradient $\sqrt{\overline{\nabla g^2}}$**	**Speckle size**		
			By sieving		**By autocorrelation**
	[grey levels]	[grey level * pixel^{-1}]	[mm]	[pixel]	[pixel]
B_SiC_50-100	13.0	4	50-100	3.50-7.00	10
C_SiC_50-100	24.1	5.6	50-100	3.50-7.00	13
C_SiC_150-200	24.5	4.3	150-200	10.50-14.00	20
C_SiC_250-315	25.5	4	250-315	17.50-22.05	28
C_BFA_250-315	21.9	4.24	250-315	17.50-22.05	24

One can observe that the σ_{GL} and $\sqrt{\overline{\nabla g^2}}$ are significantly lower for B_SiC_50-100 sample due to the lack of white layer of cement. Moreover, one can also notice that the speckle size determined by autocorrelation (as FWHM) is higher than by sieving. It is most likely due to nonregular shape of particles and the presence of particle agglomerations.

Considering only the information presented until now, one can state that C_SiC_50-100, leading to the highest $\sqrt{\overline{\nabla g^2}}$ and having relatively low speckle size, could be the best choice. However, B_SiC_50-100 prepared with the same powder but without the layer of cement could be an interesting alternative. Its value of $\sqrt{\overline{\nabla g^2}}$ is reasonable and the absence of cement layer could be highly beneficial as sample

microstructure is uncovered and there is no ambiguity whether observed deformation reflects deformation of a tested sample. Comparing different types of particles (C_SiC_250-315 and C_BFA_250-315), one can state that there are very small differences between them at this stage.

It is worth pointing out that $\sqrt{\overline{\nabla g^2}}$ at ambient temperature is about 13 grey levels * pixel^{-1}, while all values are around 5 grey levels * pixel^{-1} at 1200 °C. The increase of brightness (leading to lower $\sqrt{\overline{\nabla g^2}}$) is related to black body radiation. Even though additional lighting and blue bandpass filter were applied, the black body radiation has only been limited and it still results in a decrease of $\sqrt{\overline{\nabla g^2}}$ and in an increase of displacement uncertainty (according to Equation 3-12).

3.4.2. Effects of high temperature based on preliminary tests

3.4.2.1 *Uncertainty assessment*

Uncertainty has been assessed in this study to compare samples with different speckle patterns in order to determine the one which allows to obtain the highest precision. It should be noted that this study was performed in 2D. Taking into account that the same minimisation algorithm and interpolation are implemented in classical DIC and 2P-DIC methods, the relations between surface preparation and final experimental precision should be rather similar. Therefore, the comparative study, aiming to determine the speckle pattern allowing to obtain the highest precision (among tested), is performed using DIC method.

The displacement uncertainty is known to be dependent on speckle pattern features.[133,134,155–157] That is why the main parameters, used in this study for comparative purposes are displacement uncertainties along X direction (determined by DIC), as well as speckle pattern features, such as grey level gradients, grey level histograms and average speckle size.

Standard deviation of displacement uncertainty along X axis σ_{U_X} can be expressed by Equation 3-12, where m is subset size in the direction of the displacement, ∇g is local grey level gradient and σ_n is standard deviation of noise in the image.[116]

$$\sigma_{U_X} \propto \frac{\sigma_n}{\left[m \ . \sqrt{\overline{\nabla g^2}}\right]}$$ Equation 3-12

∝ - proportionality sign

Grey level gradients are determined by firstly deriving the image in horizonal direction and then by calculating $\sqrt{\overline{\nabla g^2}}$.[116] Grey level histograms are compared using the standard deviations of all grey levels. Average speckle size is calculated as Full Width at Half Maximum (FWHM) of autocorrelation curve.[133] This last parameter is known to be used for a good approximation of average speckle size.[155,158]

This optical study tests will be performed at ambient (~20 °C) and at high temperature (~1200 °C) under a relatively low compressive load of 50 N (just to keep the Brazilian test setup together). These experimentally stable conditions are meant to limit sample deformation, which for comparative purposes will be assumed zero.

Standard deviation of deformations along X axis $\sigma_{\varepsilon_{XX}}$ and along y axis $\sigma_{\varepsilon_{YY}}$ will be evaluated on sample surface for a given time. Strain results are insensitive to rigid body movement, which occur during the measurement and therefore are preferred to be compared in comparison to displacement. Moreover, for small deformations, the expression from Equation 3-13 is true, where L_0 is the distance between centres of two subsets.

$$\sigma_{\varepsilon_{XX}} = \frac{\sigma_{U_X}}{L_0}$$ Equation 3-13

3.4.2.2 *Uncertainties at ambient and high temperatures*

This section is dedicated to comparison of displacements and deformations evolving with time (at stable thermomechanical conditions) at 20 °C and at 1200 °C. For this purpose, all the results presented below concern the B_SiC_50-100 sample, which is considered representative because similar tendencies are observed for other samples.

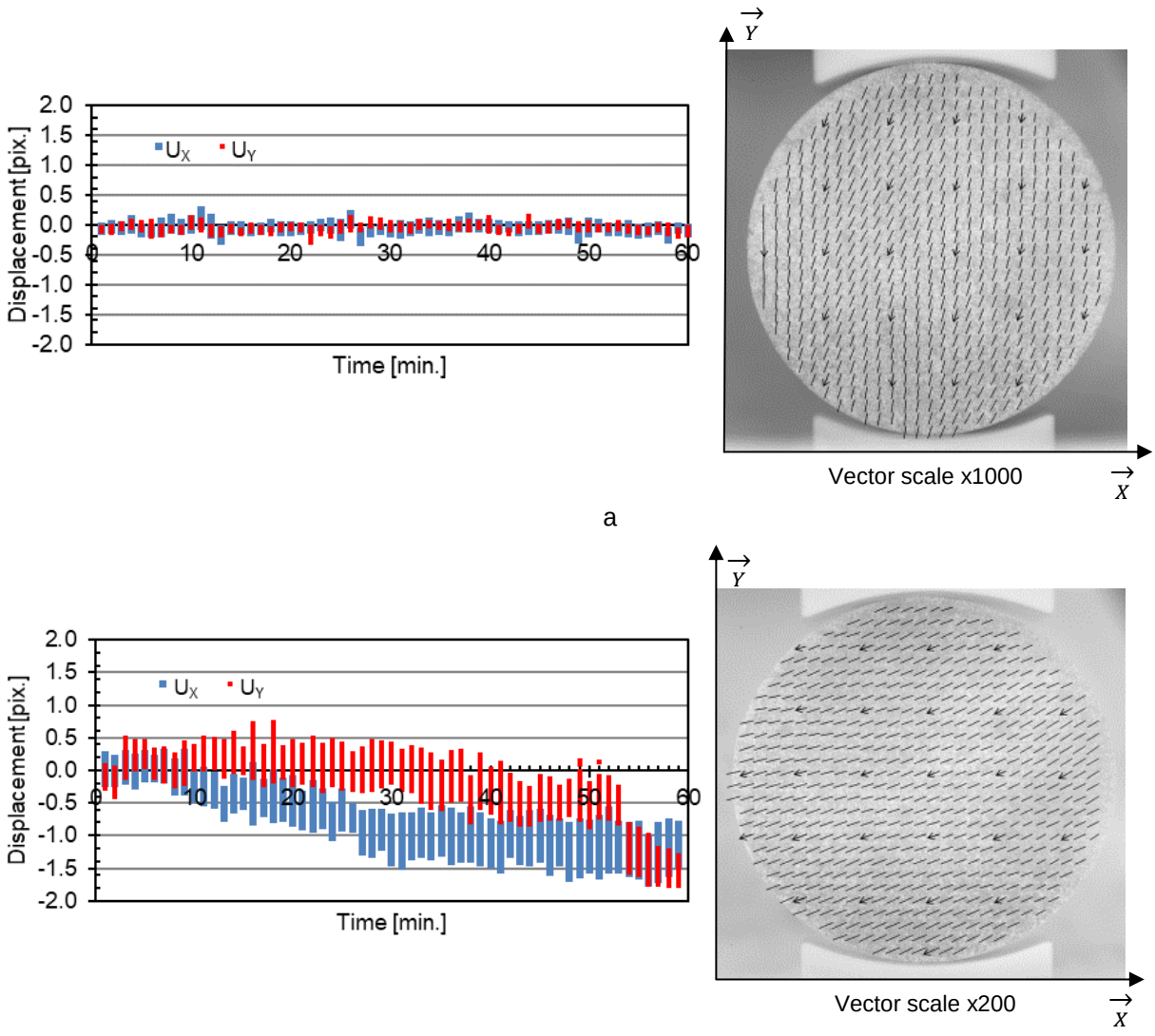

Figure 3-14. Displacement results performed on B_SiC_50-100 sample with subset size of 128x128 pixels and spacing of 64x64 pixels. Evolution of horizontal U_X and vertical U_Y displacements vs. time for all subsets (on the left) and *v*ector plot at the end of test (on the right), showing 2-dimensional displacements at: a) 20°C, b) 1200°C.[154]

Evolutions of horizontal U_X and vertical U_Y displacements vs. time during stability test performed at 20 °C and 1200 °C are presented in Figure 3-14. Displacements at 20 °C are very stable around zero with very little variations during the whole test. However, at 1200 °C global displacements deviate from the initial position and larger spread of variations can be observed. This difference is related to more harsh experimental conditions at high temperature, including black body radiation (altering σ_{GL} and $\sqrt{\overline{\nabla g^2}}$) and heat haze. Visual representation of the displacements at the end of stability tests is presented on the right sides of Figure 3-14a and b. Directions of displacements are rather uniform but the range is 10 times lower at 20 °C in comparison to 1200 °C (0.25 pix. ~ 3.5 µm at 20°C, 2.5 pix. ~ 35 µm at 1200 °C).

The cause of this displacement at 1200 °C is probably related to differences in temperature and thus in expansion of tripod legs (camera support), what is probably linked to different exposure of the legs to the heat flux from the furnace. This most probably introduces the global movement of the camera during long dwells.

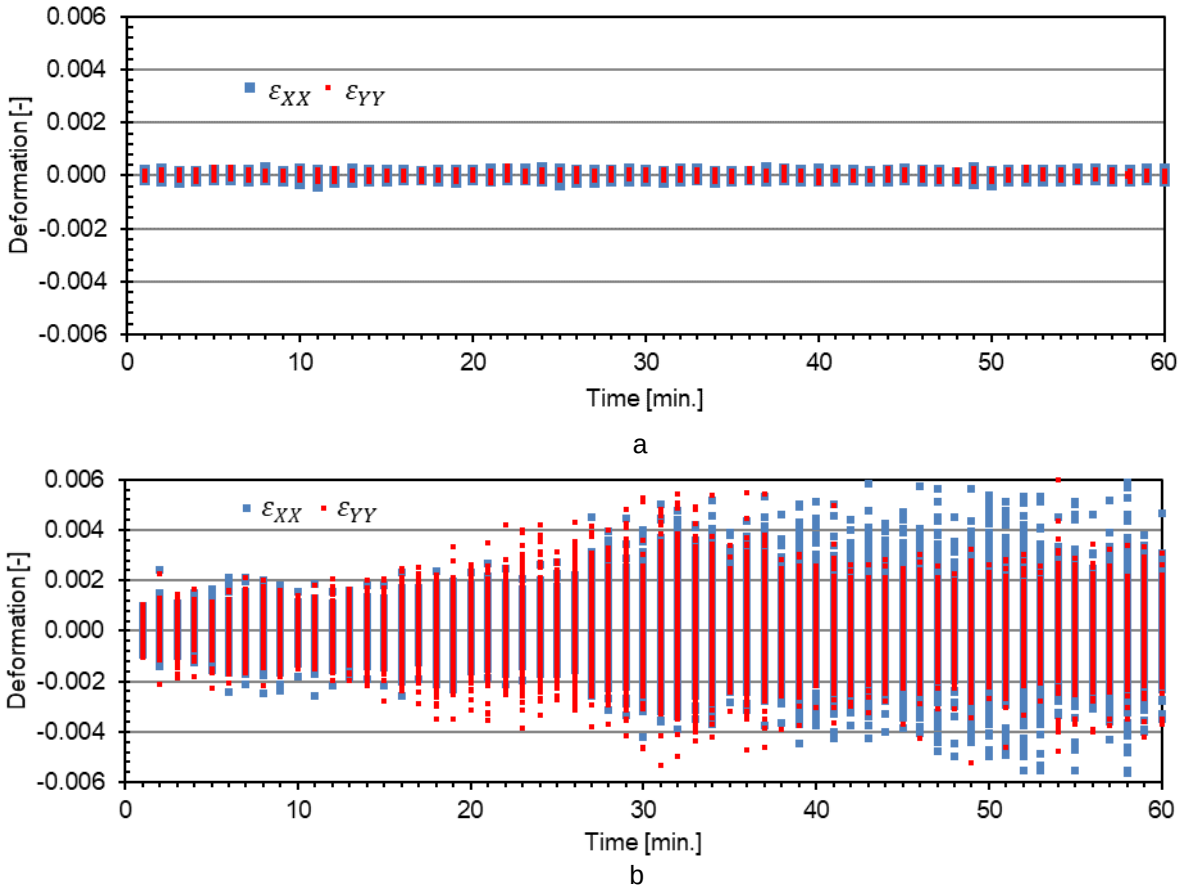

Figure 3-15. Deformation results performed on B_SiC_50-100 sample with subset size of 128x128 pixels and spacing of 64x64 pixels. Evolution of horizontal ε_{XX} and vertical ε_{YY} deformations vs. time calculated for all subsets at: a) 20°C, b) 1200°C.[154]

Evolutions of horizontal ε_{XX} and vertical ε_{YY} deformations vs. time during stability test performed at 20 °C and at 1200 °C are presented in Figure 3-15. Values of deformations measured at 20 °C are very small, as a consequence of smaller displacements, while, at 1200 °C large strains can be observed, as a consequence of larger displacements. Moreover, during the test performed at 1200 °C, one can observe an increase of deformation fluctuations after 20 minutes (being higher than a typical duration of mechanical test). It is also worth to notice that the rigid body movement detected at 1200 °C (see Figure 3-14a) does not influence deformation. Therefore, deformation values seem to be more reliable than displacement ones and thus will be used for comparative purposes. These deformation values will

be investigated for all speckle patterns only until 20 min to decrease the probability of increased deformation fluctuations. Considering that both horizontal ε_{XX} and vertical ε_{YY} deformations show similar tendencies, in further study, only horizontal strain ε_{XX} will be used.

3.4.3. Impact of different parameters on measurement uncertainty

3.4.3.1 *Low pass filtering*

Numerical low pass filter (Gaussian blur with a size of 3x3 pixels) is applied to reduce noise (measurement uncertainty). Standard deviation of the noise present on images was about 2 grey levels for all images (determined on a uniform surface). Application of this filter leads to a decrease of σ_n, but a side effect, it also reduces $\sqrt{\overline{\nabla g^2}}$ by a factor of 1.2 (in average for all patterns). Application of such filter significantly decreases measurement uncertainty (of about 50% on average), as it can be observed in an example of standard deviation of horizontal deformations $\sigma_{\varepsilon_{XX}}$ in Figure 3-16.

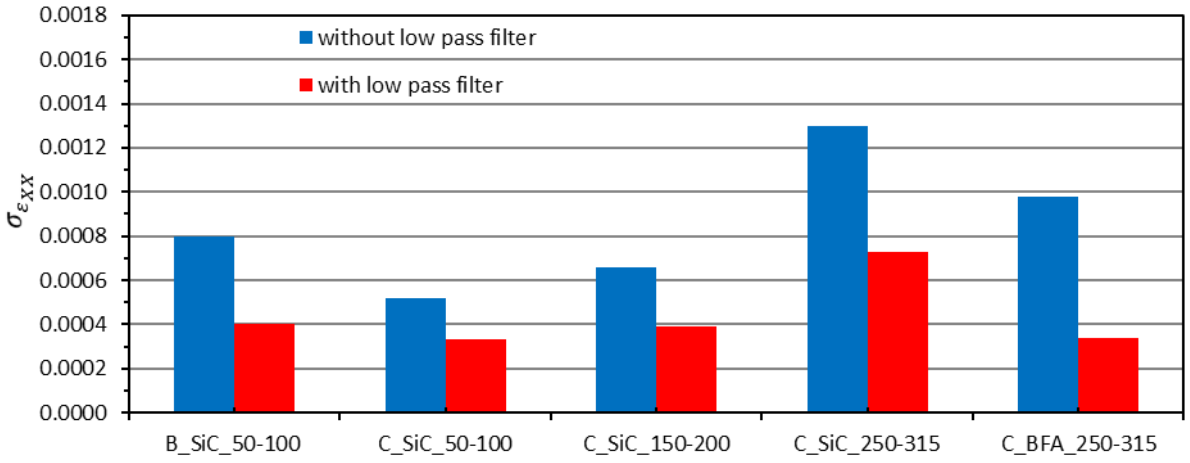

Figure 3-16. Standard deviation of horizontal deformations $\sigma_{\varepsilon_{XX}}$ during 60 minutes of stability test for all samples at 1200°C. Subset size of 128x128 pixels, spacing of 64x64 pixels, with/without add application of low pass filter.[154]

3.4.3.2 *Size of subsets and particles*

Figure 3-17 presents $\sigma_{\varepsilon_{XX}}$ for different speckle sizes (from 16x16 to 128x128) for all tested speckle patterns. For all patterns, one can observe that the increase of subset size leads to a decrease of $\sigma_{\varepsilon_{XX}}$ (well-known relation). Comparing samples prepared with the same type but different sizes of SiC grains, one can observe that an increase of speckle size leads to less accurate strain measurements (higher $\sigma_{\varepsilon_{XX}}$).

This observation is in line with the recommended speckle size, which should be relatively small, leading to high spatial resolution, but not too small to prevent aliasing.[133,139] For this aspect, the best performance is achieved for C_SiC_50-100, while the worst one for C_SiC_250-315.

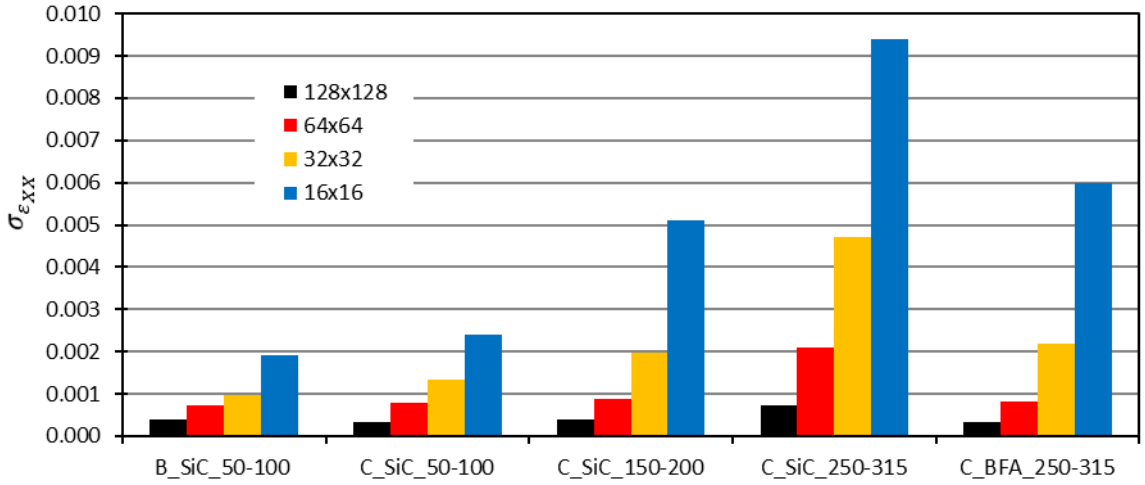

Figure 3-17. Standard deviations of deformation in horizontal direction $\sigma_{\varepsilon_{XX}}$ for 60 pictures acquired: at 1200°C during one hour of measurement (calculations performed using low pass filtering). Influence of subset size for the same spacing of 64x64 pixels.[154]

3.4.3.3 *Image resolution*

2P-DIC analysis can be very time-consuming. Especially when it is performed on full-resolution images (6576 x 4384 pixels), the calculations can take a week (2000 images tested on a workstation with 32 cores of 2.77 GHz). Therefore, knowing the relatively large speckle size of 10 pixels (for B_SiC_50-100), it appeared interesting to consider the usage of smaller images (with reduced resolution of 3288 x 2192 pixels by averaging 4 pixels to 1). The speckle size after the image reduction would be about 5 pixels (in diameter), which is still reasonable from the aliasing point of view. However, this is not the only point to verify before proceeding to calculations with smaller images. It is crucial to consider whether the standard deviations of deformation in horizontal direction $\sigma_{\varepsilon_{XX}}$ would not be much affected by this decrease in image resolution. This point is presented in the following paragraphs.

In the beginning, it should be noticed that the subset sizes m and spacings between subsets L_0 were reduced accordingly to the reduction of the image size (to ensure comparability between reduced- and full-resolution images). Figure 3-18 presents the influence of the image resolution and/or the low pass filtering (introduced in section 3.4.3) on $\sigma_{\varepsilon_{XX}}$.

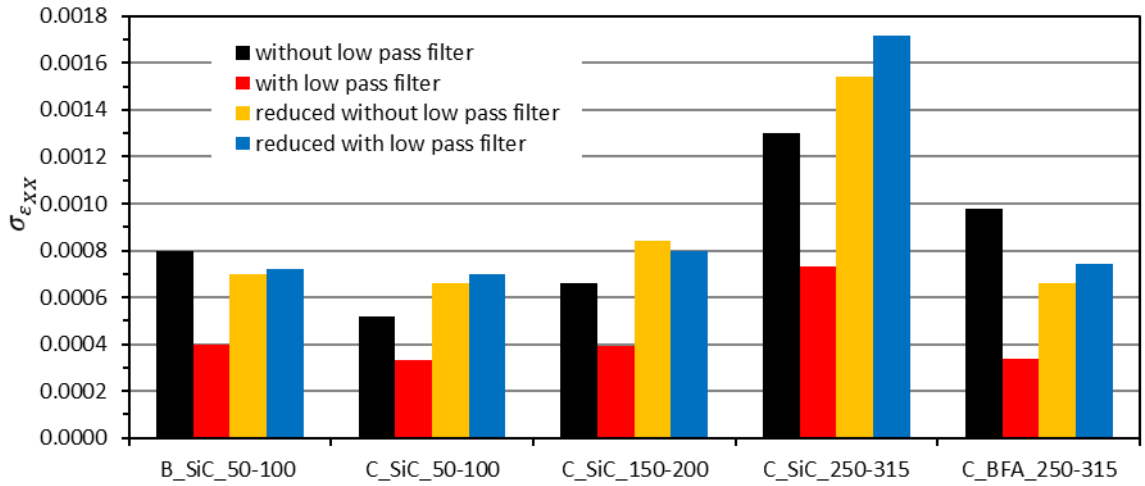

Figure 3-18. Influence of image resolution on standard deviation of horizontal deformation. Parameters of DIC calculation: subset 128x128 pixels and spacing of 64x64 pixels for initial images and subset 64x64 pixels and spacing of 32x32 pixels for reduced images.[154]

Firstly, one can observe that the reduction of image size results in a slight increase or decrease of $\sigma_{\varepsilon_{XX}}$ (depending on the sample) when compared to the full-resolution images. In general, one could say that the two types of images lead to rather similar $\sigma_{\varepsilon_{XX}}$ values. An explanation of this observation can be provided based on Equation 3-12 and Equation 3-13. The decrease of image resolution leads to changes in L_0 and σ_{U_X} (see Equation 3-13). The L_0 decreases by a factor of 2 (in pixels), while the changes of σ_{U_X} are related to σ_n, m and $\sqrt{\overline{\nabla g^2}}$ (see Equation 3-12). The values of nominator σ_n and denominator $\left[m \cdot \sqrt{\overline{\nabla g^2}}\right]$ for each case are presented in Table 3-4. It can be observed that the reduction of image resolution leads to a 2.2-fold decrease in σ_n and to a 1.4-fold decrease in $\left[m \cdot \sqrt{\overline{\nabla g^2}}\right]$ (in average). Therefore, σ_{U_X} value theoretically decreases 1.65 times (in average), what is rather close to the change of L_0 (which decreases 2 times). This approach connecting experimental measurements and theoretical considerations may indicate rather low impact of image reduction change on strain accuracy $\sigma_{\varepsilon_{XX}}$. One can conclude that this approach allowed to confirm more or less the experimental results from Figure 3-18.

Secondly, one can observe that application of low pass filter on images with reduced size does not lead to any improvement of measurement uncertainty (see Figure 3-18). This observation can be explained by more rapid decrease of $\left[m \cdot \sqrt{\overline{\nabla g^2}}\right]$ when compared to σ_n (see Table 3-4).

Thirdly, one can state that the ideal solution would be to combine full-resolution images and low pass filtering, as it allows to reduce the uncertainty $\sigma_{\varepsilon_{XX}}$ by about 2 times (see Figure 3-18). However, this solution is even more time consuming than the initially assumed calculation time performed on high-resolution images, as we apply low pass filtering on each image. Therefore, taking into account the importance of calculation time, it seems that the level of uncertainty achieved on reduced images is rather sufficient for cracks monitoring in refractories during mechanical tests. So, the images with the resolution reduced to 0.028 mm/pixel and without any numerical filtering are used for the 2P-DIC calculations (for precise crack detection). Consequently, the calculation time is then typically divided by a factor of 10.

Table 3-4. Effect of image resizing or/and applying low pass filter on the two major terms of equation 4 (numerator: noise σ_n - denominator: term $\left[m \ . \ \sqrt{\overline{\nabla g^2}}\right]$).[154]

	Full image without filter d=128 pixels (ref.)	Full image with low pass filter d=128 pixels	Resized image without filter d=64 pixels	Resized image with low pass filter d=64 pixels
		noise (σ_n)		
Average for all speckles	2.0	1.0 (ref. / 2.0)	0.9 (ref. / 2.2)	0.7 (ref. / 2.9)
		term $\left[m \ . \ \sqrt{\overline{\nabla g^2}}\right]$		
B_SiC_50-100	422	358 (ref. / 1.2)	307 (ref. / 1.4)	243 (ref. / 1.7)
C_SiC_50-100	589	513 (ref. / 1.1)	378 (ref. / 1.6)	307 (ref. / 1.9)
C_SiC_150-200	525	435 (ref. / 1.2)	416 (ref. / 1.3)	333 (ref. / 1.6)
C_SiC_250-315	448	384 (ref. / 1.2)	352 (ref. / 1.3)	282 (ref. / 1.6)
C_BFA_250-315	448	371 (ref. / 1.2)	339 (ref. / 1.3)	262 (ref. / 1.7)

3.4.3.4 *2P-DIC strain threshold*

Rectangular subsets (instead of square ones) are typically used for the 2P-DIC technique. These subsets are positioned perpendicularly to the expected crack what together with its shape allows better detection of cracks, which are searched between -60° and 60°.[138,149] In the case of Brazilian test (presented in the following sections), the cracks will most likely be vertical, so the subsets are positioned horizontally. Local pseudo strain value, being determined for each subset, is classified as a crack when it exceeds a threshold value ε_{Thres}. This threshold value was calculated for each tested sample based on the strain fields determined during the stability test where strain

is assumed to be zero (duration of 60 minutes, very low constant preload of 50 N, temperature of 1200 °C). This approach is similar to the one presented in previous sections by using a classical DIC with a difference in shape and spacing between subsets (subset size of 64x16 pixels with a spacing of 32x8 pixels). An exemplary result used for determination of pseudo strain threshold for C-SiC_50-100 is presented in Figure 3-19. Based on this graph, the pseudo strain threshold is determined as the maximal strain value, which allows to significantly reduce the noise (avoid detection of non-real cracks). It is worth noticing that the vertical axis on this graph is on a semi-logarithmic scale and that the total number of subsets exceeds 700 thousands. Therefore, an ε_{Thres} of 0.0035, where less than 10 occurrences above this threshold are detected, is the chosen value.

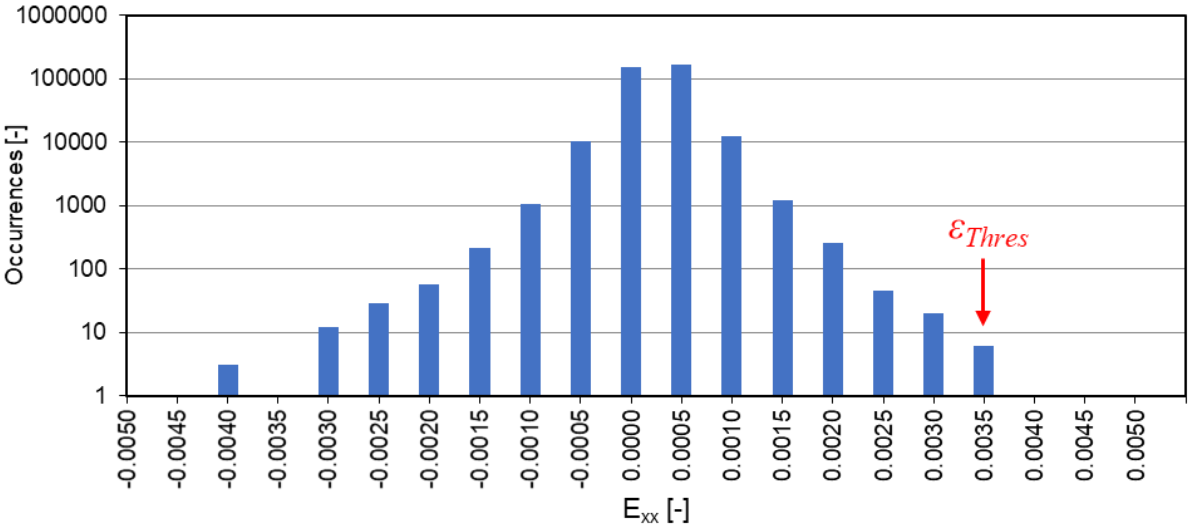

Figure 3-19. Histogram of ε_{xx} for C-SiC_50-100 case during the 60 minutes of stability test (with a very small preload of 50 N for which one can assume that no local cracks can take place).[154]

This approach was applied to all samples and allowed to determine ε_{Thres} values for which less than 10 occurrences of non-existent cracks were detected. These ε_{Thres} values are presented in Figure 3-20. It can be observed that the smallest strain threshold values are obtained for C_SiC_50-100, C_SiC_150-200 and B_SiC_50-100.

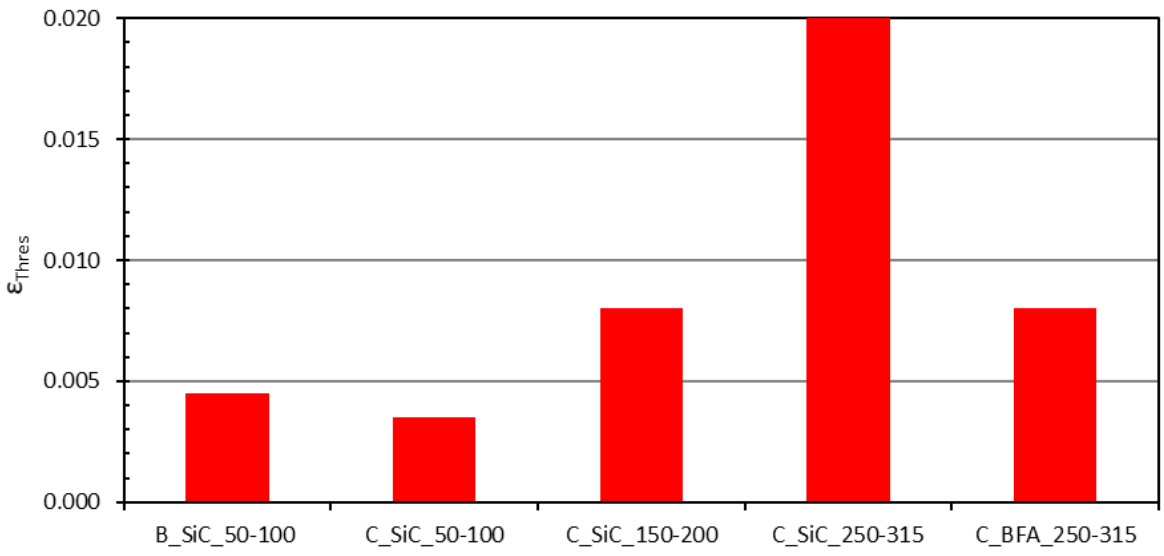

Figure 3-20. Predetermined value of pseudo strain threshold ε_{Thres} (with less than 10 subsets with a crack detected inside) for each considered speckle patterns.[154]

3.4.4. Example of sample monitoring at high temperature

3.4.4.1 *Load-displacement curves during Brazilian test at 1200 °C*

Once all the parameters are defined, it is possible to perform the mechanical test with image acquisition on samples having different speckle patterns. The exemplary load-displacement curves acquired during Brazilian test at 1200 °C are presented in Figure 3-21. The imposed displacement $\Delta\mathbf{U}$ has been measured directly on the sample by DIC (see section 3.4.4.2) between the two areas placed at the top and at the bottom of sample close to the jaws (see Figure 3-3). It is worth noticing that it is rather common to obtain significant differences between tested refractory samples, especially at high temperatures. Nevertheless, the shapes of these curves are similar, as all of them start with relatively linear dependence and then continue with non-linear dependence due to damage or plastic behaviour. This plateau corresponds to localisation of damage in the central sample part which leads to macrocracking and then to failure. The increase of load observed at above ΔU=0.2 mm typically corresponds to the loading of two halves of the disk (even if they are not completely separated) and is not interesting from the point of view of the current analysis.

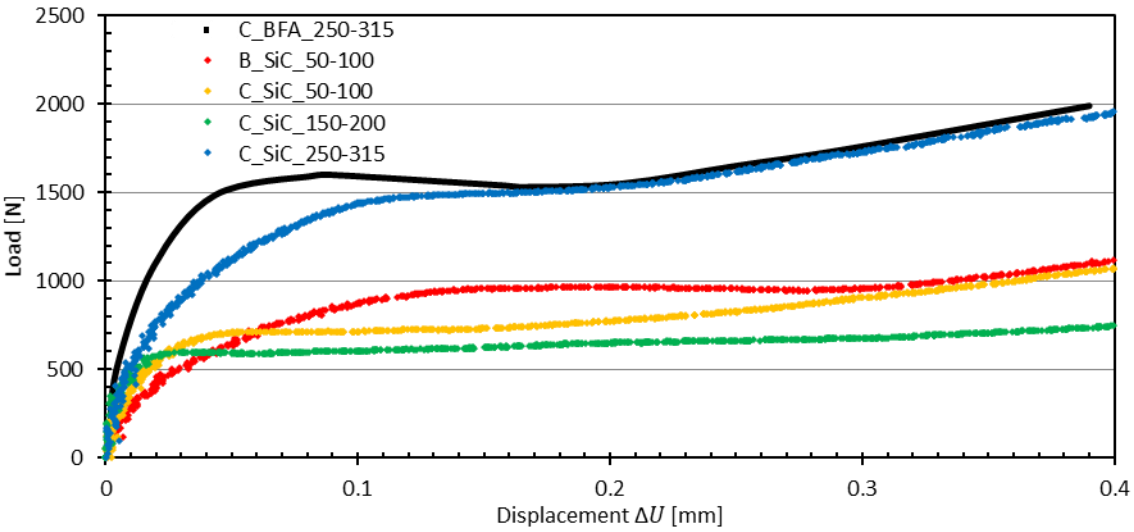

Figure 3-21. Load-displacement curves during Brazilian test at 1200°C for the different considered samples (displacement $\Delta\mathbf{U}$ measured directly on the sample by DIC between two area placed at the top and at the bottom of sample close to the jaws).[154]

2P-DIC analysis was used to determine evolutions of crack length during Brazilian tests which are presented for different speckle patterns in Figure 3-22. These curves were generated with optimized ε_{Thres} values from Figure 3-20 (see Figure 3-22a), as well as with a uniform ε_{Thres} value of 0.005 (see Figure 3-22b). The crack length evolution curves with optimized ε_{Thres} exhibit rather low level of noise, what was intended by selecting an appropriate threshold but does not allow to detect the beginning of crack at the same displacement. In contrast, when a uniform ε_{Thres} of 0.005 is applied, crack initiation displacement is similar (see Figure 3-22b). Moreover, the curves generated with a uniform ε_{Thres} show significant differences in noise levels. The highest noise is present for C_SiC_250_315, as the difference between the optimal ε_{Thres} value for this speckle pattern (being equal to 0.02) and the applied pseudo strain threshold is the highest. Therefore, one can state that speckle pattern with high optimal threshold value is not able to detect cracks with small openings leading to underestimation of crack length. The speckle patterns having similar optimal ε_{Thres} values (see Figure 3-20) lead to approximately similar performance, as crack initiation appears at similar displacement (variations depend on variability between different samples).

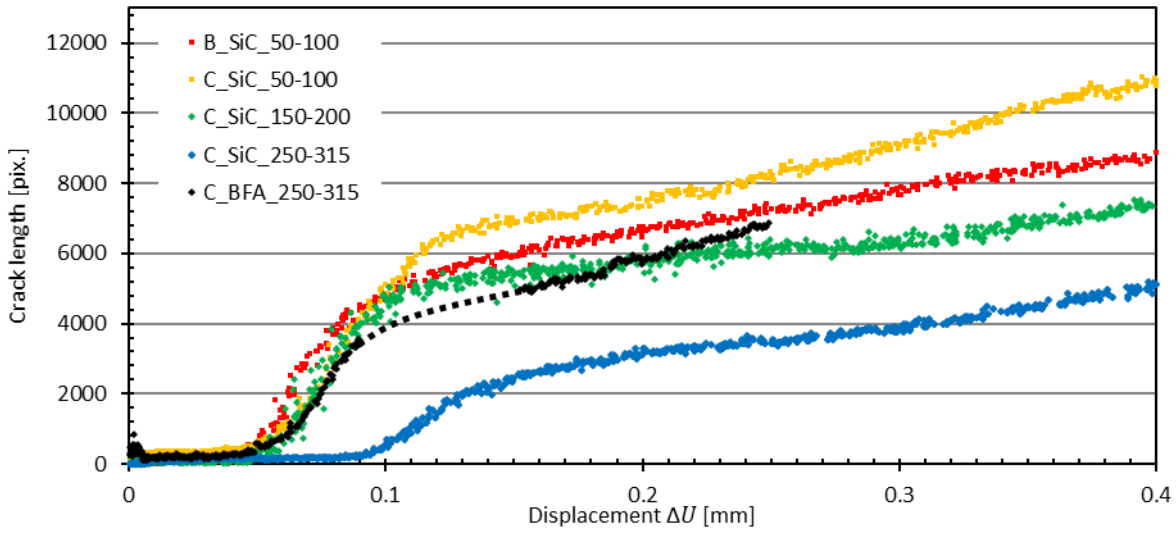

a

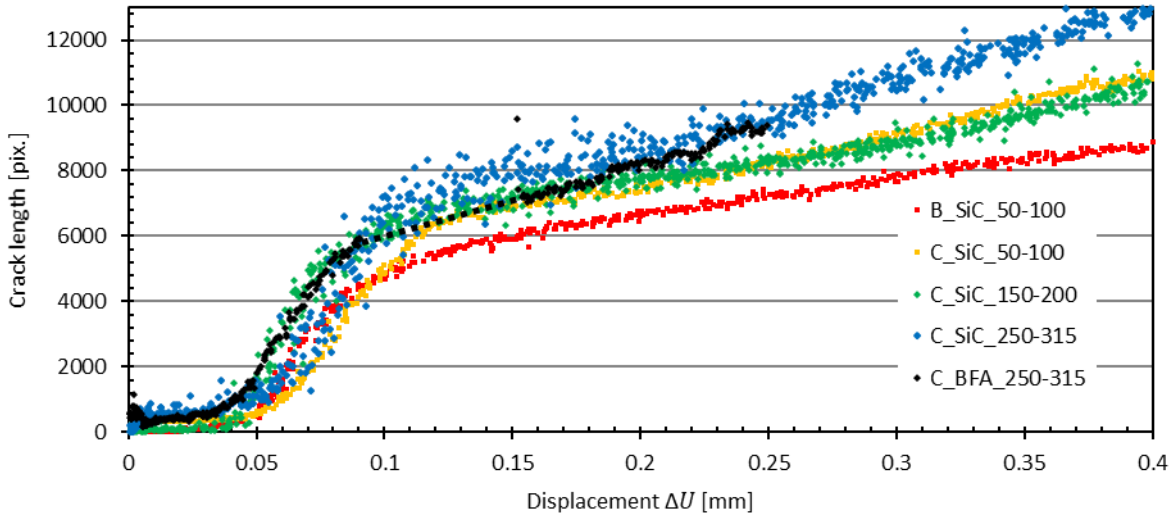

b

Figure 3-22. Crack length-displacement curves during Brazilian test: influence of different speckle grain size (a) with ε_{Thres} adapted at each speckle pattern (b) with a uniform value of ε_{Thres}=0.005.[154]

In order to quantify the dispersion in crack length (visible in Figure 3-22b), standard deviation of the difference between real values and local linear tendencies have been calculated for two displacement ranges: at the beginning (ΔU between 0 and 0.04 mm) and at the end of the test (ΔU from 0.2 to 0.4 mm). Table 3-5 reports all these values. It can be observed that the standard deviation is higher when measured at the end of the test what can be related to slight degradation of speckle pattern (removal of cement/grains when a high local strain or crack appears). A similar trend is also present at ambient temperature: at the beginning, the dispersions are very low ~0 pix. and close to the end, they reach 35 pix. (~1 mm). The largest dispersions, during the tests performed at 1200 °C, are observed for C_SiC_250-315 (big grain size

can result in insufficient contrast within some subsets), while the lowest dispersions are observed for B_SiC_50-100 and C_SiC_50-100 speckle patterns.

Table 3-5. Dispersion in crack length measurement at the beginning of the test (ΔU from 0 to 0.04 mm) and at the end of the test (ΔU from 0.2 to 0.4 mm).[154]

	Dispersion in crack length in pixel (and in mm)	
	Beginning of the test (ΔU from 0 to 0.04 mm)	End of the test (ΔU from 0.2 to 0.4 mm)
B_SiC_50-100	10.5 (0.3 mm)	94 (2.6 mm)
C_SiC_50-100	21.8 (0.6 mm)	120 (3.36 mm)
C_SiC_150-200	65.6 (1.8 mm)	278 (7.8 mm)
C_SiC_250-315	143 (4 mm)	367 (10.3 mm)
BFA_SiC_250-315	45 (1.3 mm)	130 (3.7 mm)

The crack paths detected by the 2P-DIC (with optimized ε_{Thres}) are presented in Figure 3-23. Images are presented for all speckle patterns at four loading states:

- A - at initiation of the main crack;
- B - at inflection point of main crack growing;
- C - when the load reaches a plateau;
- D - when the load starts to increase due to loading of two halves of a disc.

It can be observed that patterns with a small ε_{Thres} better imitate sample behaviour as cracks with smaller opening can be visible.

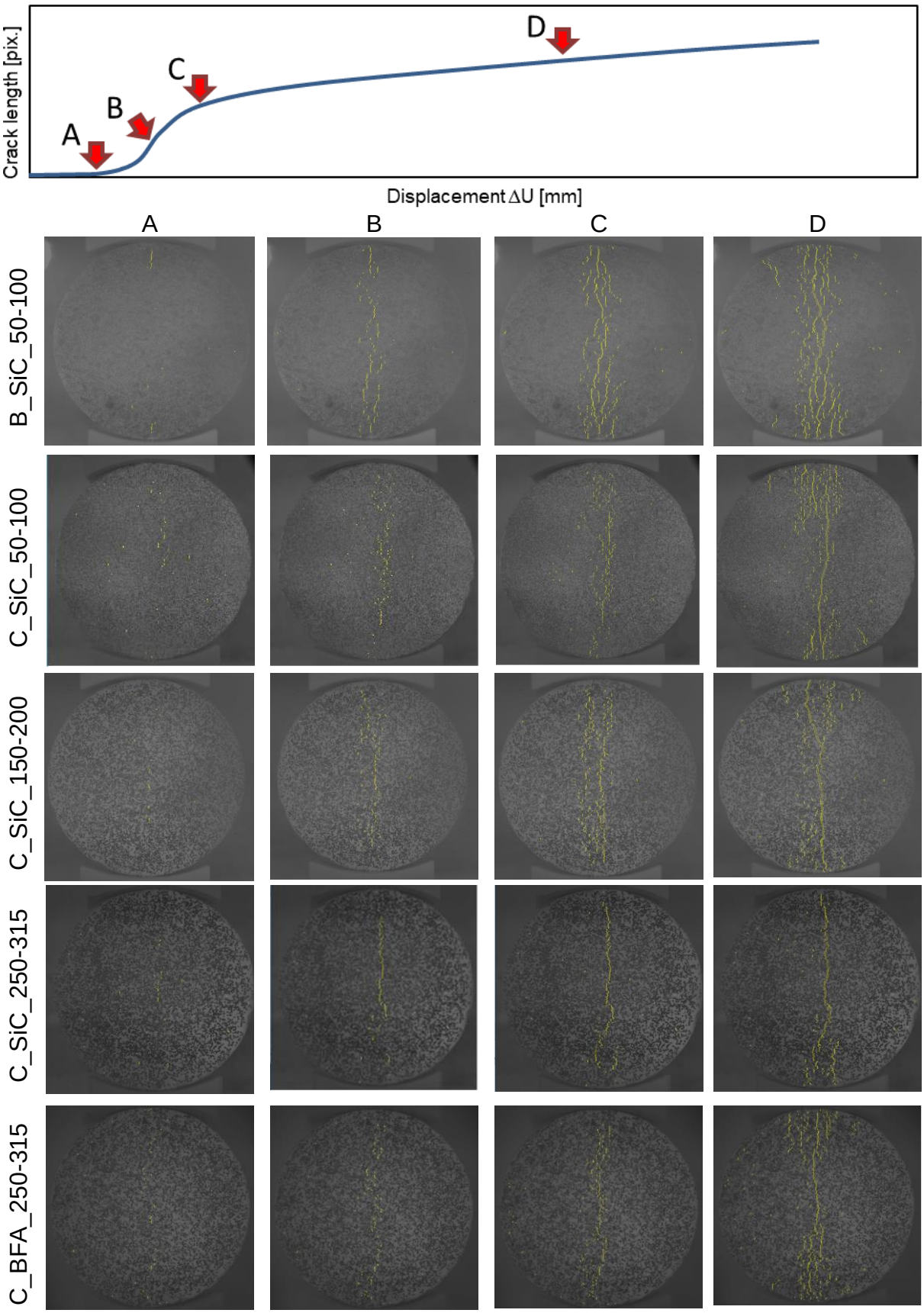

Figure 3-23. Pictures of highlighted cracks path determined by 2P-DIC numerical treatment at four key loading states during Brazilian test at 1200°C with an optimal value of ε_{Thres} adapted to each speckle pattern.[154]

3.4.4.2 *Measurement error by deviation from imposed displacement*

The imposed displacement ΔU in this study was measured by DIC, between two areas placed at the top and bottom of the sample in proximity to jaws. This is not a common practice in mechanical testing of refractories, as in most cases, the crosshead displacement of the machine is used. Figure 3-24 presents similar results as Figure 3-22b but in this case with crosshead displacement on the horizontal axis (instead of measurement by DIC).

Much larger shifts can be observed between the different curves in Figure 3-24. They are related to differences in mechanical behaviour in contact between the cylindrical sample surface and the jaws. These discrepancies are probably related to non-reproducible delays in loading at the beginning of mechanical tests. Therefore, measurement of the relative displacement seems to be more appropriate for analysis of mechanical behaviour, as it reduces measurement error (due to slight differences in contact between sample and loading jaws), which can lead to significant discrepancies.[159]

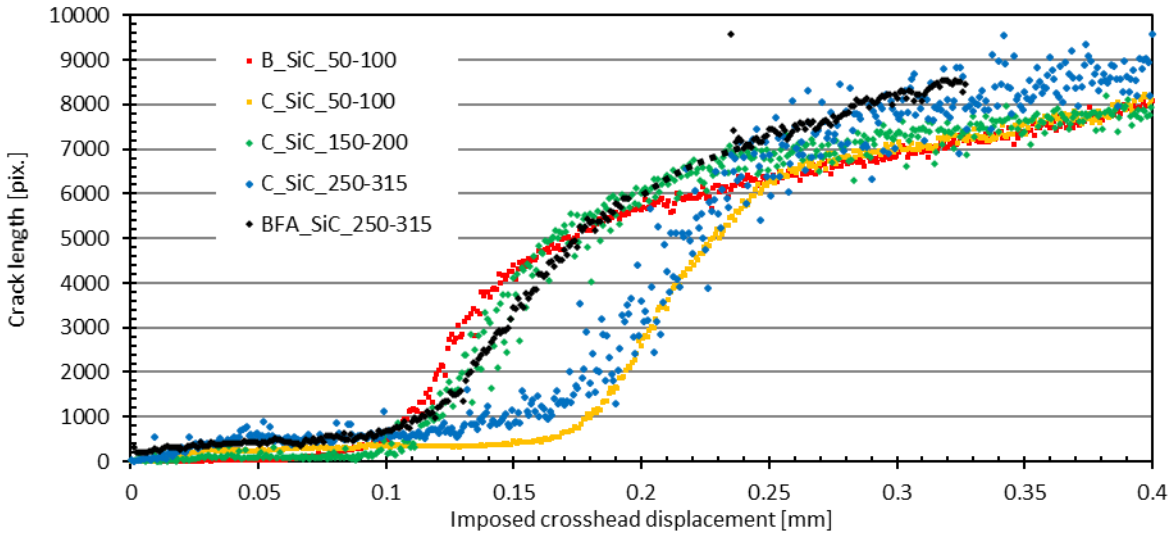

Figure 3-24. Crack length-displacement curves during Brazilian test with a uniform value of ε_{Thres}=0.005 and imposed crosshead displacement.[154]

3.4.4.3 *Fracture behaviour at 20 °C and at 1200 °C*

The objective of this study was to determine an optimized speckle pattern for high-temperature mechanical testing of refractories. As demonstrated, speckle patterns with fine grains, such as B_SiC_50_100 or C_SiC_50_100 perform the best in the current testing conditions. It is worth pointing out that the lack of cement allows

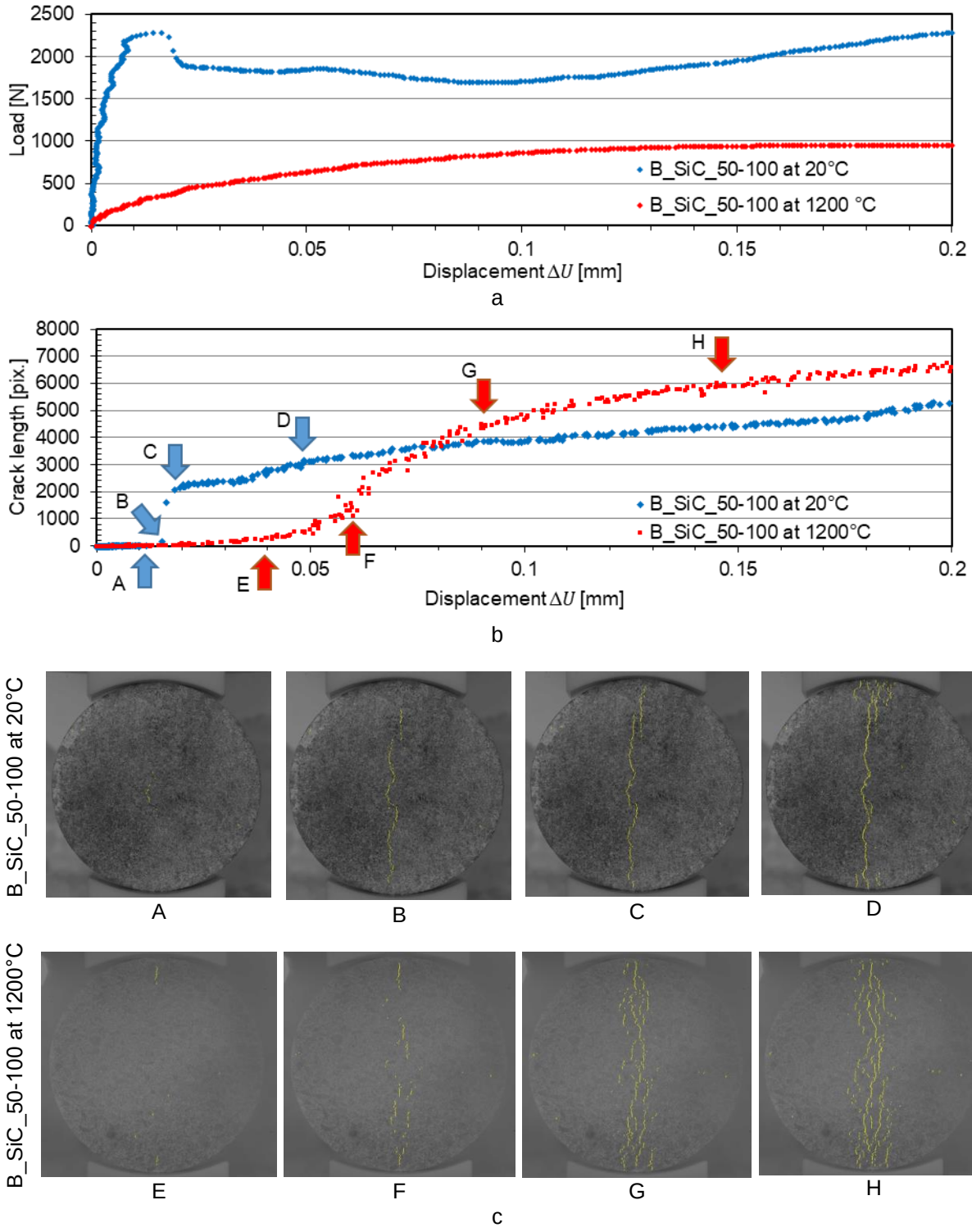

Figure 3-25. Brazilian test at 20°C and 1200°C: a) Load-displacement curves, b) Crack length-displacement curves, c) Pictures of cracks at four loading states.[154]

to see microstructure and assures that behaviour of sample surface is observed. Therefore, one concludes that B_SiC_50_100 speckle pattern is the most adapted among tested specimens. Figure 3-25 presents exemplary results of the tests performed at 20 and 1200 °C. They were obtained with an optimized ε_{Thres} values of 0.003 and 0.005 at 20 and 1200 °C, respectively. The fracture behaviour of tested

material at these two testing temperatures is diametrically different. A sudden increase of crack length (see Figure 3-25b) and rupture at a low displacement of 0.015 mm (see Figure 3-25a) is observed at 20 °C (points A, B, C are close to each other), while at 1200 °C crack length increases progressively and rupture occurs at a rather high displacement of 0.1 mm (points E, F, G are far from each other). These observations indicate a brittle fracture at 20 °C and a non-brittle one at 1200 °C. At ambient temperature, more elastic energy is stored and the material does not dissipate energy until the occurrence of the main crack. However, at high temperature, less elastic energy is stored, as the material starts to dissipate energy much earlier (initially by microcracking), what leads to a progressive failure with many cracks present within the central sample part.

3-5. Conclusions

The first two sections of this chapter were focused on selected loading devices and optical methods which could be used for high-temperature testing of fracture behaviour of refractories. Due to the challenges related to high-temperature conditions (such as black body radiation, heat haze and high-temperature resistance of speckle pattern) and lack of experience within our team with such tests at high temperature (1200 °C), there was a need to improve the experimental device which has been introduced in section 3.1.2.

The main focus of this chapter was on the study described in sections 3-3 and 3-4, which allowed determining optimized speckle patterns (with different ceramics grains) and experimental parameters for analyses of high-temperature images using DIC and 2P-DIC methods. Analyses of grey levels distributions, gradients and speckle sizes allowed understanding the performance of these speckle patterns in tested conditions. According to strain uncertainty results, two speckle patterns had remarkably good performance B_SiC_50-100 and C_SiC_50-100. However, thanks to the advantages related to the lack of cement, **B_SiC_50-100 is preferred for further investigations**. Studies on image pre-processing (images filtering, images size reduction) before DIC analysis allowed finding a compromise between good measurement accuracy and relatively short duration of processing. This experimental procedure is adapted for the detection of early cracks and measurement of their length (by 2P-DIC method) in refractories tested at high temperatures. An exemplary test performed on alumina spinel refractory at 20 and 1200 °C has been presented using

B_SiC_50-100 speckle pattern. It allowed proving the performance of the optimized speckle pattern within a large temperature range. The experimental protocol developed in this study can be used in other types of mechanical tests performed at high temperatures (1200 °C and probably higher) on refractories, including wedge splitting or thermal shock bench ATHORNA.

Chapter 4

Chapter 4. Thermomechanical behaviour of alumina spinel refractories

This chapter aims to **improve understanding about in-use behaviour of alumina spinel refractories** by focussing on relations between thermomechanical properties and microstructure. Investigated materials are an industrial alumina spinel brick (see section 4-1) and model alumina spinel castables (see section 4-2). The industrial material was investigated both to improve understanding of its in-use behaviour, as well as to provide the data being necessary for FEM/DEM modelling (used by other PhD students). The model materials were designed to compare impact of several key components, such as cement, reactive alumina and aggregates.

4-1. Case of industrial alumina spinel bricks

Investigated industrial alumina spinel bricks are known for their outstanding performance e.g. in the barrel part of steel ladle lining. It is well-known that alumina-based spinel-containing refractories can be designed to achieve rather high corrosion resistance, which could already significantly contribute to their performance. At the same time, thermomechanical behaviour of this material is not well explained in the literature and this knowledge is obviously of interest e.g. regarding material potential for stress relaxation (explained in section 1.1.3). Therefore, an objective in this section is to **better understand thermomechanical behaviour of industrial alumina spinel bricks in relation to microstructure**.

Note: Additionally, acquired data has been used as an input in numerical modelling performed by other PhD students from ATHOR.

4.1.1. Presentation of investigated fired alumina spinel brick

The alumina spinel bricks, investigated in this study are rather similar to the industrial ones which are used in steel ladles studied within ATHOR. In fact, to deliver similar bricks to all research activities performed within ATHOR, a specific batch of material has been processed by an industrial partner.

The processing route involved a uniaxial pressing of the raw materials and a firing stage (typically at about 1680 °C).[160] The final microstructure is composed of alumina grains (up to 3 mm) and alumina spinel matrix (see Figure 4-1). The material's density and apparent porosity are about 3.1 g/cm^3 and 19.7 % (measured by the Archimedes' principle), respectively. Phases detected at ambient temperature by Rietveld refinement of X-ray diffractograms are alumina (77.62 wt. %, JCPDS

No. 01-071-1123), alumina-rich spinel (22.02 wt. %, JCPDS No. 01-073-1959) and diaoyudaoite (0.36 wt. %, JCPDS No. 01-079-2288). EDS analysis (not presented here) allowed to detect traces of sodium inside alumina grain (originating from the Bayer process) and a very small amount of silicon in the matrix (voluntary added in form of aluminium silicate).

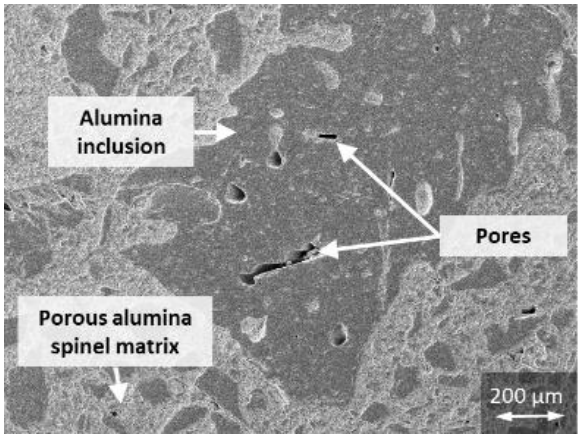

Figure 4-1. SEM image of the alumina spinel brick.[161]

Please notice: All results presented in this section with the thermal treatment performed up to 1500 °C followed the same thermal cycle with a heating/cooling rate of 3 °C/min and 1 h dwell.

4.1.2. Thermal expansion during thermal treatment

Thermal expansion has been investigated by dilatometry measurement up to 1500 °C, as presented in Figure 4-2. Even though the material processing probably includes a firing stage above testing temperature (typically at around 1680 °C),[160] a permanent linear change of 0.08 % (heat treatment with 1 h dwell at 1500 °C), which mainly occurred above 1300 °C (a visible increase of linear expansion rate) could still be observed. Since pressing direction could have induced slight differences from one direction to another, the measurement has been managed in the pressing and perpendicular to the pressing directions. Nevertheless, both curves are very similar.

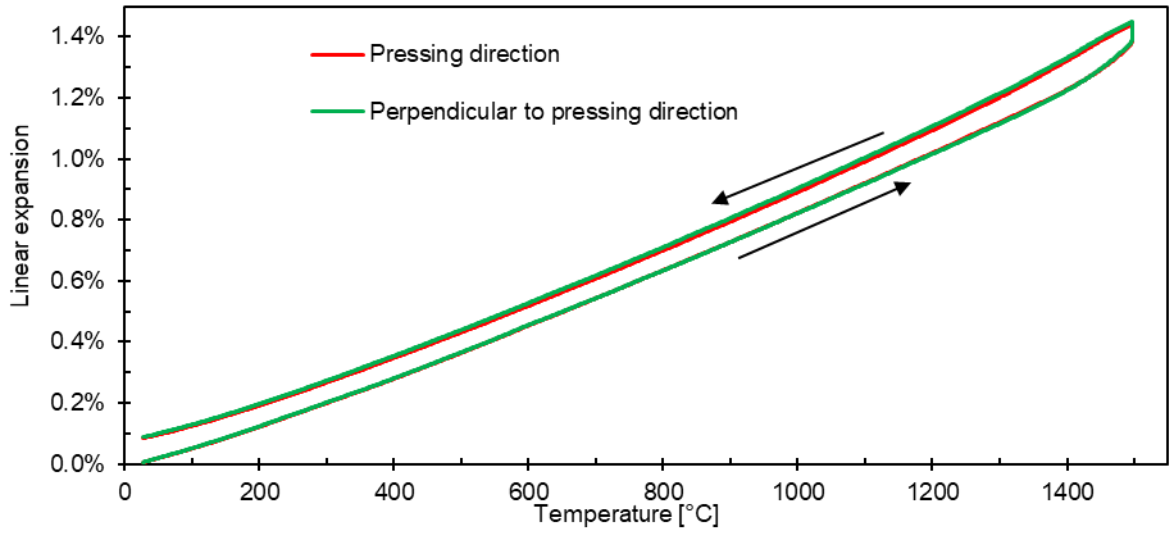

Figure 4-2. Dilatometry curve for alumina spinel brick measured from different directions.[161]

Evolution of Coefficient of Thermal Expansion (CTE) with temperature, determined as a derivation of linear expansion, is plotted in Figure 4-3. One can observe that the thermal expansion coefficient is much smaller in the low-temperature range (below 500 °C) and starts to increase above 1300 °C. This increase in CTE is related to microstructural changes and will be discussed in the following sections of this chapter.

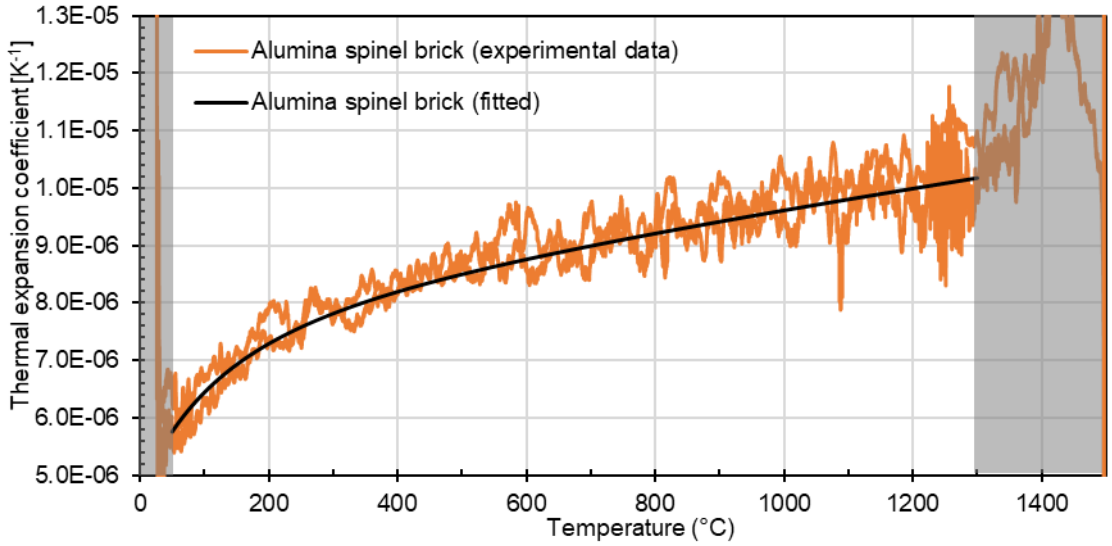

Figure 4-3. Evolution of thermal expansion coefficient for alumina spinel brick. Fitting between 50 and 1300 °C.

Subsequently, a classical equation for thermal expansion related to temperature (see Equation 4-1) has been used to fit the experimental data, where α is a thermal expansion coefficient at a given temperature, and a_0, a_1 and a_2 (≤ 0) are constants.

Considering only the valid derivative data between 50 and 1300 °C (in Figure 4-3), this fitting allowed to determine the a_0, a_1 and a_2 constants, which equal to $7.6 \cdot 10^{-6}$, $1.7 \cdot 10^{-9}$ and $-2.5 \cdot 10^{-1}$, respectively.

$$\alpha(T) = a_0 + a_1 \mathrm{T} + a_2 \mathrm{T}^{-2} \qquad \text{Equation 4-1}$$

Figure 4-4 presents the evolution of thermal expansion coefficients of alumina spinel brick (fitted from experimental data), as well as values for constitutive mineral phases from literature.[162,163] Due to different crystallographic structures (cubic for spinel and rhombohedral for alumina) thermal expansion is the same for all crystallographic axes for spinel but different thermal expansions are observed in axes a and c for alumina. Therefore, from the value of spinel and the values of alumina (average, as well as in directions a and c), one can observe that the thermal expansion coefficient of alumina spinel brick (black curve) in the upper part of the curve (above 750 °C) is perfectly in between the values of the two major constitutive phases. In the low-temperature range (especially below 500 °C), the thermal expansion coefficient of alumina spinel brick becomes significantly smaller. This point will be discussed in more detail in section 4.1.4.

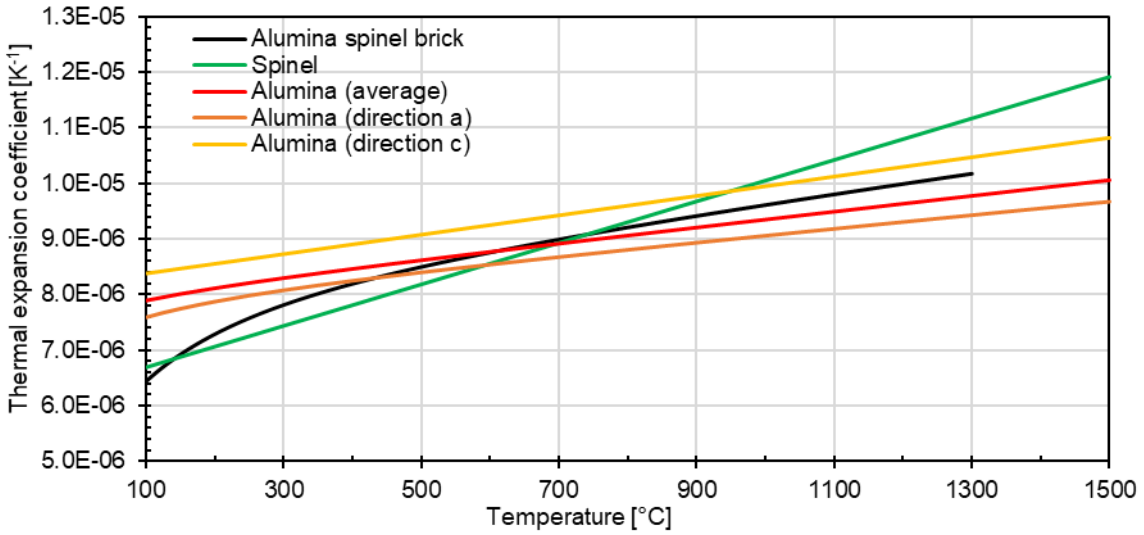

Figure 4-4. Evolution of thermal expansion coefficient for alumina spinel brick, as well as for crystals of alumina and spinel.[162,163]

4.1.3. Young's modulus evolution during thermal treatment

Figure 4-5 shows evolutions of Young's modulus and acoustic activity during the first thermal cycle. In order to facilitate the interpretation of these results, one should keep in mind that a stable material (with no microstructural changes, including

no phase transformations) normally exhibits a linear decrease of Young's modulus vs. temperature during heating which is completely reversible during cooling. In such case, no acoustic emissions should be detected (Figure 1-13a).

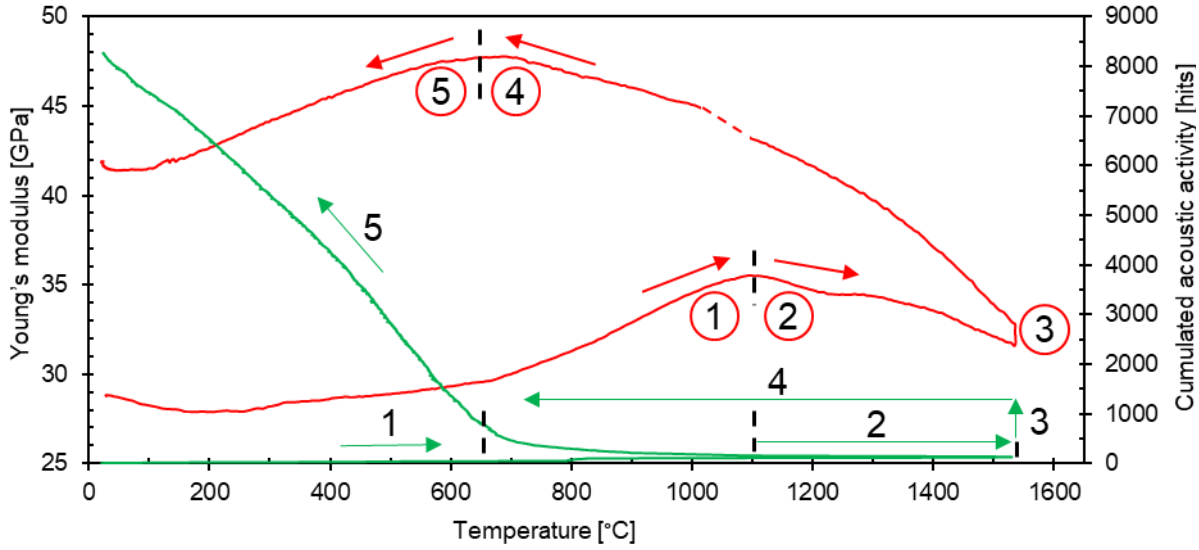

Figure 4-5. Young's modulus (red) and cumulated acoustic activity (green) evolutions during thermal treatment for alumina spinel brick.

Obviously, alumina spinel brick exhibits a complex evolution of Young's modulus, associated in some conditions with acoustic emissions. The results will thus be explained considering these significant deviations from the stable material. From this point of view, five different stages have been identified in Figure 4-5: two during heating (No. 1 and 2), one at dwell (No. 3) and two during cooling (No. 4 and 5). These different key stages of Young's modulus variations are summarized in Table 4-1 and will be explained in the following sections.

Table 4-1. Key stages of Young's modulus and acoustic emissions variations.

Stage	Temperature range [°C]	Young's modulus evolution	Acoustic emissions
1	Up to 1100	E↑↑	AE↑ (800-1100 °C)
2	1100-1500	E↓↓	-
3	1500 (dwell)	E ↑↑	-
4	1500-700	E↑↑↑	-
5	Below 700	E↓↓	AE↑↑↑

4.1.4. Microcracking in low-temperature range due to CTE mismatch

Evolutions of Young's modulus (see Figure 4-5), as well as acoustic activity (see Figure 4-5) and even CTE (see Figure 4-3) at low-temperature range (below 1100 °C) allow observing behaviour related to microcracking. In fact, during heating the microstructure of material expands, leading to the closure of microcracks, related to an increase of physical rather than chemical contacts within the microstructure. This microcracks closure is visible during heating by an increase of the CTE (below 500 °C), and then by an increase of Young's modulus (especially between 800 and 1100 °C). Moreover, during cooling (below 650 °C), one can observe relatively high acoustic activity (detection of microcracking), a decrease of Young's modulus (as a result of microstructure weakening), as well as a decrease of CTE. Taking into account the above-mentioned, alumina spinel brick obviously contains microcracks in the as-received state.

The origin of these microcracks can be related to CTE mismatch between different constitutive phases (alumina and spinel) or/and due to anisotropy of aggregates (alumina being rhombohedral). Considering the first potential reason, being related to the average CTE mismatch between alumina and spinel phases, one may state that there are some differences between the CTE of both phases (see Figure 4-5). Taking into account that the investigated material consists of an alumina spinel matrix and large white fused alumina aggregates, one can assume that, in a low-temperature range (below 700 °C), the CTE of the matrix is lower than the CTE of the alumina aggregates. This CTE mismatch could result in debonding of the aggregates at the end of the cooling stage.

The second potential reason for microcracking is related to thermal expansion anisotropy of large aggregates of white fused alumina, which are constituted of rather large single crystals (up to a few mm). Such a large size of single crystals can generate microcracks by thermal expansion anisotropy.[164] Even though the occurrence of microcracks is detectable by acoustic emission and ultrasonic devices, the degree of microcracking remains relatively low (low number of acoustic activity and low decrease in Young's modulus). Therefore, it is difficult to indicate the predominant mechanism for this particular case. Nevertheless, another study presented later in section 4.2.5 (comparison between two castables with sintered or fused alumina aggregates), indicates a high probability of the second option.

4.1.5. Brittle-ductile transition at about 1100 °C

In order to better understand what changes between the first and the second stage on Young's modulus evolution curve (see Figure 4-5), one decided to study mechanical behaviour at these two stages. For this reason, two types of tests were performed: a Brazilian creep test (to detect potential viscous behaviour) and a symmetric alternating loading test (to determine types of mechanical behaviours at given temperatures). Additionally, this part of the work also aims to provide stress-strain law in tension at different temperatures for the purpose related to FEM (or DEM) modelling. Thus, two tensile tests have been managed up to rupture, one at room temperature and one at 1200 °C.

4.1.5.1 *Brazilian creep test*

Brazilian creep tests were performed on the device introduced in section 3.1.2. However, in this case, no optical device was used because only vertical deformation vs. time was required and this data was easily accessible using the vertical displacement measured directly by the testing machine. It is worth noticing that this initial result is purely qualitative and is solely used to check whether there is a significant difference in mechanical behaviour between the two stages (see Figure 4-5).

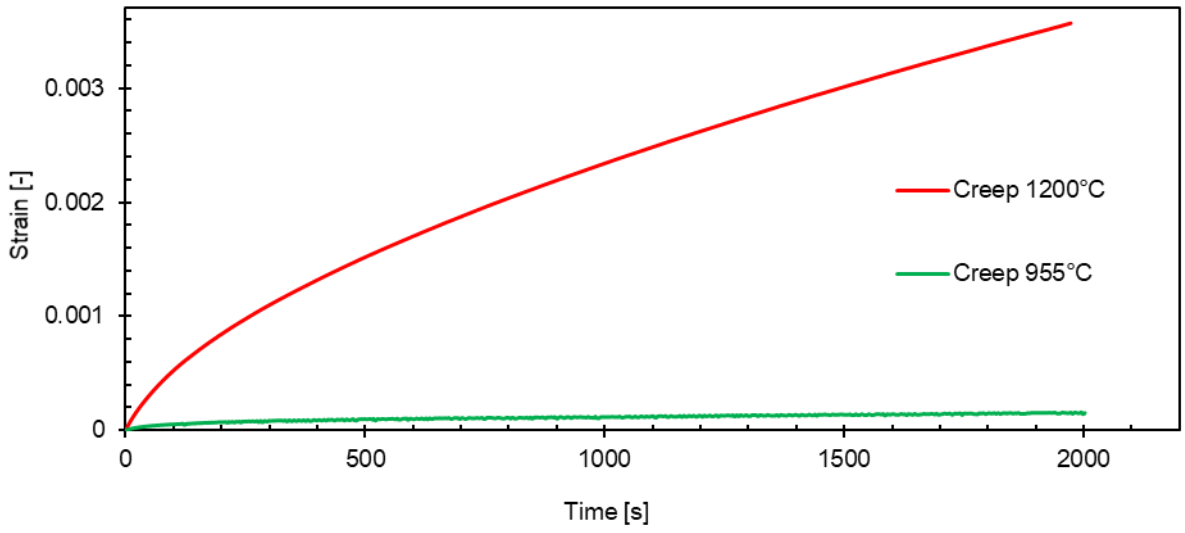

Figure 4-6. Results of the Brazilian creep test performed at 955 °C and 1200 °C.

This test was performed at the end of the 1st stage (at 955 °C) and at the beginning of the 2nd stage (at 1200 °C). Each one was preceded by heating with a constant rate of 5 °C/min. and by about 40 min. dwell. These Brazilian creep results,

as an evolution of vertical strain (calculated as the vertical displacement of the crosshead divided by the disc diameter) vs. time under the load of 2000 N (corresponding to the central tensile stress of σ_t ~ 2 MPa), are presented in Figure 4-6. One can observe a significant difference in creep behaviours determined at these two temperatures.

These very first qualitative results inspired further investigations, aiming to detect types of mechanical behaviour in uniaxial loading at different temperatures and to determine a more precise temperature at which the behaviour changes. This information has been obtained by the symmetric alternating loading test, as presented in the following section.

4.1.5.2 *Symmetric alternating loading test*

Figure 4-7 presents the results of the symmetric alternating loading test, carried out at several temperatures: 25 °C, 800 °C, 900 °C, 1000 °C, 1100 °C, 1200°C. It is worth noticing that a 40 min. dwell preceded each mechanical test in order to equilibrate temperature conditions. The results shown in Figure 4-7, allows detecting the elastic behaviour until 1000 °C which is represented by a linear and reversible stress-strain dependence with no hysteresis loop. Starting from 1100 °C, a small hysteresis loop can be noticed which translates with each cycle towards negative strain values (the loop and translations are more pronounced at 1200 °C). The presence of the hysteresis loop indicates the viscoelastic behaviour and the translation of this loop indicates plasticity. The conclusion can thus be made as follows: a decrease of Young's modulus at the second stage is related to the increase of viscoelastoplastic behaviour. The plasticity in alumina-rich spinels has also been reported by other authors and is explained by an enhanced mass transport due to the presence of cation vacancies.[64] The work of C. Baudin et al. at 1200 °C indicates that plastic behaviour related to defect rearrangement will lead to grain boundary sliding and microcracks formation at low loading rates.[63]

In conclusion, the decrease of Young's modulus during heating on the 2nd stage of the E(T) curve (see Figure 4-5) can be explained as an increase of viscous behaviour of alumina rich spinel. In the same way, this phenomenon could also explain the increase of Young's modulus during cooling on the 4th stage.

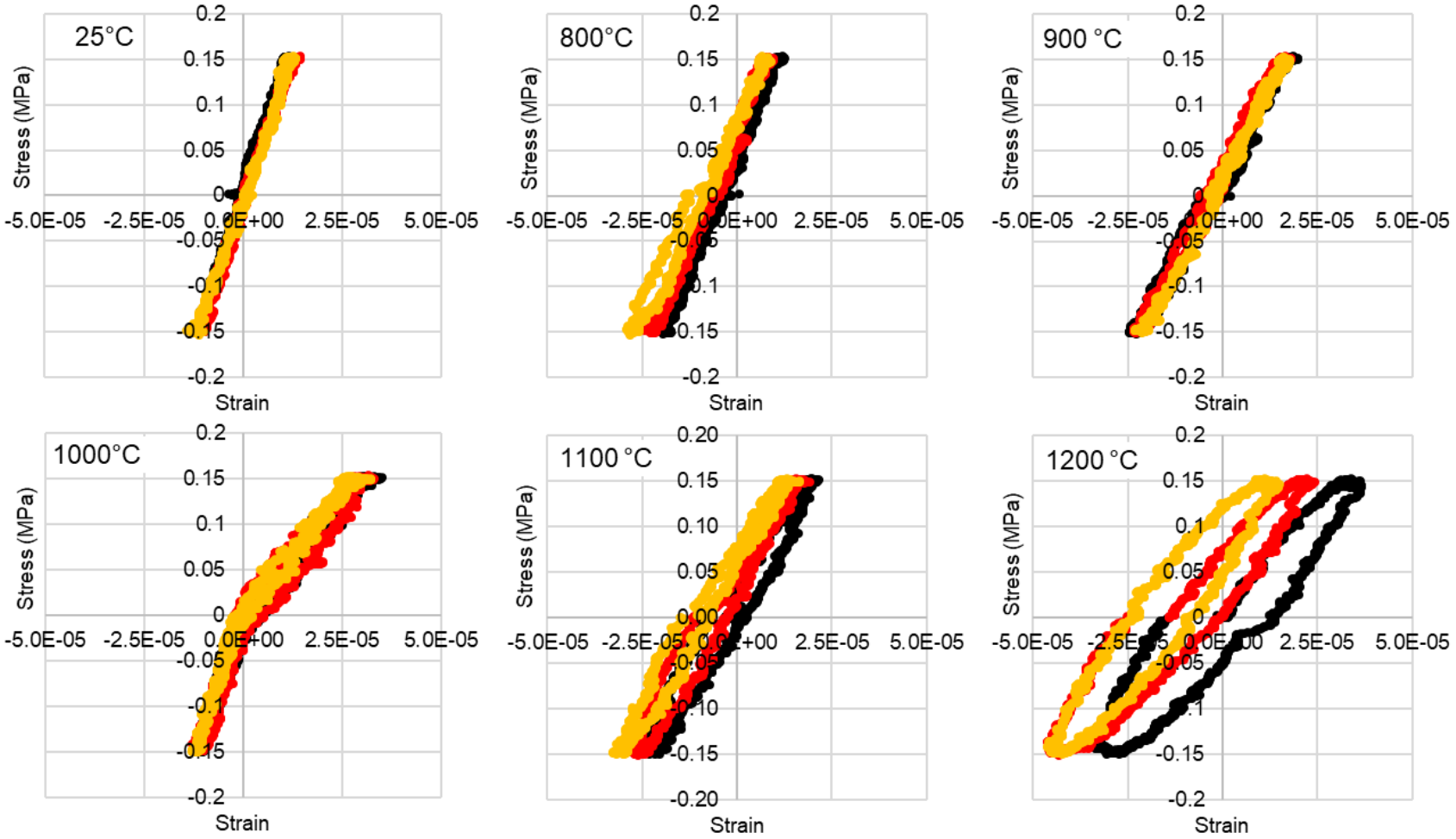

Figure 4-7. Stress-strain curves for symmetric alternate loading tests (tension and compression) performed at different temperatures on alumina spinel brick.

4.1.5.3 *Tensile loading tests*

Incremental tensile loading tests were performed at 20 and 1200 °C and are presented in Figure 4-8. The test performed at 20 °C (see Figure 4-8a and b) shows a non-linear behaviour, where the sample fracture is firstly preceded by few elastic cycles with rather low damage (low strain increase) and then secondly undergoes several loading cycles where strain increase indicates progressive damage (high strain increase). In refractories, such nonlinear behaviour before reaching maximum stress at room temperature usually comes from initial microcracking resulting from material processing which promotes further diffused damage during loading. This significant increase of strain before reaching the maximum stress indicates that the material is able to behave non-linearly, by accumulating some damage and maintaining a significant level of strength. Despite this slight nonlinearity, damage starts to localise at a low strain level of $1.8 \cdot 10^{-4}$, then the sample reaches the maximal tensile strength of 1.57 MPa (at the strain of $2.6 \cdot 10^{-4}$) after which the final rupture occurs. After this maximum, the post-peak behaviour is rather limited and the fracture takes place in a very short time which does not allow to record many points on this part of the curve (after the strain of about $4 \cdot 10^{-4}$).

Concerning the test performed at 1200 °C, one should notice that in order to save time, this test was carried out after symmetric alternate loading tests, where the sample was subjected to several loading cycles with very low stress (0.15 MPa - see Figure 4-7). Due to the character of the preceding tests, this tensile test result is considered not much affected by this loading history. From Figure 4-8b and c, one can notice an extensive nonlinear behaviour leading to high sample deformation. In this temperature range, exhibited strain during loading cycles could be attributed to both damage and plastic deformation within the microstructure. Taking into account the permanent strain after each cycle, plasticity becomes most-probably dominant mechanism at 1200 °C. The three first cycles lead to the observation of the maximum value of sustained stress of 0.96 MPa after which a large post-peak behaviour is observed. During this post-peak part of the curve, it is worth noticing that the increase of strain did not lead to a dramatic decrease of stress level, but rather to a slow decrease of it over the long deformation (strain of about $30 \cdot 10^{-4}$ during the 10^{th} cycle). This behaviour (strain to rupture about 8 times higher than at ambient temperature) is very advantageous for high-temperature applications, as the applied

materials can slightly deform (e.g. during handling by crane) while maintaining their strength.

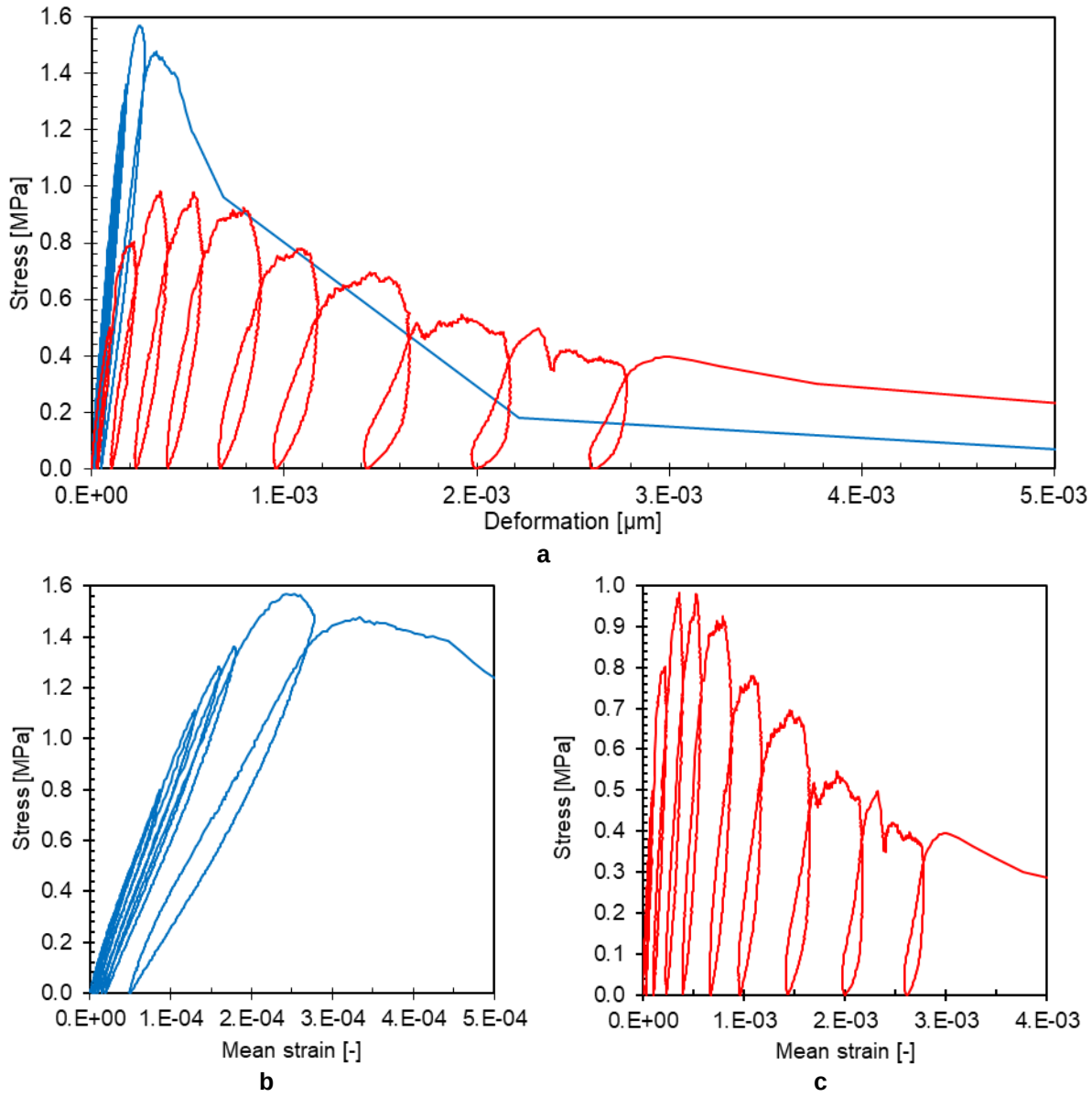

Figure 4-8. Tensile test results performed at: a) 20 °C, b) 1200 °C (this test was performed after symmetric alternating loading test presented in Figure 4-7).

4.1.6. Change of spinel content and stoichiometry at high temperature

This section is dedicated to description of microstructural changes caused by the thermal treatment with 1h dwell at 1500 °C. The X-ray diffractograms (acquired at ambient temperature) were acquired before and after the thermal treatment and are presented in Figure 4-9. It can be observed that the same types of phases are present in two cases.

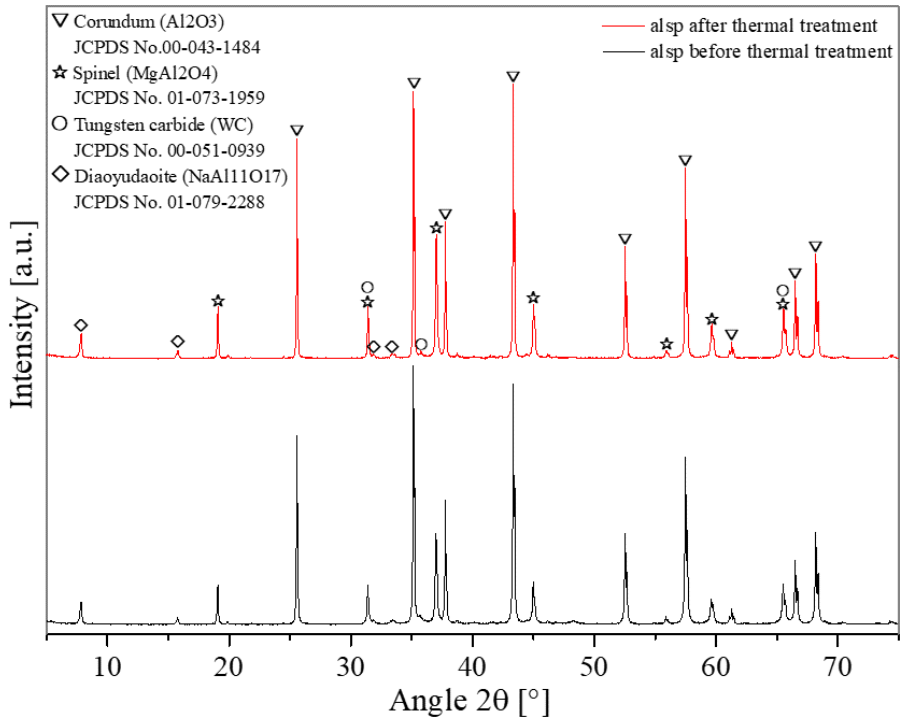

Figure 4-9. X-ray diagrams of alumina spinel refractory before and after thermal treatment.

The quantified results obtained by Rietveld refinement of these diffractograms (presented in Table 4-2) allowed detecting some interesting differences. First of all, one can observe that this thermal treatment led to an increase of spinel content and to a decrease of alumina content of about 5 wt. %. Moreover, the spinel's lattice parameter, related to spinel's stoichiometry, decreases by about 0.009 Å, which corresponds to the alumina enrichment of spinel of about 1-2 wt. % (assuming a linear dependence between alumina content and lattice constant, indicated by the black curve from Figure 1-6). Even though material processing includes a firing stage (typically at temperature higher than 1500 °C), the present result demonstrates that some microstructural changes could occur at lower temperatures. As indicated by the alumina-magnesia phase diagram (see Figure 1-5), spinel stoichiometry is strongly dependent on temperature in the range of 1000-2000 °C. Thus, probably due to a low cooling rate in the industrial sintering cycle, spinel contains between 76-77 wt. % of alumina (slightly alumina-rich spinel) in the as-received state, which means that it is in equilibrium at a temperature between 1300-1400 °C. When kept in laboratory furnace at 1500 °C for 1h, and cooled down (with a rate of 3 °C/min.) an enrichment in alumina of this spinel could be observed up to 77-78 wt. %.

Table 4-2. Quantitative comparison of phase contents before and after thermal treatment.

Crystalline phase	Before thermal treatment	After thermal treatment	Difference
	[Weight %]		
Corundum (Al_2O_3)	77.4	72.3	-5.1
Spinel ($MgAl_2O_4$)	22.0	27.3	5.3
Diaoyudaoite ($NaAl_{11}O_{17}$)	0.4	0.4	0.0
Tungsten carbide (WC)	0.3	0.1	-0.2
Spinel's lattice parameter [Å]	8.056	8.047	-0.009

The potential explanation of observed microstructural changes is as follows. The material treated at 1500 °C is not in equilibrium what leads to an interaction between alumina and spinel phases (temperature-dependent equilibrium for spinel stoichiometry), which consists in counterdiffusion of Al^{3+} and Mg^{2+} cations between alumina and spinel phases (see Figure 4-10). This results in an increase of spinel content, with simultaneous alumina enrichment of spinel.

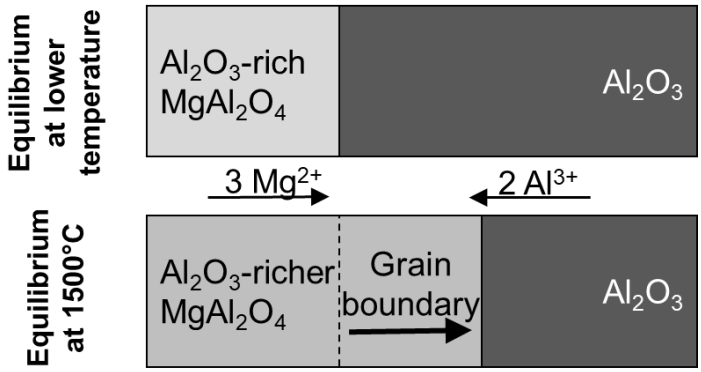

Figure 4-10. Wagner's mechanism adapted to the tested case.

The expansive increase of spinel content above 1300 °C (detected increase of linear expansion rate - see Figure 4-3) is related to the differences between the densities of alumina (3.99 g/cm^3) and spinel (3.58 g/cm^3).

4.1.7. Conclusions

This part of the study provided better understanding of thermomechanical behaviour of industrial alumina spinel bricks that have been proven successful in application conditions. Additionally, the present study provided accurate input data for FE modelling performed by several PhD students from ATHOR project. Even if these materials are already used for a couple of years at an industrial partner, the present work allowed to highlight interesting changes that (to our best knowledge) were not available in the literature. The most interesting features include microcracking

(during cooling after sintering), brittle-ductile transition (around 1100 °C), evolution of spinel content and stoichiometry during thermal treatment.

Microcracking, detected below 650 °C (during cooling), has been attributed to thermal expansion anisotropy of white fused alumina aggregates. **Brittle-ductile transition** has been detected around 1100 °C thanks to symmetric alternating test at very low stress and strain levels. **The evolution of spinel content and stoichiometry** has been discovered using XRD, dilatometry and Young's modulus evolution curves. Observations above 1300 °C indicate that the interaction between alumina and spinel occurred, leading to an increase of spinel content (with simultaneous decrease of alumina content) of about 5 wt.%. Moreover, spinel's stoichiometry change indicated that thermal treatment increased alumina content within spinel by about 1-2 wt. %.

One could state that microcracks formation (during cooling after sintering) could have beneficial effect on thermal shock resistance during preheating and the first filling of the ladle. An increase of volume thanks to irreversible thermal expansion, observed above 1300 °C, most likely have a positive impact on closure of joints between bricks. Temperature-dependent stoichiometry of spinel could have potentially positive impact on cracks healing, as counter-diffusion between these two phases is driven by this temperature-dependent change of equilibrium.

4-2. Case of model alumina spinel castables

The study presented in this section is focused on investigation of several model alumina spinel castables in order to **determine potential influence of different types of compounds on thermomechanical behaviour of these castables**. Investigated compounds include two types of cements, three types of reactive aluminas and two types of aggregates. In some cases, impact of compounds on thermomechanical properties is not yet well-understood by scientific community. Therefore, there is a need to improve knowledge on this topic by providing explanation, which could be relevant regarding potential performance of the castables under given thermomechanical conditions.

4.2.1. Presentation of investigated model alumina spinel castables

Even if alumina spinel bricks were used for a couple of years at an industrial partner, alumina spinel castables constitute another option for wear lining of steel ladles.[49] Thus, model alumina spinel castables have been specially designed for ATHOR project in order to manage some investigations on these alternative refractory materials for steel ladle. The recipes of these model castables have been based on minerals coming from Imerys (cement and alumina aggregate), Almatis (spinel) and Alteo (fine alumina). Detailed compositions of these model castables are summarized in Table 4-3. The objectives of these investigations were to compare influence of different types of cements (see compositions 1 & 2), aggregates (see compositions 3 & 6) and reactive aluminas (see compositions 3, 4 & 5) on thermomechanical behaviour.

Comparison of the commonly used classical CAC and the novel CMA cement is worth studying, as the CMA is a relatively novel formulation with enormous potential for improved corrosion resistance thanks to its fine spinel content. However, until now (according to the author's best knowledge) there are just a few studies on microstructural and thermomechanical characterization of castables based on this CMA cement.

There is also an interest in the comparison between TA or WFA aggregates, as due to their specific properties (described in section 1.2.4.6), they may lead to significantly different thermomechanical behaviour.

Table 4-3. Compositions of model alumina spinel castables.

Raw materials	Grain size/Type	Model number / Reference / Composition [wt. %]					
		1	2	3	4	5	6
		12S6CMA-T-A	12S6CAC-T-A	6S12CMA-T-A	6S12CMA-T-B	6S12CMA-T-C	6S12CMA-W-A
Aggregate: Tabular Alumina (TA)	6-3 mm	23	23	23	23	23	-
	3-1 mm	10	10	10	10	10	-
	1-0.5 mm	19	19	19	19	19	-
	0.5-0.0 mm	24	24	24	24	24	-
Aggregate: White Fused Alumina (WFA)	6-3 mm	-	-	-	-	-	23
	3-1 mm	-	-	-	-	-	10
	1-0.5 mm	-	-	-	-	-	19
	0.5-0.0 mm	-	-	-	-	-	24
Calcined Alumina	d_{50}=5µm	2	2	2	2	2	2
Type of Bimodal Reactive Alumina	A	3	3	3	-	-	3
	B	-	-	-	3	-	-
	C	-	-	-	-	3	-
AR78 Spinel	< 45 µm	5	5	-	-	-	-
	< 20 µm	7	7	6	6	6	6
Type of Cement	CMA	6	-	12	12	12	12
	CAC	-	6	-	-	-	-
Dispersing Additive	-	1	1	1	1	1	1
		Contents of selected components [wt. %]					
Total CaO	-	0.6	1.8	1.2	1.2	1.2	1.2
Spinel as AR78	Added as AR78	12	12	6	6	6	6
Spinel from CMA	From CMA	4.2	0	8.4	8.4	8.4	8.4
Total spinel	Total amount	16.2	12	14.4	14.4	14.4	14.4
Water	Batch I	3.10	3.30	3.46	3.49	3.90	3.90
	Batch II	3.57	3.43	3.26	3.29	3.48	5.57

The impact of reactive aluminas are also worth understanding, as being fine and well distributed within the microstructure, they can play a crucial role especially when tested at high temperatures. Table 4-4 details characteristics of the three types of bimodal reactive aluminas that have been considered here. Particular attention has been paid to different particle size distribution (see types A and B), as well as to different content of impurities (see types A and C), such as silica and soda (which could both negatively impact mechanical properties at high temperature). It can be observed, that when the quantity of soda is reduced, the amount of silica increases. This is very typical, because the soda-purification process consists in high-temperature thermal treatment of alumina hydroxide with quartz (leaving some traces after this process).[165]

Table 4-4. Characteristics of the three bimodal reactive aluminas used in model castables.

Type	Soda level	Silica level	Fines proportion	D_{10} [µm]	D_{50} [µm]	D_{90} [µm]
A	500 ppm (low)	700 ppm (high)	Medium	0.4	2.5	4.8
B	500 ppm (low)	700 ppm (high)	High	0.2	1.4	4.5
C	2300 ppm (high)	130 ppm (low)	Medium	0.4	2.5	4.8

A notation used during the investigation of model castables is presented in Figure 4-11. It contains information on the content of the preformed spinel, the type and content of cement, as well as the types of alumina aggregate and reactive alumina.

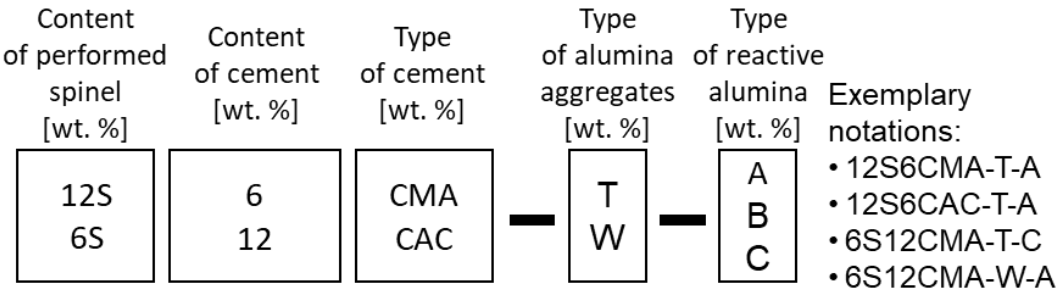

Figure 4-11. The notation used to identify castable formulations.

All these model castables have been processed (mixing, casting, curing, drying) at Saint-Gobain Research Provence in a dedicated room with a controlled temperature of 23 °C and humidity of 50 % H_2O. For each composition, all raw materials were mixed in a VMI mixer in the following sequence: mixing of dry components for 1 min., water addition, mixing with water for 5 min. Subsequently, materials were cast into PVC moulds (23x11.5x6 cm^3). After 24 hours, castables were demoulded and left for another 24h (total curing of 48h) in the climatic room. In the end, the castables were dried at 110 °C to ensure conversion of hydrates to C_3AH_6 and AH_3 products.

4.2.2. Thermomechanical behaviour of the reference material

The present section is dedicated to a detailed description of the reference material. This approach will facilitate reading the next sections of this chapter by focusing only on the key differences exhibited by the other materials.

The selected reference material is 12S6CMA-T-A. Figure 4-12 shows Young's modulus evolution during the first three heating cycles. As it can be observed, the major microstructural changes, related to Young's modulus evolution, occur during the first heating cycle. Then, during the two subsequent cycles, the microstructure seems to be relatively stable. Therefore, one would mainly focus on Young's modulus

evolution during the first heating cycle. Considering the trend of Young's modulus evolution, the curve can be divided into 6 regions. Table 4-5 presents the most probable microstructural changes and predominant causes explaining the evolution of Young's modulus for each stage.

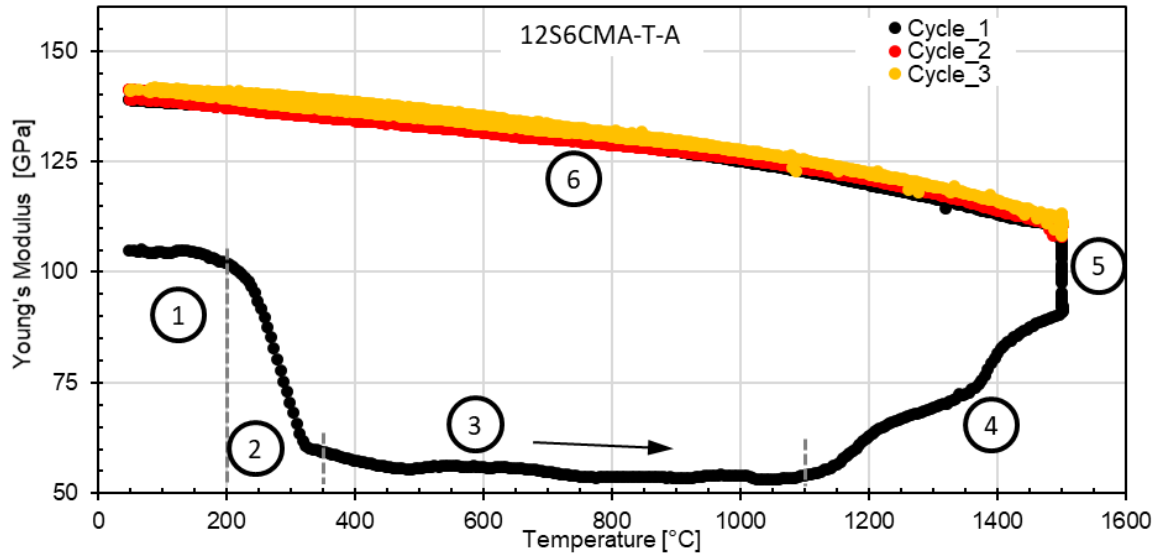

Figure 4-12. Young's modulus evolution curve for 12S6CMA-T-A (obtained by RFDA).

At the first stage, Young's modulus is relatively stable. At the second one, it decreases significantly. In this context, it is interesting to compare the evolution of Young's modulus and dilatometry measurements of a similar type of castable and its matrix from the PhD study of Jean-Michel Auvray (see Figure 4-13).[166] One can observe that the drop of Young's modulus (see Figure 4-13a) correlates with significant shrinkage of the matrix (see Figure 4-13b). However, the castable does not shrink much (see Figure 4-13b). In this temperature range, dehydration induces contraction of the matrix thus forming microcracks at the interface between matrix and aggregates.[166]

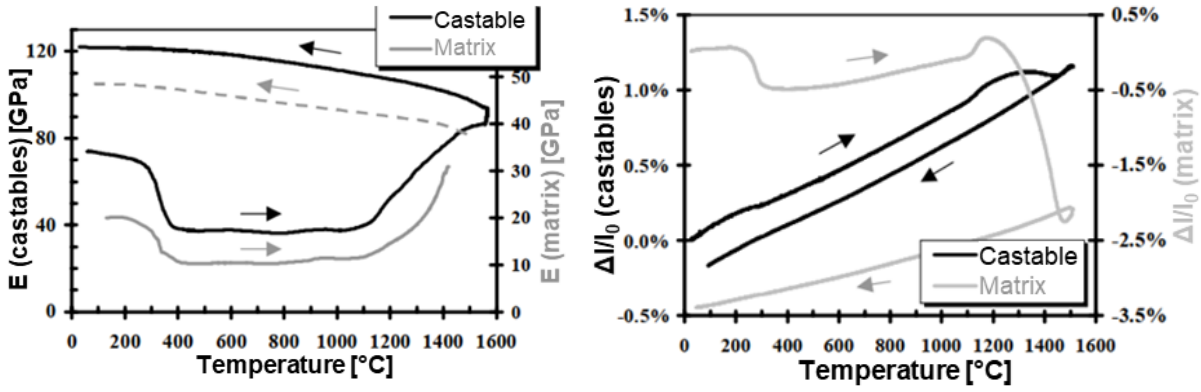

a b

Figure 4-13. Thermomechanical behaviour of alumina spinel castable R14T66S12 and its matrix: a) Young's modulus evolution with temperature, b) dilatometry.[166]

At the third stage, Young's modulus is relatively stable. The fourth and fifth stages exhibit a general upward trend. On microstructural level in this temperature range, one expects densification caused by sintering of the matrix above 1200 °C (see Figure 4-13b), formation of CA_2, CA_6, as well as potential modifications of spinel stoichiometry. Densification and formation of these phases strengthen microstructure (especially CA_6) most likely leading to an increase of Young's modulus. At the sixth step (during cooling), Young's modulus continuously increases without any major change of trend, which indicates a relatively stable microstructure. It is worth pointing-out, that the inclined E(T) dependency (observed during cooling of the first cycle, as well as during the second and third cycle) is typical for materials having stable microstructure, such as alumina.

Table 4-5. Microstructural changes and causes of Young's modulus variations attributed to each stage.

Stage	Temperature range [°C]	Young's modulus evolution	Microstructural changes	Predominant cause of Young's modulus change
1	30-200	(E stable)	-	-
2	200-350	(E↓↓↓)	Dehydration reactions	Contraction of matrix leads to formation of microcracks at the interface between matrix and aggregates
3	350-1100	(E stable)	Recrystallization of CA	-
4	1100-1500	(E↑↑↑)	Formation of CA_2 and CA_6,* as well as change of spinel stoichiometry	Densification/sintering and formation of phases which strengthen microstructure
5	1500 (dwell)	(E↑↑↑)		
6	1500-30	(E↑)	Stable microstructure	Typical tendency resulting from atomic vibrations (temperature-related)

4.2.3. Comparison of castables with CMA or CAC cement

Since the spinel has been introduced to castables both directly in preformed form and indirectly as a constituent phase of CMA cement, it is interesting to perform XRD measurements with Rietveld refinement in order to detect potential changes and temperature-induced microstructural evolutions. This technique has been used to characterize castables at ambient temperature (before and after thermal treatment), as well as at high temperature (during thermal treatment).

Ambient-temperature XRD tests were performed on castables in two states: after drying at 110 °C (before thermal treatment) or after firing at 1500 °C (after thermal treatment with heating/cooling rate of 5 °C/min and 1h dwell at maximal temperature).

Table 4-6 reports lattice constants of spinels, present in model castables, in the two states (dried - before thermal treatment; fired - after thermal treatment). Since the "2nd spinel" was absent only in the X-ray diffractograms of castable 12S6CAC-T-A (which was the only one that did not contain CMA cement), one can assume that this "2nd spinel" corresponds to the one indirectly added with the CMA cement and the "1st spinel" corresponds to the one directly added in the preformed form to the formulation of castables. Once the spinel types are identified, one can estimate their stoichiometry (alumina content) based on values of lattice constants (see section 1.2.2). Just after drying at 110 °C, the spinel added in preformed form and the one included in the CMA cement, have a lattice constant in the range of 8.053-8.056 Å and 8.086-8.087 Å, respectively. Based on an additional measurement of the industrial AR78 spinel powder (alumina-rich spinel with 78 wt. % of alumina), having a lattice constant of 8.054 Å (see Figure 1-6), and values coming from literature[40–42], the preformed spinel (1st spinel) can be classified as alumina-rich with 78 wt. % of alumina. The 2nd type of spinel, from the CMA cement, seems to be close to stoichiometric form. However, it is difficult to state its stoichiometry solely based on lattice constant, since literature results present quite similar lattice parameters both for stoichiometric and for magnesia-rich compositions (see section 1.2.2).

Another interesting observation is related to the change of lattice constant during firing. Figure 4-14 presents the evolution of selected spinel peaks of these two types of spinel during thermal treatment between 900 and 1500 °C (measured by high-temperature XRD). One can observe, both from this figure (peaks merge) and from Table 4-6 that after firing only one type of magnesium aluminate spinel can be detected what makes it difficult to distinguish spinel peaks depending on their origin. The spinel, originating from the CMA cement, becomes alumina-richer increasing from 72 wt. % to 75-77 wt. % (depending on assumed relation between lattice constant and spinel stoichiometry) and the stoichiometry of directly added spinel decreases from 78 wt. % to 77 wt. %. According to Figure 4-14, these changes of stoichiometry mainly occur above 1100 °C and from 1300 °C a single spinel peak can be observed.

Table 4-6. Lattice constants of the 1st (preformed form) and the 2nd (constitutive phase of CMA cement) types of spinel after drying (at 110 °C) or after firing (at 1500 °C).

	12S6CMA-T-A		12S6CAC-T-A		6S12CMA-T-A		6S12CMA-T-B		6S12CMA-T-C		6S12CMA-W-A	
	Dried	Fired	Dried	Fired	Dried	Fired	Dried	Fired	Dried	Fired	Dried	Fired
Lattice constant of the 1st spinel [Å]	8.053	8.052	8.054	8.061	8.056	8.059	8.056	8.061	8.056	8.060	8.056	8.060
Lattice constant of the 2nd spinel [Å]	8.086		-		8.087		8.087		8.087		8.086	

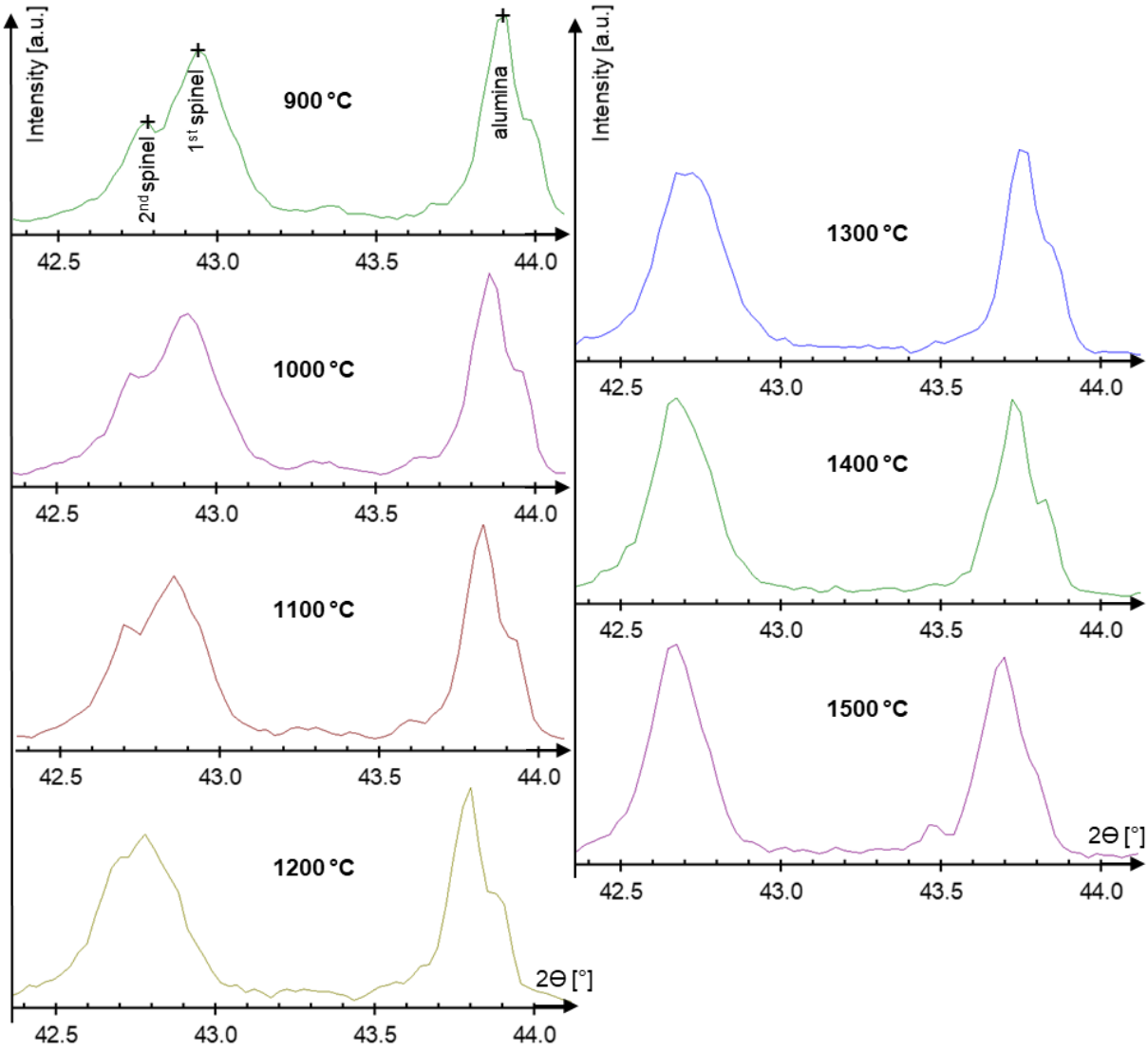

Figure 4-14. High-temperature X-ray diffraction diagram in the 2Θ angle range of 42.4-44.1 ° aiming to compare an alumina peak from two spinel peaks for 12S6CMA-W-A castable.

Comparing the Refractoriness Under Load (RUL) curves from Figure 4-16a, one can observe that these two model castables, containing different types of cement, exhibit rather similar behaviour up to 1400 °C (similar T_0 values in Table 4-7). The contraction occurring from about 1250 °C can be attributed to sintering

of the matrix (leading to shrinkage of the matrix - see Figure 4-13b) and/or formation of a liquid phase (probably related to sodium impurities).[95,166] However, the expansive peak from 1450 °C is more pronounced in the case of the CAC-containing material, in comparison to the CMA-containing one. This difference is most likely linked to the expansive formation of CA_6, which is more pronounced in CAC-containing castables due to three times higher CaO content. Creep In Compression (CIC) curves, presented in Figure 4-15b, show slightly better resistance to creep at 1600 °C in the case of the sample containing CAC (see the creep rate estimated between 3rd and 4th hour of dwell from Table 4-7). Better performance of CAC-containing cement is probably also related to the higher content of CA_6 phase (due to three times higher CaO content), which exhibits relatively good high temperature properties.

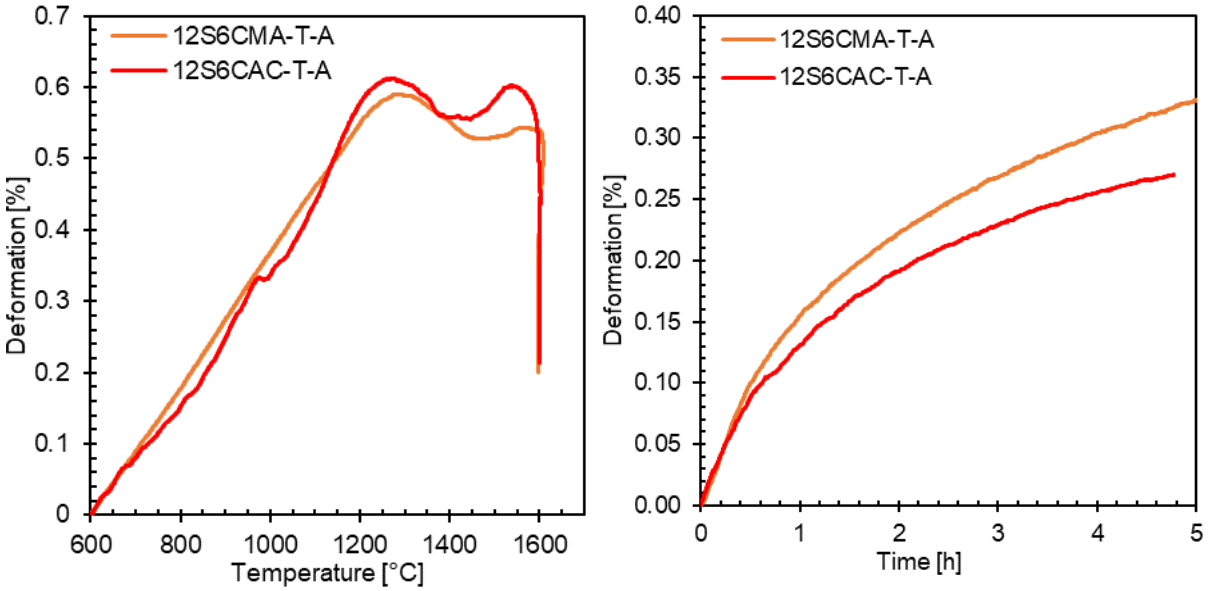

Figure 4-16. Comparison of high temperature mechanical behaviour between castables containing CMA or CAC: a) RUL, b) CIC at 1600 °C.

Table 4-7. Selected RUL and CIC parameters for model castables containing CMA or CAC.

Castable type	Temperature at maximal expansion T_0 [°C]	Creep rate between 3rd and 4th hour of dwell at 1600 °C [%/h]
12S6CMA-T-A	1279	0.0366
12S6CAC-T-A	1274	0.0264

Figure 4-17 shows the Young's modulus evolution curves during three first thermal treatments of the castables containing CMA or CAC cements. The highest differences in Young's modulus evolution can be observed during the first heating cycle. The initial value of Young's modulus, present at the first stage, is higher

for the CAC-containing castable, due to much higher content of calcium aluminate phases, which are able to react with water and form hydraulic bonds. In contrast, spinel present in CMA, due to resistance to water dissolution, may limit the improvement of material strength during curing, thus leading to lower initial stiffness. At the second stage, a higher drop of Young's modulus occurs for CMA cement. It may be linked to a higher shrinkage of the CMA-containing matrix, which could be reasonable due to the presence of very fine spinel grains within CMA particles. However, in order to be sure, complementary measurements should have been performed (not managed due to the lack of time), such as dilatometry of the fines only.

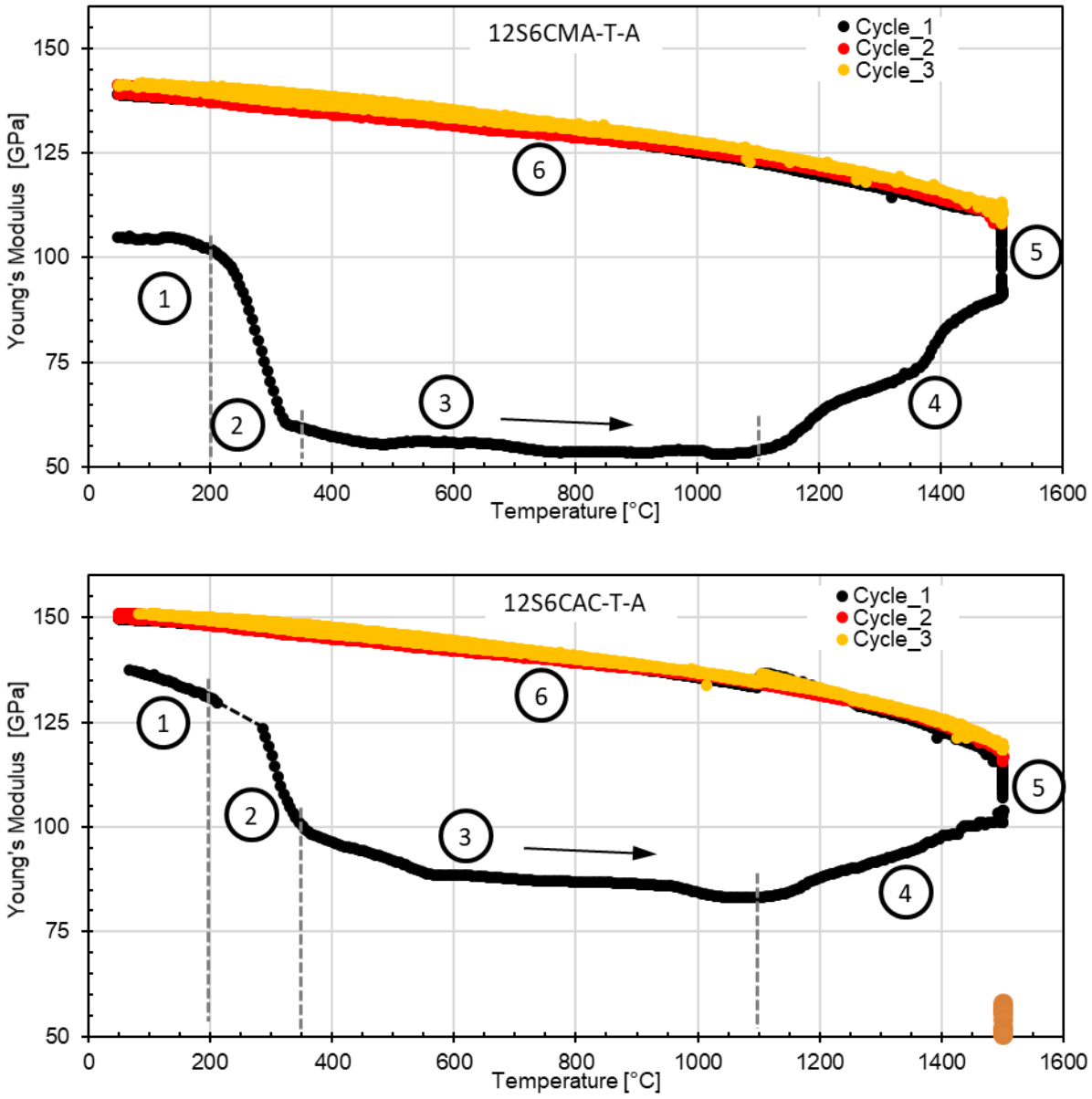

Figure 4-17. Young's modulus evolution with temperature for castables with different types of cement: a) CMA, b) CAC. Applied thermal treatment includes three thermal cycles with a heating/cooling rate of 5 °C/min and 1h dwell at max. temp. of 1500 °C.

At stage 3, Young's modulus is relatively stable. Then, during the 4th and 5th stages, an upward trend occurs. This increase is more pronounced in the case of the CMA-containing castable. The higher increase of Young's modulus in this material is most likely due to chemical interaction of fine spinel from the CMA cement with surrounding microstructure - both with alumina (leading to alumina enrichment of spinel) and with CAx phases (potentially resulting in the formation of CA_6 through the intermediate CMA phases). During cooling (6th stage) microstructure seems to be stable and, at ambient temperature, reaches in both cases rather similar values of Young's modulus.

Figure 4-18 shows the microstructure of two castables, containing CMA or CAC cement, after three thermal treatments (heating/cooling rate of 5 °C/min, 1h dwell at max. temp. of 1500 °C). Presented parts of microstructure allow observing the impact of cement type on evolution of microstructure. It seems that the CMA particle (see Figure 4-18a) after three heating cycles is better integrated with the microstructure than the CAC particle (see Figure 4-18b), which in this particular case is surrounded by a porosity. This porosity could be related to the water dissolution process: just after casting - water dissolves the cement particle gradually and the recrystallization of hydrates could take place in another area. In contrary, CMA particles could maintain initial volume thanks to the presence of MA skeleton, which does not dissolve (see the schema of cement particles from Figure 1-8).

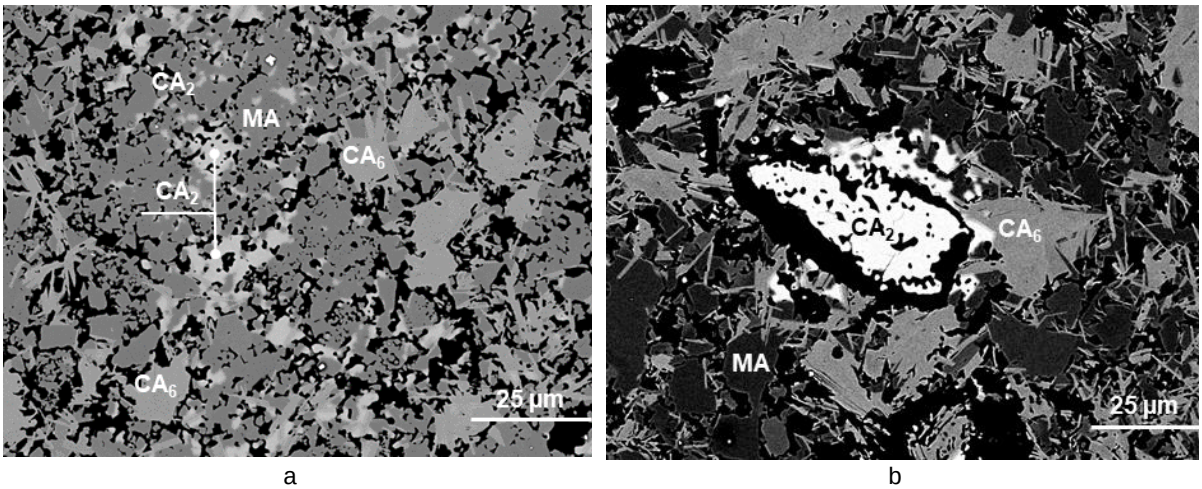

a b

Figure 4-18. SEM image showing microstructures of two castables after three thermal treatments (up to 1500 °C with 1h dwell at each time) which contain different cement particles: a) 12S6CMA-T-A castable (with CMA cement), b) 12S6CAC-T-A castable (with CAC cement).

4.2.4. Comparison of castables containing different reactive alumina

Reactive alumina, being a part of castable matrix, has a significant impact on numerous castable properties, including hot mechanical properties. This section is dedicated to a comparison of the three types of investigated reactive aluminas whose characteristics are presented in Table 4-4. The main differences between them are related to different contents of impurities (soda and silica), as well as to different contents of fines. Both type A and type B reactive aluminas have reduced soda content (related to a slight increase of silica content which is used in the soda purification process). Type A has a regular content of fines, while type B has a relatively high content of fines. Type C reactive alumina has a regular content of fines and relatively high level of soda, as it did not undergo the purification process.

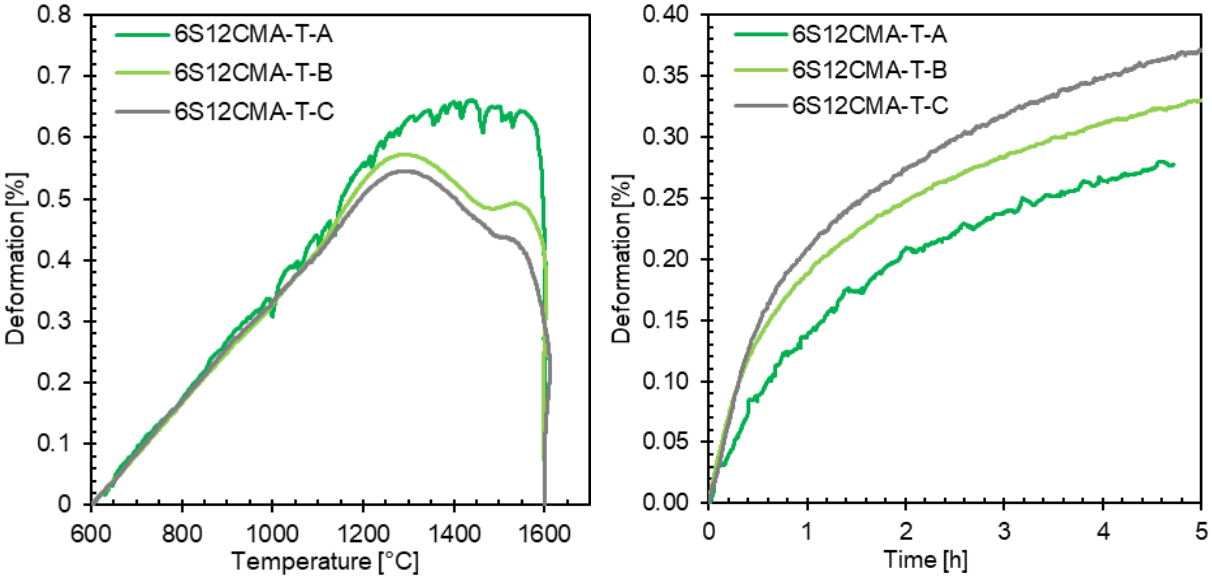

Figure 4-19. Experimental results for castables containing different types of reactive alumina: a) RUL, b) CIC.

RUL curves of the castables containing different types of reactive alumina unveil significant differences at high temperatures (see Figure 4-19a). First of all, the castable with A-type reactive alumina does not exhibit contraction above 1300 °C, contrary to the castables containing B- or C-types of reactive alumina, and it has thus a higher T_0 value (see Table 4-8). The behaviour of castable containing B-type reactive alumina, is intermediate between the two others. In the same way, creep in compression (see Figure 4-19b) for castable with A-type reactive alumina is significantly lower than the one containing C-type. Again, the behaviour of castable containing B-type reactive alumina is intermediate between the two others. This classification could also

be observed through the creep rates estimated between 3rd and 4th hour of dwell and presented in Table 4-8. This superior performance during CIC tests of castables with type A or B reactive aluminas is most likely related to the reduction of soda content, which is not the case for C-type. In addition, the lower refractoriness and higher creep of castables containing B- (in comparison to A-) type is related to a higher content of fines.

Table 4-8. Selected RUL and CIC parameters for castables containing different types of reactive alumina.

Castable type	Temperature at maximal expansion T_0 [°C]	Creep rate between 3rd and 4th hour of dwell at 1600 °C [%/h]
6S12CMA-T-A	1435	0.0262
6S12CMA-T-B	1288	0.0273
6S12CMA-T-C	1289	0.0305

Even if these results could appear quite logical (with the presence of soda and the grain size of the investigated reactive alumina), it would have been preferable to check the experimental reproducibility. In fact, RUL and CIC curves presented here were obtained using different devices and therefore, one cannot exclude the impact of experimental setup on these results.

In a similar way to the other castables, Young's modulus evolutions have been monitored during three thermal cycles up to 1500 °C and the results show rather similar behaviour for the three castables with different types of reactive aluminas (see Figure 4-20). The visible of Young's modulus is most likely related to a slightly higher water content added to this castable (see water addition to Batch I indicated in Table 4-3). The higher is water content, the higher is material porosity and the lower is the material's stiffness.

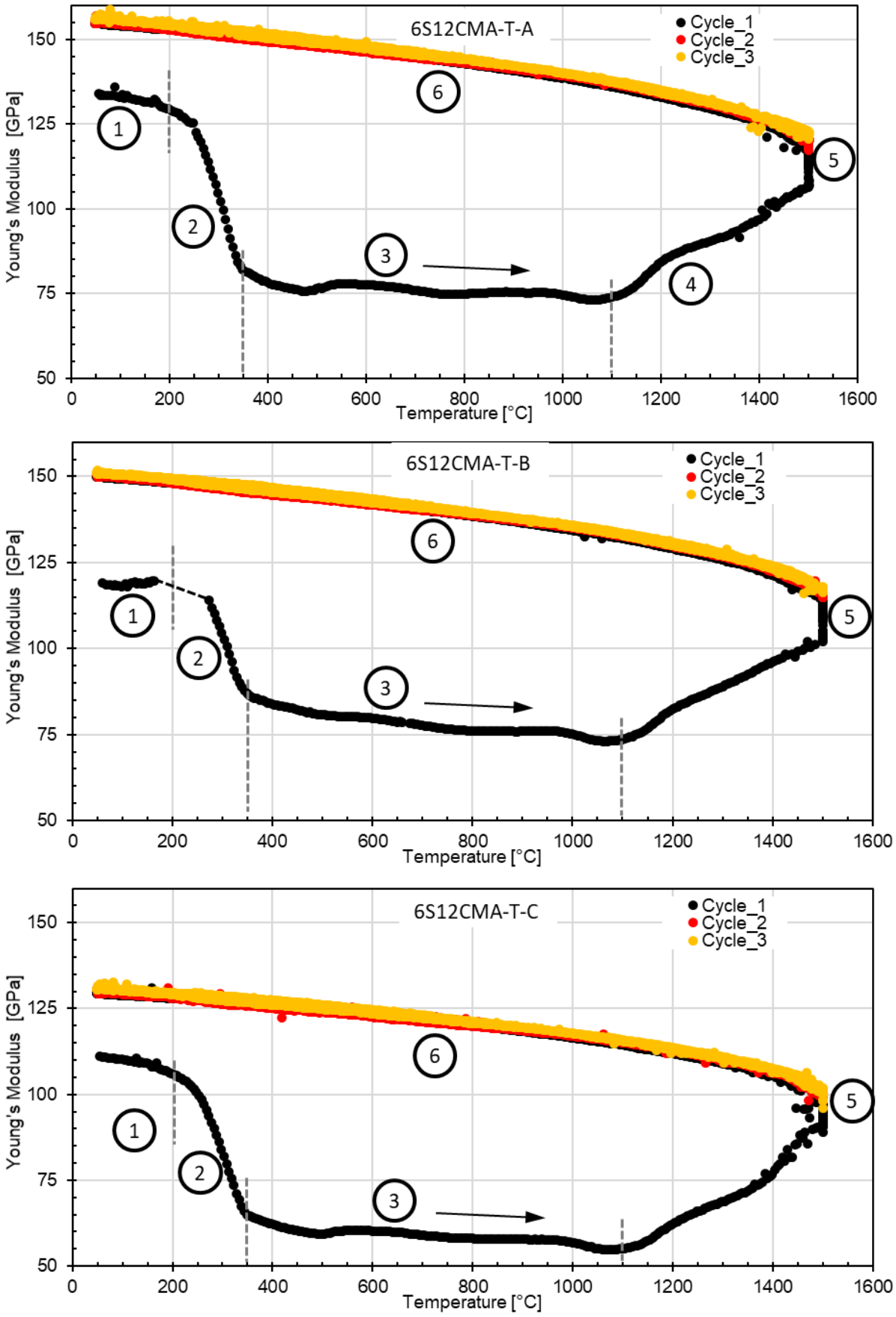

Figure 4-20. Young's modulus evolution with temperature for castables with different types of reactive alumina.

4.2.5. Comparison of castables containing TA and WFA aggregates

Tabular Alumina (TA) and White Fused Alumina (WFA) aggregates have been introduced in section 1.2.4.6 and the key differences between them have already been indicated. The type of alumina aggregates added to alumina spinel castables could have significant impact on many castable properties. In order to identify these potential impacts, TA-containing and WFA-containing castables will be compared in this section.

RUL curves of the castables, containing TA or WFA aggregates, are presented in Figure 4-21. One could observe that softening of material containing TA starts at 1300 °C, in comparison to 1400 °C for WFA-containing one. This difference may be linked to availability of impurities, mainly soda which can react with other impurities (from the matrix), forming a liquid phase, negatively impacting castable performance during RUL and CIC tests.[95] Availability of soda impurities from TA aggregates may be greater, as impurities are more uniformly distributed, the particles have lower density and its microstructure contains many small pores. These aspects may facilitate the release of soda from TA aggregates. In contrary, WFA aggregates are denser and the concentration of both soda and pores vary significantly from very low to relatively high values depending on the considered area of each aggregate. Thus, in the case of WFA, it means that the release of soda can be globally more difficult and as soda is available locally.[95]

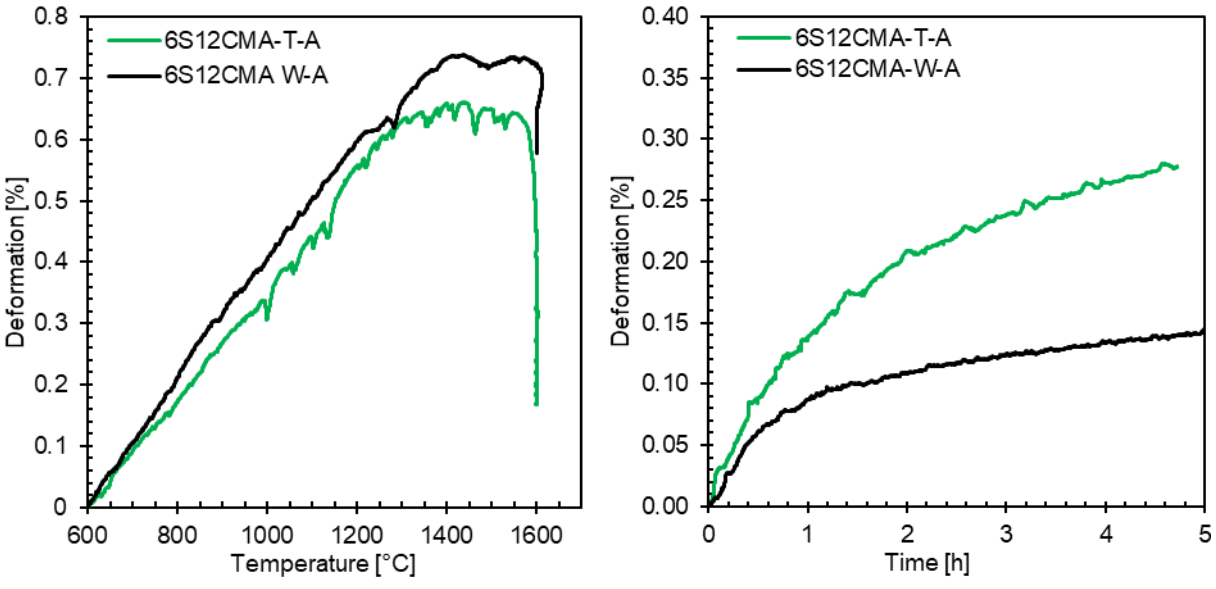

a b

Figure 4-21. Experimental results for castables containing TA or WFA aggregates: a) RUL, b) CIC.

In the same trend, CIC curves from Figure 4-21b unveil better creep resistance of the castable based on WFA aggregates. This difference is especially visible when the creep rates (estimated between 3rd and 4th hour of creep) are compared (see Table 4-9). In addition to chemistry aspects previously explained, better creep resistance of WFA-containing castable can also be related to more angular shape of these aggregates, which promote interlocking under compression.

Table 4-9. Selected RUL and CIC parameters for castables containing different alumina aggregates (TA or WFA).

Castable type	Temperature at maximal expansion T_0 [°C]	Creep rate between 3rd and 4th hour of dwell at 1600 °C [%/h]
6S12CMA-T-A	1435	0.0262
6S12CMA-W-A	1437	0.0099

Figure 4-22 shows Young's modulus evolution curves during three subsequent thermal treatments of the castables containing TA or WFA aggregates. The initial difference between values of Young's modulus of these two materials is most likely related to the water content (see Batch I from Table 4-3), which unfortunately impacted material porosity and stiffness. Stages 2 and 3 look rather similar for both castables. However, at stage 4, one can distinguish two stages (4a and 4b) in WFA-containing castables, which will be explained in the following paragraph, and only one stage (4) in TA-containing one. Then, at the 5th and at the beginning of the 6th stage (until about 650 °C), Young's modulus evolution curves look rather similar. An interesting change can be observed while cooling below 650 °C (at 6th stage). At this temperature, a trend inversion is observed in the case of WFA-containing castable and Young's modulus decreases until cooling down to ambient temperature.

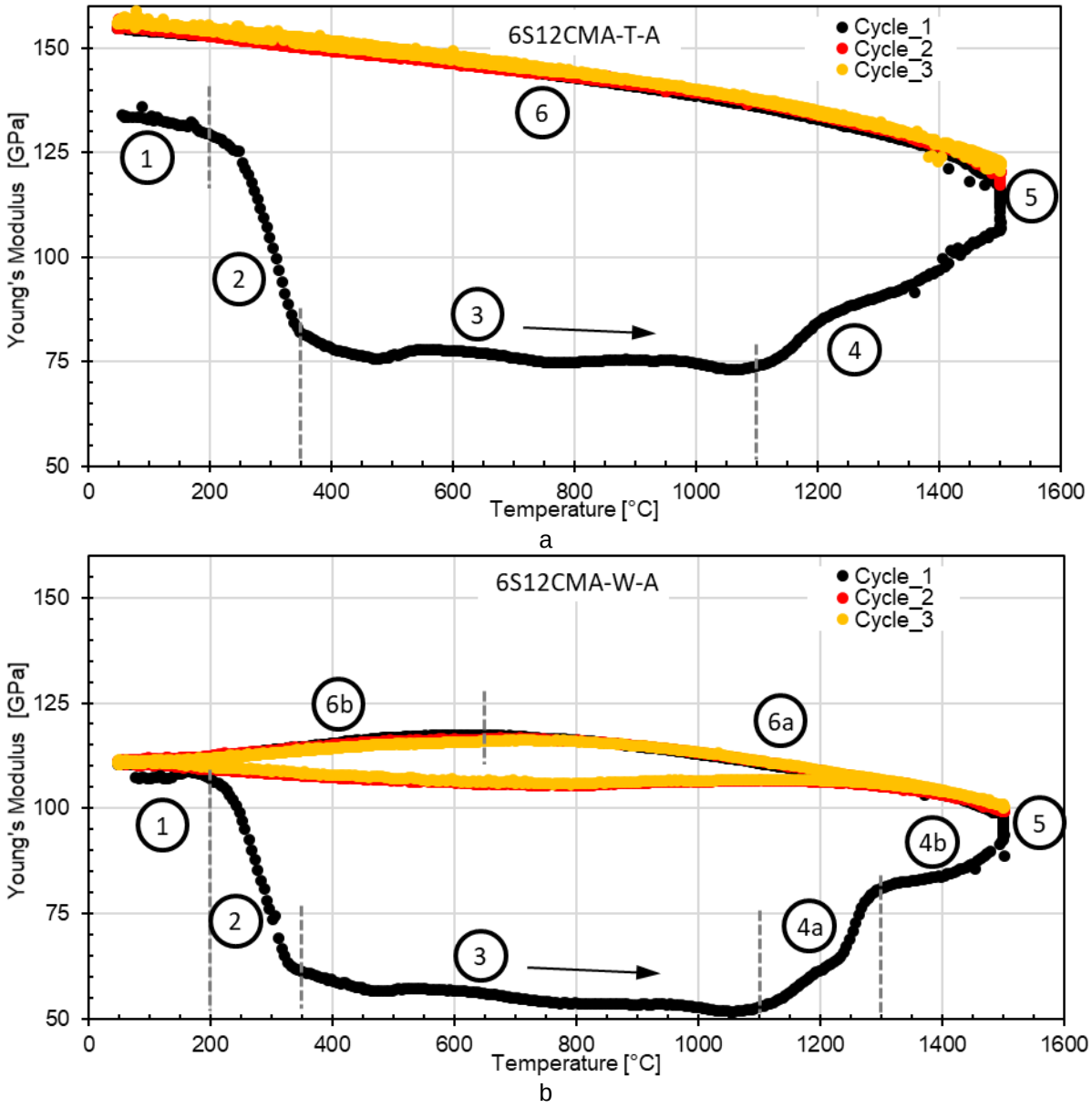

Figure 4-22. Young's modulus evolution with temperature for castables with different types of aggregates: a) 6S12CMA-T-A (with TA aggregates), b) 6S12CMA-W-A (with WFA aggregates). The applied thermal treatment includes three thermal cycles with a heating/cooling rate of 5 °C/min and 1h dwell at max. temp. of 1500 °C.

In the 4th stage for which the WFA-containing castable exhibits two sub-stages, a characteristic sharp increase of Young's modulus can be observed between 1250 and 1300 °C (stage 4a). In this temperature range, formation of hibonite (CA_6) is usually reported for similar types of materials.[111] The SEM observations of the castables after three thermal cycles demonstrate a typical presence of hibonite on the borders of the alumina aggregates (see Figure 4-23). These observations highlight a significant difference between the two castables: with tabular (see Figure 4-23a) or white fused alumina (see Figure 4-23b) aggregates. One may observe that in the case of WFA aggregate the thickness of CA_6 layer formed at the border is larger

and more uniform than in the case of TA ones. If the sharp increase of Young's modulus (end of stage 4a) and thickness of CA_6 layer are related to each other, one may suppose that this difference can be due to the size of crystallites within alumina aggregates, which are larger in the case of WFA. The larger size of crystallites could potentially improve the kinetics of reaction occurring at this temperature range, such as CA_6 formation, thus leading to an intense increase in Young's modulus. This improved kinetics may result in formation of a thicker CA_6 layer in the case of WFA-containing castable, in comparison to TA-containing one.

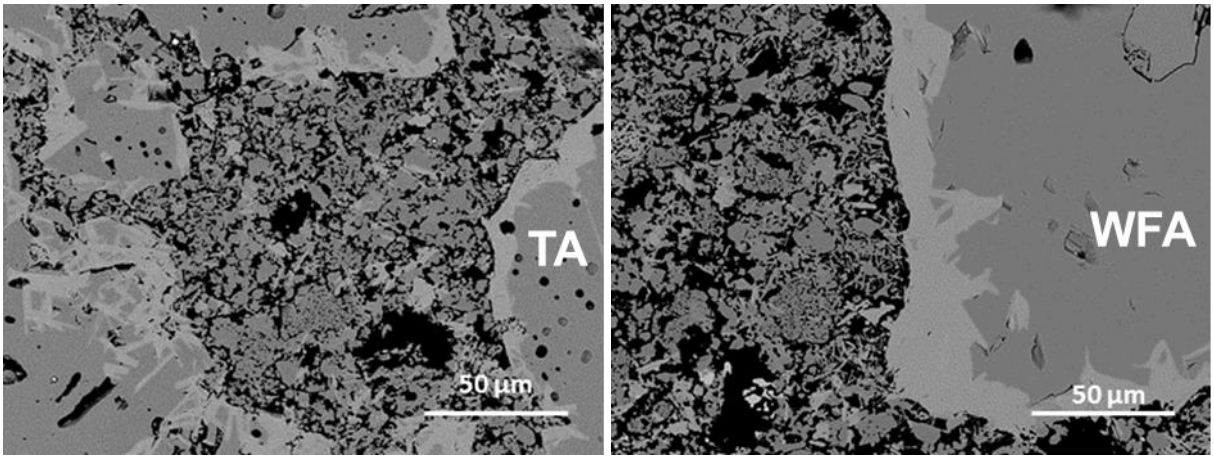

a B

Figure 4-23. SEM images showing microstructures of the two castables after three thermal treatments (up to 1500 °C with 1h dwell at each time) which contain different aggregates: a) 6S12CMA-**T**-A castable (with tabular alumina), b) 6S12CMA-**W**-A castable (with white fused alumina).

Considering the trend of Young's modulus evolution observed in WFA-containing material, the 6th stage should be divided into two parts: 6a (classical increase between 1500 and 650 °C) and 6b (non-classical decrease between 650 and 30 °C). This decrease of Young's modulus during cooling (in this case below 650 °C) is usually related to formation of microcracks. This interpretation is confirmed by the acoustic emission from Figure 4-24. On one hand, WFA-containing castable exhibits significant acoustic emissions (between 1500 and 3200 cumulated hits) during cooling and on the other hand, TA-containing castable exhibits a very low level of acoustic emissions (less than 400 cumulated hits). In fact, in the case of WFA-containing castable, the acoustic emissions (which is a very sensitive technique) starts at 1000 °C, even if Young's modulus decrease, appears just below 650 °C. These results demonstrate that WFA aggregates introduced to alumina spinel castable promote microcracks formation, contrary to TA.

How could this behaviour be explained? Firstly, one can consider microcracking in dense alumina ceramics. Case et al.[164] investigated the impact of grain size

on thermomechanical behaviour of dense polycrystalline alumina and he determined the value of the critical grain size for microcracking in polycrystalline alumina. It is worth noticing that a critical crystal size can be typically defined for dense brittle ceramics above which the specimens with larger crystals microcrack while the ones with smaller crystals (below the critical crystal size) do not.[164] Coming back to the castables containing TA or WFA aggregates, it seems reasonable to attribute different microcracking behaviour to the differences in crystal sizes of these aggregates. It is known that WFA grains have much bigger crystals than TA, which can lead to the amplified effect of thermal expansion anisotropy, resulting in higher internal stresses and/or in microcracking.

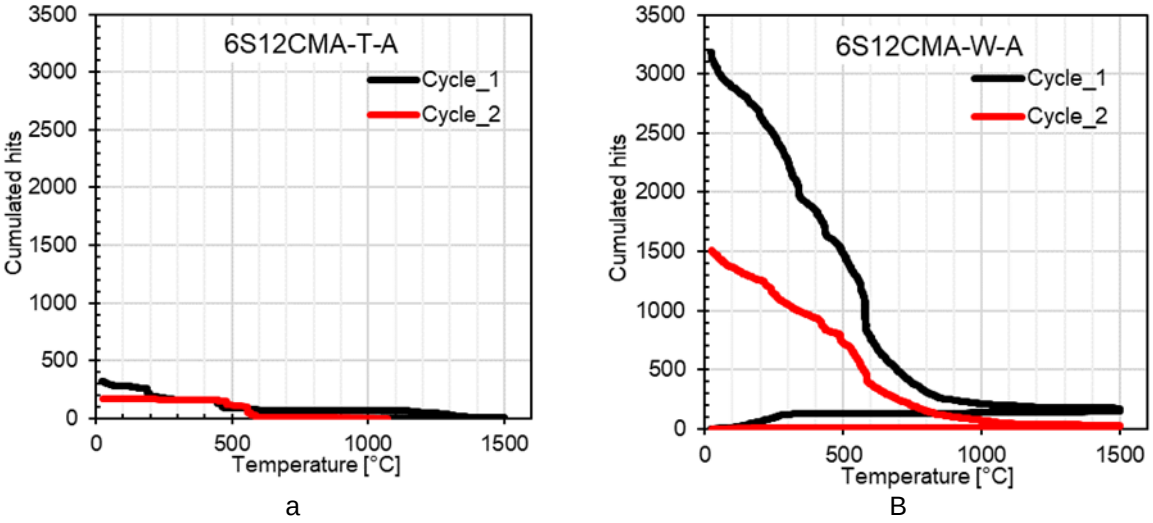

a B

Figure 4-24. Acoustic emission curves presenting cumulated hits vs. Temperature during the first two cycles of castables : a) 6S12CMA-T-A, b) 6S12CMA-W-A.

4.2.6. WST after different pre-treatments

Wedge Splitting Test (WST) is used to investigate fracture behaviour of model castables after different pre-treatments. This investigation can be relevant for precast shapes (applied in secondary metallurgy), such as purging plugs, which are exposed to thermal shocks. These plugs are often pre-treated at relatively low temperatures in order to remove plastic sheets. Then, when applied to steel ladle, they are exposed to a significant gradient of temperature (low temperature, due to the inlet of argon, and high temperature, due to the contact with liquid steel). The thermal treatments which have been considered here were designed to understand fracture behaviour both after the first pre-treatment (at rather low temperature) or after the contact with liquid steel. In fact, this work has been managed by Raphael Gull a master student from Montanuniversität Leoben, who completed the WST during an internship in 2020

at the University of Limoges. The overall results from this study have been described in detail in the Master thesis of Raphael Gull[167] and are just summarized very briefly in Table 4-10.

These investigations were focused on four model castables, depending on cement type (12S6CMA-T-A vs. 12S6CAC-T-A) or type of alumina aggregates (6S12CMA-T-A vs. 6S12CMA-W-A), which are tested after three different pre-treatments (at 110 °C, 600 °C or 1500 °C). The Wedge Splitting Test (WST) used for this study was coupled with an optical acquisition system. After each test, post-treatment was performed on acquired images by numerical methods, such as DIC (for measurement of crack opening displacement between the two sample parts) and 2P-DIC (for accurate measurement of crack length). This approach allowed to determine and compare material properties, such as nominal notch tensile strength σ_{NT}, specific fracture energy G_{f}', brittleness number B, as well as crack length after drop to 15% of the maximal horizontal load $l_{15\%\,\mathrm{F}_{H\,max}}$. The objective of the present section is to sum up the key conclusions from this work.

In the beginning, one can focus on general impact of pre-treatment on all types of tested castables. In general, samples cured at 110 °C often exhibit higher values of σ_{NT} and B, as well as lower G_{f}' and $l_{15\%\,\mathrm{F}_{H\,max}}$, when compared to samples pre-treated at 600 °C. This difference is due to dehydration of the hydraulic bonds (mainly occurring between 200 and 350 °C) what weakens bonds between grains. The pre-treatment at 1500°C leads to the development of ceramic bonds by formation of CA, CA_2 and CA_6 phases. This treatment significantly increased σ_{NT}, and B and reduced the mean crack length at 0.15 $F_{H,max}$ (material became very resistant to fracture initiation and very brittle). These are the general trends often observed after the different pre-treatments, which are obviously dependent on material microstructure evolution, as explained in the following paragraphs.

The type of cement has a significant impact on σ_{NT}, B and $l_{15\%\,\mathrm{F}_{H\,max}}$. Castable containing CAC cement is more resistant to crack initiation and more brittle, which is represented by a decrease of the mean crack length, especially after pre-treatments at 110 °C and 1500 °C. This difference is most likely related to three times higher CaO content in CAC (1.8 wt. % of CaO), in comparison to CMA (0.6 wt. % of CaO). This higher content of calcia may lead to the development of higher amount of hydraulic bonds after curing at 110 °C and to an increased content of ceramic bonds (CAx

phases, especially the strong CA_6 phase) after pre-treatment at 1500 °C. In this context, CMA, being less brittle could be preferred from the fracture behaviour point of view.

The type of aggregates also has an impact on σ_{NT}, B and $l_{15\%\,F_{H\,max}}$. WFA grains leaded to lower σ_{NT} and B values for pre-treatments at 110 °C and 600 °C, indicating a higher fracture resistance of this castable over the TA-containing one. This could be of interest in precast shapes (which can be pre-treated at rather low temperatures in the case of purging plug e.g. 600 °C) which operate in thermal shock conditions. However, after pre-treatment at 1500 °C, the brittleness of WFA-containing material is slightly higher than that of TA-containing one. It can be related to small pores present in TA aggregates, which in some conditions could act as crack arresters.[95] If the matrix is stronger, the probability of the crack propagating through the aggregate is higher. This could explain the little difference observed after thermal treatment at 1500 °C.

One should also note that the second batch of castables was unfortunately produced with slightly different water contents, which could also have had an impact on the results (see water addition in Batch II from Table 4-3).

Table 4-10. Summary of the key results from the Master thesis of Rafael Gull.[167]

Reference	Treatment [°C]	E [GPa]	σ_{NT} [MPa]		$G_f{}'$ [N/m]		B [-]		$l_{15\%\,F_{H\,max}}$ [mm]	
		$\bar{X}$	$\bar{X}$	σ	$\bar{X}$	σ	$\bar{X}$	σ	$\bar{X}$	σ
12S6CMA-T-A	110	104.4	6.9	0.4	151.3	12.3	0.20	0.02	60.8	8.0
	600	55.9	5.3	0.5	154.5	31.2	0.23	0.07	59.4	5.6
	1500	139.0	16.7	1	172.3	34.4	0.79	0.13	52.7	8.5
12S6CAC-T-A	110	135.9	10.5	0.5	159.9	18.4	0.34	0.02	54.4	1.3
	600	88.5	8.3	1.1	224.5	38.2	0.23	0.03	59.8	2.3
	1500	149.6	20.9	0.8	206.3	38.0	0.98	0.24	48.7	4.3
6S12CMA-T-A	110	132.7	11.3	0.5	193.7	19.3	0.33	0.03	61.6	4.1
	600	77.6	9.0	0.7	275.0	38.1	0.25	0.03	62.3	4.5
	1500	154.7	20.1	1.0	211.4	60.1	0.91	0.35	48.0	6.4
6S12CMA-W-A	110	107.2	7.0	0.6	141.3	19.8	0.21	0.01	63.5	7.6
	600	56.8	5.3	0.4	208.1	10.9	0.16	0.02	69.0	9.1
	1500	110.5	16.4	0.8	169.3	12.7	0.96	0.12	49.1	2.9

4.2.7. Conclusions

Study on model alumina spinel castables allowed to compare thermomechanical behaviour depending on different recipes. Even if these castables are not applied in the steel ladle considered in ATHOR project, such refractory lining is of interest in some steel plants. This type of model castables are quite well documented in the literature and the most interesting results from the present work are summarized here. The main findings concern the effects of different types of cements, aggregates or reactive aluminas on behaviour of the castables.

First of all, **stoichiometry changes** have been detected **in two types of spinels**: one added directly in preformed form and the other one added indirectly with CMA cement. XRD measurements performed at ambient and at high temperatures allowed to unveil merging of spinel peaks, which occurs above 1100 °C. This results in an increase of alumina content within the indirectly added spinel from about 72 wt. % to 75-77 wt. % (depending on assumed relation between the lattice constant and spinel stoichiometry) and in a decrease of alumina content in the directly added spinel from 78 wt. % to 77 wt. %.

Additionally, **types of cements significantly impact microstructures** and **thermomechanical properties**, especially during the first thermal treatment. Differences in thermomechanical behaviour, observed during the first heating by RFDA and RUL, are caused by three times higher CaO content in CAC, compared to CMA, and different microstructures organization within these cement grains. In fact, SEM images allowed observing formation of pores around CAC grains (under these particular experimental conditions) which is probably related to water solubility of calcium aluminates. Grains could partially dissolve in water from the external side and recrystallization could take place in another area thus forming pores. On the contrary, CMA particles maintain initially occupied volume thanks to presence of MA skeleton (not reacting with water) what allows development of more reliable microstructure with lower content of big pores.

Secondly, types of **bimodal reactive aluminas** can have effect **on mechanical properties at high temperature**. Reduction of soda content in reactive alumina seems to increase refractoriness and resistance to creep of the castable. However, the presence of increased content of fines within reactive alumina can involve slightly lower refractoriness and resistance to creep of the castable.

Thirdly, **types of aggregates** have substantial impact on **developed microstructures and thermomechanical properties of castables**. Addition of WFA aggregates lead to higher refractoriness, better creep resistance and increased microcracking during cooling below 650 °C, in comparison to castables with TA aggregates.

Observed changes can be interpreted in relation to behaviour in steel ladle lining. First of all, the presence of non-stoichiometric spinel could result in high temperature-induced viscous phenomena (see section 4-1), which can be beneficial for thermal shock resistance. CMA and CAC lead to similar stiffness after the first thermal treatment (at 1500 °C) and similar evolution of Young's modulus in the subsequent cycles. However, CMA cement can lead to an improved corrosion resistance (thanks to the presence of dispersed small grains of spinel), as well as to the development of microstructure with reduced content of big pores (presence of water-resistant MA skeleton). Thus, this CMA cement could be the preferred choice over CAC. Regarding reactive alumina, it seems that the type with lower soda content and regular content of fines, leads to increased refractoriness and better resistance to creep of the castable. Usage of WFA aggregates for the castable skeleton, in comparison to TA aggregates, also leads to better refractoriness and resistance to creep. A clear advantage of WFA-based castables can be observed after lower pre-treatments. However, the fracture behaviour after pre-treatment at 1500 °C is rather similar for both castables. On one hand, WFA aggregates promote microcracking during cooling, which can improve fracture behaviour. On the other hand, this pre-treatment improves strength of the matrix, which increases probability of a crack to propagate through porous TA aggregates and these pores can act as crack arresters also improving fracture behaviour.

Chapter 5

Chapter 5. Thermal shock monitoring with a thermal shock bench ATHORNA

This chapter is dedicated to the novel advanced thermal shock testing bench, named ATHORNA (referring both to the association of “ATHOR” and “New Aquitaine”, as well as to “Advanced measurement for in-situ Thermo-mechanical mOnitoRing of large sample uNder thermal grAdient”).

Before introducing the main objective of this device, it is worth reminding a typical scientific approach used for prediction of materials behaviour. The typical approach consists in deep characterization of non-linear material properties (thermal conductivity, thermal expansion, stress-strain law in tension/compression) evolving with temperature and using them as input in FEM models. Such procedure allows predicting sample behaviour in thermal gradient conditions, mimicking real applications. However, how can one assure whether numerical models are valid or not? One can confront results from numerical modeling with accurate experimental data in order to validate numerical models. The need for such data fostered development of the ATHORNA device. It targets to **provide accurate thermal and mechanical data measured on rather large samples under transient thermal state**. In this primary objective, section 5-1 aims to describe key experimental aspects of the ATHORNA device , and section 5-2 presents first interesting results obtained on alumina spinel that have been successfully compared to some FE modelling.

Another potential usage of this device (described in Annex A, entitled “Comparative testing of thermal shock resistance with ATHORNA “) concerns **verification whether ATHORNA device can be used for comparative studying of refractories resistance to thermal shocks** in a similar way as Wedge Splitting Test (WST). However, tests performed on ATHORNA device could have some advantages over WST, as the stress state generated during thermal shock tests is dependent on thermal material parameters (thermal conductivity and thermal expansion coefficient). For this reason, within this Annex A, some parameters determined from ATHORNA measurements are correlated with the ones obtained from WST.

5-1. Experimental device

This thermal shock bench has been firstly developed, in the framework of the European program SFERA2 in order to monitor (firstly by acoustic emission) the behaviour of a cylindrical disk (10 to 15 cm in diameter) subjected to a concentrated solar irradiation (solar furnace at PROMES laboratory). The current version

of ATHORNA device has been significantly improved by: on one hand applying a different heat source (CO_2 laser instead of solar irradiation) and on the other hand, implementing other types of measurements (infrared camera for 2D temperature field monitoring and stereoscopic vision system for 3D strain field monitoring). In addition, a FE model was developed to perform the first validation of numerical model using the ATHORNA device applied to refractory materials well-documented in terms of thermomechanical properties.

One should bear in mind that the development of such a complex thermomechanical system has only been possible thanks to the contribution of people with complementary skills from different institutions (indicated later).

5.1.1. Devices dedicated to thermal shock monitoring

Refractory materials in their applications (e.g. steel ladle lining) are exposed to periodic thermal shocks. Resistance to thermal shocks can be evaluated by several types of testing, such as mechanical fracture tests (monotonic loading at stable temperature),[168] mechanical fatigue tests (strain cycling at stable temperature)[169,170] and thermal shock tests (thermal cycling without mechanical loading).[171]

This section is dedicated to thermal shock testing, which is often considered to be more realistic, for the estimation of thermal shock resistance, than the mechanical ones. That is because the samples undergo a thermal gradient which generates internal stresses and can lead to damage. In most cases, thermal shock tests are simple, consisting e.g. on sample heating to a given temperature and subsequent rapid cooling in water. In such case, quantification of damage can be performed by *a posteriori* non-destructive measurement of Young's modulus or by destructive measurement of strength in bending. Taking into account this approach, two questions arise: Is this applied thermal shock really representative of the real application conditions? Does this type of measurement allow a good understanding of damage mechanisms, which are active during thermal shock? In this aim, researchers devoted their work over the years to develop different methods, in particular trying to in-situ monitor sample behaviour during thermal shock. In the last decades, several articles were published, where parameters, such as temperature, acoustic emission, and strain were in-situ monitored on samples subjected to thermal gradients. Some interesting works on this topic are introduced in the following paragraphs.

According to E. Brochen et al.[101], a disk irradiation method, using halogen irradiation as a heating source was firstly developed in the 1980s (PhD thesis published in 1989)[172] and was initially designed to determine critical thermal shock stress intensity factor under ascending thermal shocks. Subsequently, this device was improved to test refractory materials (sample diameter of Ø75 and thickness of 5 mm minimum). This improved device (published in 2017) consisted of disk irradiation at the central points from both sample sides, using focused halogen lights (see Figure 5-1a).[173] During the test, two temperatures are monitored by pyrometers (at the central point and at the edge of the sample) and damage is detected using an acoustic emission sensor.

In 2009, F. Damhof et al.[179] published a paper where high-temperature gradients were tested with a dedicated thermal shock device (see Figure 5-1b). This device consisted of a cuboid-shaped sample placed at the surface of a molten aluminium bath (T=1000°C). Other sample surfaces were insulated to generate a linear temperature gradient between the two flat surfaces. After a given time, the sample was air-cooled. Temperatures were monitored during the test by linearly distributed thermocouples (with different distances from the hot surface). Depending on the applied thermal gradient, the distribution of damage (uniform or non-uniform) was *a posteriori* quantified along the axis of the sample, using ultrasonic measurements.

In 2011, H. Kamio et al.[175] published an article, where an interesting thermal shock device (see Figure 5-1c) was applied to test refractories with an in-situ strain field monitoring, using Digital Image Correlation (DIC). This work is probably one of the first (if not the first one), where DIC is applied to monitor refractory behaviour during testing at high temperatures. This interesting test consisted in a single side heating (burner) of a cuboid-shaped sample (112x65x35 mm^3) and on monitoring of the top sample surface (being perpendicular to the heat flux) by an optical camera. Acquired images were then used to calculate in-plane deformations on the top sample surface. Additionally, numerical simulations were performed to compare experimental deformation with simulated results.

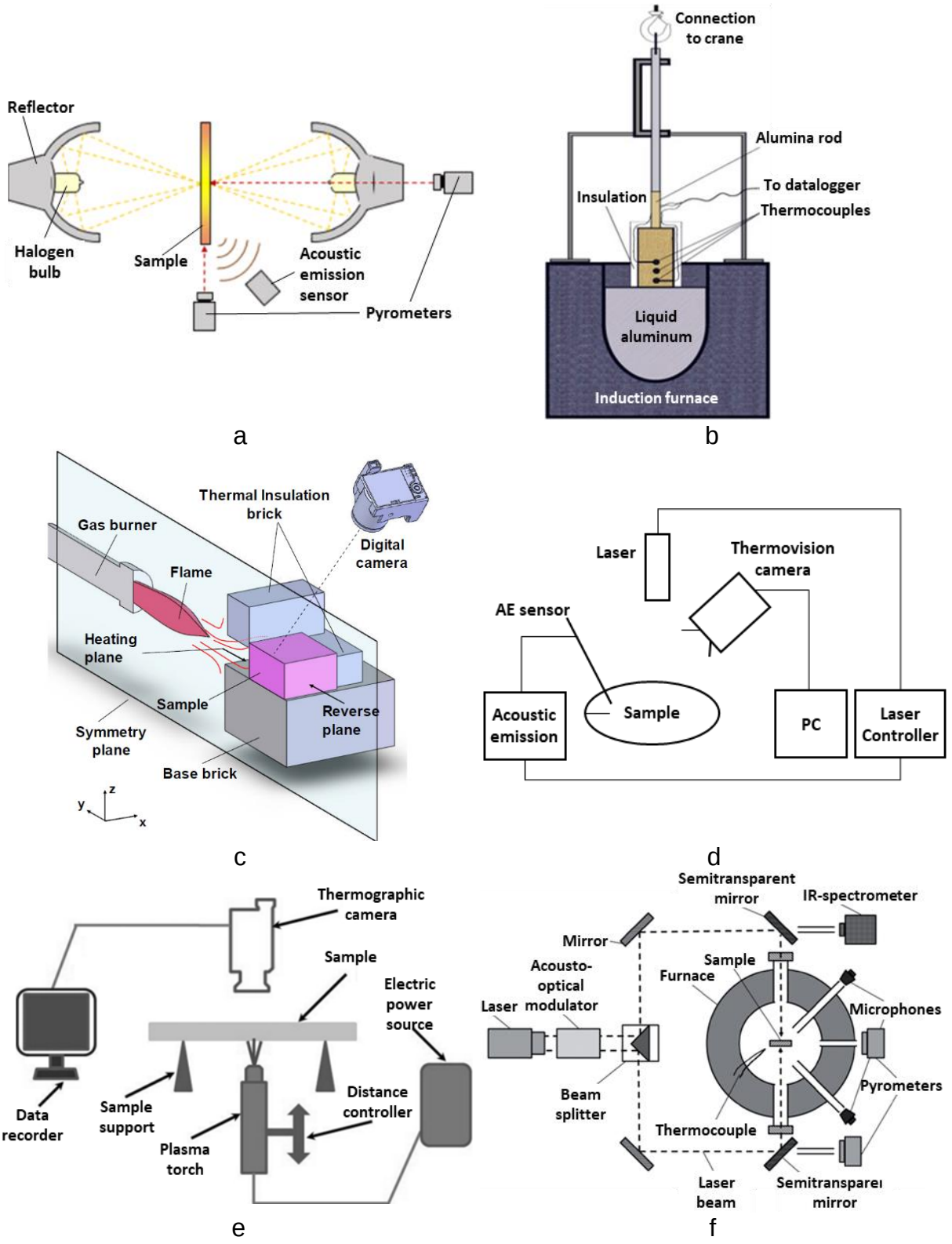

Figure 5-1. Schemas of different thermal shock testing devices with parameters monitoring: a) Disk irradiation test by halogen light,[173] b) Immersion test in liquid aluminium,[174] c) Flame burning test,[175] d) Disk irradiation test by laser irradiation,[176] e) Plasma thermal shock test,[177] f) ThermoOptical Measuring (TOM) device.[178] (Notice: Figures were slightly modified to facilitate readability.)

D. Gruber and H. Harmuth, in an article published in 2014,[176] described a laser irradiation test (see Figure 5-1d) coupled with finite element modelling, which was used in order to determine mechanical fracture parameters of zirconia refractory. It is worth mentioning here, that this device was not at that time designed for thermal shock monitoring, but to characterize some thermomechanical properties of the tested material. Nevertheless, this device is still interesting in the context of this paragraph, as one can observe effect of laser irradiation on a thin notched ceramic disk (sample dimensions in mm: Ø50x1; radial notch length in mm: 10) by monitoring of both temperature field of the upper sample surface (by IR camera) and damage progression (by acoustic emissions). By combining such experimental results with FEM modelling, authors succeeded to determine tensile strength and specific fracture energy of tested material.

In 2013 and 2016, W. Zhang et al.[177,180] published papers about an instrumented test of refractories under thermal gradient (see Figure 5-1e). A disk-shaped alumina sample (dimensions in mm: Ø40x2), with or without a notch, was locally heated by a plasma beam at the central part of the bottom surface with simultaneous recording of the temperature field at the upper sample surface, using an IR camera. A coupling between experimental and numerical simulation methods was then developed to overcome the lack of traditional tests which could be used to accurately determine some experimental parameters, such as heat flux boundary conditions and application conditions. Based on the experimentally-measured temperature fields, the developed FEM simulation was used to determine thermally-induced stress fields.

Since the 2000s, several scientific articles have been published on a specific "ThermoOptical Measuring" device (TOM).[181,182] Initially focused on the measurement of thermal properties, an evolution of this device has been proposed in 2018 to evaluate the behaviour of refractory materials subjected to hot thermal shocks.[178] A disk-shaped sample (diameter of Ø35 mm) placed in a furnace (operating up to 1800 °C) is irradiated on central points of both plane surfaces by a split CO_2 laser beam. Sample temperatures at the centre and at the edge are measured by two pyrometers and damage is monitored using four acoustic emission sensors.

5.1.2. General description of ATHORNA device

Section 5.1.1 introduces the state of the art concerning thermal shock devices which induce thermal gradient within sample and allow monitoring of the sample

behaviour during testing. ATHORNA device, already briefly presented in section 3.1.3, is the advanced thermal shock bench which has been developed to study material behaviour under thermal gradient (generated by CO_2 laser irradiation) with a use of visual (see section 5.1.2.5), infrared (see section 5.1.2.4) and acoustic sensors (see section 5.1.2.6).

The CO_2 laser is used to apply an intense thermal flux at the centre of the top sample surface (also called a hot face) with controlled laser power (in the range of 0-2 kW) and laser irradiation procedure. The disk-shaped sample is placed on alumina support (composed of three isostatic rods arranged circularly at 120°) allowing free deformation, according to thermal gradient. In this configuration, allowing only 3 small points of contact, the sample can be cooled by air convection from all surfaces. These experimental boundary conditions can be simply represented in FEM modelling (from both thermal and mechanical points of view).

The temperature field of the bottom sample surface is monitored by infrared camera during the test. At the same time, this surface is also monitored by stereovision system, which allows 3D displacement and strain fields monitoring of the surface with a use of optical methods (such as DIC or mark tracking). A refined 2P-DIC technique allows accurate monitoring of crack evolutions throughout the test. Damage occurring within the sample is also monitored during the test by 6 acoustic sensors arranged circularly at 60°. This set of acoustic sensors allow spatiotemporal localization of events detected, as it has already been explained in the publications.[183,184]

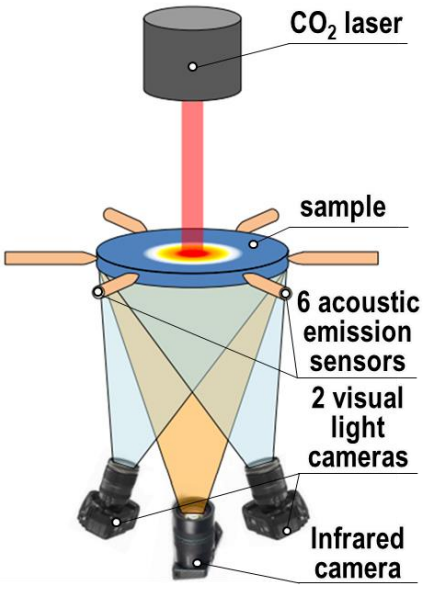

Figure 5-2. Schematic representation of ATHORNA device.

5.1.2.1 *Selected sample geometry and material*

Tested samples have disk shape with dimensions varying between 100 and 150 mm in diameter and 5-30 mm in thickness. Sample dimensions are selected for each material considering both the biggest aggregate size as well as possibility to perform investigations at laboratory scale. Consequently, a disk-shaped sample with dimensions of Ø100x10 mm^3 has been selected for these investigations. Such dimensions could allow considering the sample as homogeneous in FEM modelling despite the rather coarse-containing microstructure of refractory materials. The material selected for the study, dedicated to validation of numerical model, is alumina spinel brick which was introduced in section 4.2.1.

5.1.2.2 *Heat source*

A CO_2 laser beam is used to irradiate the top sample surface. This beam is applied with pre-defined power cycles which could be finely tuned depending on the targeted thermal gradient within the sample (below or above occurrence of damage) and maximum temperature targeted on central point of the hot face (to avoid local melting). The laser heat flux spatial distribution over the top sample surface is illustrated in Figure 5-3a.

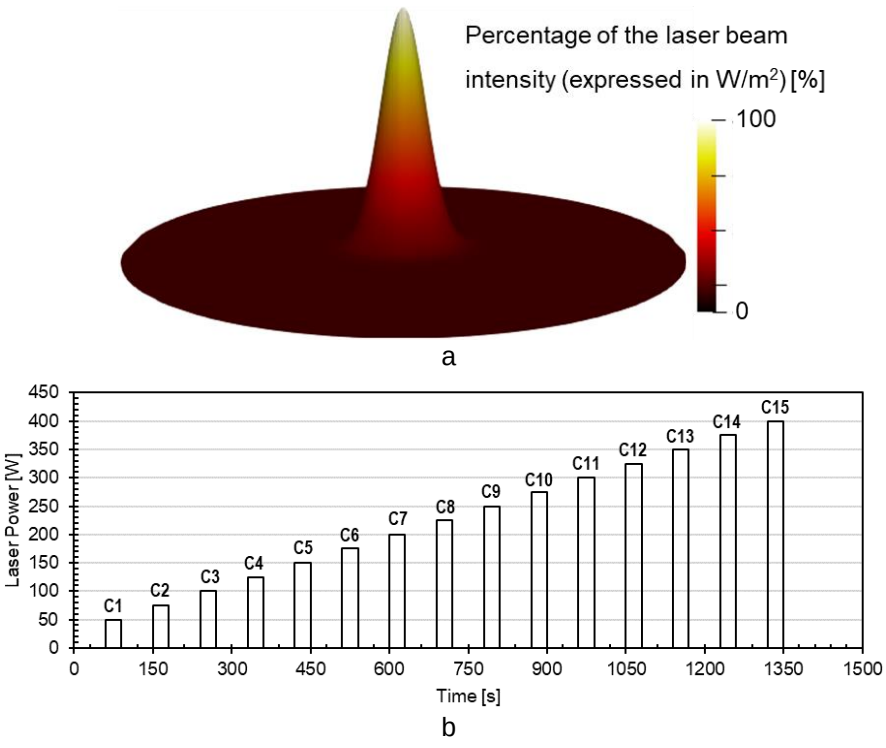

Figure 5-3. Characteristics of the CO2 laser beam used as heat source on top surface of the alumina spinel disk: a) Normalised spatial distribution of the heat flux over all top surface, b) Temporal applied cycles determining the global laser power applied through the overall top surface.

This spatial distribution has been calculated from the cartesian position of the considered point (x and y being the coordinates from the central point) thanks to Equation 5-1,[185] where I_0 is the maximum heat flux applied in the centre, and w is the typical waist of the laser beam, (corresponding to the radius for which the intensity decreases by factor of $1/e^2$=0.135 in comparison to the central point). The waist w of the CO_2 laser that has been used for the present investigations at ILP Laser company is equal to 8 mm.

$$I(x,y) = I_0 \times e^{-\frac{2(x^2+y^2)}{w^2}} \qquad \text{Equation 5-1}$$

The total power applied in the sample is expressed by the integration of Equation 5-1, as expressed in Equation 5-2.

$$Power = \iint I(x,y) \qquad \text{Equation 5-2}$$

Thanks to FEM modelling and preliminary investigations, the sequence of laser heat flux has been specifically set up in the case of alumina spinel material. The first cycle has been applied with very low power (50 W) in order to avoid any damage within the disk. Then, the laser power has been increased progressively (increments of 25 W per cycle) to reach thermal gradients that can generate first damage with the alumina spinel material (which can be anticipated by FEM modelling). During the whole sequence, laser power has been voluntarily limited to restrain as much as possible the temperature in the middle of the top surface (avoid local melting). In this aim, fifteen cycles (60 sec of idle time, 30 s of laser on) have been defined starting from 50 W to 400 W with increments of 25 W per cycle. The laser cycles are shown in Figure 5-3b.

5.1.2.3 *Stable frame*

Different optical methods are used in ATHORNA device to monitor thermomechanical behaviour of brittle refractories. These techniques use cameras to record images of the bottom face of the sample. To set up very precise and constant position for the used optical cameras, a dedicated rigid frame has been designed. For thermomechanical investigations of refractories which are rather brittle materials, strain fields must be in fact measured within a deformation range of about 10^{-4}. Thus,

any disturbing deformation that could come from this frame should absolutely be reduced to values much lower than 10^{-4}.

This rigid frame has been thus designed using a specific cinematic chain (Figure 5-4), inspired by Serrurier truss (telescope tube assembly construction). The constitutive tubes of the frame are made of silica (very low thermal expansion of $0.6 \cdot 10^{-6}$ K^{-1}) interconnected using metallic joints with drilled channels in order to maximize parts made of silica. This type of construction allows thus to reduce truss flexing, as well as potential measured deformations (on bottom face of the sample) coming from frame vibrations and thermal drift.

Two USB cameras (IDS UI-3480CP-M-GL: CMOS sensor 2560 x 1920 $pixels^2$ and 256 grey levels) have been fixed on the cross horizontal silica tube of the frame to monitor the bottom face of the sample as shown in Figure 5-4. Furthermore, an infrared (IR) camera is placed between the two cameras in such a way that its optical axis is almost perpendicular to the bottom surface of the sample.

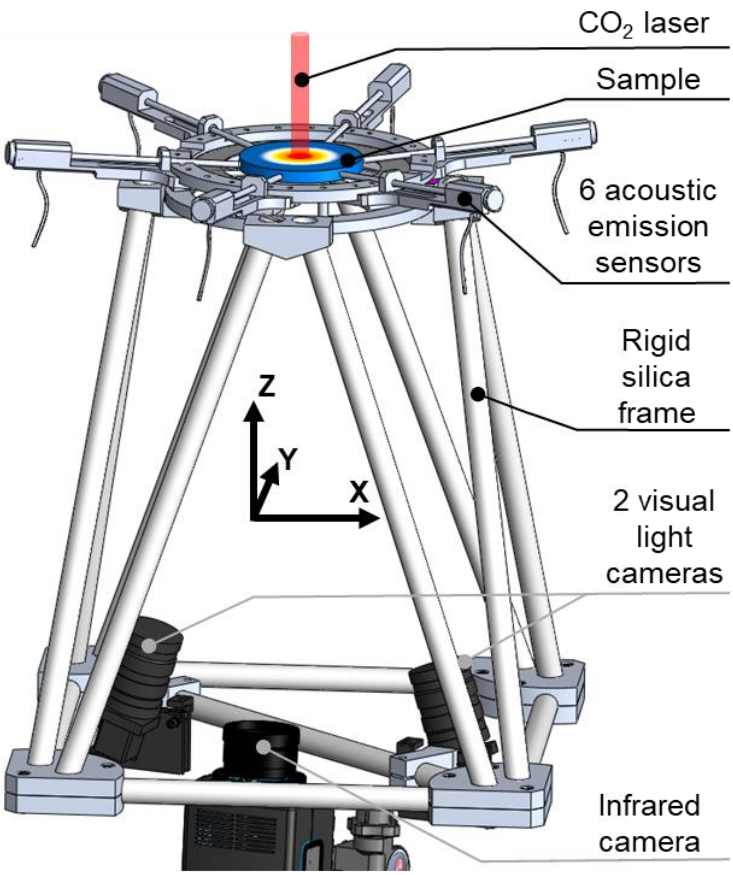

Figure 5-4. Schematic representation of the silica rigid frame connecting the stereoscopic vision system and the infrared camera with the disk-shaped sample (diameter 100 mm, thickness 10 mm).

5.1.2.4 *Thermal measurement (thermal camera)*

The infrared camera used to monitor the sample back surface is a FLIR SC3000 (QWIP detector 320 x 240 pixels^2). Taking into account the size of the sample (diameter = 100mm) and IR camera resolution, the magnification is 0.5 mm/pixel with an acquisition frequency of 0.5 frame/second. Previous heat tests have been led by comparing the temperatures from thermocouples and IR camera and demonstrate that emissivity of the cold surface covered with a white and black speckle pattern is well equal to one. For a measurement range above 200 °C, the temperature standard deviation is about 1°C.

5.1.2.5 *Optical measurements on sample with speckles or markers*

Optical methods, such as mark tracking, DIC and 2P-DIC (introduced in sections 3.2.1, 3.2.3 and 3.2.4, respectively), are applied during thermal shock test in order to monitor displacement and strain values locally (at selected areas) as well as globally (on the whole sample surface). Three-dimensional displacement and strain fields are determined thanks to the usage of stereovision, which is introduced in section 3.2.5. Mark tracking is used in this study exclusively for testing stability of experimental device by measuring displacements on silica ring (not presented here). DIC is applied (on sample) for monitoring of strain field and determination of crack opening displacement, while 2P-DIC allows to determine crack path and crack length.

Three-dimensional displacement and strain fields calculations are, in the case of ATHORNA device, mostly performed on subsets with a size of 64x64 pix.^{2} being distributed with a spacing of 32 pix. both along X and Y axes (magnification 13 pix./mm). Strain calculation requires a set of 4 subsets, which are typically selected as the closest ones with one subset spacing (see section 3-2). However, in such case the original gauge length L_0 is quite small what results in low accuracy. In the case of refractory materials, high accuracy is very important as analysed phenomena occur at very low strains. Therefore, in order to increase accuracy of strain measurement, the original gauge length L_0 needs to be increased by selecting subsets located at higher distance. In the present case, the original gauge length L_0 has been set to four subset spacings $L_0 \approx 10$ mm (see Figure 5-5).

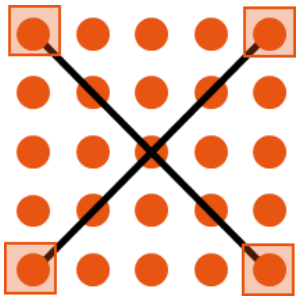

Figure 5-5. Representation of the 4 subsets selected for strain measurement associated to the central point where the black lines cross. Dots correspond to centres of each subsets.

5.1.2.6 *Acoustic emission sensors*

Since 2P-DIC technique is only able to detect cracks at the bottom surface of the sample, it is also very useful to have other sensors that could detect and localize occurrence of defects in other areas of the disk-shaped sample. In order to do so, ATHORNA device is also equipped with 6 acoustic emission sensors (Mistras µ80) connected to a dedicated electronic device (acoustic emission system Mistras Express 8). This equipment arrived at IRCER laboratory only in February 2020, thus no experiment was managed during the present PhD. Nevertheless, previous experience with similar system was acquired during the PhD of Yasmine Lalau (University of Perpignan via Domitia, 2017),[186] which led to three scientific articles.[183,184,187] For spatiotemporal localisation of the events, crack monitoring by acoustic emissions is performed by the set of 6 acoustic sensors arranged circularly at 60° around the sample (see Figure 5-4). More details about this part of ATHORNA device could be found in the work of Yasmine Lalau.

5.1.3. Characterization of strain field measurement

5.1.3.1 *Strain field uncertainty*

The strain uncertainty mainly depends on the distance between two selected subsets (L_0 defined in Figure 3-9) and hereafter named derivation pitch. Figure 5-6 shows the standard deviation of the 1st principal strain for the 20 first acquired images (assumed to be zero before any thermal loading) versus the derivation pitch. These first results allow determining a reasonable derivation pitch of 5 mm (64 pixels) which leads to a standard deviation in strain measurement of about 9.10^{-5}. In addition, it should be noticed at this stage that optical images have been acquired with a frame rate of two images per second and IR images have been acquired with a frame rate of 0.5 image per second (limit of IR camera). As a consequence, for later confrontation

between optical and IR measurements, most of the results will be presented later every 2 seconds, but considering all acquired optical images thanks to a temporal average filtering from 9 optical images (-4 images / +4 images). In such a way, thanks to this temporal filtering, the strain uncertainty can be divided by a factor of 1.4 compared to the result without temporal filtering (Figure 5-6) and leads finally to a standard deviation in strain measurement of about 6.10^{-5} for the same derivation pitch of 5 mm (64 pixels).

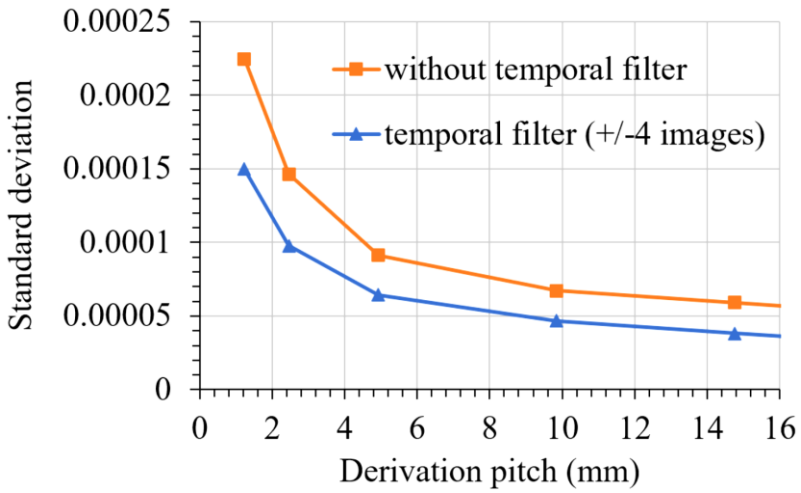

Figure 5-6. Standard deviation of the first principal strain for the 20 first acquired images (before any thermal loading) for several derivation pitch and influence of considered temporal filter.

5.1.3.2 *Orientation of the principal strains*

DIC method allows determining the ε_{XX}, ε_{XY}, ε_{YY} strain fields, which are then used for calculation of the principal strain fields (ε_1, ε_2) by diagonalization of the strain tensor. Orientation of the first principal strain can then be determined by its angle referred to the horizontal X-axis in Figure 5-7a. As reported in this Figure 5-7, especially in Figure 5-7b (measurements managed on aluminium disk-shaped sample - used for the pedagogical purpose), this angle is close to 0° (green colour) around the horizontal axis and to 90° (red colour) around the vertical one. This indicates that the first principal strain mainly has a radial direction within the disk-shaped sample. Taking into account that the second principal strain is perpendicular to the first one, one can state that this second principal strain occurs mainly in the circumferential (hoop) direction. Figure 5-7c presents similar results for an alumina-spinel refractory sample. Even if in this case, due to the lower coefficient of thermal expansion (compared to aluminium) and material heterogeneity, results are less obvious, the same tendency can clearly be observed.

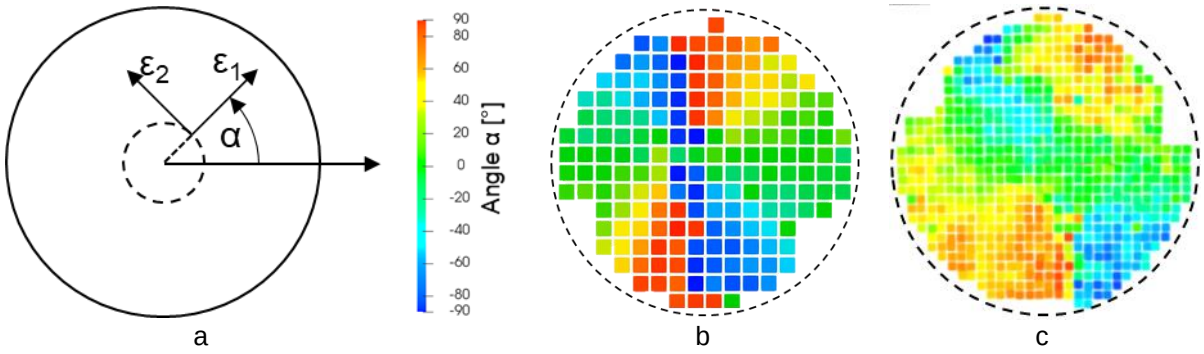

Figure 5-7. Angle α between the first principal strain ε_I and the horizontal X of the disk-shaped sample: a) geometrical representation of angle α with direction of the first ε_1 and the second ε_2 principal strains axis, b) pedagogical case of an aluminium sample (quite obvious results), c) case of alumina spinel refractory sample (less obvious).

5.1.3.3 *Strain field decomposition*

Since the total observed strain field results from the superposition of both thermal and mechanical strain fields, optical measurements can be post-treated in order to determine mechanical strain fields by subtracting the thermal strain fields (which can be estimated from IR measurements), according to the equation $\varepsilon_{1mech} = \varepsilon_1 - \varepsilon_T$. The temperature field can be in fact simply calculated using the equation $\varepsilon_T=(\Delta T*\alpha)$, where ΔT and α represent respectively the local temperature evolution since the initial stage and the thermal expansion coefficient of the investigated material. For pedagogical purpose, an exemplary result of strain field decomposition for an aluminium sample is firstly presented in Figure 5-8a. These results clearly demonstrate that even if the first principal total strain ε_1 is positive (left picture), due to ε_T which is obviously always positive (central picture), the first principal mechanical strain ε_{1mech} (right picture) in the central part of the sample is negative (compression). Note that this first principal mechanical strain ε_{1mech} (negative in the middle) increases thus from the centre to the border (to reach zero at the border). In the same way, similar results can be observed on an alumina spinel refractory sample as demonstrated in an example from Figure 5-8b).

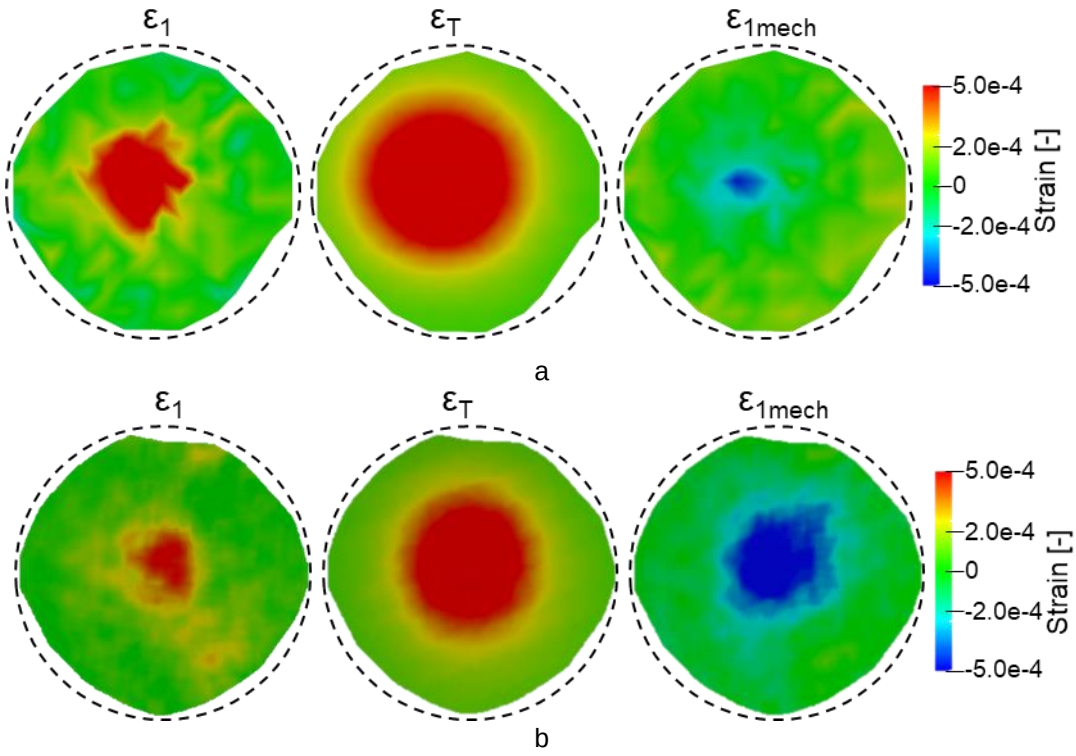

Figure 5-8. Determination of the mechanical strain field (right pictures) in the radial direction by subtraction of the temperature field (central picture) obtain by IR measurements from the 1st principal total strain field (left pictures) obtained by optical measurements: a) case of an aluminium sample, b) case of an alumina spinel refractory sample.

5-2. First results obtained on alumina spinel disk

This section is focused on alumina spinel brick which has been characterized in section 4-1. Based on these thermomechanical results, as well as on thermal results obtained by another PhD student from ATHOR project,[188] a FE numerical model (elastic linear) has been built and briefly introduced in section 5.2.1. Experimental measurements on alumina spinel disks with ATHORNA device are then developed in the following sections and compared with FEM results.

5.2.1. Introduction to numerical modelling

Sample behaviour under thermal gradient was simulated using ABAQUS software.[189] Please note that this part has been prepared in a strong collaboration with a group of researchers from the University of Orleans (France) and Rafael Oliveira from the University of Coimbra in (Portugal). In fact, Rafael performed most of numerical simulations presented in this section. Even if this numerical part has been mainly managed by Rafael, it is very useful to understand the results and show potential of the device.

Both materials were modelled with a temperature-dependent linear elastic behaviour, the thermo-mechanical properties are presented in Table 1. The emissivity of the alumina spinel was set to 0.80 for the surfaces free of painting and 1.0 for the painted surfaces (bottom surface). The convection coefficient was taken as 12 W/(m^2°C) for both samples,[190] this value was defined interactively during the numerical simulations.

The sample was modelled using solid elements C3D8R, defined as a continuum (C), three-dimensional (3D), hexahedral and eight-node brick (8) with reduced integration (R), hourglass control and linear interpolation. These elements have three degrees of freedom per node, corresponding to translations in the three directions [Abaqus User Manual]. After evaluation of the influence of the finite element mesh, it was found that good results could be obtained by using finite elements of approximately 1.4x1.4x1.4 mm^3, as shown in Figure 5-9.

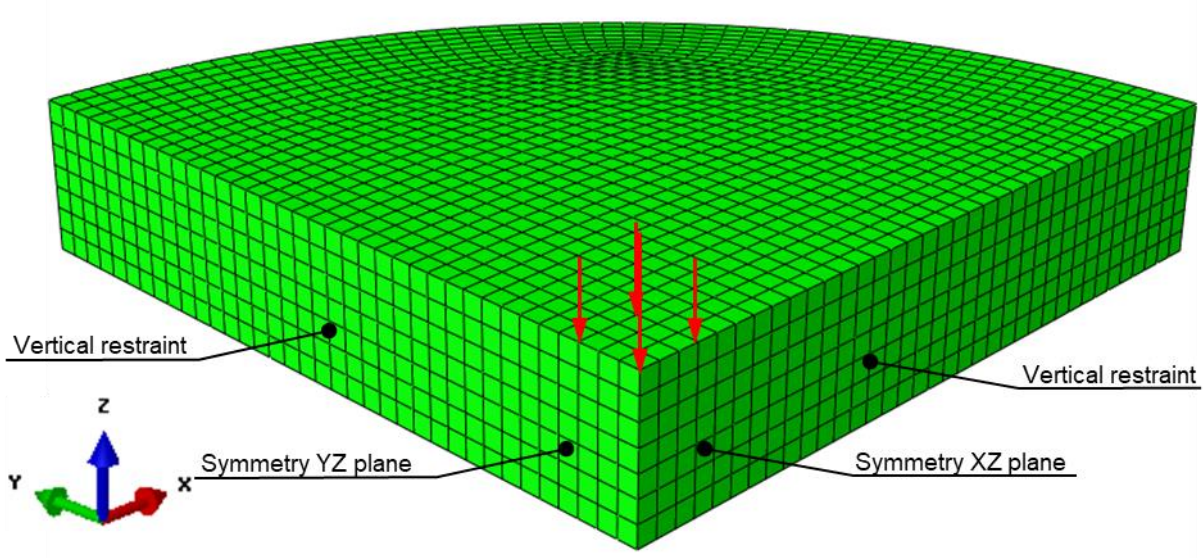

Figure 5-9. Finite element mesh, boundary conditions and heat flux.

Due to the symmetry of the system two planes of symmetry (YZ and XZ) were taken into account to reduce the computation time (see Figure 5-9). To simulate the support of the disk two vertical restraint were considered in the vertices of the sample. The CO_2 laser beam was applied as a surface heat flux distributed on the top surface according to the analytical equation (see Equation 5-1), introduced in section 5.1.2.2.

Table 5-1. Thermal and mechanical properties of aluminium and alumina-spinel material.

Media	Considered properties			Values	References
External air	Thermal properties	Temperature		16.9 ºC	(Measured during the test)
		Convection factor		12 W/(m2ºC)	(Inverse identification)
Alumina spinel	Thermal properties	Emissivity	Top face and lateral face	0.8	(Inverse identification)
			Bottom	1	
		Specific Heat (J/kg°C)		$c_p(T) = b_0.T^{b_1}$ with $b_0 = 563.5$ and $b_1 = 0.12$	188
		Thermal conductivity (J/kg°C)		$\lambda(T) = c_0 \ln(T) + c_1$ with $c_0 = -1.01$ and $c_1 = 9.68$	188
		Thermal expansion		$a(T) = a_0 + a_1.T + a_2.T^{-2}$ with $a_0 = 7.6\ 10^{-6}$, $a_1 = 1.7\ 10^{-9}$ and $a_2 = -2.5\ 10^{-1}$	161
	Mechanical properties	Young Modulus (GPa)		$E(T) = d_0 + d_1.T + d_2.T^2 + d_3.T^3$ $\mathrm{d_0} = 2.9663.\mathrm{E}\,1$, $\mathrm{d_1} = -1.5457.\mathrm{E}-2$, $\mathrm{d_2} = 3.5035.\mathrm{E}-5$ and $\mathrm{d_3} = -1.5361.\mathrm{E}-8$	161
		Density		3130 kg/m^3	191

The developed finite element model comprised two types of analysis, that were performed separately: i) heat transfer analysis, and ii) general static mechanical analysis. The heat transfer analysis is used to determine the temperature fields in the sample along the test. Then, the general static mechanical analysis is used to calculate the displacements, strains and stresses developed within the sample due to the thermal load. The maximum increment of time was set as 1 second and the maximum allowable temperature change per increment was 15ºC.

5.2.2. Temperatures and induced thermal gradient within the sample

5.2.2.1 *Temperature fields*

A laser beam, arriving at the top sample surface induces a thermal gradient within the sample. Thanks to the observation of the bottom sample surface with the IR camera, it is possible to monitor generated temperature fields. Three exemplary

temperature fields of the bottom surface are presented in Figure 5-10b for the maximal temperature values occurring during the 5th, 10th and 15th cycles, as indicated in Figure 5-10a. Within the representation (see Figure 5-10b), the temperature is indicated both in the z-axis and using the colour code. The initial temperature of the sample is about 20 °C (before the 1st cycle) and can reach values close to 500 °C at the centre of the bottom surface during the last thermal cycle.

During the 15 thermal cycles, one can observe that the central hot area becomes larger and steeper with each subsequent cycle, indicating a higher radial thermal gradient at the bottom surface (more detailed in the following section).

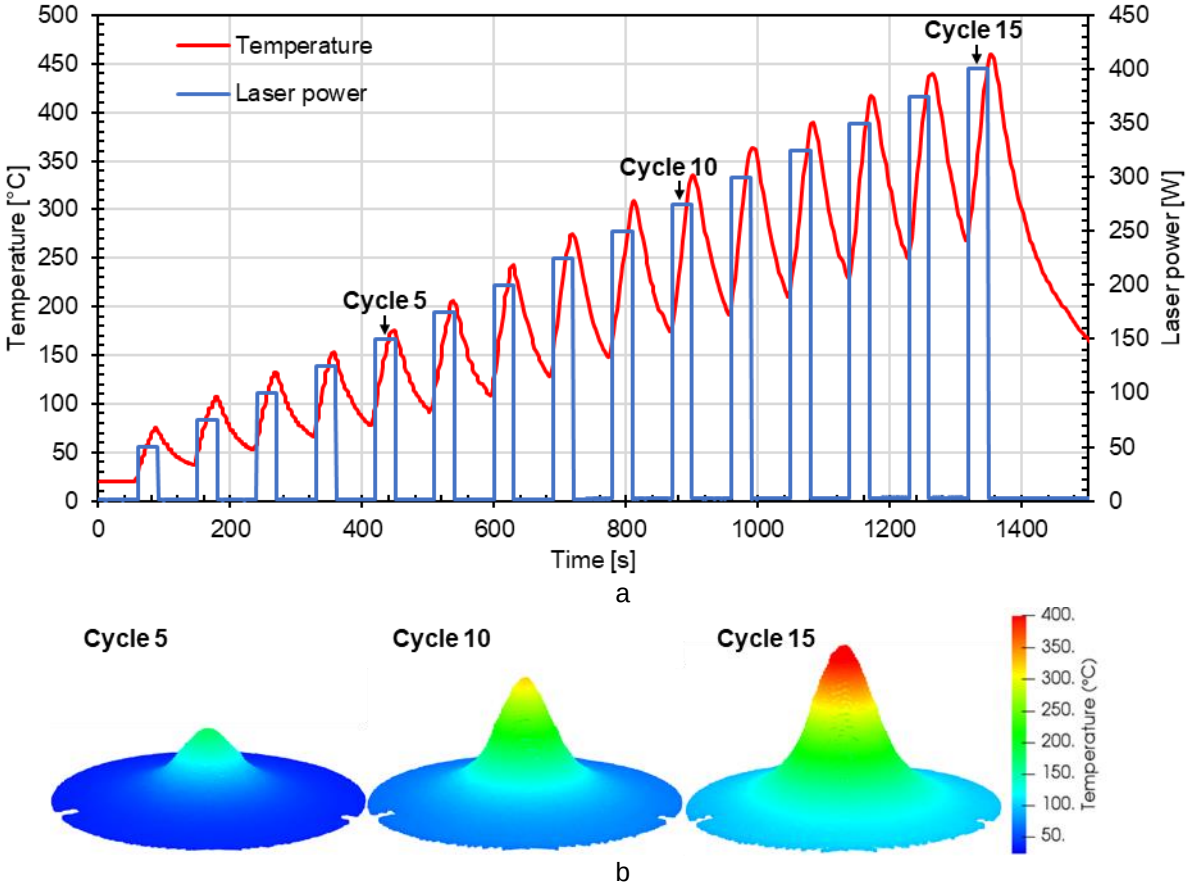

Figure 5-10. Representation of temperature on the bottom surface obtained with IR camera: a) applied laser sequence and evolution of temperature at the central point vs. time, b) three exemplary temperature fields from 5th, 10th and 15th cycles.

Thermal modelling allowed comparing the numerically predicted thermal results with the experimental ones. Temporal evolutions of the temperature at the central point of the bottom sample surface is presented in Figure 5-11. Based on the fact that the heat transfer analysis was performed with the thermal material properties and exchange conditions reported in Table 5-1 (without any optimization), one can observe some differences in the temperature evolution. Despite this small difference,

a rather good agreement can be noticed between these experimental and numerical results, which allows to validate (in first approximation) the heat transfer analysis performed by FEM.

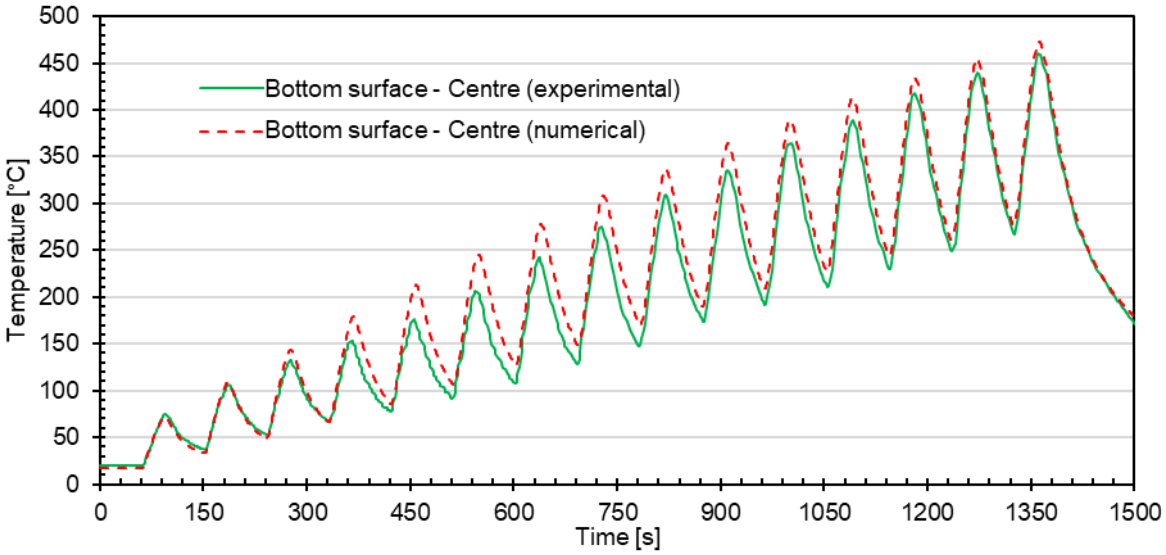

Figure 5-11. Temperature evolution on the central point of the bottom sample surface in alumina spinel sample.

Since the temperatures at the top sample surface are not experimentally measured, it is interesting to use FE modelling in order to estimate them. The numerical prediction of temperatures occurring at the centre of the top and of the bottom sample surfaces are reported together in Figure 5-12. The sample is at ambient temperature at the beginning of the test and temperatures at these points oscillate during the subsequent thermal cycles. Much higher amplitudes are observed at the centre of the top surface where the laser beam heats the sample. The following heating cycles lead to a severe increase of temperature at the top central point, which is most likely related to the increase of laser power. The maximal temperature difference (in the range of 1600-1700 ºC) between the central points of the top (more than 2100 ºC) and the bottom (less than 500 ºC) surfaces occur at the 15th heating cycle, corresponding to the laser power of 400 W (20 % of the max. laser power). It is worth noticing that the temperature at the centre of the top surface is rather close to the melting temperatures of alumina and spinel, which are 2054 and 2135 °C, respectively.[192] Moreover, one could also notice a shift between the end of the laser sequence and the maximal temperature at the centre of the bottom surface, which is simply related to the time required for thermal transfer from the top surface to the bottom one.

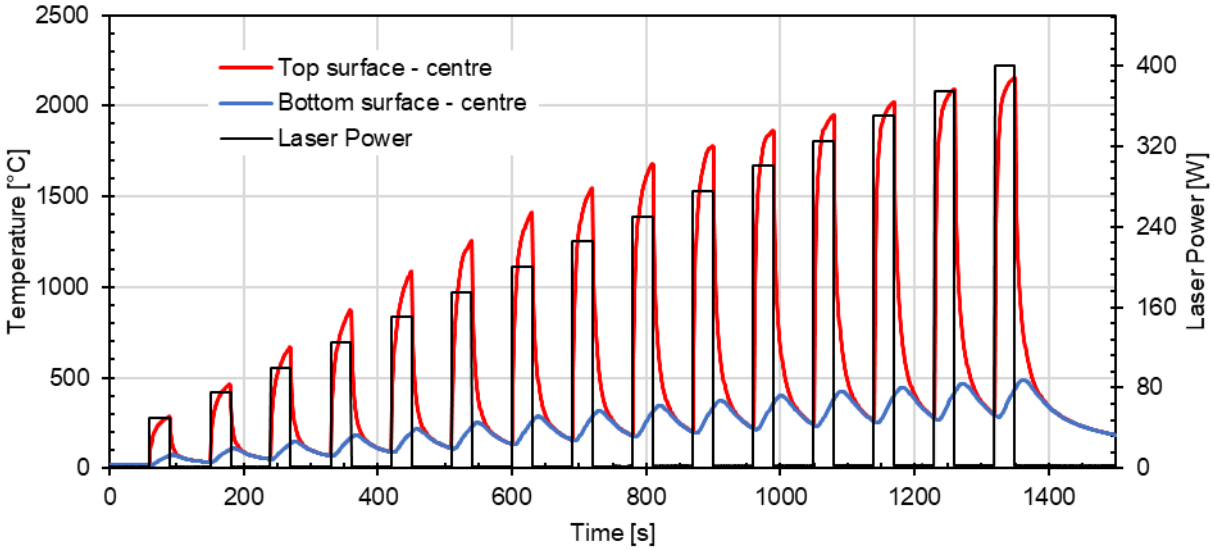

Figure 5-12. Predicted evolution of temperatures for the central point of the top and bottom sample surfaces.

From the fracture behaviour point of view, it is interesting to analyse deeper the temperature field occurring at the 5th thermal cycle, at which the localisation of damage occurs (see section 5.2.6). The temperature profiles at the beginning and at the end of the 5th thermal cycle along the radius are presented in Figure 5-13a and b for the top and bottom surfaces, respectively. One can observe that at the beginning of the heating cycle, the temperature is rather similar on both surfaces and ranges from 50 to 100 °C. At the end of the 5th heating cycle (t=450 s.), a significant difference in temperatures can be observed, which for the top and bottom surfaces are in the ranges of 50-1080 °C and 50-200 °C, respectively. An average thermal gradient through the sample thickness has been calculated based on temperature distributions of the top and bottom surfaces (see Figure 5-13c). One can notice that at the beginning of heating, thermal gradient is almost zero, while at the end of heating it can reach about 90 °C/mm.

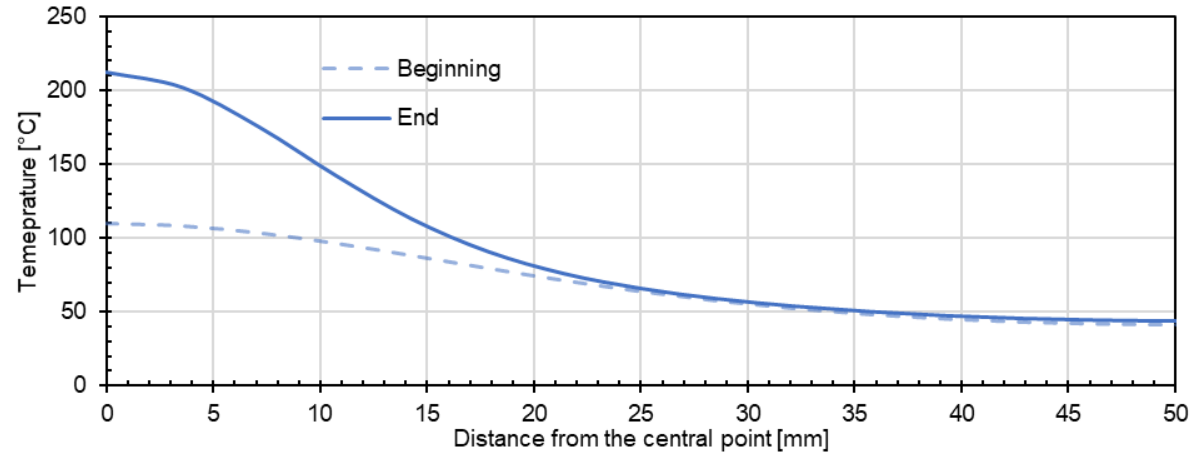

a

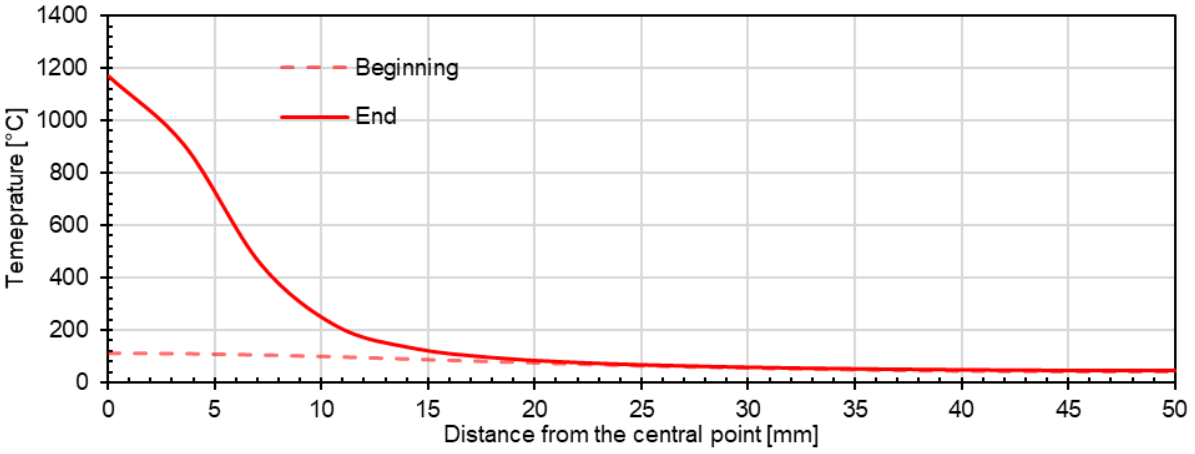

b

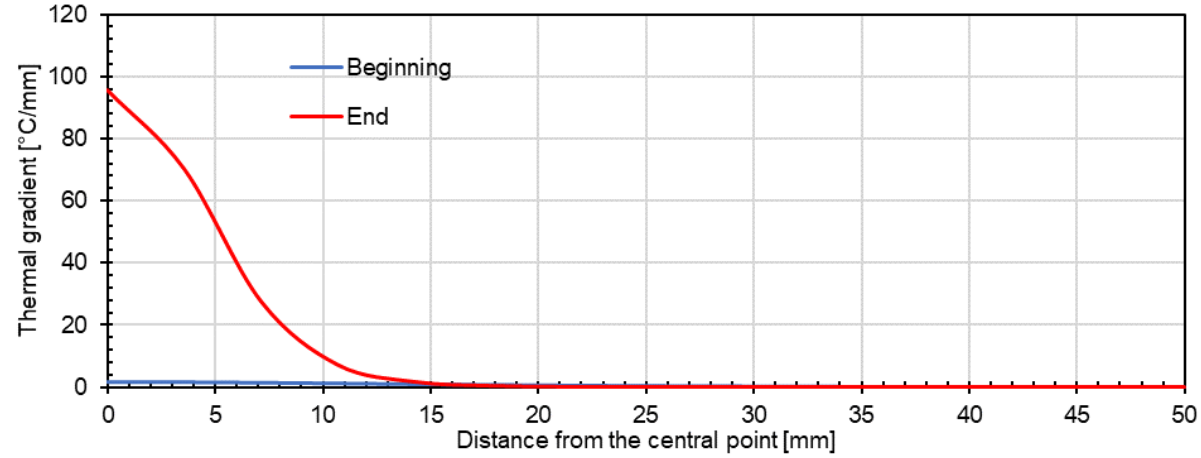

c

Figure 5-13. Temperature representations at the beginning and at the end of the 5th heating cycle: a) temperature profile along the radius of the top surface, b) temperature profile along the radius of the bottom surface, c) average thermal gradient through the thickness along the radius of the sample (based on data from the top and bottom surfaces).

5.2.2.2 *Thermal gradients*

As it could be observed from above-presented figures, the thermal gradient increases with the subsequent heating cycles (at which incremental laser power was applied). In this section, one will analyse thermal gradients based on their directions. One distinguishes the vertical z-direction corresponding to the sample thickness and the radial direction.

5.2.2.2.1 Thermal gradient through the thickness

The gradient in the z-direction is not quantified experimentally but can be estimated from FE modelling (see Figure 5-12). Figure 5-14 presents the evolution of the average thermal gradient through-thickness vs. time, based on the measurement at the centres of the top and the bottom surfaces. Such thermal cycles lead to an increase of thermal gradient which reaches about 175 ºC/mm at the last thermal cycle. It is worth highlighting that the maximal local thermal gradient (not presented here) measured between the central node at the top face and the neighbouring node from the bottom can reach much higher value, close to 900 ºC/mm.

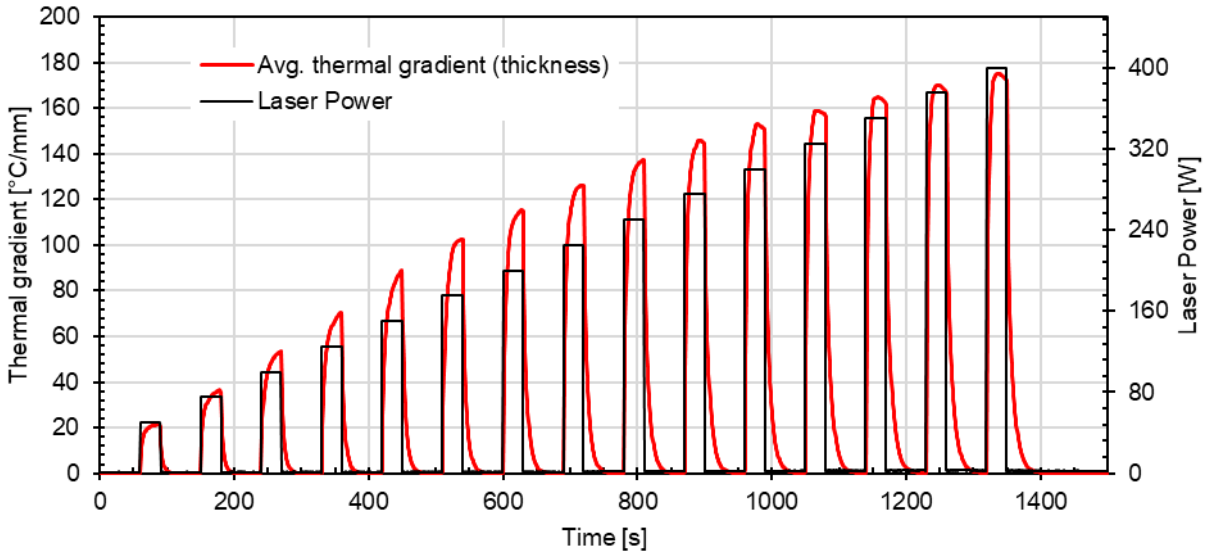

Figure 5-14. Evolution of the average thermal gradient through thickness vs. time (based on numerical results of the central points of the top and bottom surfaces).

5.2.2.2.2 Radial thermal gradient

The gradient in the radial direction could be obtained both from experimental measurement and numerical simulation at the bottom surface and only using numerical simulation at the top surface (see temperature distributions from Figure 5-11b

and Figure 5-13). Thanks to FEM results, these gradients have been calculated for nodes located around a radius of 6 mm (maximum slope in Figure 5-13a) and a radius of 9 mm (maximum slope in Figure 5-13b) for the top and the bottom surfaces, respectively.

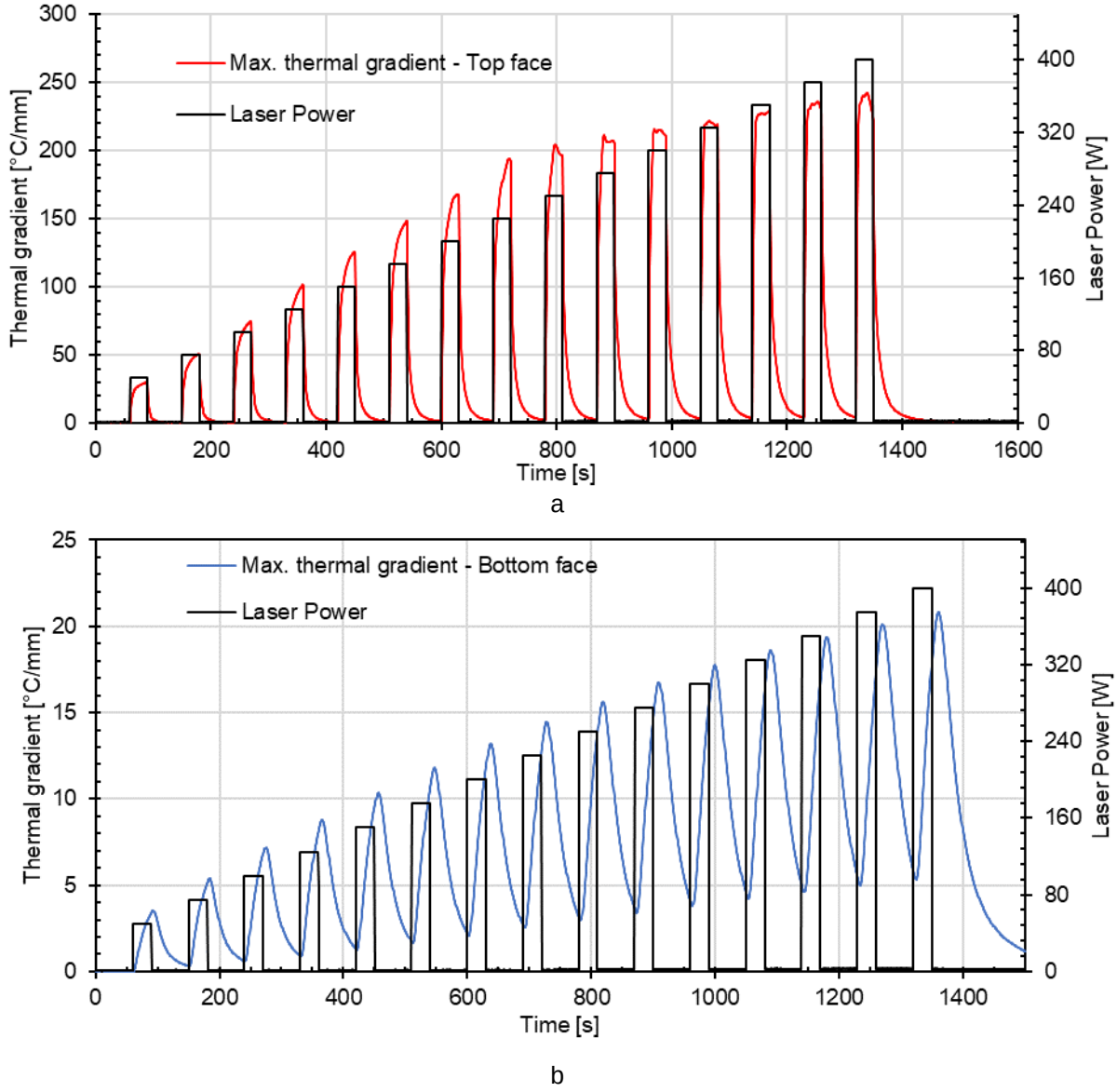

Figure 5-15. Evolution of the maximal local thermal gradients in radial direction: a) at the top surface (measured between the nodes located around a radius of 6 mm), b) at the bottom surface (measured between the nodes located around a radius of 9 mm).

In this way, Figure 5-15 shows the evolution of the maximal local thermal gradients at the top and at the bottom surfaces. This local thermal gradient increases with each cycle and reaches about 240 °C/mm at the top surface and about 20 °C/mm at the bottom surface. Thus, the thermal gradient is much higher at the top surface, compared to the bottom one. As mentioned previously, due to the time required

for thermal transfer between the top and the bottom surfaces, one could notice that the maximum gradient at the bottom surface takes place later, compared to the top surface. This time shift is about 15 seconds at the last cycle.

5.2.3. Distribution of thermomechanical stresses within the sample

Since there is a rather good agreement between the measured and the simulated temperature fields, determined at the bottom sample surface, one can use the numerical simulation to better understand the stress state (time of occurrence, localisation and orientation of the most important stresses) within the sample during the thermal cycling. The calculation was performed assuming that only elastic deformation occurs before the localisation of damage (damage by microcracks nor plasticity is not considered here). Again, the 5th cycle has been selected for this part of discussion. The first and the second principal stresses (σ_1 and σ_2) analysed here stand for radial and hoop stresses, respectively. Three relevant moments around the 5th cycle are considered: just before heating (t = 420 s.), at the end of heating (t = 450 s.) and 30 seconds after heating (t = 480 s.). For these three moments, the calculated radial distributions of the two principal stresses are presented in Figure 5-16 and their three-dimensional distributions are presented in Figure 5-17 and Figure 5-18.

From these numerical results, one can observe that radial stresses are all in compression with the highest values at the centre and decrease to 0 at the sample border (see Figure 5-16a and c, as well as Figure 5-17). At the same time, hoop stresses exhibit both areas under compression (close to the centre) and under tension (close to the border). In fact, the highest compressive hoop stresses always occur at the sample centre, while the maximum tensile hoop stresses appear in different positions depending on the moment of the thermal cycle. This distribution of hoop stresses, presented in Figure 5-16b and d, is related to the restraint of the central part from the thermal elongation by the cold lateral area.

Let us consider now the progressive development of stresses around the 5th heating cycle. As reported in Figure 5-15, just before heating, the sample exhibits a very low thermal gradient, therefore the induced stresses are quite low (see Figure 5-17a, Figure 5-18a, b and blue curves in Figure 5-16). At this stage, the maximal compressive radial stress reaches only -3.5 MPa (at the centre of both the top and the bottom surfaces). In parallel, the hoop stresses range between -3.5 MPa (compression at the centre) and 2.4 MPa (maximal tension at the radius of 43 mm).

The transition between compressive and tensile stresses occurs at a radius of 21 mm (both at the top and at the bottom surfaces).

Then, at the end of heating (red curves in Figure 5-16), a significant thermal gradient is present within the sample (see Figure 5-15). This thermal gradient leads to the development of much higher compressive radial stresses, which reach -127 MPa (at the centre of the top surface) and -21 MPa (at the centre of the bottom surface). In parallel, the hoop stresses (see Figure 5-16 b, d and Figure 5-18 c, d) at the top surface range between -127 MPa (compression at the centre) and 13.5 MPa (maximal tension at the radius of 14 mm) and at the bottom surface between -21 MPa (compression at the centre) and 3 MPa (maximal tension at the radius of 40 mm). The transition between compressive and tensile stresses occurs at a radius of 8 mm for the top surface and 17 mm for the bottom surface.

For the third considered moment, corresponding to 30 seconds after heating, the thermal gradient decreases together with an overall decrease of temperature and with equilibration of temperature across the sample. At this stage, the maximal compressive radial stresses are equal to -8.8 MPa at the centre of the top surface and -8.6 MPa at the centre of the bottom surface. In parallel, the hoop stresses range on the top surface between -8.8 MPa (centre of the bottom surface) and 4 MPa (at the radius of 40 mm) and on the bottom face between -8.6 MPa and 4 MPa (at the radius of 40 mm). The transition between compressive and tensile stresses occurs at a radius of 17 mm (both at the top and at the bottom surfaces).

Globally, these results indicate that stress level are rather the same across the thickness for the two moments: before the 5th heating cycle (at t=420 s.) and 30 seconds after this heating cycle (at t=480 s.). However, at the end of heating (at t=450 s.), a significant thermal gradient (through the thickness and along the radius) results in the development of high stresses at the top sample surface (compressive at the centre and tensile at the radius of 14 mm). These high levels of stresses would lead for sure to local sample damage which can in fact even start during previous heating cycles. At this point, it is important to highlight that the linear elastic model cannot be considered as reliable for comparison of stress values, as it does not take into account damage nor plasticity. However, this very first approach using an elastic linear model is exclusively meant to observe the evolution of stresses (in general) and to identify the areas and moments at which the damage is most likely to occur. Taking into account the obtained results, the development of methods (in addition to strain

field monitoring by DIC on the bottom face) allowing early detection of damage, probably occurring close to the top sample surface, are of interest. One experimental possibility is related to damage monitoring using microcracks detection and localisation thanks to the usage of six acoustic emission sensors. This instrumentation (shortly explained in section 5.1.2.6) is currently in development at IRCER (Limoges, France) but was not yet available at the time of the presented tests.

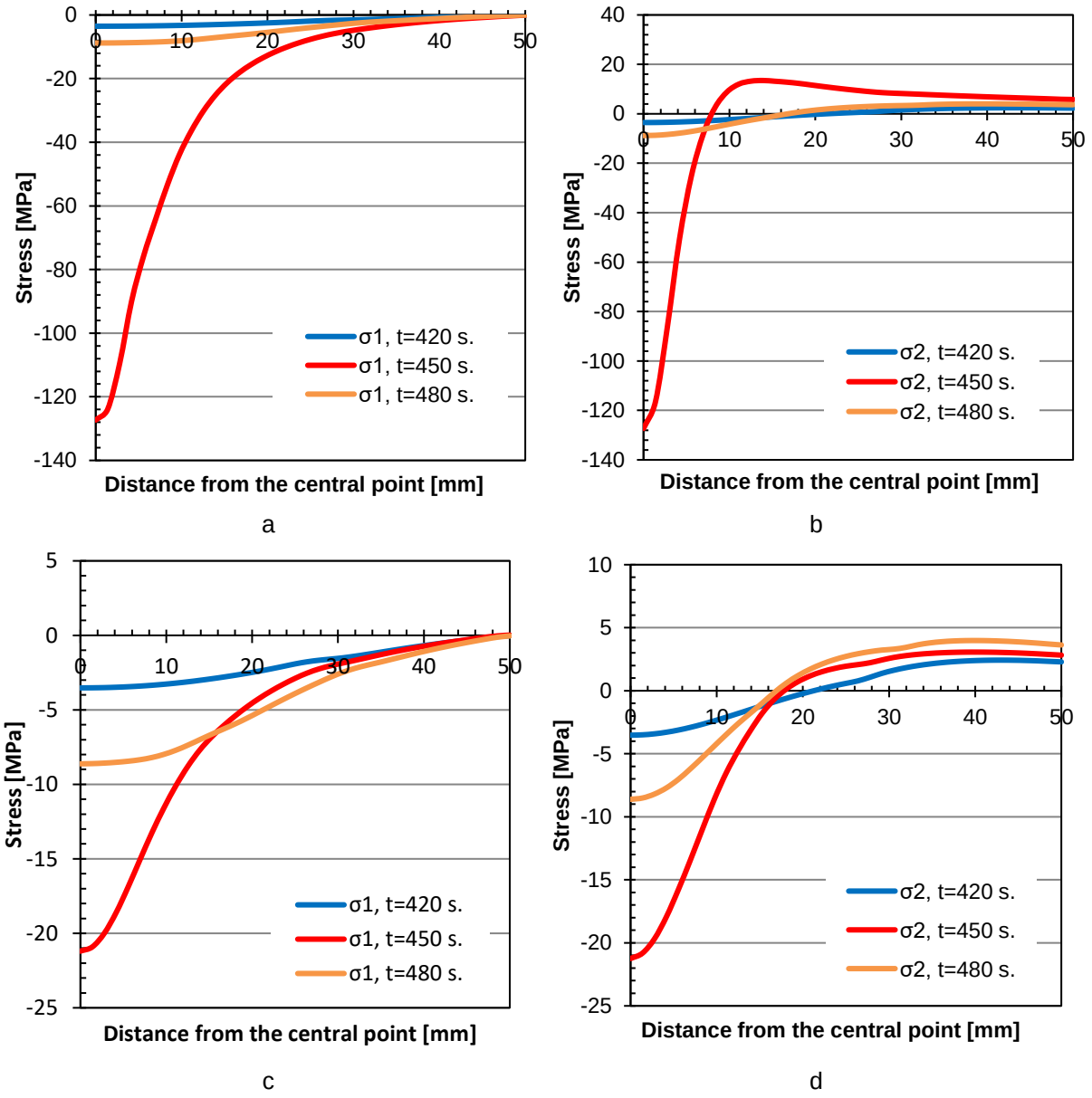

Figure 5-16. Stress distribution along sample radius developed at three relevant moments around the 5th cycle: just before heating (t=420 s.), at the end of heating (t=450 s.) and 30 seconds after heating (t=480 s.). a) The first principal stress (radial) at the top surface, b) the second principal stress (hoop) at the top surface, c) the first principal stress (radial) at the bottom surface, d) the second principal stress (hoop) at the bottom surface.

Another perspective is related to FEM modelling which should, in the future, take into account both damage and plasticity. This improvement seems very crucial,

especially when observing -127 MPa of compressive stresses at the centre of the top sample surface, which is simply unrealistic for the investigated material. In fact, the alumina spinel material is expected to be damaged at much lower stress levels as the compressive strength is around -30 MPa and tensile strength is about 1.6 MPa, using tensile test, and about 3.4 MPa, using Brazilian test.[161,191]

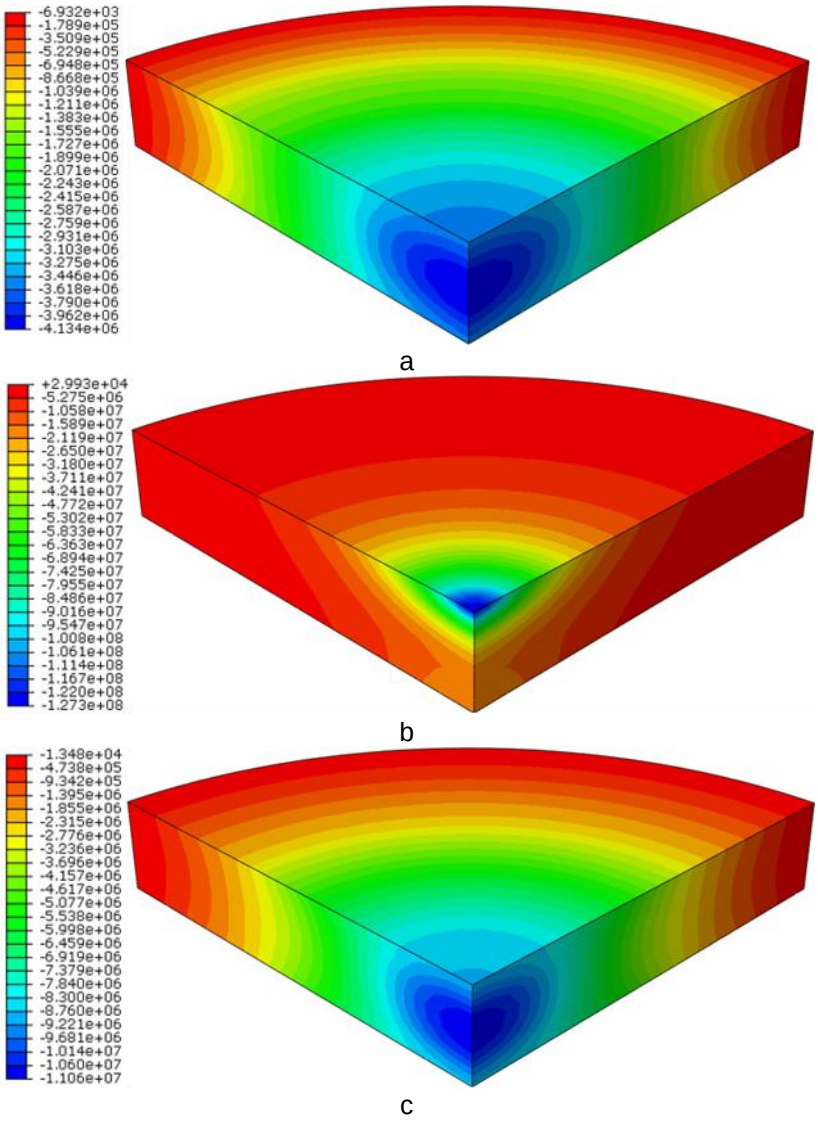

Figure 5-17. 3D distribution of the first principal (radial) stress [MPa] across the sample developed at three relevant moments around the 5th cycle: a) just before heating (t=420 s.), b) at the end of heating (t=450 s.), c) 30 seconds after heating (t=480 s.).

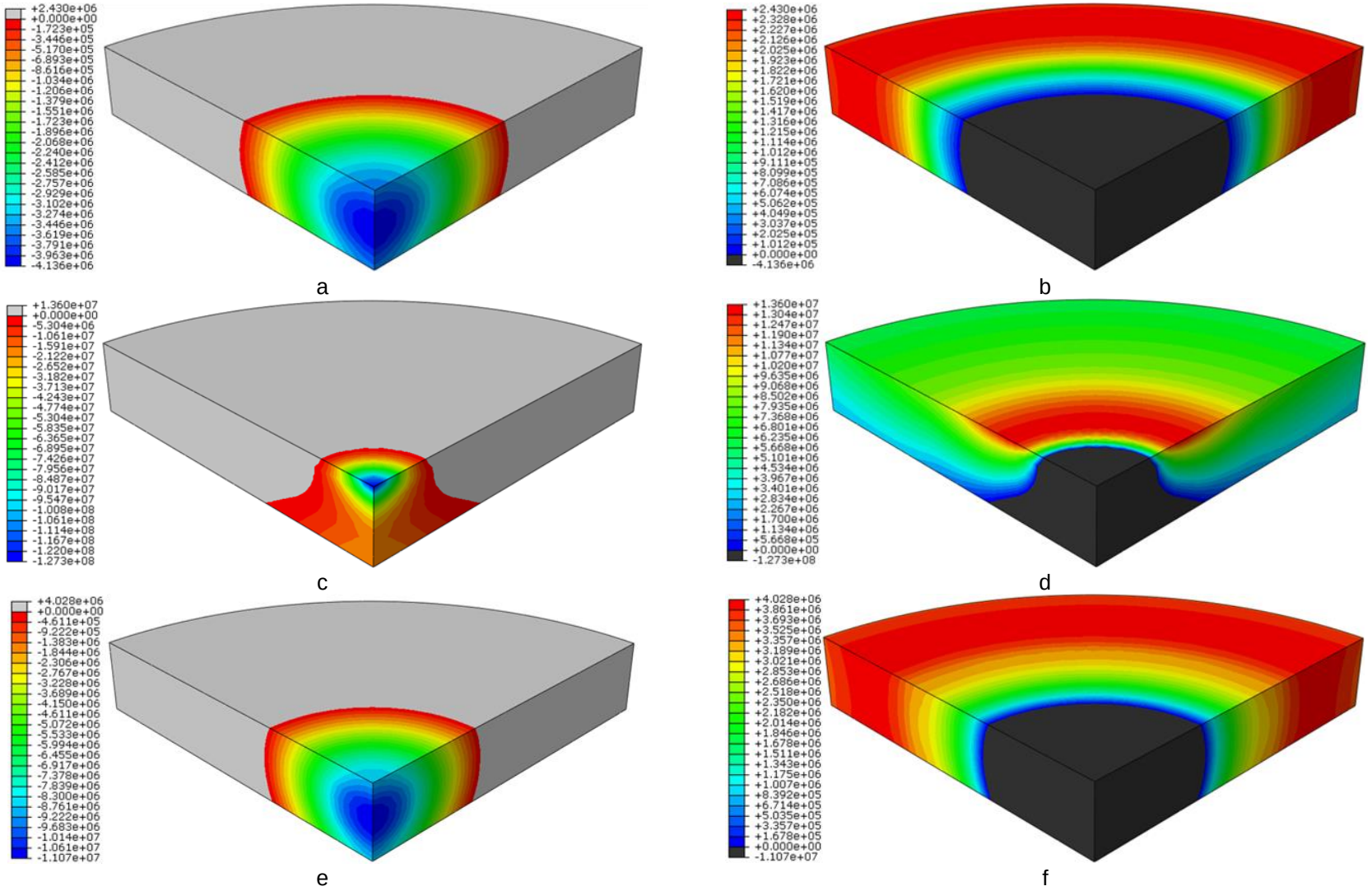

Figure 5-18. 3D distribution of the second principal (hoop) stress [MPa] across the sample developed at three relevant moments around the 5th cycle: a) compressive stresses at t = 420 s., b) tensile stresses at t = 420 s., c) compressive stresses at t = 450 s., d) tensile stresses at t = 450 s., e) compressive stresses at t = 480 s., f) tensile stresses at t = 480 s.

Due to the much lower tensile strength of alumina spinel material, in comparison to the compressive strength, the tensile hoop stresses could potentially lead to sample failure. It is worth noticing that on the bottom surface, monitored by DIC, tensile hoop stresses increase for the three investigated moments from 2.4 MPa (before the 5th heating cycle) through 3 MPa (at the end of the heating cycle) to 4 MPa (at 30 seconds after the 5th heating cycle). These tensile stresses are, in fact, close to tensile strength values reported for alumina spinel brick (values indicated above), which could indicate that the localization of damage observed from the bottom surface (presented in section 3.5) occurs at reasonable stress levels.

5.2.4. Out-of-plane displacements at the bottom surface

As explained in section 5.2.2.2.1, when the laser heats the top surface, a significant thermal gradient is observed through the thickness (see Figure 5-14). This high gradient during heating leads to the development of high level of compressive stresses in the centre of the top surface (see Figure 5-17b and Figure 5-18c, d). As a consequence, similarly to a bimetallic strip system, an out-of-plane displacement in the Z direction could occur. In the present case, this phenomenon (thermal bowing) could be related to the differential thermal expansion between the hotter top surface and the colder bottom one. In order to confirm this fact, 3D DIC measurements (as explained in section 5.1.2.5) have been managed on the bottom surface during the thermal cycles. In spite of very small displacements (in the range of tens of microns) the DIC system was successfully used to determine them. In order to obtain the highest accuracy, the out-of-plane displacements coming from experimental perturbations (not related to sample) have been quantified (by measuring out-of-plane displacement of the markers deposited on the silica ring) and subtracted. These corrected out-of-plane displacement fields are presented in Figure 5-19 for the bottom sample surface at the ends of the first six heating cycles (focussing mainly on the first cycles where there is no crack). These experimental results confirm that the heating cycles, applied to alumina spinel sample, led to thermal bowing. On the one hand, one can observe that the lateral area of the bottom surface exhibit zero out-of-plane displacement, as it is positioned on three isostatic points. On the other hand, the central area of the bottom surface obviously reaches the highest out-of-plane displacement value. This displacement corresponds to an upward movement with a maximum of about 45 µm for the 5th thermal cycle. Evolution of the out-of-plane displacement

vs. time for the very central point of the bottom surface can be observed in Figure 5-20 (see the green curve). The out-of-plane displacement at this point is close to zero when the laser does not heat the sample. Then, during heating, an upward movement of the sample is progressively observed. Subsequently, when the laser is turned off, the heat rather quickly diffuses through the sample thickness and a rather rapid downwards movement is thus observed. This thermal bowing, occurring during heating results from high thermal gradient through the thickness (see Figure 5-14) which leads to high compressive stresses close to the top sample surface (as presented in Figure 5-17b and Figure 5-18c). Additionally, a crack initiation (more discussed in section 5.2.6) can be observed in the out-of-plane displacement fields corresponding to the 5th and 6th cycles (see Figure 5-19).

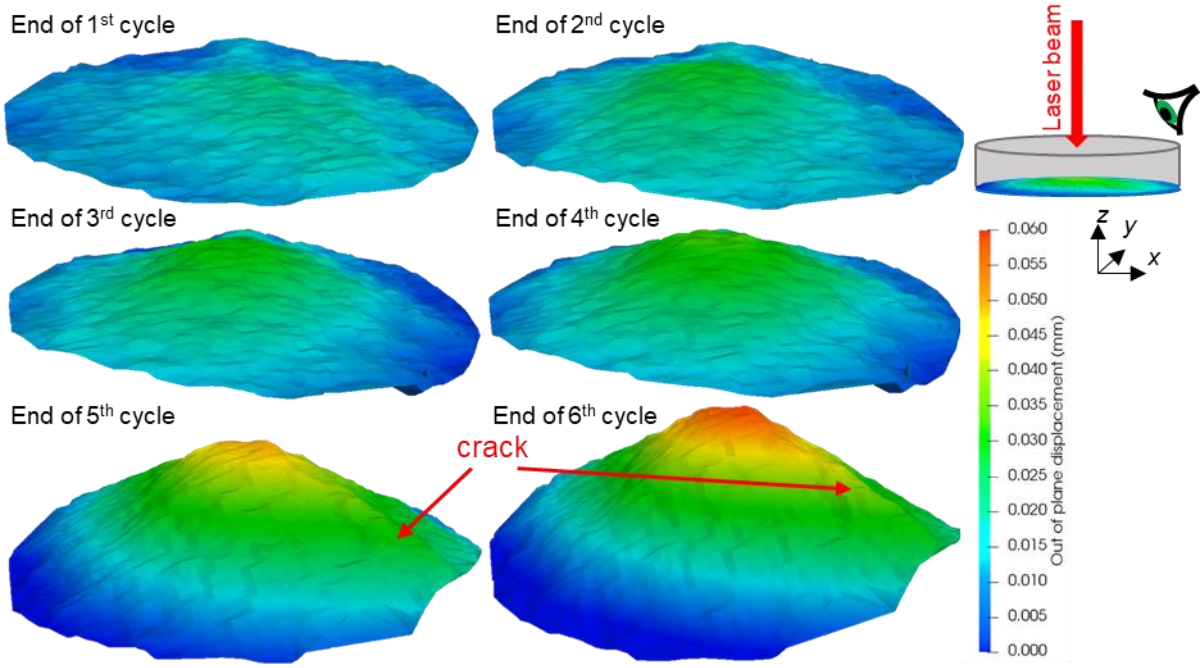

Figure 5-19. Out-of-plane displacements of the bottom surface at the ends of the first six heating cycles (for the moments when the displacements reach the maximal values). These images were obtained with temporal average filtering (±4 images).

In the next step, one can compare experimental and simulated out-of-plane displacement results for the central point of the bottom surface. These experimental and simulated results, presented in Figure 5-20, are in quite good agreement during the first heating cycles. In fact, the crack localisation (initiation of the main crack) was clearly detected (on the bottom surface) during the 5th heating cycle. As a consequence, probably due to low level of damage present before the 5th cycle, the simulated results until this moment fit quite well with real measurements. Later,

a larger amount of damage is present within the sample, but since the simulation does not consider any non-linear behaviour resulting from this damage, the simulated results slightly deviate from the experimental ones.

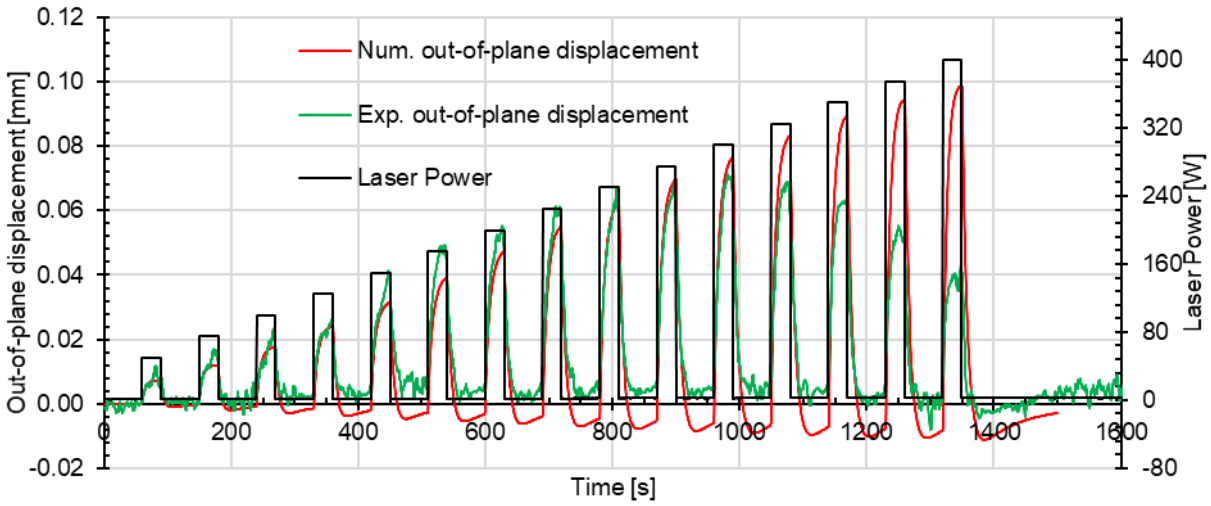

Figure 5-20. Experimental and simulated out-of-plane displacement results for the central point of the bottom surface of an alumina spinel sample during the entire laser sequence.

5.2.5. In-plane thermomechanical strain at the bottom surface

DIC method allowed to experimentally determine in-plane thermomechanical strain at the bottom sample surface. The same information was also predicted using the numerical simulation. Figure 5-21 presents a comparison between the experimental and numerically simulated strain curves plotted for the central point of the bottom surface. At this central point, the first and the second principal strains are supposed to be equal (and the simulated results are equal). However, the experimental results exhibit some differences which are most likely related to material heterogeneity (typical for refractories), not perfectly centered laser and not symmetrical damage. In fact, results from Figure 5-21 demonstrate that until localisation of damage, which occurs at the 5th heating cycle, simulated results of the first principal strain show a relatively good agreement with the experimental ones. Taking into account that numerical simulation does not consider material damage, it is natural to observe discrepancy between these results after the appearance of the macrocrack. In reality, this cracking affects stress and strain fields leading to stress relaxation, which enables higher increase of strain at the central point of the bottom surface (see Figure 5-21). Moreover, at this central point, the difference between the first and the second principal stress increases significantly due to the loss of symmetry caused by cracking. Therefore, the experimental out-of-plane

displacement results are considered relevant before the macrocracking which occurred during the 5th heating cycle.

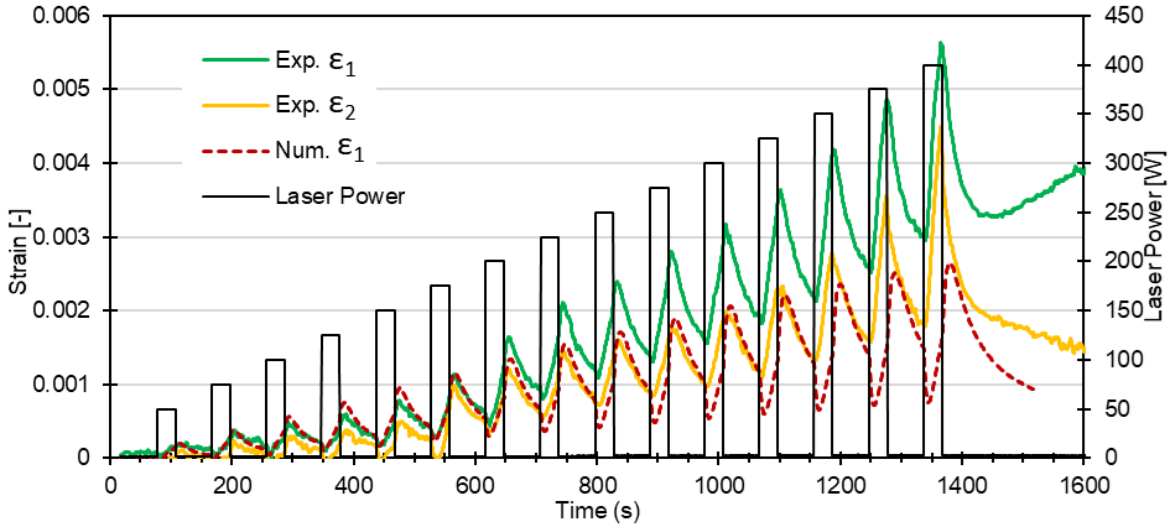

Figure 5-21. Strains in the alumina spinel sample at the centre of the bottom surface.

The principal strains, presented in Figure 5-21, contain both mechanical and thermal contributions, which result in a relatively high strain values being mainly driven by thermal expansion. However, as already explained in section 5.1.3.3, by subtracting thermal strains ε_T from total strains (ε_1 or ε_2), mechanical contribution ε_{1mech} can be determined, as illustrated for the first principal strain ε_1 in Equation 5-3.

$$\varepsilon_1 - \varepsilon_T = \varepsilon_{1mech} \qquad \text{Equation 5-3}$$

As demonstrated in Figure 5-8, the experimental instrumentation allows the determination of the total strains (using visible light cameras and DIC) and thermal strains (using infrared camera and isotropic thermal expansion). However, for better understanding (avoiding noise from experimental measurements), strains obtained from numerical simulations will be discussed here. Figure 5-22 presents total, thermal and mechanical strains along the radius of the bottom surface for the first and the second principal strains. It can be observed that total principal strains reach relatively high values, which are mainly related to thermal contribution. It is interesting to notice that mechanical strains along radius in both radial and hoop directions look very similar to the radial distribution of stresses (from Figure 5-16). These mechanical strains in the radial direction have compressive character, reaching the highest values at the centre and decreasing to zero while approaching the sample border. However, the mechanical strains in the hoop direction have a compressive character close to the centre and tensile character on the lateral sample part.

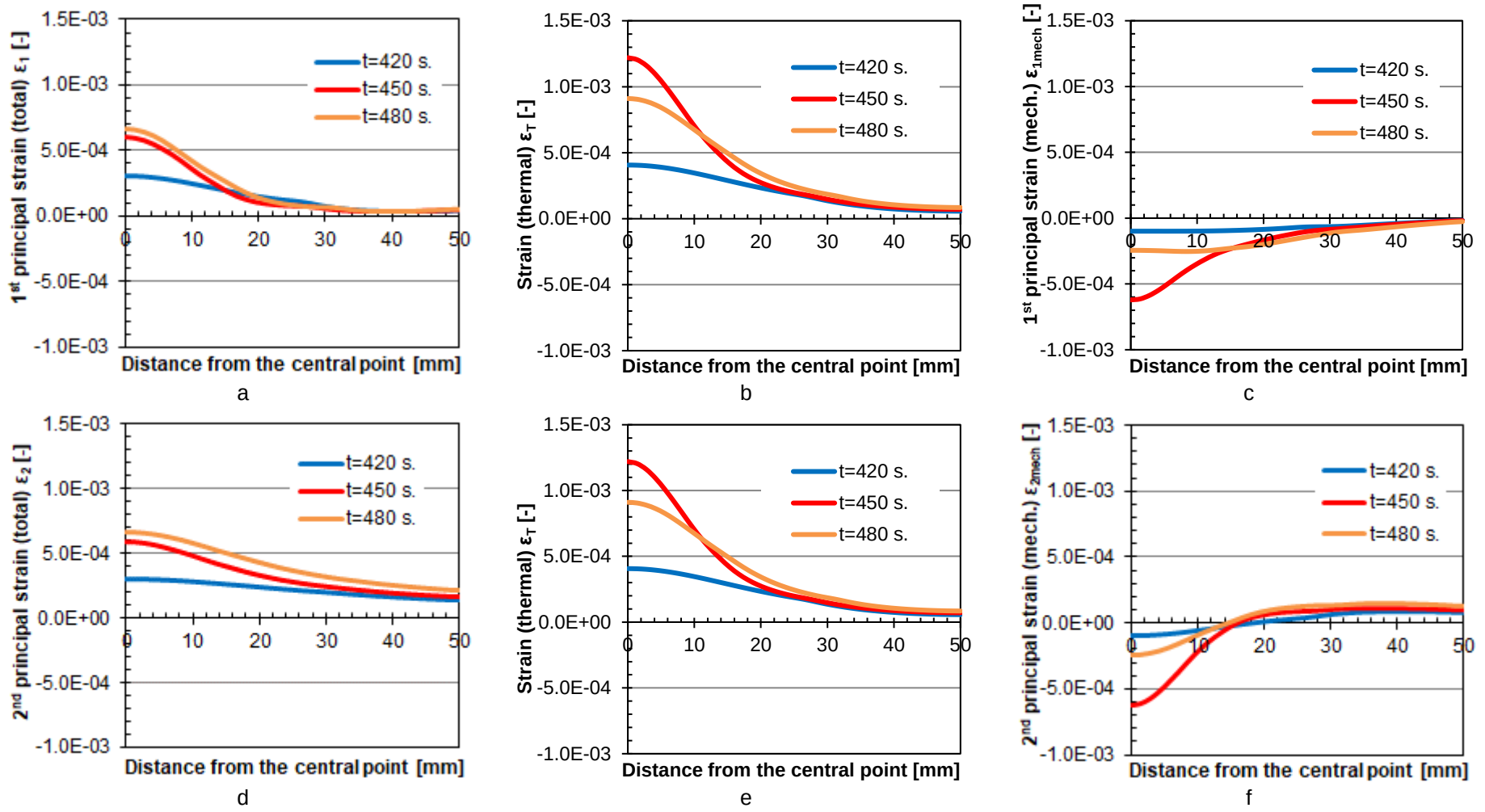

Figure 5-22. Strain profiles along the radius on the bottom sample surface developed at three relevant moments around the 5th cycle: just before heating (t=420 s.), at the end of heating (t=450 s.) and 30 seconds after heating (t=480 s.). a) the first principal strain (total), b) thermal strain, c) the first principal strain (mechanical), d) the second principal strain (total), e) thermal strain (the same as b), f) the second principal strain (mechanical).

5.2.6. Crack monitoring by optical techniques

DIC and 2P-DIC techniques allow to determine temporal evolutions of Crack Opening Displacement (COD) and Crack Length (CL) during thermal shock test. Crack Opening Displacement (COD) is measured by applying “virtual extensometers” (using DIC) to the images of sample surface. Each virtual extensometer consists of a set of two subsets located around an area of interest e.g. on both sides of the crack initiation area (close to the border). Relative displacement (being COD) is then measured between these two subsets. This approach requires knowledge about a position of crack initiation. This position is determined with a use of 2P-DIC method, which allows observing evolution of the crack path with high resolution. Once the position of the crack initiation is well-known, this method is used to place the virtual extensometer(s), as presented in Figure 5-23. In this specific case, two virtual extensometers have been positioned: one (red colour) in the area where a crack occurs (to measure temporal evolution of COD) and one (light blue colour) in the area where no (macro)crack is detected. Subset dimensions are 80x80 pix.^{2} and the initial distance between their centres is about 120 pix. (with magnification equal to 13 pix/mm). Crack Length (CL) evolution with time is determined (as the total instantaneous crack length) from 2P-DIC method (as already explained in section 3.2.4).

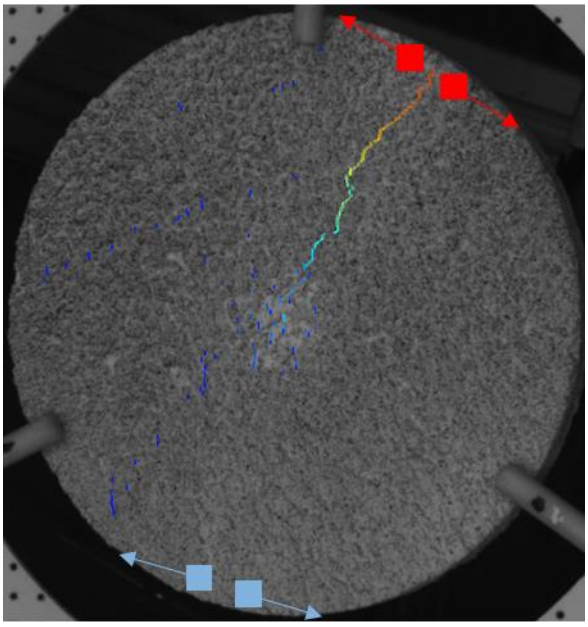

Figure 5-23. Picture taken at the end of the testing sequence with already developed crack (highlighted by 2P-DIC). The two red squares indicate the exemplary initial positions of the subsets used to monitor Crack Opening Displacement (COD). The two light blue squares indicate the initial positions of the subsets used for determination of strain increase (where no macrocrack is detected).

The temporal evolutions of both COD and CL during the laser heating program are presented in Figure 5-24 and Figure 5-25. In this case, both curves were smoothed by average filtering with a window size of 9 (+/- 4 values). One can observe that both COD and CL begin to increase significantly at the 5th cycle. COD significantly increases from 443 s., which is about 4 s. earlier than CL. This difference is related to the pseudo strain threshold which needs to be applied in the case of 2P-DIC method to separate cracks from noise. On the contrary, COD, representing relative displacement between points located on both sides of the area where the crack emerge, does not require any threshold and therefore is able to earlier detect emergence of a localised crack.

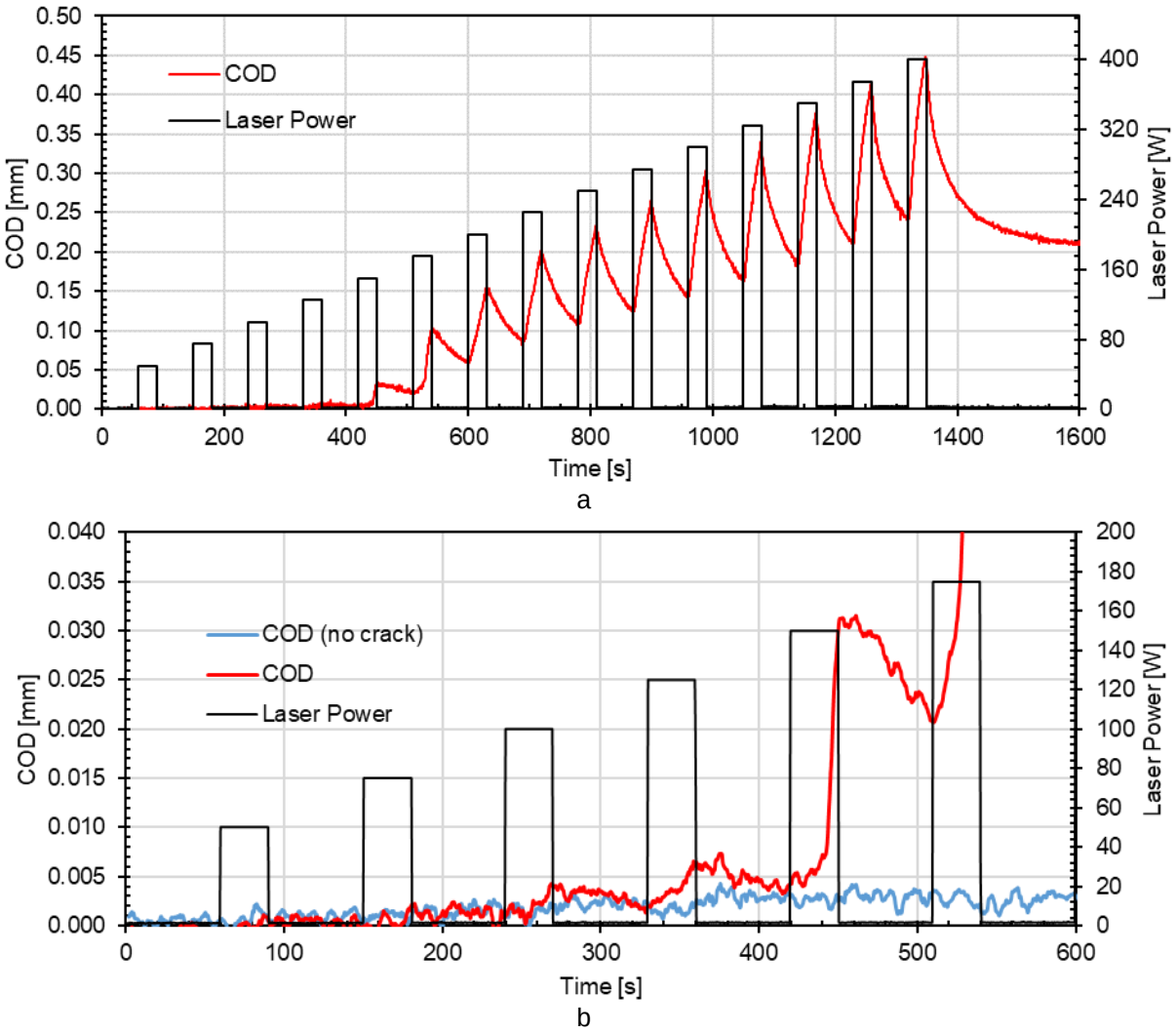

Figure 5-24. Evolution of Crack Opening Displacement (COD) vs. time: a) the entire curve, b) zoom until the emergence of macrocrack.

Figure 5-24b and Figure 5-25b present zooms for COD and CL evolution curves in order to analyse the signals before localisation of the macrocrack in the 5th cycle. One can observe no CL evolution during the preceding thermal shock cycles. However,

COD visibly varies during the 4th thermal cycle (increase during heating and decrease during cooling) and maybe even during the 3rd thermal cycle. The “COD” evolution for the area without evolution of macrocrack has been plotted for comparative purposes, using light blue coloured set of subsets. In this case, one cannot distinguish clear cycling of the “COD” value related to applied heating cycle(s). It could indicate that the area where the crack localized during the 5th heating cycle could have been slightly damaged during the previous heating cycles. This point is interesting for future tests with acoustic emissions monitoring which could allow detect and localise microcracking occurring before localisation of macrocrack.

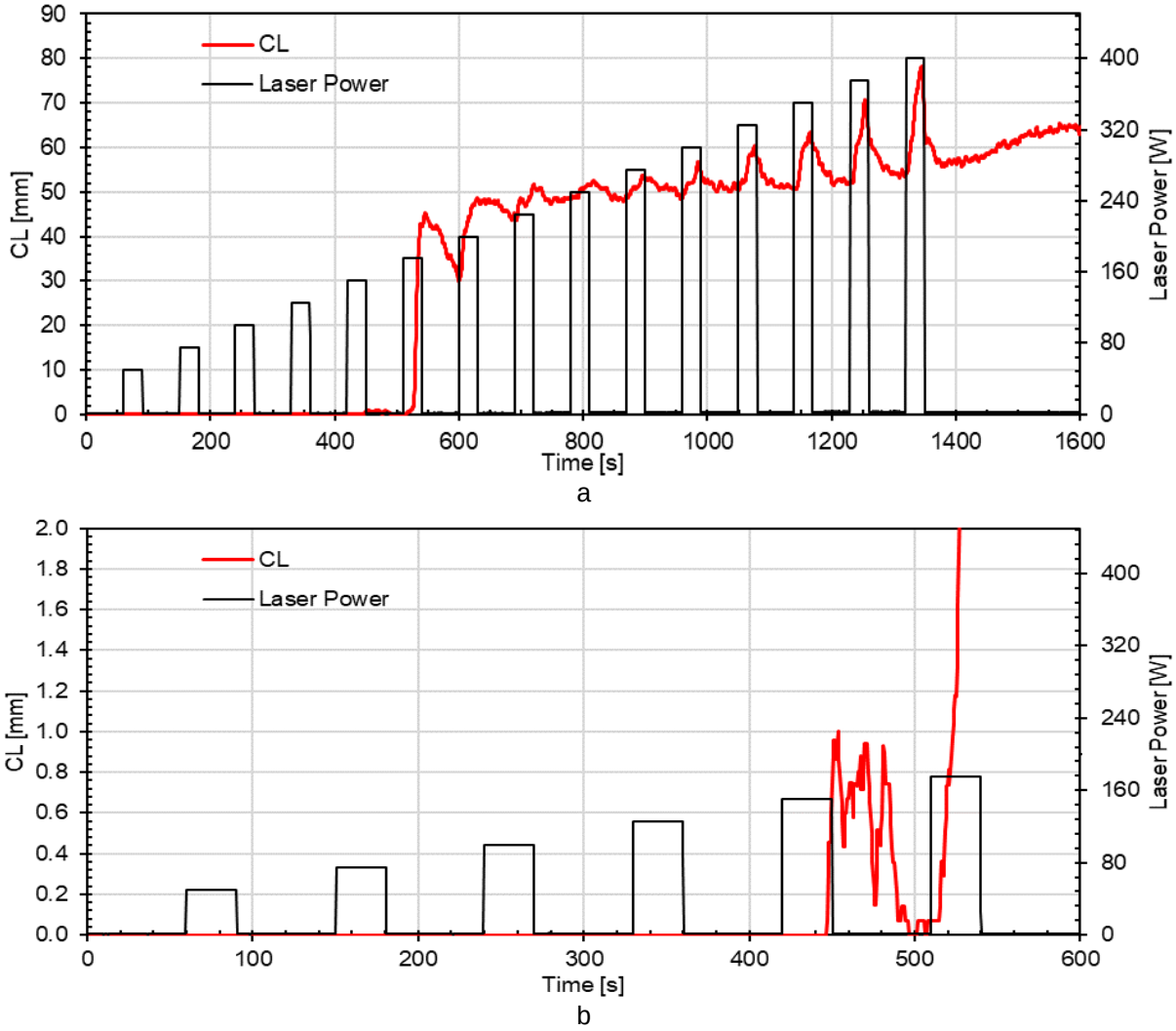

Figure 5-25. Evolution of Crack Length (CL) vs. time: a) the entire curve, b) zoom until the emergence of macrocrack.

According to stress distributions (see Figure 5-16, Figure 5-17 and Figure 5-18), one can observe that the highest level of tensile stresses is present during heating on the top sample surface, and therefore, this area is potentially the most subjected

to failure. Therefore, it is reasonable to assume that any crack present on the bottom surface can be a result of the crack propagation, initially generated at the top sample surface and thus it may be observed with a slight delay.

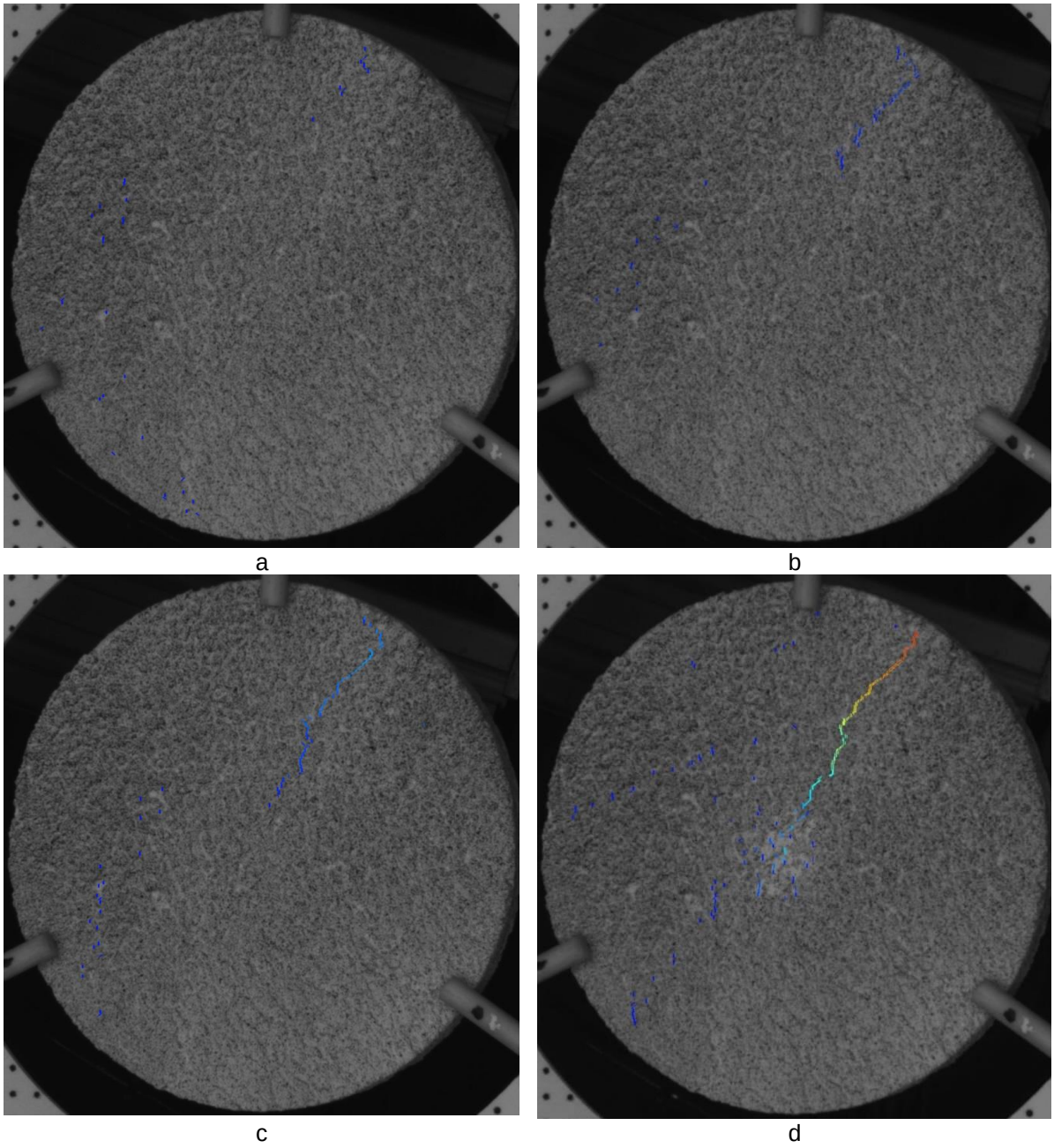

Figure 5-26. View of the bottom sample surface with a crack generated by 2P-DIC method at: a) 450 s. (end of 5th heating cycle), b) 532 s. (6th heating cycle - after the first sharp increase of crack length), c) 630 s. (end of 7th heating cycle), d) 1344 s.(close to the end of the 15th heating cycle). Legend for the cracks colour: blue and red colour correspond to the crack opening displacement of ~ 0.03 µm and ~ 0.43 µm, respectively.

Exemplary pictures with crack representation, obtained using 2P-DIC are presented for four different moments in Figure 5-26. One can observe that crack at the end of the 5th heating cycle (see Figure 5-26a) appears discontinuous, probably

due to the reason that measured strain values for some areas of the crack did not exceed the pseudo-strain threshold (0.004). Moreover, some small cracks can be observed in different areas of the sample, which could indicate potential diffused damage before localisation of the macrocrack. Then, at the following cycle, crack length increases (see Figure 5-26b) and looks more continuous. At the end of the 7th heating (see Figure 5-26c), both crack length and crack opening visibly increase and diffused damage is visible on the left sample part. At the last heating cycle (see Figure 5-26d), one crack with a huge crack opening is visible together with heterogeneous diffused damage on the sample surface.

5.2.7. Potential crack monitoring by acoustic emissions

As mentioned in section 5.1.2.6, no result has been obtained with acoustic emission part of ATHORNA device during the present PhD study. Nevertheless, just to showcase briefly, a typical result that could be obtained (see Figure 5-27) demonstrates that acoustic events could be detected and localised during thermal cycle. Such results obtained by Yasmine Lalau on SiC sample demonstrates that acoustic emission localisation results are in quite good accordance with crack observed on the sample after the test. Taking into account this result, one can quite interesting results measured on refractories in the near future.

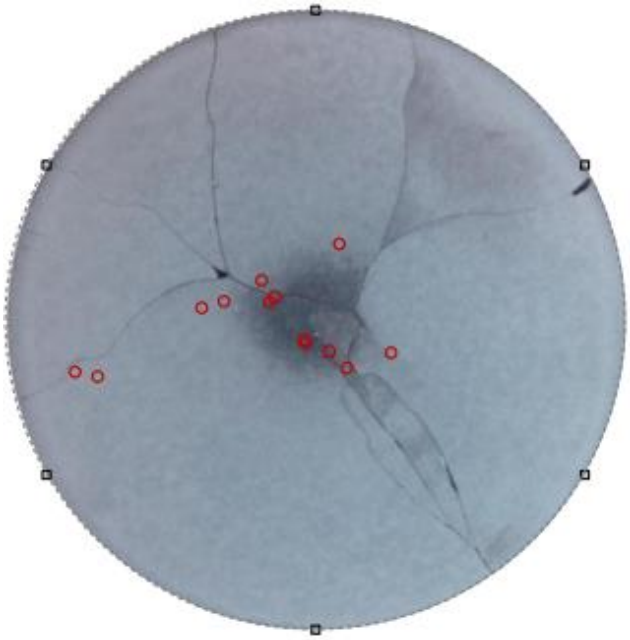

Figure 5-27. Photo of SiC sample after the thermal shock test (visible cracks) with superposed localized acoustic events detected during the test (red circles).[186]

5.2.8. Conclusions

As mentioned in section 5.1.1, widely used thermal shock techniques with a posteriori evaluation (of Young's modulus or modulus of rupture) provide little information about sample behaviour during thermal shocks. In order to improve understanding on the progression of damage during thermal shocks, several research groups developed testing devices with in-situ monitoring of sample behaviour. Presented ATHORNA device, thanks to sophisticated heating source as well as optical, thermal and acoustic emission sensors, ranks among the most promising devices in this category.

Additionally, ATHORNA device targets to compare experimental measurements with numerical results (FEM) in order to validate modelling approach. In fact, the experimental part is complex and challenging, due to the need to perform tests at high temperature with in-situ measurements, involving quick change of parameters and low range of variations (especially for strain field). Thanks to the previous studies,[99,186] several experimental trials (not presented here) have been performed and some improvements of this technique have been performed. The present work allowed to demonstrate that ATHORNA device can be used to acquire experimental data with rather high precision. The numerical part is also demanding, as several temperature-dependent parameters (most of them are presented in section 4-1) had to be experimentally measured in order to build the FE model.

Finally, by comparison of experimental and numerical results **it was possible to validate** with quite good agreement **evolution of temperature, as well as out-of-plane displacement and strain in the centre of the bottom sample surface**. It should be noted that validation of the displacement and strain fields is relevant until the initiation of the macrocrack (detected during the 5th heating cycle), as damage was not considered in presented simulations. Once the damage would be introduced in a more complex model, validation of displacement and strain fields after the damage initiation should also be possible.

General conclusions

This work had two main objectives. On one hand, one aimed to **better understand in-use behaviour of alumina spinel refractories** (dedicated to steel ladle). On the other hand, significant effort has been made to **improve advanced experimental devices**. As a consequence, the general conclusions have been divided into two parts: the first one is material-oriented (alumina spinel bricks and castables) and the second one concerns the improved experimental methods (high temperature mechanical tests and thermal shock bench “ATHORNA”, both coupled with DIC methods).

Findings related to investigated materials

Case of alumina spinel bricks

The study performed on alumina spinel bricks allowed to **provide accurate data for numerical modelling** and to improve understanding of thermomechanical behaviour. The most interesting findings include microcracking occurring during cooling (after sintering), brittle-ductile transition (around 1100 °C) as well as evolution of spinel content and stoichiometry (resulting in permanent material expansion) due to the applied thermal treatment.

Detected **microcracking** has been attributed to thermal expansion anisotropy of white fused alumina aggregates. **Brittle-ductile transition**, occurring around 1100 °C, was attributed to the increased plasticity of alumina-rich spinel probably due to enhanced mobility of cations with presence of cations vacancies. However, the **evolution of spinel content** (increase of 5 wt. %) **and stoichiometry** (1-2 wt. % of alumina enrichment) due to the thermal treatment (with 1h dwell at 1500 °C), indicates an interaction between alumina and spinel phases.

This behaviour most likely has positive impact in application. Firstly, the formed microcracks can improve thermal shock resistance during the first convertor tapping. Secondly, permanent thermal expansion (occurring above 1300 °C), related to increase of spinel content, can promote joints closure. Moreover, temperature-dependent stoichiometry of alumina-rich spinel induces counter-diffusion between alumina and spinel which could result in crack healing during thermal cycling.

Potential perspectives for investigation of alumina-spinel bricks could be related to microstructural and thermomechanical changes depending on different

pre-treatments applied from 1100 °C to 1900 °C (range over which stoichiometry of alumina-rich spinel changes). Depending on considered temperature, spinel stoichiometry and relative spinel/alumina content would be different what can play a significant role in thermomechanical behaviour. Especially, it could be interesting to provide more information about viscoplastic behaviour of alumina rich spinel at high temperatures e.g. in relation to alumina content within spinel. Until now this topic is not exhaustively documented in the literature.

Case of model alumina spinel castables

The investigation of model alumina spinel castables **provided more information about thermomechanical and microstructural effects of different types of cements, reactive aluminas and alumina aggregates** on final castable properties. The most interesting findings could be summarized as follows.

CMA cement grains lead to **formation of smaller pores around the cement grains** (under the specific testing conditions) when compared to CAC. Origin of this difference has been attributed to two phenomena. Firstly, high water solubility of calcium aluminate phases can result in dissolving the external part of CAC grains which can be followed by recrystallization in another area. In the case of CMA grains, the initial volume can be better maintained thanks to the presence of MA skeleton (not reacting with water). However, in the case of CAC particles, the initial particle size is likely to be reduced. Secondly, a detected **change of spinel stoichiometry** (alumina enrichment of 3-5 wt. %), due to thermal treatment up to 1500 °C, happens with a permanent local expansion which can contribute to reduction of pore size in the area of the initial CMA grain. Other thermomechanical differences observed between these cements are related to higher CaO content within CAC particles.

The type of **bimodal reactive alumina seems to have a significant impact on mechanical properties of castable at high temperatures**. The alumina with reduced soda content seems to increase refractoriness and resistance to creep of the castable, while the alumina with higher fines content could result in slightly lower refractoriness and resistance to creep of the castable. **The type of alumina aggregate influences castable mechanical properties** (especially high temperature ones) **and evolution of Young's modulus during thermal treatment.** The WFA-based castables exhibit higher refractoriness, better creep resistance, as well as improved fracture behaviour after pre-treatments at lower temperatures (at 110 and 600 °C),

compared to TA-based ones. However, after pre-treatment at 1500 °C, thermal shock behaviour of both types of castables is rather similar.

As a perspective, the tests performed using WST after different pre-treatments could be repeated by e.g. modifying particle size distribution (excluding certain fractions of grains) as it could lead to relevant differences in fracture behaviour and thus in thermal shock resistance. Additionally, microstructure of TA and WFA aggregates and their impact on microcracking in TA- and WFA-based castables could be more investigated in relation to both crystal size and orientation, e.g. using EBSD. Another interesting topic is related to addition of spherical alumina fines instead of angular reactive alumina, obtained by grinding. Its impact on flow is rather clear, however its potential impact on mechanical properties is not yet documented.

Findings related to improved methods

The work dedicated to experimental methods was focused on improvement of high-temperature optical methods applied to mechanical tests as well as on development of the new thermal shock testing device.

The improvement of high temperature optical measurement required to focus on sample surface preparation (speckle), acquisition conditions (minimization of high temperature disturbances) as well as on optimal parameters for numerical treatments. Different speckle patterns, potentially stable at high temperature, have been investigated, using BFA and SiC grains with different sizes. According to this study, **the best performing speckle pattern for the considered setup consisted of silicon carbide grains with a grain size between 50 and 100 µm**. **High-temperature related disturbances** (heat haze, black body radiation) **have been reduced** thanks to application of the blue bandpass filter (transmits blue light, being the least affected by black body radiation) and air blowing (reducing heat haze). Thanks to the improved image acquisition setup **relatively stable images have been acquired at 1200 °C** (maximal operational temperature of the furnace). Tests on image processing (image filtering, image size reduction) preceding DIC and 2P-DIC analyses allowed to find a compromise between high measurement accuracy and relatively short duration of processing. Exemplary application of the improved procedure to mechanical tests has been presented using Brazilian test at 20 and 1200 °C. This improved setup and investigation procedure can be transposed to other high-temperature experimental setups such as wedge splitting test or thermal shock bench (ATHORNA).

Due to the fact that the most popular thermal shock testing approaches provide very little information on refractory behaviour during thermal shock (a posteriori evaluation of damage), it appeared relevant to study thermal shock behaviour with the novel ATHORNA device. Thanks to well-controlled heating source as well as optical, thermal and acoustic emission sensors, this device ranks among the most promising ones dedicated to in-situ monitor samples subjected to thermal gradient. The investigations performed on ATHORNA device had two main objectives: one aiming to approach validation of FE models with experimental results and another one with a goal to experimentally compare thermal shock behaviours of different materials.

During this very first experimental campaign with ATHORNA device, **comparison of experimental and numerical results allowed to validate evolution of temperature, out-of-plane displacement and strain on the bottom sample surface with a relatively good agreement**. At this stage, FE modelling did not consider any damage progression within the sample, thus validation of displacement and strain fields was only relevant until initiation of macrocrack (detected during 5th heating cycle).

A comparative study performed on different magnesia-based spinel-containing materials (reported in Annex A) highlighted **potential application of ATHORNA device in better understanding materials behaviour under thermal shock conditions**. For comparative purposes, a set of parameters has been defined. They originated from both ATHORNA and WST devices, as well as from material composition (spinel inclusions content). All these parameters have been summarized in the correlation matrix to facilitate comparison. It has been revealed that the increase of spinel inclusions content delays initiation of localised damage, most likely by diffused damage (microcracking) before the occurrence of a macrocrack. Moreover, the correlation between the increase of strain before crack initiation (from ATHORNA device) and the measure of brittleness (from WST device) indicates that less brittle materials can withstand higher strain before crack initiation (probably related to diffused damage). This demonstrates that ATHORNA device could potentially be used to rank materials (in a similar way as WST) depending on their resistance to thermal shocks. Additional observation is related to an increase of inclusion content that often results in more progressive crack opening after crack initiation, as well

as in higher final crack opening and final crack length probably due to higher tortuosity of crack path which hinders closure.

Regarding perspectives, one should bear in mind that ATHORNA device is still a prototype and many enhancements can be implemented. First of all, the CO_2 laser is not yet available in the laboratory (planned to be purchased) and the current study was performed thanks to the cooperation with ILP Laser company which allowed to access their laser. This resulted in limited testing possibilities and thus, only several experimental tests were managed. Obviously, it would be useful to perform more experiments, e.g. to verify repeatability of the defined parameters. Secondly, acoustic emission measurement has been installed in Limoges at the very end of this PhD study and, so far, only calibration tests were performed with these sensors. It should be noted that the efficiency of these acoustic emission sensors has already been demonstrated in framework of another PhD study, performed at Promes laboratory (in 2017). Further analysis, comparing the output of optical and acoustic measurements would be very interesting. In particular, it could lead to much better understanding of sample degradation during the thermal shock tests, especially for determination the onset of internal damage. Moreover, the currently used IR camera has rather low resolution and low acquisition frequency (1 image per 2 seconds) and thus better camera could improve the spatio-temporal resolution of thermal field.

Concerning the numerical part, more advanced mechanical models can also be used in subsequent studies, such as damage plasticity model. It would allow to describe more accurately materials with significant non-linear behaviour, e.g. magnesia hercynite refractory (studied alumina spinel bricks had rather moderate non-linear behaviour).

Annex A. Comparative testing of thermal shock resistance with ATHORNA

Studying thermal shock behaviour of refractory materials is a very attractive topic, especially when measurements are performed on advanced devices with multiple sensors. The objective of this part of study was to **determine whether ATHORNA device can be used for comparative studying of refractories resistance to thermal shocks**. Materials selected for this investigation originate from the PhD study of Imad Khlifi (performed in frames of the FIRE network) who worked on magnesia-based refractories with spinel aggregates.[99] The key point of their microstructure consists on introduction of magnesium aluminate spinel ($MgAl_2O_4$) and/or iron aluminate spinel ($FeAl_2O_4$) aggregates, being well-known for improving both fracture and thermal shock resistances of magnesia-based refractories. Therefore, simple variations in volume fraction and/or in type of spinel aggregates within such system, inducing significant differences in fracture behaviour, appeared very suitable for this particular investigation.[99]

A-1. Presentation of investigated model magnesia spinel bricks

Model refractory magnesia spinel bricks selected for this study are presented in Table A-1. Each material has a specific reference, which is composed of several symbols:

- M stands for magnesia;
- S, H or SH refer to the type of coarse spinel aggregates, where S - spinel, H - hercynite and SH - a mixture of spinel and hercynite;
- 5 or 15 refer to the content of coarse aggregates in wt. %.

In total, seven materials were tested, including one magnesia refractory without spinel aggregates, three magnesia refractories with 5 wt. % and three magnesia refractories with 15 wt. % of coarse aggregate additions. More details concerning these materials are presented in the publicly available PhD thesis of Imad Khlifi.[99]

Table A-1. Composition of model magnesia and magnesia spinel bricks.

Reference	MgO	$MgAl_2O_4$	$FeAl_2O_4$	$MgAl_2O_4$ & $FeAl_2O_4$
M	100%	-	-	-
MS5	95%	5%	-	-
MS15	85%	15%	-	-
MH5	95%	-	5%	-
MH15	85%	-	15%	-
MSH5	95%	-	-	5%
MSH15	85%	-	-	15%

A-2. Applied heating cycle

Taking into account experiences from previous trials with the CO_2 laser (as a heating source), the heating procedure was specifically designed to detect changes in fracture behaviour between different samples. This heating procedure, presented in Figure A-1, consists in irradiating sample's hot face by applying 21 heating cycles with the duration of 30 seconds (alternating with 60 seconds break) and with gradually increasing laser power (from 100 to 400 W with the increments of 15 W).

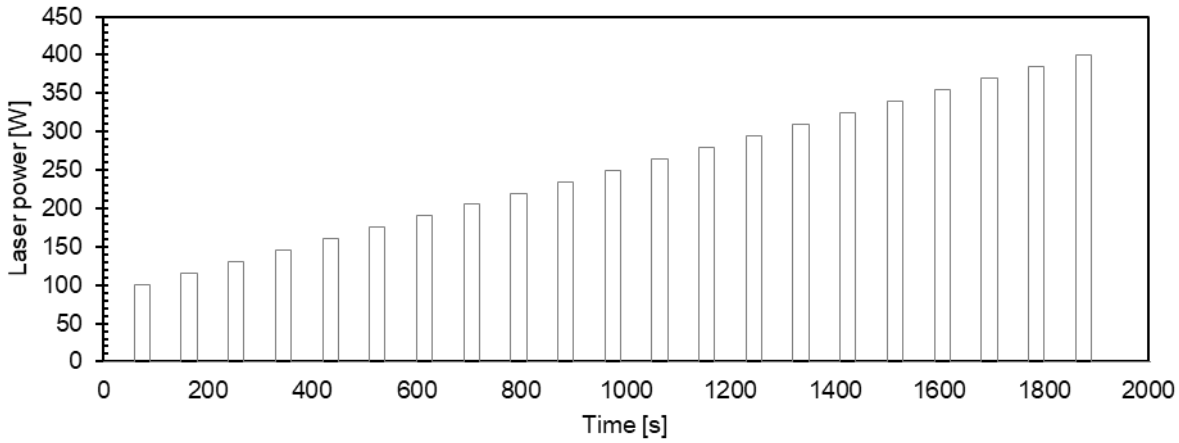

Figure A-1. Programmed heating procedure composed of 21 heating cycles with gradually increasing laser power (ranging from 100 to 400 W with the increments of 15 W).

A-3. Analysed results and definition of selected parameters

The type of results which has been targeted for this study are the evolutions vs. time of crack opening and crack length of all tested materials. The purpose of this sub-section is to briefly present different parameters that have been measured thanks to the ATHORNA vision system combined with DIC and 2P-DIC methods (see Figure A-2) and to demonstrate key results that could be obtained. The main discussion concerning these results will be detailed in the next sub-section.

The methodology used to measure the Crack Opening Displacement (COD) has been explained in section 5.2.6. The results of Crack Opening Displacement are presented in Figure A-3a and Figure A-3b for M and MS15 materials, respectively. One can notice that these curves exhibit significant differences. In order to precisely quantify and discuss these differences, it is necessary to introduce some measurable parameters.

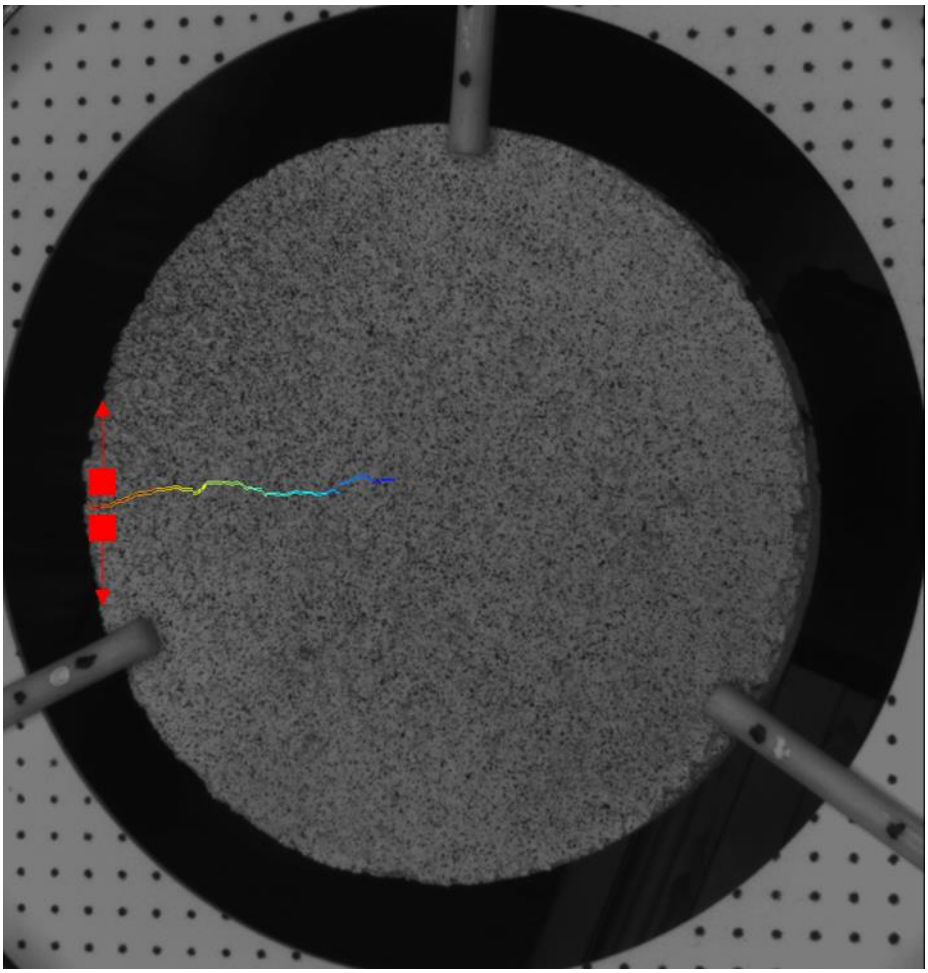

Figure A-2. Picture taken at the end of the testing sequence with already developed crack. The two red squares indicate the exemplary initial positions of the subsets which are used to monitor Crack Opening Displacement (COD).

First, it is worth mentioning that before the initiation of a crack (before ~700 s. for M and ~1400 s. for MS15), the COD does not exactly refer to a real crack opening, since no crack (no localised damage) is detected at this stage by 2P-DIC. However, a non-zero value can be measured, corresponding, in fact, to local thermal expansion which could be accompanied by some diffused damage (microcracking) just before localized damage. Therefore, during this first period, COD values can be used to determine the level of local strain before crack initiation. This value is calculated by dividing the COD right before crack initiation by the initial distance between the subsets. Other interesting parameters are (see Figure A-3b):

- crack initiation time;
- increase of the crack opening between the peaks from the first (P1) and the second cycle (P2), which follow the crack initiation;

- increase of the crack opening between the peaks from the second (P2) and the third cycle (P3), which follow the crack initiation;
- maximal crack opening during the test (usually the last peak);
- final crack opening (after ~2070 s.).

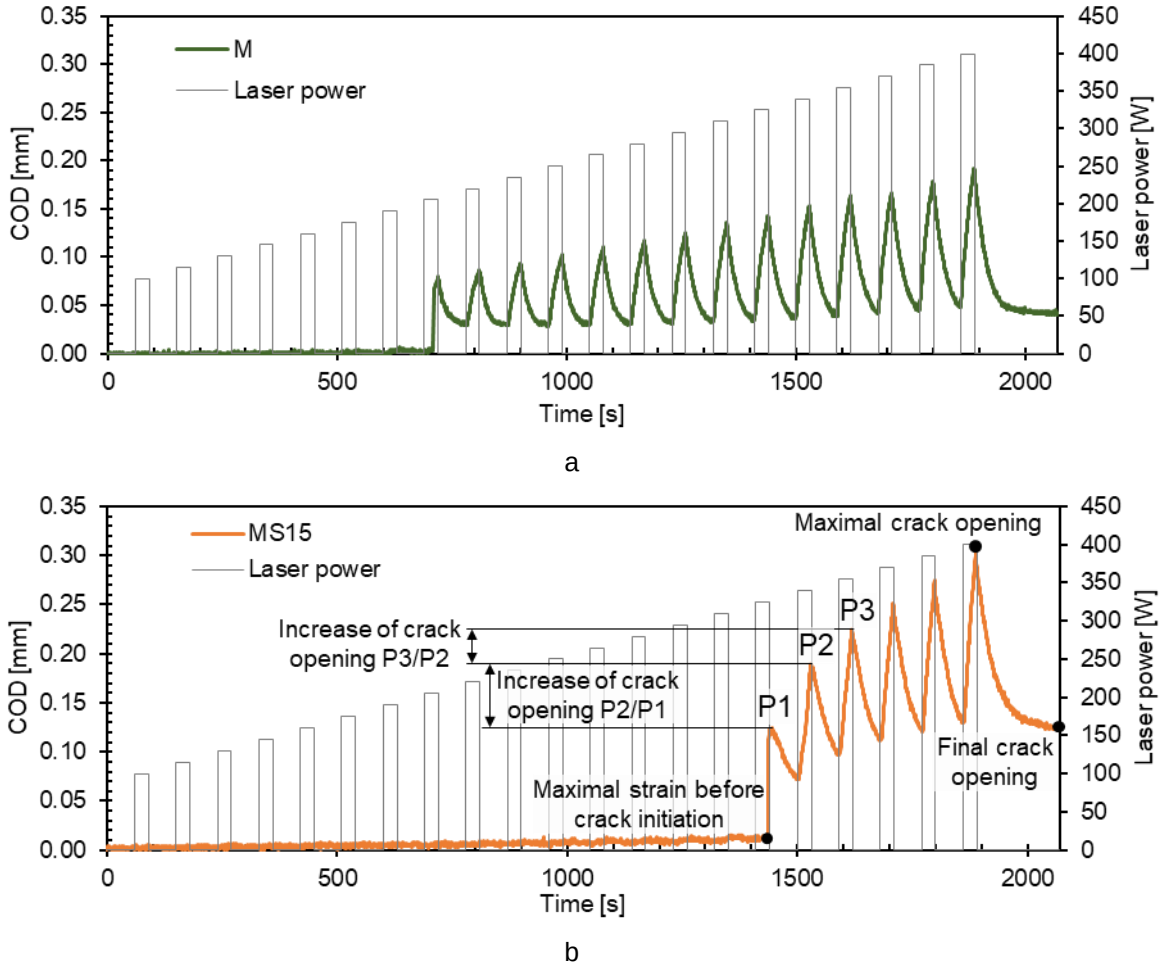

Figure A-3. Crack Opening Displacement (COD) evolution with time for: a) M, b) MS15. The few selected parameters are presented in figure b.

The crack length evolutions with time are presented in Figure A-4a and Figure A-4b for M and MS15 materials, respectively. Once again one can observe significant differences in the behaviour of these two materials. Therefore, another parameter has been added, as presented in Figure A-4b. This parameter is determined as an increase of crack length between the peaks from the first (P1) and the second cycles (P2), which follow the crack initiation.

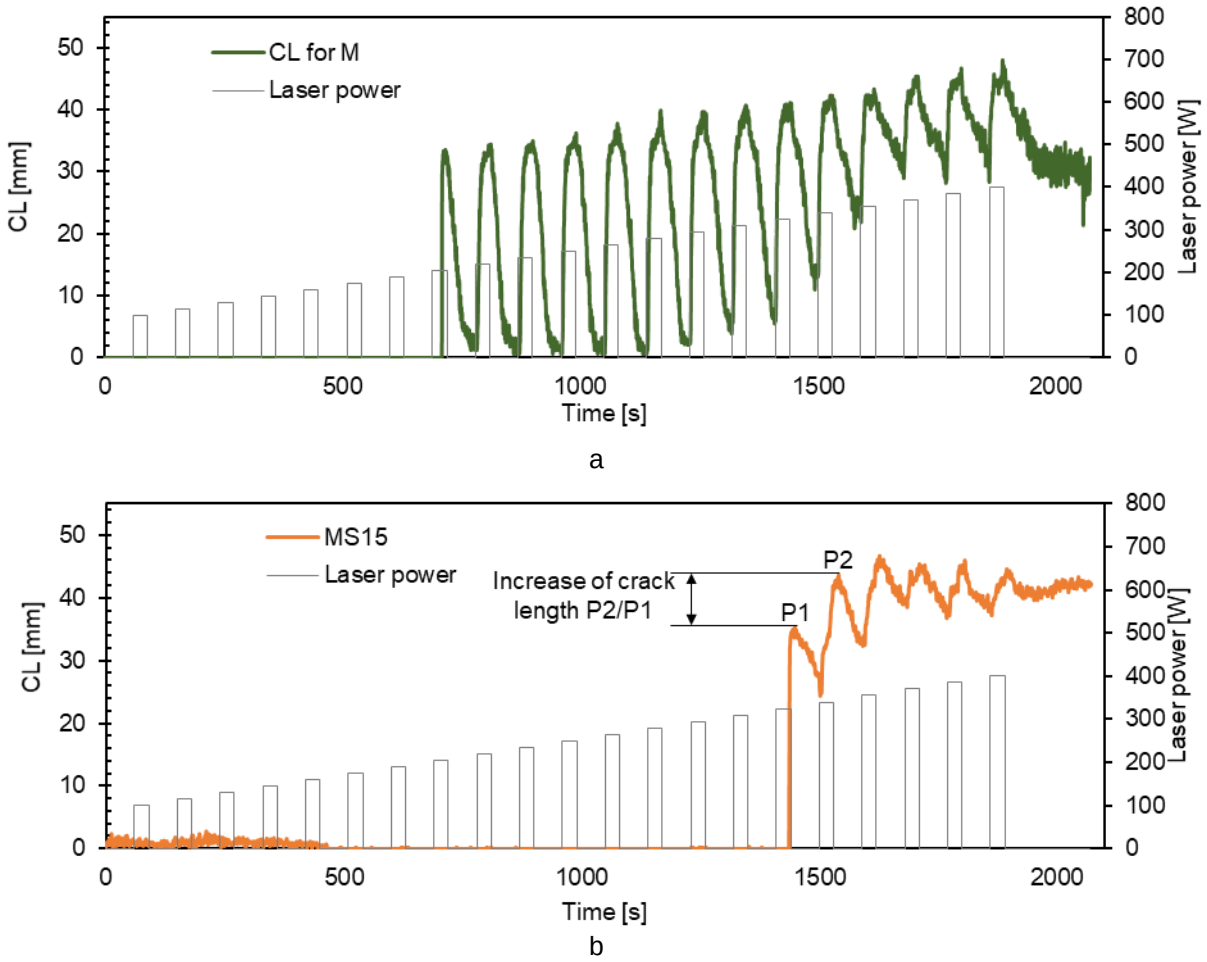

Figure A-4. Crack Length (CL) evolution with time for: a) M, b) MS15. The selected parameter is presented in figure b.

For pedagogical purpose, the curves of crack length evolution with time for materials with different contents and types of aggregates are presented in Figure A-5. One can clearly observe that the addition of coarse aggregates, in all investigated cases, leads to delaying of crack initiation time.

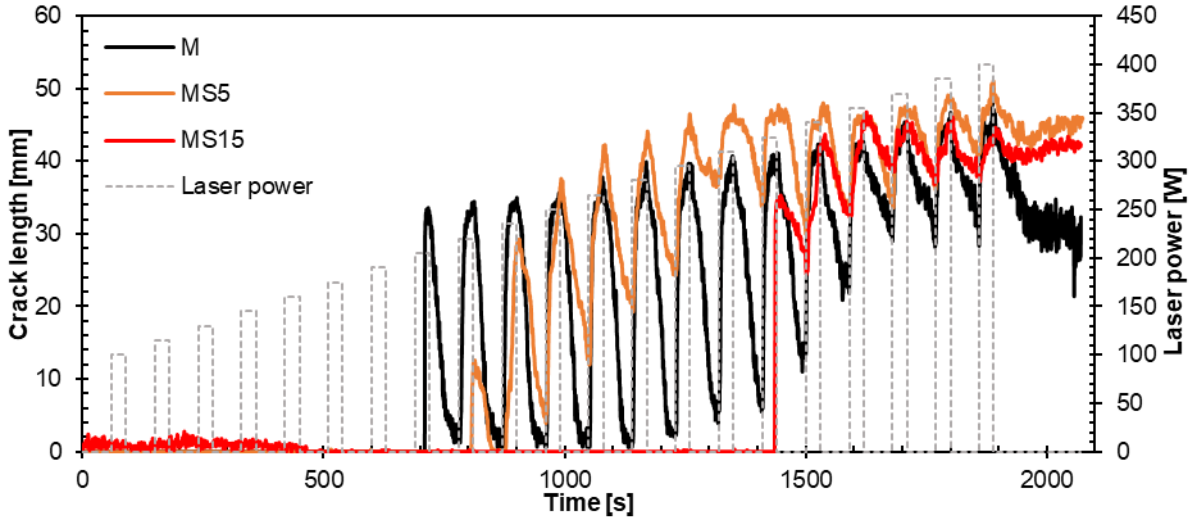

a

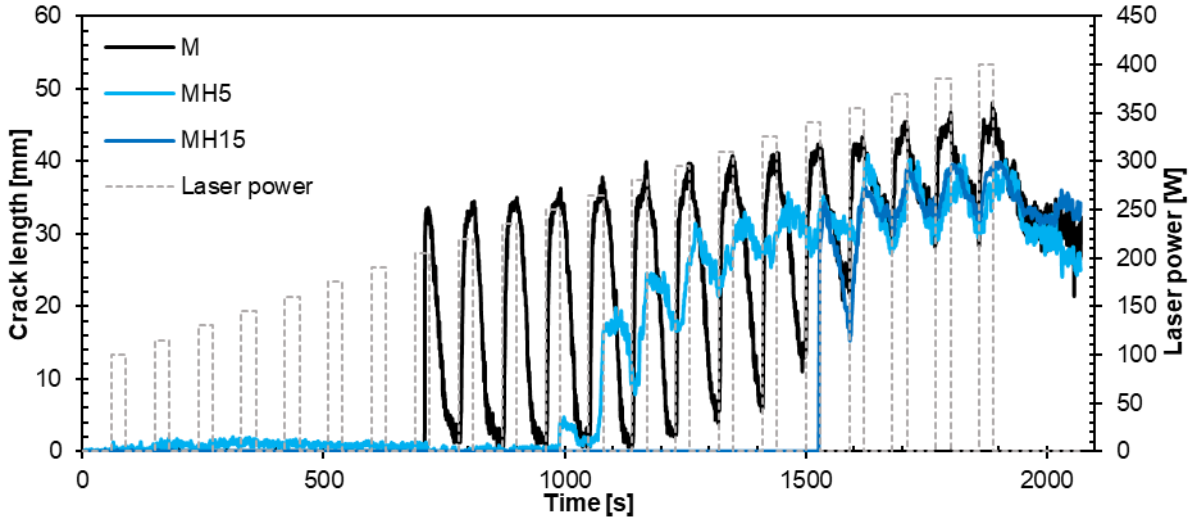

b

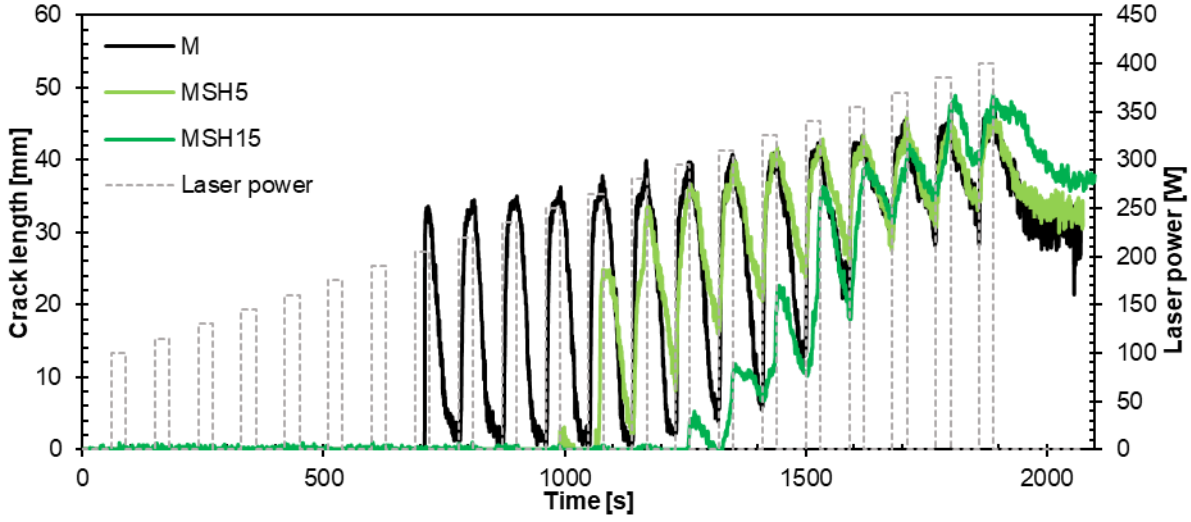

c

Figure A-5. Crack Length (CL) evolution curves for materials having different content of: a) spinel, b) hercynite, c) mix of spinel and hercynite.

A-4. Correlation matrix of selected parameters with discussion

The purpose of this sub-section is to correlate the results obtained by ATHORNA device on these model magnesia spinel materials and the results previously obtained using WST (thanks to the PhD of Imad Khlifi).[99] In this aim, Table A-2 shows the matrix of the Pearson-type correlation coefficients r (linear correlation between two sets of data). The values of these coefficients can be in a range [-1; 1] and each of them is calculated as a covariance of two variables divided by the product of their standard deviations. This calculated value is an indication of correlation between variables:

- if the value is close to 1, it indicates a strong positive correlation between variables (Y increases linearly as X increases);
- if the value is close to -1, there can be a strong negative correlation between variables (Y decreases linearly as X increases);
- if the value is close to 0, there is no correlation between variables.

It is safe to consider each value of the Pearson-type correlation coefficient as an indication of potential correlation and it is a good practice to check scatter plots of the two sets of variables for each analysed coefficient. In this aim, Table A-2 indicates correlation coefficients for the set of selected parameters and the most interesting parameters are also presented on scatterplots in Figure A-6.

Table A-2. Matrix of Pearson type correlations between the parameters originating from experimental ATHORNA and WST devices, as well as from material design (inclusions content).

	1	2	3	4	5	6	7	8	9	10	11	12
1. Crack initiation time	1.00											
2. Final crack opening	0.80	1.00										
3. Maximal crack opening	0.47	0.84	1.00									
4. Strain before crack initiation	0.40	0.59	0.49	1.00								
5. Increase of crack opening between P2 & P1	0.77	0.67	0.68	0.30	1.00							
6. Increase of crack opening between P3 & P2	0.55	0.56	0.70	0.34	0.91	1.00						
7. Increase of crack length between P2 & P1	-0.40	-0.06	0.29	0.43	-0.03	0.35	1.00					
8. Final crack length	-0.02	0.44	0.70	0.57	0.21	0.21	0.39	1.00				
9. Specific fracture energy G_f	0.68	0.66	0.27	0.76	0.32	0.26	-0.01	0.04	1.00			
10. Nominal notch tensile strength σ_{NT}	-0.55	-0.85	-0.76	-0.87	-0.48	-0.53	-0.36	-0.54	-0.79	1.00		
11. Measure of brittleness G_f/σ_{NT}	0.67	0.78	0.45	0.82	0.32	0.27	0.05	0.23	0.96	-0.88	1.00	
12. Inclusions content	0.89	0.87	0.48	0.60	0.52	0.31	-0.35	0.17	0.86	-0.73	0.89	1.00

The parameters indicated in Table A-2 come from ATHORNA device (numbers 1-8), WST device (numbers 9-11) and material design (number 12). The correlation coefficient of the parameters No. 11 and 12 is relatively high (R = 0.89) and together with the scatterplot from Figure A-6a allow to identify a linear correlation between them. In other words, the increase of inclusions content correlates with reduced brittleness (increase of G_f'/σ_{NT}). This is a well-known relationship as aggregates are typically added to decrease material brittleness.

Another correlations can be observed between the crack initiation time and the inclusions content (No. 1 and 12, R = 0.89, Figure A-6b) as well as between the strain before crack initiation and the inclusions content (No. 4 and 12, R = 0.60, Figure A-6c). It could mean that an increase of inclusions content could promote diffused damage (microcracks), thus delaying initiation of localised damage and leading to a higher strain before initiation of the macrocrack. Completely linked to this point, a relatively significant linear correlation can be observed between the strain before crack initiation and the measure of brittleness (No. 4 and 11, R = 0.82,

Figure A-6d). The measure of brittleness (by investigation of fracture behaviour using wedge splitting test) is in fact often used to estimate material's resistance to thermal shocks. In some way, the result obtained here, with the use of correlation matrix, confirms the link between the brittleness and the ability of the material to sustain a certain level of strain (by diffused microcracking), before the onset of the macrocrack (when localisation of the damage occurs).

In the next step of cracking, a correlation between the increase of crack opening from the first to the second peak and the inclusions content (No. 5 and 12, R = 0.52, Figure A-6e) can be observed. In some way, this correlation demonstrates that an increase in inclusions content could lead to more progressive crack opening by limiting crack propagation.

In the end, one can also identify a relatively strong correlation between the final crack opening and the inclusions content (No. 2 and 12, R = 0.87, Figure A-6f), as well as rather moderate one between the final crack opening and the final crack length (No. 2 and 8, R = 0.44, Figure A-6g). Thus, the increase of inclusions content leads in all investigated cases to higher final crack opening (at the end of thermal shock cyclic test). This increase of final crack opening is probably related to presence of extensive microcracking before initiation of the main crack and to higher tortuosity of crack path (detected in some cases as higher crack length) which hinders closure.

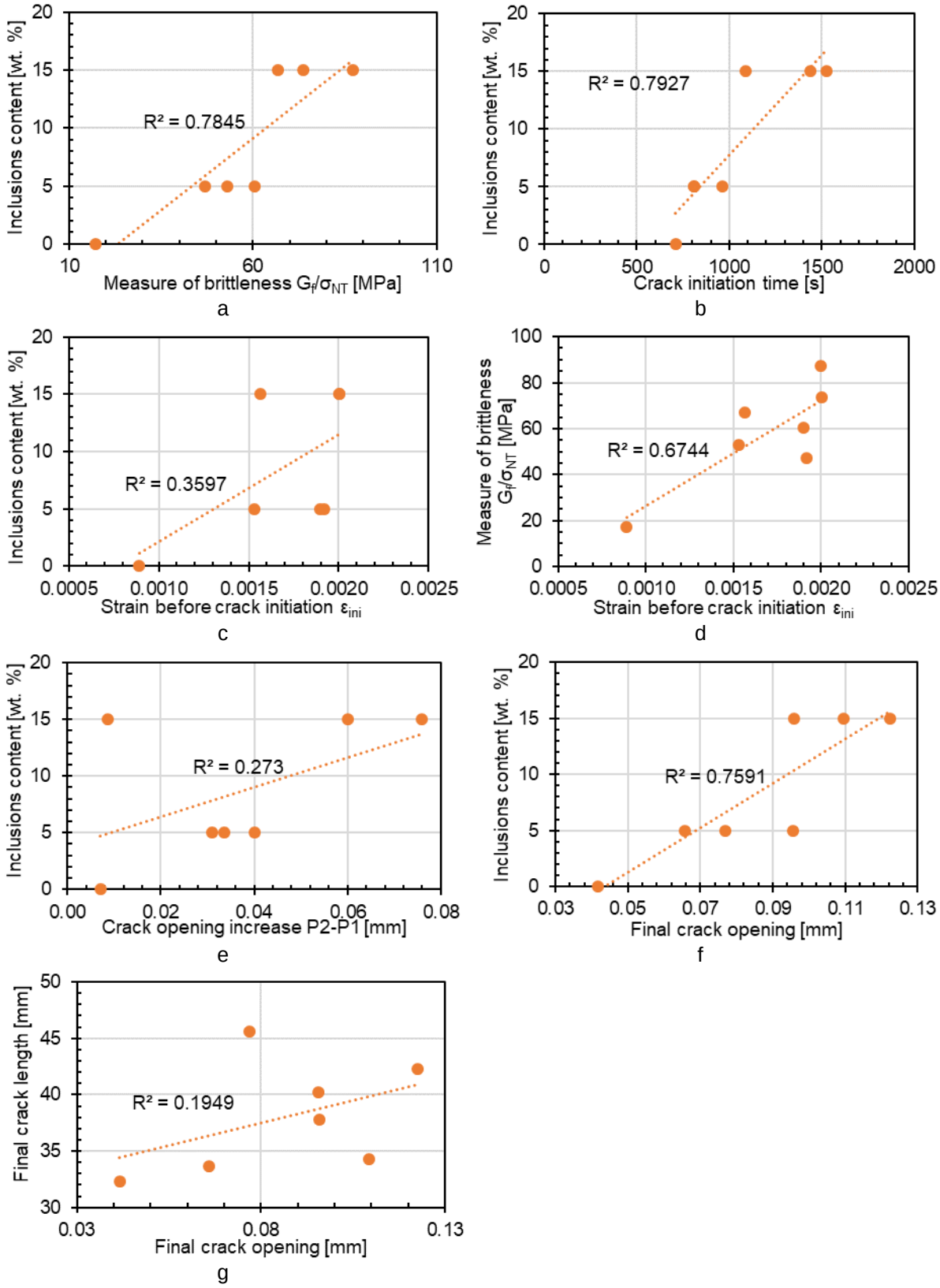

Figure A-6. Scatterplots between: a) inclusions content and the measure of brittleness, b) inclusions content and crack initiation time, c) inclusions content and strain before crack initiation, d) measure of brittleness and strain before crack initiation, e) inclusions content and crack opening increase P2&P1, f) inclusions content and final crack opening g) final crack length and final crack opening.

A-5. Conclusions

This additional study, performed on model magnesia-based materials, highlights another potential application of ATHORNA device which consists in comparing resistance to thermal shocks of different refractory materials. This purely experimental study unveiled that one can better understand material behaviour under cyclic thermal shock conditions. Correlation between the parameters originating from ATHORNA and WST devices, as well as from inclusions content, allowed to draw several reasonable conclusions.

First of all, one has observed that the increase of inclusions content delays initiation of localised damage, probably related to occurrence of diffused damage (microcracking) before occurrence of a macrocrack. Moreover, the relation between the increase of strain before crack initiation (from ATHORNA device) and the measure of brittleness (from WST device) indicates that less brittle materials can withstand higher strain before crack initiation (most likely due to diffused damage). This interesting observation indicates that probably the strain before crack initiation, detected on ATHORNA device, could also allow (like the measure of brittleness) to rank materials depending on their resistance to thermal shocks (for given conditions).

Additional rather obvious observations are related to the increase of inclusions content. On the one hand, an increase of inclusions content leads to more progressive crack opening by limiting crack propagation. On the other hand, higher number of inclusions leads to higher final crack opening. This increased final crack opening often coexists with a higher final crack length, probably due to higher tortuosity of the crack path, which could hinder crack closure.

References

1. LMM GROUP. Development characteristics of the global refractory industry. https://www.lmmgroupcn.com/development-characteristics-of-the-global-refractory-industry/.
2. Gocha, A., Liverani, S. & De Guire, E. Ceramics and glass - Materials for diverse industries: A 2016 industry profile and manufacturing forecast. *Am. Ceram. Soc. Bull.* **95**, 10–20 (2016).
3. KUMAR T, A. & SANKARALINGAM, G. EU-28 Steel Industry Eyeing Recovery from a Slowdown in 2019. *Metals & Minerals Practice, Frost & Sullivan* https://ww2.frost.com/frost-perspectives/eu-28-steel-industry-eyeing-recovery-from-a-slowdown-in-2019/ (2020).
4. Commission, E. *High-level Round Table on the future of the European Steel Industry Recommendations*. (2013).
5. Statista. Apparent steel use per capita in the European Union (EU-28) from 2009 to 2018. *2019*.
6. Kreuels, N. A view on the European refractory industry. *Bol. la Soc. Esp. Ceram. y Vidr.* **48**, 245–254 (2009).
7. Andus Buhr et al. Dream Ladle Lining. in *VDEh Proceedings, 9th International Symposium Refractory Technology: Steel Ladle Lining* 13–15 (2016).
8. Ghenda, J. T. European Steel: The Wind of Change. (2018).
9. Hites, B. E. The growth of EAF steelmaking. *Recycling Today* (2020).
10. Proposal of the H2020-MSCA-ITN ATHOR project. (2017).
11. Thermo-Calc Software. Application Example: Kinetics of Steel Refining in a Ladle Furnace. https://www.thermocalc.com/solutions/example-calculations/kinetics-of-steel-refining-in-a-ladle-furnace/.
12. Hubble, D. H., Russel, R. O., Vernon, H. L. & Marr, R. J. Chapter 4: Steelmaking Refractories. in *The Making, Shaping, and Treating of Steel* (ed. Fruehan, R. J.) 227–290 (AISE Steel Foundation, 1998).
13. Samuelsson, P. & Sohlberg, B. ODE-based modelling and calibration of temperatures in steelmaking ladles. *IEEE Trans. Control Syst. Technol.* (2010) doi:10.1109/TCST.2009.2016668.
14. Palco, S., Frechette, M.-H., Rigaud, M. & Divry, E. New Insulation Concept for Steelmaking Ladle-Tundish Systems. (2004).

15. Kor, G. J. W. & Glaws, P. C. Chapter 11: Ladle Refining and Vacuum Degassing. in *The Making, Shaping, and Treating of Steel* (ed. Fruehan, R. J.) 661–713 (1998).
16. Poirier, J. *et al.* Corrosion of Refractories: The Fundamentals. in *FIRE Compendium Series* 1–41 (2017).
17. Ghosh, A. & Chatterjee, A. Refractories for Secondary Steelmaking. in *Ironmaking and Steelmaking: Theory and Practice* 395 (2008).
18. Schnabel, M., Buhr, A., Exenberger, R. & Rampitsch, C. Spinel : In situ versus Preformed – Clearing the Myth. *Refract. Worldforum* **2**, 87–93 (2010).
19. Jansson, S. *A Study on Molten Steel/Slag/Refractory Reactions during Ladle Steel Refining*. (2005).
20. Big Improvements to Ultra Low Carbon Steel Production Modern. in *The Journal of Refractory Innovations. Steel & Industrial Edition* (eds. Schriebl, S., Dietrich, M., Maranitsch, A., Spanring, A. & Tomas, M.) 5 (RHI Feuerfest GmbH, 2017).
21. Zhang, H., Hong, Y., Li, H. & Yang, B. Thermal fatigue behavior of ladle purging plug. *Adv. Mater. Res.* **105**–**106**, 158–161 (2010).
22. Buhr, A. Refractories for Steel Secondary Metallurgy. *CN-REFRACTORIES* **6**, 19–30 (1999).
23. Sugita, K. Historical overview of refractory technology in the steel industry. *Nippon Steel Tech. Rep.* 8–17 (2009).
24. Goto, K., Hanagiri, S., Kohno, K., Matsui, T. & Ikemoto, T. Progress and perspective of refractory technology. *Nippon Steel Tech. Rep.* 21–25 (2013).
25. Sugita, K. *Refractories for Iron- and Steelmaking — A History of Battle over High Temperature*. (Chijinshokan Co. Ltd., 1995).
26. Matsumoto, O., Isobe, T., Nishitani, T. & Genba, T. Alumina-spinal monolithic refractories. (1991).
27. Nagai B. et al. -. *Taikabutsu* **42**, 418 (1990).
28. M. Hoteiya et al. -. *Taikabutsu* **48**, 611 (1996).
29. Tomiya, H., Tada, H. & Iida, E. Development of unburned Al2O3-MgO brick for steel ladle. in *Proceedings of the Unified International Technical Conference on Refractories* 470–473 (GRA, 2007).
30. Poirier, J., Gaubil, M. & Rigaud, M. Corrosion of Refractories: The Impact of Corrosion. in *FIRE Compendium Series Vol. 2C.* (Göller Verlag, 2018).
31. Braulio, M. A. L., Rigaud, M., Buhr, A., Parr, C. & Pandolfelli, V. C. Spinel-

containing alumina-based refractory castables. *Ceram. Int.* **37**, 1705–1724 (2011).

32. Kingery, W. D., Bowen, H. K., Uhlmann, D. R. & Frieser, R. Structure of crystals. in *Introduction to Ceramics* 25–90 (1977). doi:10.1149/1.2133296.
33. Luz, A. P., Braulio, M. A. L. & Pandolfelli, V. C. Spinel-containing alumina-based refractory castables. in *F.I.R.E. Compendium Series Vol. 1: Refractory castable engineering* (ed. Rigaud, M.) 497–592 (Göller Verlag, 2015).
34. Zhang, S. & Lee, W. E. Spinel-containing refractories. in *Refractories Handbook* (ed. Schacht, C. A. (Org. .) 215–257 (Marcel Dekker Inc., 2004).
35. Sarkar, R. Chromite and MgO-Cr2O3 Refractories (Chrome-Mag and Mag-Chrome). in *Refractory Technology : Fundamentals and Applications* 179–192 (CRC Press, 2017).
36. Braulio, M. A. L., Rigaud, M., Buhr, A., Parr, C. & Pandolfelli, V. C. Spinel-containing alumina-based refractory castables. **37**, 1705–1724 (2011).
37. Nakagawa, Z., Enomoto, N., Yi, I. S. & Asano, K. Effect of corundum/ periclase sizes on expansion behavior during synthesis of spinel. in *Proceedings of UNITECR'95* 1312–1319 (1995).
38. Harper, C. A. *Handbook of ceramics, glasses and diamonds*. *McGraw -Hill Companies Inc.* (2001).
39. William D. Callister, J. *Fundamentals of Materials Science and Engineering*. (2001).
40. Zawrah, M. F. Investigation of lattice constant, sintering and properties of nano Mg-Al spinels. *Mater. Sci. Eng. A* (2004) doi:10.1016/j.msea.2004.05.074.
41. NAVROTSKY, A., WECHSLER, B. A., GEISINGER, K. & SEIFERT, F. Thermochemistry of MgAl2O4-Al8/3O4 Defect Spinels. *J. Am. Ceram. Soc.* (1986) doi:10.1111/j.1151-2916.1986.tb04772.x.
42. Shou-Yong, J., Li-Bin, L., Ning-Kang, H., Jin, Z. & Yong, L. Investigation on lattice constants of Mg-Al spinels. *J. Mater. Sci. Lett.* (2000) doi:10.1023/A:1006710808718.
43. Poirier, J. Impact of refractory materials on inclusionary cleanliness and steel quality. *CFI Ceram. Forum Int.* (2008).
44. Sako, E. Y., Braulio, M. A. L. & Pandolfelli, V. C. Al2O3-MgO castables performance in an expansion constrained environment. *Ceram. Int.* (2012) doi:10.1016/j.ceramint.2011.12.039.

45. Braulio, M. A. L., Martinez, A. G. T., Luz, A. P., Liebske, C. & Pandolfelli, V. C. Basic slag attack of spinel-containing refractory castables. *Ceram. Int.* (2011) doi:10.1016/j.ceramint.2011.02.007.
46. Nagayi, B., Matsumoto, O., Isobe, T. & Nishiumi, Y. Wear mechanism of castables for steel ladle by slag. *Taikabutsu* **42**, 418–426 (1990).
47. Mori, J. *et al.* Material design of monolithic refractories for steel ladle. *Am. Ceram. Soc. Bull.* (1990).
48. Nakamura, R., Kaneshige, T., Matsumura, K. & Sasaki, H. *The current status of ladle castables and application of clean shot system to steel ladles*. vol. 42 (1999).
49. Sugawara, M. & Asano, K. The recent developments of castable technology in Japan. in *Proceedings of the Unified International Technical Conference on Refractories (UNITECR'05)* 30–34 (2005).
50. Zhang, S., Sarpoolaky, H. & Lee, W. E. Dissolution of MgAl2O4 (MA) spinel grain in CaO-MgO-Al2O3-SiO2 melt. in *Proc. 44th Intl. Colloq. on Refractories* 64–67 (2001).
51. Sarpoolaky, H., Zhang, S. & Lee, W. E. Corrosion of high alumina and near stoichiometric spinels in iron-containing silicate slags. *J. Eur. Ceram. Soc.* (2003) doi:10.1016/S0955-2219(02)00170-X.
52. Rigaud, M., Kovác, V., Xing, C., Palco, S. & Rybar, A. Spinel and forsterite bonded magnesia castables for steelmaking applications. *Iron Steelmak. (I SM)* (1998).
53. Zhang, S. & Lee, W. E. Use of phase diagrams in studies of refractories corrosion. *Int. Mater. Rev.* (2000) doi:10.1179/095066000101528304.
54. Ko, Y. C. & Lay, J. T. Thermal expansion characteristics of alumina-magnesia and alumina-spinel castables in the temperature range 800°-1650 °C. *J. Am. Ceram. Soc.* (2000) doi:10.1111/j.1151-2916.2000.tb01650.x.
55. Braulio, M. A. ., Milanez, D. H., Sako, E. Y., Bittencourt, L. R. M. & Pandolfelli, V. C. Expansion Behavior of Cement Bonded Alumina–Magnesia Refractory Castables. *Am. Ceram. Soc. Bull.* **86**, 9201–9206 (2007).
56. Fuhrer, M., Hey, A. & Lee, W. E. Microstructural evolution in self-forming spinel/calcium aluminate-bonded castable refractories. *J. Eur. Ceram. Soc.* **18**, 813–820 (1998).
57. Buhr, A., Baier, B., Aroni, J. M. & McConnell, R. W. Raw Material Concepts for

SiO2 free High Strength Castables in the Temperature Range up to 1200 °C. in *43. Conference of Metallurgists* (2004).

58. Braulio, M. A. L., Bittencourt, L. R. M., Porier, J. & Pandolfelli, V. C. Micosilica Effects on Cement Bonded Alumia-magnesia Refractory Castables. *J. Tech. Assoc. Refract.* **28**, 180–184 (2008).
59. Chen, S. S.-K., Cheng, M. M.-Y., Lin, S. S.-J. & Ko, Y.-C. Y. Thermal characteristics of Al2O3–MgO and Al2O3–spinel castables for steel ladles. *Ceram. Int.* **28**, 811–817 (2002).
60. MacZura, G., Madono, M., Kriechbaum, G. W. & Sewell, B. Low moisture regular corundum/spinel castables with superior properties. in *Proc. Unified Intl. Tech. Conf. on Refractories* 179–186 (1995).
61. Vance, M. W. *et al.* Influence of spinel additives on high-alumina/spinel castables. *Am. Ceram. Soc. Bull.* (1994).
62. Ko, Y. . & Chan, C. . Effect of spinel content on hot strength of alumina-spinel castables in the temperature range 1000–1500°C. *J. Eur. Ceram. Soc.* **19**, 2633–2639 (1999).
63. Baudín, C., Martínez, R. & Pena, P. High-Temperature Mechanical Behavior of Stoichiometric Magnesium Spinel. *J. Am. Ceram. Soc.* **78**, 1857–1862 (1995).
64. Mitchell, T. E., Hwang, L. & Heuer, A. H. Deformation in spinel. *J. Mater. Sci.* **11**, 264–272 (1976).
65. Sarkar, R. Particle size distribution for refractory castables: A review. *InterCeram Int. Ceram. Rev.* **65**, 82–86 (2016).
66. Lee, W. E. *et al.* Castable refractory concretes. *International Materials Reviews* (2001) doi:10.1179/095066001101528439.
67. Homeny, J. & Bradt, R. C. Aggregate distribution effects on the mechanical properties and thermal shock behavior of model monolithic refractory systems. *Fish. R, ed. Adv. Ceram.* **13**, 110–130 (1985).
68. MacZura, G., Gnauck, V. & Rothenbuehler, P. Fine aluminas for high performance refractories. in *Proceedings of the First International Conference on Refractories* 560–575 (The Tech. Asso. of Refrac., 1983).
69. DINGER, D. & FUNK, J. Particle packing. II: Review of packing of polydisperse particle systems. *Interceram* (1992).
70. Myhre, B. & Hundere, A. M. The use of particle size distribution in the development of refractory castable. in *Proceedings of the XXV ALAFAR*

Congress (1996).

71. FUNK, J. & DINGER, D. Particle packing. I: Fundamentals of particle packing monodisperse spheres. *Interceram* (1992).
72. DINGER, D. & FUNK, J. Particle packing. III: Discrete versus continuous particle sizes. *Interceram* (1992).
73. Myhre, B. & Sunde, K. Alumina based castables with very low content of hydraulic compound, Part 1: The effect of binder and PSD on flow and set. in *Proceedings of UNITECR'95* (1995).
74. Sarkar, R. & Parija, A. Effect of alumina fines on a vibratable high-alumina low-cement castable. *InterCeram Int. Ceram. Rev.* **63**, 113–116 (2014).
75. Sarkar, R. & Parija, A. Effect of alumina fines on high alumina self-flow low cement castables. *Refract. World Forum* **6**, 73–77 (2014).
76. Sarkar, R. Particle size distribution and distribution coefficient of castables. (2013).
77. Product Data Sheet. http://www.secar.net/documents/FC-S71-RE-GB-KFR.pdf (2008).
78. Wöhrmeyer, C. *et al.* New Spinel Containing Calcium Aluminate Cement for Corrosion Resistant Castables. in *Proceedings of the Unified International Technical Conference on Refractories* (2011).
79. *Calcium aluminate cements in construction: A re-assessment*. (The Concrete Society, 1997).
80. Eguchi, T., Takita, I., Yoshitomi, J., Kiritani, S. & Sato, M. Eguchi, T. Takita, I. Yoshitomi, J. Kiritani, S. Sato, M. *Taikabutsu Overseas* **9**, 10–25 (1989).
81. Nishikawa, A. *Technology of monolithic refractories*. (Plibrico Japan Co. Ltd, 1984).
82. Parker, K. M. The microstructure of refractory calcium aluminate cements. (University of Sheffield, 1983).
83. Kopanda, J. E. & MacZura, G. Production processes, properties and applications for calcium aluminate cements. in *Alumina Chemicals Science and Technology Handbook* (eds. Hart, L. D. & Lense, E.) 171–183 (Wiley-American Ceramic Society, 1990).
84. Nonnet, E., Lequeux, N. & Boch, P. Elastic properties of high alumina cement castables from room temperature to 1600°C. *J. Eur. Ceram. Soc.* **19**, 1575–1583 (1999).

85. Bussem, W. Proc. Symp. ‘Chemical cements’. *Ceram. Abstr.* **19**, 154 (1940).
86. Zhu, B., Song, Y., Li, X., Chen, P. & Ma, Z. Synthesis and hydration kinetics of calcium aluminate cement with micro MgAl2O4 spinels. *Mater. Chem. Phys.* **154**, 158–163 (2015).
87. Zhu, B., Wang, Y. & Li, X. Effect of phase distribution on rheological behavior of calcium aluminate cement with built-in alumina-magnesia spinel. *Kuei Suan Jen Hsueh Pao/Journal Chinese Ceram. Soc.* (2014) doi:10.7521/j.issn.0454-5648.2014.11.06.
88. Göbbels, M., Woermann, E. & Jung, J. The Al-Rich Part of the System CaO-Al2O3-MgO. *J. Solid State Chem.* **120**, 358–363 (1995).
89. Iyi, N., Göbbels, M. & Matsui, Y. The al-rich part of the system cao-al2o3-mgo. Part II. Structure refinement of two new magnetoplumbite-related phases. *J. Solid State Chem.* (1995) doi:10.1006/jssc.1995.1421.
90. De Aza, A. H., Iglesias, J. E., Pena, P. & De Aza, S. Ternary system Al2O3-MgO-CaO: Part II, Phase relationships in the subsystem Al2O3-MgAl2O4-CaAl4O7. *J. Am. Ceram. Soc.* **83**, 919–927 (2000).
91. Sako, E. Y., Braulio, M. A. L., Zinngrebe, E., Van Der Laan, S. R. & Pandolfelli, V. C. In-depth microstructural evolution analyses of cement-bonded spinel refractory castables: Novel insights regarding spinel and CA 6 formation. *J. Am. Ceram. Soc.* (2012) doi:10.1111/j.1551-2916.2012.05161.x.
92. Schnabel, M. *et al.* Technology Trends Perceptions and Characteristics of Fused and Sintered Refractory Aggregates. *Refract. WORLD FORUM* **7**, (2015).
93. Munuswami, M., Chatterjee, S., Mukherjee, S. & Buhr, A. Role of Tabular Alumina as a suitable aggregate for emerging applications – focus on dry ramming mix. in *Proceedings of the 10th India International Refractories Congress* 97–103 (2014).
94. Liu, X., Yanqing, X., Keming, G., Buhr, A. & Büchel, G. Tabular Alumina for High Purity Corundum Brick. (2007).
95. Möhmel, S., Weissenbacher, M., Kurz, B. & Joubert, O. The influence of different raw materials on the bahaviour of low cement castables. *14th Bienn. Worldw. Congr. Unified Int. Tech. Conf. Refract. UNITECR 2015, conjunction with 58th Int. Colloq. Refract.* (2015).
96. Schnabel, M., Buhr, A., Kockegey-Lorenz, R., Schmidtmeier, D. & Dutton, J. Benefit of matrix alumina and modern dispersing systems in low cement

castables. *InterCeram Int. Ceram. Rev.* **63**, 281–285 (2014).
97. Gürel, S. B. & Altun, A. Reactive alumina production for the refractory industry. *Powder Technol.* **196**, 115–121 (2009).
98. Gruber, D. & Harmuth, H. Steel Ladle Linings - Key lssues Regarding Thermomechanical Behaviour. *RHI Bull.* 19–23 (2014).
99. Khlifi, I. Optimisation of optical methods for strain field measurements dedicated to the characterisation of the fracture behaviour of refractories: Application to magnesia-based materials. (University of Limoges, 2019).
100. Renaud Grasset-Bourdel, Marc Huger & Thierry Chotard. Structure/property relations of magnesia-spinel refractories: experimental determination and simulation. (University of Limoges, 2011).
101. Brochen, E., Clasen, S., Dahlem, E. & Dannert, C. Determination of the Thermal Shock Resistance of Refractories. *Refract. Worldforum* **8**, 79–85 (2016).
102. Harmuth, H. & Bradt, R. C. Investigation of refractory brittleness by fracture mechanical and fractographic methods. *InterCeram Int. Ceram. Rev.* 6–10 (2010).
103. Huger, M., Ota, T., Tessier-Doyen, N., Michaud, P. & Chotard, T. Microstructural effects associated to CTE mismatch for enhancing the thermal shock resistance of refractories. *IOP Conf. Ser. Mater. Sci. Eng.* **18**, (2011).
104. Lord, J. D. & Morrell, R. *Elastic Modulus Measurement*. *A NATIONAL MEASUREMENT GOOD PRACTICE GUIDE* (2006) doi:10.1016/b978-0-12-803581-8.03417-2.
105. Mashinsky, E. I. Differences between static and dynamic elastic moduli of rocks: Physical causes. *Geol. i Geofiz.* **44**, 953–959 (2003).
106. Zheltov, Y. P. Strain in rocks [in Russian]. 198 (1966).
107. Vovk, A. A. Deformation of compressible solids at dynamic loading [in Russian]. 175 (1971).
108. Rabotnov, Y. N. Mechanics of strained solids [in Russian]. 744 (1979).
109. Tutuncu, A. N., Podio, A. L., Gregory, A. R. & Sharma, M. M. Nonlinear viscoelastic behavior of sedimentary rocks, Part I: Effect of frequency and strain amplitude. *Geophysics* (1998) doi:10.1190/1.1444311.
110. Gouraud, F. Influence des transformations de phase de la zircone sur le comportement thermomécanique de réfractaires à haute teneur en zircone. (Université de Limoges, 2016).

111. Simonin, F. Comportement thermomécanique de bétons réfractaires alumineux contenant du spinelle de magnésium. (INSA Lyon, 2000).
112. GIVAN, G. V., HART, L. D., HEILICH, R. P. & MacZura, G. Curing and firing high purity calcium aluminate-bonded tabular alumina castables. *Am. Ceram. Soc. Bull.* **54**, 710–713 (1975).
113. Kolli, M., Hamidouche, M., Fantozzi, G. & Chevalier, J. Elaboration and characterization of a refractory based on Algerian kaolin. *Ceram. Int.* **33**, 1435–1443 (2007).
114. Ghassemi Kakroudi, M., Huger, M., Gault, C. & Chotard, T. Damage evaluation of two alumina refractory castables. **29**, 2211–2218 (2009).
115. Schafföner, S., Dietze, C., Möhmel, S., Fruhstorfer, J. & Aneziris, C. G. Refractories containing fused and sintered alumina aggregates: Investigations on processing, particle size distribution and particle morphology. *Ceram. Int.* **43**, 4252–4262 (2017).
116. Khlifi, I., Pop, O., Dupré, J.-C., Doumalin, P. & Huger, M. Investigation of microstructure-property relantionships of magnesia-hercynite refractory composites by a refined digital image correlation technique. *J. Eur. Ceram. Soc.* **39**, 3893–3902 (2019).
117. Hayun, S. *et al.* Experimental methodologies for assessing the surface energy of highly hygroscopic materials: The case of nanocrystalline magnesia. *J. Phys. Chem. C* (2011) doi:10.1021/jp2087434.
118. Rietveld, H. M. A profile refinement method for nuclear and magnetic structures. *J. Appl. Crystallogr.* **2**, 65–71 (1969).
119. Mccusker, L. B., Von Dreele, R. B., Cox, D. E., Louër, D. & Scardi, P. Rietveld refinement guidelines. *J. Appl. Crystallogr.* **32**, 36–50 (1999).
120. Bahr, O., Schaumann, P., Bollen, B. & Bracke, J. Young's modulus and Poisson's ratio of concrete at high temperatures: Experimental investigations. *Mater. Des.* **45**, 421–429 (2013).
121. Kakroudi, M. G. Comportement thermomécanique en traction de bétons réfractaires: influence de la nature des agrégats et de l'histoire thermique. (Université de Limoges, 2007).
122. Younes Belrhiti. Etude de matériaux réfractaires à comportement mécanique non linéaire par mesure de champs de déformations. (University of Limoges, 2015).

123. Hasselman, D. P. H. Unified Theory of Thermal Shock Fracture Initiation and Crack Propagation in Brittle Ceramics. *J. Am. Ceram. Soc.* **52**, 600–604 (1969).
124. Y. Belrhiti *et al.* Combination of Brazilian test and digital image correlation for mechanical characterization of refractory materials. **37**, 2285–2293 (2017).
125. *Recent Developments in Computer Modeling of Powder Metallurgy Processes*. vol. 176 (IOS Press, Ohmsha, NATO Scientific Affairs Division, 2001).
126. ASTM Subcommittee: D18.12. Standard Test Method for Splitting Tensile Strength of Intact Rock Core Specimens. (2001).
127. Ye Jianhong, F. Q. Wu & J. Z. Sun. Estimation of the tensile elastic modulus using Brazilian disc by applying diametrically opposed concentrated loads. **46**, 568–576 (2009).
128. Lilleheden, L. Mechanical properties of adhesives in situ and in bulk. *Int. J. Adhes. Adhes.* **14**, 31–37 (1994).
129. Creath, K. & Schmit, J. INTERFEROMETRY | Phase-Measurement Interferometry. in *Encyclopedia of Modern Optics* (ed. Guenther, R. D.) 364–374 (2005).
130. Davidson, R. J. A comparison of Moiré interferometry and digital image correlation. (Air Force Air University, 2008).
131. N. Bretagne, V. Valle, J.C. Dupre. Development of the marks tracking technique for strain field and volume variation measurements. 1–9 (2004).
132. Rotinat, R., Tié, R., Valle, V. & Dupré, J. C. Three optical procedures for local large-strain measurement. *Strain* vol. 37 89–98 (2001).
133. Bornert, M. *et al.* Assessment of digital image correlation measurement errors: Methodology and results. *Exp. Mech.* **49**, 353–370 (2009).
134. Y. Barranger, P. Doumalin, J. C. Dupre & A. Germaneau. Strain Measurement by Digital Image Correlation: Influence of Two Types of Speckle Patterns Made from Rigid or Deformable Marks. **48**, 357–365 (2012).
135. Valla, A. *et al.* Comparison of two optical methods for contactless, full field and highly sensitive in-plane deformation measurements using the example of plywood. *Wood Sci. Technol.* **45**, 755–765 (2011).
136. Pan, B., Wang, B. & Lubineau, G. Comparison of subset-based local and FE-based global digital image correlation: Theoretical error analysis and validation. *Opt. Lasers Eng.* **82**, 148–158 (2016).
137. Gazeau, C., Gillibert, J., Blond, E., Geffroy, P.-M. & Richet, N. Experimental set

up for the mechanical characterization of plane ITM membrane at high temperature. *J. Eur. Ceram. Soc.* **35**, 3853–3861 (2015).

138. Jean-Christophe Dupré *et al.* Detection of cracks in refractory materials by an enhanced digital image correlation technique. **53**, 977–993 (2018).
139. Bigger, R. *et al.* A Good Practices Guide for Digital Image Correlation. *Int. Digit. Image Correl. Soc.* 94 (2018) doi:10.32720/idics/gpg.ed1.
140. Reu, P. All about speckles: Speckle size measurement. *Exp. Tech.* (2014) doi:10.1111/ext.12110.
141. Reu, P. All about speckles: Edge sharpness. *Exp. Tech.* (2015) doi:10.1111/ext.12139.
142. Reu, P. All about speckles: Contrast. *Exp. Tech.* (2015) doi:10.1111/ext.12126.
143. Orteu, Ã. 3-D computer vision in experimental mechanics To cite this version : HAL Id : hal-01644891 3-D computer vision in experimental mechanics. **47**, 282–291 (2018).
144. Germaneau, A. *et al.* Experimental analysis of mechanical response of stabilized occipitocervical junction by 3D mark tracking technique. *EPJ Web Conf.* **6**, (2010).
145. Dupre, J. C. *et al.* Experimental study of the hygromechanical behaviour of a historic painting on wooden panel: devices and measurement techniques. *J. Cult. Herit.* **46**, 165–175 (2020).
146. Brémand, F. *et al.* Mesures en mécanique par méthodes optiques. (2011).
147. Lyons, J. S., Liu, J. & Sutton, M. A. High-temperature Deformation Measurements Using Digital-image Correlation. **36**, 64–70 (1996).
148. Paul Leplay, Olivier Lafforgue, F. H. Analysis of Asymmetrical Creep of a Ceramic at 1350°C by Digital Image Correlation. **98**, 2240–2247 (2015).
149. Dusserre, G., Nazaret, F., Robert, L. & Cutard, T. Applicability of image correlation techniques to characterize asymmetric refractory creep during bending tests. **33**, 221–231 (2013).
150. Xiang Guo, J. L. High-temperature digital image correlation method for full-field deformation measurement captured with filters at 2600°C using spraying to form speckle patterns. **53**, (2014).
151. Bing Pan, D. W. High-temperature digital image correlation method for full-field deformation measurement at 1200 °C. **22**, (2010).
152. Behrad Koohbor, G. V. Thermo-mechanical Properties of Metals at Elevated

Temperatures. **3**, 117--123. (2016).

153. Guillermo Valeri, B. K. Determining the tensile response of materials at high temperature using DIC and the Virtual Fields Method. **91**, 53–61 (2017).
154. Kaczmarek, R. *et al.* High-temperature digital image correlation techniques for full-field strain and crack length measurement on ceramics at 1200°C: Optimization of speckle pattern and uncertainty assessment. *Opt. Lasers Eng.* **146**, 106716 (2021).
155. Bornert, M. *et al.* Assessment of Digital Image Correlation Measurement Accuracy in the Ultimate Error Regime: Improved Models of Systematic and Random Errors. *Exp. Mech.* **58**, 33–48 (2018).
156. Wang, Y. Q., Sutton, M. A., Schreier, H. A. & Bruck, H. W. Quantitative Error Assessment in Pattern Matching: Effects of Intensity Pattern Noise, Interpolation, Strain and Image Contrast on Motion Measurements. *Strain An Int. J. Exp. Mech.* **45**, 160–178 (2009).
157. Amiot, F. *et al.* Assessment of digital image correlation measurement accuracy in the ultimate error regime: Main results of a collaborative benchmark. *Strain* (2013) doi:10.1111/str.12054.
158. Heilbronner, R. P. The autocorrelation function: an image processing tool for fabric analysis. *Tectonophysics* **212**, 351–370 (1992).
159. Belrhiti, Y. *et al.* Application of optical methods to investigate the non-linear asymmetric behavior of ceramics exhibiting large strain to rupture by four-points bending test. *J. Eur. Ceram. Soc.* **32**, 4073–4081 (2012).
160. Chatterjee, S., Buhr, A., Kockegey-Lorenz, R., Pal, A. R. & Singh, B. Effectiveness of fired Alumina-Spinel brick in secondary metallurgy. *UNITECR 2017, Unified Int. Tech. Conf. Refract. 15th Bienn. Worldw. Congr. Refract. Santiago, Chili, 26-29 Sept. 2017* Paper O.076, pp.289–292 (2017).
161. Kaczmarek, R. *et al.* Thermomechanical behaviour of an alumina spinel refractory for steel ladle applications. in *UNITECR Proceedings* 2–5 (2019).
162. Fei, Y. *Thermal expansion*. *Mineral Physics & Crystallography: A Handbook of Physical Constants, Volume 2* (1995). doi:10.1201/9780429261701-33.
163. Aldebert, P. & Traverse, J. P. αalumina: A high-temperature thermal expansion standard. *High Temp. Press.* **16**, 127–135 (1984).
164. Case, E. D., Smyth, J. R. & Hunter, O. Microcracking in Large-grain Al2O3. *Mater. Sci. Eng.* **51**, 175–179 (1981).

165. Park, S. C., Kim, D. W., Heo, I. W. & Lee, S. J. De-soda process using silica for fabrication of low soda alumina powder. *J. Korean Ceram. Soc.* **52**, 192–196 (2015).
166. Jean-Michel AUVRAY. Elaboration et caracterisation a haute temperature de betons refractaires a base d'alumine spinelle. (University of Limoges, 2003).
167. Gull, R. Fracture mechanical characterization of model castables with wedge splitting tests. (Montanuniversität Leoben, 2020).
168. Harmuth, H. & Tschegg, E. K. A fracture mechanics approach for the development of refractory materials with reduced brittleness. *Fatigue Fract. Eng. Mater. Struct.* (1997) doi:10.1111/j.1460-2695.1997.tb01513.x.
169. Andreev, K. *et al.* Thermal and mechanical cyclic tests and fracture mechanics parameters as indicators of thermal shock resistance – case study on silica refractories. *J. Eur. Ceram. Soc.* **39**, 1650–1659 (2019).
170. Andreev, K., Luchini, B., Rodrigues, M. J. & Alves, J. L. Role of fatigue in damage development of refractories under thermal shock loads of different intensity. *Ceram. Int.* **46**, 20707–20716 (2020).
171. Hino, Y. & Kiyota, Y. Fatigue failure and thermal spalling tests to evaluate dynamic fatigue fracture of MgO-C bricks. *ISIJ Int.* **51**, 1809–1818 (2011).
172. Schneider, G. A. Thermoschockverhalten von Hochleistungskeramik. (Stuttgart Unviersity, 1989).
173. Dahlem, E. & Dannert, C. Acoustic Emission Analysis to Recognize the Fracture Pattern of Refractory Materials During Thermal Shock. in *Proceedings of the Unified International Technical Conference on Refractories* 301–304 (2017).
174. Damhof, F. *Numerical-experimental analysis of thermal shock damage in refractory materials*. (2010). doi:10.6100/IR675493.
175. Kamio, H., Sasatani, Y. & Sugawara, M. Analyses of the thermal deformation behavior of the Al2O3-MgO castables by digital image correlation method. *Proc. UNITECR 2011 Congr. 12th Bienn. Worldw. Conf. Refract. - Refract. to Sustain Glob. Environ.* 512–515 (2011).
176. Gruber, D. & Harmuth, H. A laser irradiation disc test for fracture testing of refractory fine ceramics. *J. Eur. Ceram. Soc.* **34**, 4021–4029 (2014).
177. Zhang, W. *et al.* Investigation of the thermal shock behavior of ceramic using a combination of experimental testing and FE-simulation methods. *Adv. Eng. Mater.* **15**, 480–484 (2013).

178. Seifert, G., Raether, F. & Baber, J. A New Device for Measuring Hot Thermal Shock, Thermal Cycling and Other High Temperature Properties of Refractories. *Technol. Trends Refract. WORLDFORUM* **10**, 77–80 (2018).
179. Damhof, F., Brekelmans, W. A. M. & Geers, M. G. D. Experimental analysis of the evolution of thermal shock damage using transit time measurement of ultrasonic waves. *J. Eur. Ceram. Soc.* **29**, 1309–1322 (2009).
180. Zhang, W., Doynov, N., Ossenbrink, R. & Michailov, V. Physical and FE-Simulation of Thermal Shock Behaviour of Refractory Ceramics. *Refract. Worldforum* **8**, (2016).
181. Raether, F., Springer, R. & Beyer, S. Optical dilatometry for the control of microstructure development during sintering. *Mater. Res. Innov.* (2001) doi:10.1007/s100190000101.
182. Raether, F. G. Current state of in situ measuring methods for the control of firing processes. in *Journal of the American Ceramic Society* (2009). doi:10.1111/j.1551-2916.2008.02683.x.
183. Lalau, Y. *et al.* A method for experimental thermo-mechanical aging of materials submitted to concentrated solar irradiation. *Sol. Energy Mater. Sol. Cells* **192**, 161–169 (2019).
184. Lalau, Y. *et al.* IMPACT: A novel device for in-situ thermo-mechanical investigation of materials under concentrated sunlight. *Sol. Energy Mater. Sol. Cells* **172**, (2017).
185. Dumeige, Y. & Roch, J.-F. Etude d'un laser He–Ne en "kit" Cavite optique et faisceaux gaussiens. 1–16 (2002).
186. Lalau, Y. Etude du comportement thermomécanique de matériaux céramiques sous irradiation solaire concentrée : développement expérimental et modélisation. (Universite de Perpignan via Domitia, 2018).
187. Lalau, Y. *et al.* IMPACT: A new device for thermo-mechanical investigation on central receiver materials. *AIP Conf. Proc.* **2033**, (2018).
188. Vitiello, D. Thermo-physical properties of insulating refractory materials. (University of Limoges, 2021).
189. Smith, M. Abaqus Analysis User's Guide (6.14). (2017).
190. Drysdale, D. *An Introduction to Fire Dynamics, 3rd Edition*. (2011).
191. Oliveira, R. L. G., Rodrigues, J. P. C., Pereira, J. M., Lourenço, P. B. & Ulrich Marschall, H. Normal and tangential behaviour of dry joints in refractory

masonry. *Eng. Struct.* **243**, 112600 (2021).

192. Schacht, C. a. (Org. . Refractories Handbook. *Mech. Eng.* 500 (2004) doi:10.1017/CBO9781107415324.004.

Abstract

Improvement of strain field monitoring at high temperature and thermomechanical characterization of alumina spinel refractory materials

Alumina spinel refractories are known for their good performance in several areas of steel ladle lining. This study includes a thermomechanical investigation of an industrial alumina spinel bricks which allowed to detect microcracking (while cooling below 650 °C), brittle-ductile transition (at around 1100 °C) and variations of spinel content and stoichiometry being dependent on applied thermal treatment. Another investigation, related to model alumina spinel castables, reveals impacts of different types of aggregates, reactive aluminas and cements. Results obtained from both above-mentioned studies are interpreted in relation to likely performance in application. Apart from the material-oriented investigations, a significant part of this PhD study is dedicated to an improvement of two experimental techniques. The first one, used for high-temperature mechanical testing coupled with Digital Image Correlation (DIC) methods, has been improved to accurately monitor strain fields at high temperatures (1200 °C). This investigation includes optimization of high-temperature resistant speckle pattern and image pre-treatment for more accurate DIC measurements. The second type of improved experimental technique is a novel thermal shock bench (ATHORNA device). In this case, the experimental results, obtained by optical methods, are compared with finite element modelled results, being the first attempt to validate the numerical model with this device. Additionally, an investigation comparing ATHORNA and wedge splitting test results, performed on model magnesia spinel materials, allowed to demonstrate that ATHORNA can also be used for comparing thermal shock resistance of refractories.

Keywords: alumina spinel refractories, thermomechanical behaviour, microcracking, digital image correlation, speckle pattern, thermal shock monitoring

Résumé

Optimisation de la mesure de champ de déformation à haute température et caractérisation thermomécanique de matériaux réfractaires d'alumine spinelle

Les réfractaires d'alumine spinelle sont connus pour leurs bonnes performances en tant que revêtement de poche d'acier. Une première partie de l'étude s'est focalisée sur le comportement thermomécanique de briques industrielles d'alumine spinelle et a permis de mettre en évidence le développement de microfissures (au cours du refroidissant en dessous de 650 °C), une transition ductile fragile (aux environs de 1100 °C) et des changements de teneurs en spinelle et de stœchiométrie étroitement liés au traitement thermique appliqué. Une deuxième partie de l'étude concerne des bétons modèles d'alumine spinelle, et a permis de révéler l'impact de différents types d'agrégats, de différents types d'alumines réactives et de différents ciments. En sus des investigations portant sur les propriétés thermomécaniques des matériaux, une partie importante de cette thèse a également été consacrée à l'amélioration de deux techniques expérimentales. La première concerne des mesures de champs de déformations par corrélation d'images numériques (DIC) lors d'essais mécaniques à haute température (1200 °C). Afin d'optimiser la précision de mesures dans ces conditions expérimentales difficiles, une optimisation a spécifiquement porté sur des mouchetis résistant à haute température et sur l'application de prétraitements d'images avant les mesures DIC proprement dites. La deuxième concerne un nouveau banc de choc thermique (dispositif ATHORNA) qui est en cours de développement. Les résultats expérimentaux, obtenus sur ce banc par des méthodes optiques, ont pour la première fois pu être comparés aux résultats de modélisés par éléments finis. En outre, une étude comparant les résultats des tests d'ATHORNA et des essais de wedge splitting, réalisée sur des matériaux modèles de spinelle de magnésie, a permis de démontrer qu'ATHORNA pouvait également être utilisé pour comparer la résistance aux chocs thermiques de réfractaires.

Mots clés: réfractaires d'alumine spinelle, comportement thermomécanique, microfissuration, corrélation d'images numériques, mouchetis, chocs thermiques